



Optimisation of Fe₃O₄ Thin Films and Nanostructures for Atom Trapping Applications

Ruth Catharine Bradley

Department of Materials Science and Engineering

The University of Sheffield

Thesis submitted for the degree of

Doctor of Philosophy

July 2017

Abstract

Thin films and nanostructures of Fe_3O_4 have been investigated and analysed with the aim of being used for an exciting application where the stray magnetic field from domain walls in nanowires are used to trap ultra-cold atoms.

In this thesis, polycrystalline Fe_3O_4 thin films have been successfully grown on Si using reactive dc magnetron sputtering from a Fe target. It has been shown that by using different growth temperatures produces different iron oxide phases. Fe_3O_4 was grown at substrate temperatures of 200 – 500 °C with a mixed iron oxide phase of Fe_3O_4 & $\alpha\text{-Fe}_2\text{O}_3$ produced at RT & 100 °C.

In contrast to the polycrystalline, granular films on Si, Fe_3O_4 thin films grown on MgO (100) have been shown to be textured with a smooth surface. However, multiple different surface morphologies have been found for the $\text{Fe}_3\text{O}_4/\text{MgO}$ films. The coercivity of the Fe_3O_4 films has a negative trend with the film thickness for both substrates, whereas the grain size ($\text{Fe}_3\text{O}_4/\text{Si}$) has a positive trend with both film thickness and growth temperature.

Following an annealing treatment of Fe_3O_4 thin films at 250 °C the composition of the film was altered to become a mixed iron oxide of Fe_3O_4 & $\gamma\text{-Fe}_2\text{O}_3$. Dramatic changes in coercivity have been observed, with a large increase seen for the films on Si and negligible change seen for the films on MgO. However, a significant decrease in coercivity has been seen for a smooth film on MgO and the increase in coercivity on Si is dependent on the presence of Fe_3O_4 regions amongst the mixed iron oxide.

Nanostructures of Fe_3O_4 were created from thin films on Si & MgO, with the nanorings remaining in a saturated state after an in-plane magnetic field is removed. Applying a small negative field to the nanorings on MgO produces a magnetic structure similar to that seen in nanostructures with a 4-fold magnetocrystalline anisotropy.

Acknowledgements

Firstly, I would like to acknowledge and thank my project supervisors Dr. Tom Hayward and Prof. Dan Allwood for all their encouragement and guidance through this journey. I am very grateful for their support along the treacherous mission that is working with magnetite thin films!

I'd like to give a huge thank you to all the members of SCAMMD during my time at Sheffield, especially Dr. Matt Hodges, Dr. Jim Wheelwright, Dr. Weigang Yang, Mr Tom Broomhall, Mr. Jonathon Wood & Mr Alex Wynn. You have all definitely made this new part of my life exciting and lively. I would also like to give a special thanks to Dr. Laura Gardner for her amazing support and friendship over these eventful years.

Acknowledgement needs to be given to several people who have assisted me with learning and using experimental equipment. A big thank you to Ms Dawn Bussey, Dr. Nik Reeves-McLaren, Mr Richard Frith, Dr. Paul Fry, Dr. Ken Kennedy and Wayne Frankish & the EEE Workshop. I would also like to thank Dr. Anders Barlow and the NEXUS XPS group for performing XPS measurements on my samples and aiding with the analysis.

A huge thank you to my parents, Arthur & Barbara, and to my sister, Rachel. Your love and support have helped me through all the highs and lows of this project, and you have always been there for a much needed "walk and talk". Finally, I would like to thank the most important person to me during this project and that is my partner, Mike Shaw. You have been there through the challenging times and still been able to put a smile on my face.

Thank you!

Table of Contents

ABSTRACT	I
ACKNOWLEDGEMENTS	II
TABLE OF CONTENTS	III
1. INTRODUCTION	1
1.1. THESIS OUTLINE.....	3
REFERENCES	6
2. THEORY	11
2.1. INTRODUCTION TO MAGNETISM.....	11
2.2. CLASSES OF MAGNETIC MATERIALS.....	14
2.2.1. Diamagnetism	14
2.2.2. Paramagnetism	15
2.2.3. Ferromagnetism	18
2.2.4. Anti-Ferromagnetism	24
2.2.5. Ferrimagnetism	26
2.3. FREE ENERGY OF FERROMAGNETIC MATERIALS.....	28
2.3.1. Exchange energy	28
2.3.2. Magnetostatic energy	29
2.3.3. Magnetocrystalline anisotropy.....	31
2.3.4. Zeeman Energy.....	33
2.4. IRON OXIDES.....	34
2.4.1. Structure	35
2.4.2. Magnetism of Iron Oxides	39
REFERENCES	41
3. LITERATURE REVIEW	43

TABLE OF CONTENTS

3.1.	ATOM TRAPPING	43
3.2.	MAGNETIC TRAPS	45
3.2.1.	<i>How atoms react in a magnetic field</i>	45
3.2.2.	<i>Magnetic microtraps based on current carrying wires</i>	47
3.2.3.	<i>Free standing wires to atom chips</i>	49
3.2.4.	<i>Mobile domain wall traps</i>	52
3.3.	MAGNETITE THIN FILMS	57
3.3.1.	<i>Verwey Transition</i>	58
3.3.2.	<i>Anti-Phase Boundaries</i>	59
3.3.3.	<i>Magnetite thin film growths</i>	62
3.3.4.	<i>APB density reduction methods</i>	70
3.4.	MAGNETITE NANOSTRUCTURES	78
	CONCLUSION	87
	REFERENCES	89
4.	EXPERIMENTAL TECHNIQUES	97
4.1.	GROWTH AND FABRICATION TECHNIQUES	98
4.1.1.	<i>Sputtering</i>	98
4.1.2.	<i>Nanostructure formation</i>	101
4.1.2.1.	<i>Electron beam lithography</i>	102
4.1.2.2.	<i>Thermal evaporation</i>	104
4.1.2.3.	<i>Ion milling</i>	106
4.2.	COMPOSITIONAL AND PHASE ANALYSIS	108
4.2.1.	<i>X-ray diffraction</i>	108
4.2.2.	<i>Raman spectroscopy</i>	113
4.2.3.	<i>X-ray photoelectron spectroscopy</i>	117
4.3.	SURFACE IMAGING	121
4.3.1.	<i>Atomic force microscopy</i>	121
4.3.2.	<i>Spectroscopic ellipsometry</i>	124

4.4.	ELECTRICAL ANALYSIS.....	126
4.4.1.	<i>Four-point collinear probe method</i>	126
4.5.	MAGNETIC ANALYSIS.....	129
4.5.1.	<i>Magneto-optic Kerr effect magnetometer</i>	129
4.5.2.	<i>Magnetic force microscopy</i>	132
4.5.3.	<i>Magnetic Transmission X-ray Microscopy</i>	133
	REFERENCES	135
5.	GROWTH AND INITIAL CHARACTERISATION OF IRON OXIDE THIN FILMS	139
5.1.	INTRODUCTION.....	139
5.2.	ANALYSIS OF IRON THIN FILMS ON SILICON SUBSTRATES.....	139
5.2.1.	<i>Magneto-optical Kerr effect magnetometry</i>	141
5.2.2.	<i>Glancing angle x-ray diffraction</i>	144
5.2.3.	<i>Resistivity measurements</i>	145
5.3.	SUBSTRATE TEMPERATURE DEPENDENCE ON IRON OXIDE GROWTH.....	147
5.3.1.	<i>Compositional analysis</i>	148
5.3.1.1.	<i>Glancing angle x-ray diffraction</i>	149
5.3.1.2.	<i>X-ray photoelectron spectroscopy</i>	151
5.3.1.3.	<i>Raman spectroscopy</i>	155
5.3.1.4.	<i>Ellipsometry</i>	159
5.3.2.	<i>Magneto-optical Kerr effect Magnetometry</i>	161
5.3.	CONCLUSION.....	167
	REFERENCES	170
6.	ANALYSIS AND OPTIMISATION OF THE MORPHOLOGY AND MAGNETIC PROPERTIES OF Fe₃O₄/SI AND Fe₃O₄/MGO (100) THIN FILMS	173
6.1.	INTRODUCTION.....	173
6.2.	SAMPLE GROWTH	174
6.3.	TEXTURE ANALYSIS OF Fe ₃ O ₄ /MGO (100) THIN FILMS.....	175
6.4.	STUDY OF SURFACE MORPHOLOGIES OF Fe ₃ O ₄ /SI & Fe ₃ O ₄ /MGO (100) THIN FILMS.....	180

TABLE OF CONTENTS

6.4.1.	<i>Surface morphology of Fe₃O₄/Si thin films</i>	180
6.4.2.	<i>Surface morphology of Fe₃O₄/MgO (100) thin films</i>	185
6.5.	ANALYSIS OF MAGNETIC PROPERTIES OF Fe ₃ O ₄ /SI AND Fe ₃ O ₄ /MGO THIN FILMS.....	196
6.6.	INVESTIGATION INTO THE MAGNETIC SWITCHING MECHANISM FOR Fe ₃ O ₄ /Si ₃ N ₄	206
6.7.	RESISTIVITY MEASUREMENTS	211
6.8.	CONCLUSION.....	214
	REFERENCES	216
7.	COERCIVITY MODIFICATION OF Fe₃O₄ THIN FILMS USING ANNEALING TREATMENT.....	219
7.1.	OXIDATION METHODOLOGY.....	220
7.2.	INITIAL OXIDATION.....	221
7.2.1.	<i>Compositional analysis</i>	221
7.2.2.	<i>Surface morphology</i>	232
7.2.3.	<i>Magnetic analysis</i>	233
7.3.	REPEATABILITY OF ANNEALING TREATMENT	236
7.3.1.	<i>Magnetic analysis</i>	237
7.3.2.	<i>Raman spectroscopy</i>	240
7.3.3.	<i>Surface morphology</i>	247
7.3.4.	<i>Discussion</i>	253
7.4.	CONCLUSION.....	255
	REFERENCES	257
8.	STUDY OF Fe₃O₄ NANOSTRUCTURES ON SI & MGO (100) SUBSTRATES.....	259
8.1.	INTRODUCTION.....	259
8.2.	DESIGN AND FABRICATION OF NANOSTRUCTURES.....	260
8.3.	MAGNETIC FORCE MICROSCOPY OF RING-SHAPED NANOWIRES FOLLOWING SATURATION.....	261
8.4.	MAGNETIC FORCE MICROSCOPY OF RING-SHAPED NANOWIRES FOLLOWING APPLICATION OF REVERSE MAGNETIC FIELDS.....	272
8.5.	USING A MAGNETISED Fe ₃ O ₄ NANOSTRUCTURE AS A NANOSCALE MAGNETIC FIELD SOURCE	277
8.6.	CONCLUSION.....	280

TABLE OF CONTENTS

REFERENCES	282
9. CONCLUSION	283
LIST OF ACRONYMS, SYMBOLS AND CONSTANTS	287

TABLE OF CONTENTS

1. Introduction

Nanomagnetism is an area of research that explores the magnetic properties of materials that have at least one dimension that is in the nanoscopic range. These nanoscale materials (such as thin films, 3D nanoparticles and 2D/pseudo 2D nanostructures) exhibit magnetic properties and behaviours that are different from their bulk equivalents, and these result in a wide range of practical applications for nanomagnetic materials and devices. These applications include the use of ferrofluids in loudspeakers [1, 2], nanoparticles for drug delivery [3, 4], and thin films and nanostructures for use in magnetic recording and hard-disk drives (HDDs) [5, 6].

There has recently been great interest in the behaviour of domain walls (DWs) in planar magnetic nanowires due to proposed applications for their use as data carriers in magnetic memory [5] and logic technologies [7, 8]. One of the appeals of domain walls for these applications is their particle-like properties, which allow them to be transported and manipulated around complex nanowire networks using applied fields or electric currents [9, 10]. The motion of domain walls also allows binary data encoded in the direction of domains (one of the two directions along the nanowires) to transport data in solid state devices [8], which is in contrast with conventional HDDs where the sensors move to the data [6]. This is exciting as it will allow the data bits to move to the position of a read head without the need to physically move any components.

It has also been shown that DWs in nanowires can also be used for more novel applications. For example, it has been theoretically shown that the fields emanating

INTRODUCTION

from DWs in Permalloy nanowires could be used to trap and transport ultra-cold paramagnetic atoms around a nanowire circuit [11, 12]. With their weak interactions with the external world, ultra-cold atoms are attractive candidates for quantum information processing (QIP). The combination of the magnetic field minima produced above the DWs in the magnetic nanowires providing tight confinement and controlled motion of trapped atoms, and the weak interactions of the ultra-cold atoms with the external world make this an exciting and promising candidate system for performing QIP. However, in metallic nanowires thermally-induced electrical noise limits the lifetimes of trapped atoms through the generation of RF radiation, which can cause spin-flip transitions of the trapped atoms [13]. Such spin-flip transitions to untrapped Zeeman sublevels can cause the atoms to be ejected from their traps [14-16]. Using an oxide material with a higher electrical resistivity and a large enough magnetisation saturation to support the trap, such as Fe_3O_4 , would substantially increase trap lifetimes. Fe_3O_4 appears a particularly good choice among magnetic insulators for the atom trapping application due to its high Curie temperature ($T_C = 860$ K) and large room temperature magnetisation saturation ($M_S = 471$ kA/m).

Fe_3O_4 or magnetite has been the focus of scientific research for nearly a century due to its attractive magnetic and electrical properties. It was the first material found to exhibit a Verwey transition, where there is a dramatic increase in resistivity and a large drop in the magnetisation below 125 K due to changes in the crystal structure [17-20]. Magnetite is also predicted to be half-metallic [21-23], which when combined with its large saturation magnetisation and high Curie temperature, leads to it being a promising material for spintronic devices such as magnetic tunnel junctions [24, 25]. Another interesting feature and a focus of research Fe_3O_4 thin films is the presence of thin film growth defects called anti-phase boundaries (APBs) where the Fe-sublattice

is disrupted. The presence of APBs in magnetite films drastically alters their magnetic and electrical properties from bulk values [26, 27].

The objective of this thesis is to develop Fe_3O_4 thin films grown using reactive sputtering for nano-patterning into domain wall (DW) atom traps. The ultimate aim is to fabricate and pattern a high resistivity material that is magnetically soft enough to produce head-to-head DWs in a nanostructure, thus creating a system that could be used to create DW atom traps with long trap lifetimes. This investigation can be split into three main sections: creating Fe_3O_4 thin films (Chapter 5), optimising the film properties (Chapters 6 & 7) and then patterning said films into nanostructures (Chapter 8). Currently, there is little research into Fe_3O_4 planar nanowires which makes this project an exciting and challenging study.

1.1. Thesis Outline

This thesis has been divided into 9 chapters (with this introduction being Chapter 1).

The subsequent chapters will cover the following areas:

Chapter 2 introduces the basic theory of magnetism, the different classes of magnetic materials and the magnetic energy terms that govern the magnetisation configuration formed in ferromagnetic thin films and nanostructures. A brief review of the basic structure and magnetism of bulk iron oxides is also included.

Chapter 3 comprises of a review of the literature relating to the aims of this project, and is split into two halves. The first section briefly introduces techniques used to trap atoms including optical and magnetic traps, before describing a technique of trapping

INTRODUCTION

atoms using mobile domain walls above nanowires. This is followed by a review of the properties of Fe_3O_4 thin films including the Verwey transition, anti-phase boundaries (APBs), as well as APB density reduction methods. A review of the magnetic and electrical properties that various authors have measured for Fe_3O_4 thin films is also presented as a comparison to the results obtained in this thesis. Finally, the chapter discusses previous studies of planar Fe_3O_4 nanostructures.

Chapter 4 describes the experimental techniques used in this thesis, and is split into 5 sections: growth and fabrication techniques, compositional and phase analysis, surface imaging, electrical analysis and magnetic analysis.

Chapter 5 first describes the growth and characterisation of Fe thin films on Si substrates for comparison with the iron oxide thin film growth. This is followed by a study of the growth of iron oxide thin films using reactive DC magnetron sputtering on Si substrates at a variety of substrate temperatures.

Chapter 6 studies effects of film thickness, substrate choice and growth temperature on the coercivity, resistivity and grain size of Fe_3O_4 thin films. The analysis of these films provides a guide to the thickness, substrate and temperature combination from which a Fe_3O_4 film with optimised properties for patterning into magnetic nanostructures.

Chapter 7 comprises of magnetic, compositional and electrical analysis of Fe_3O_4 thin films before and after annealing treatment, which was used as a coercivity adjustment technique. This is with the goal of reducing the coercivity value of the thin films in Chapter 6 to increase the probability of producing domain walls in nanostructures patterned from Fe_3O_4 films.

Chapter 8 investigates magnetisation states and switching behaviour of nanostructures patterned from the thin films developed in Chapter 6, with the ultimate aim of assessing the feasibility of forming domain walls in planar Fe₃O₄ nanowires.

Chapter 9 brings the results of the preceding chapters together in order to draw a conclusion from the study, and also presents ideas for further research to extend the work described in this thesis.

References

- [1] K. Raj and R. Moskowitz, "Commercial applications of ferrofluids," *Journal of Magnetism and Magnetic Materials*, vol. 85, pp. 233-245, 1990.
- [2] K. Raj, B. Moskowitz, and R. Casciari, "Advances in ferrofluid technology," *Journal of Magnetism and Magnetic Materials*, vol. 149, pp. 174-180, 1995.
- [3] C. Sun, J. S. H. Lee, and M. Zhang, "Magnetic nanoparticles in MR imaging and drug delivery," *Advanced Drug Delivery Reviews*, vol. 60, pp. 1252-1265, 2008.
- [4] M. Arruebo, R. Fernandez-Pacheco, M. R. Ibarra, and J. Santamaria, "Magnetic nanoparticles for drug delivery," *Nanotoday*, vol. 2, pp. 22-32, 2007.
- [5] S. S. P. Parkin, M. Hayashi, and L. Thomas, "Magnetic domain-wall racetrack memory," *Science*, vol. 320, pp. 190-194, 2008.
- [6] R. Wood, "Future hard disk drive systems," *Journal of Magnetism and Magnetic Materials*, vol. 321, pp. 555-561, 2009.
- [7] D. A. Allwood, G. Xiong, M. D. Cooke, C. C. Faulkner, D. Atkinson, N. Vernier, *et al.*, "Submicrometer ferromagnetic NOT gate and shift register," *Science*, vol. 296, pp. 2003-2006, 2003.
- [8] D. A. Allwood, G. Xiong, C. C. Faulkner, D. Atkinson, D. Petit, and R. P. Cowburn, "Magnetic domain-wall logic," *Science*, vol. 309, pp. 1688-1692, 2005.
- [9] M. Negoita, T. J. Hayward, and D. A. Allwood, "Controlling domain walls velocities in ferromagnetic ring-shaped nanowires," *Applied Physics Letters*, vol. 100, pp. 072405-072409, 2012.

- [10] A. Kunz and J. Vogeler-Wunsch, "Application of local transverse fields for domain wall control in ferromagnetic nanowire arrays," *Applied Physics Letters*, vol. 101, pp. 192402-192405, 2012.
- [11] D. A. Allwood, T. Schrefl, G. Hrkac, I. G. Hughes, and C. S. Adams, "Mobile atom traps using magnetic nanowires," *Applied Physics Letters*, vol. 89, pp. 014102-014104, 2006.
- [12] T. J. Hayward, A. D. West, K. J. Weatherill, T. Schrefl, I. G. Hughes, and D. A. Allwood, "Nanomagnetic engineering of the properties of domain wall atom traps," *Journal of Applied Physics*, vol. 110, pp. 123918-123925, 2011.
- [13] R. Folman, P. Kruger, J. Schmiedmayer, J. Denschlag, and C. Henkel, "Microscopic atom optics: From wires to an atom chip," *Advances in Atomic, Molecular, and Optical Physics*, vol. 48, pp. 263-356, 2002.
- [14] D. M. Harber, J. M. McGuirk, J. M. Obrecht, and E. A. Cornell, "Thermally induced losses in ultra-cold atoms magnetically trapped near room-temperature surfaces," *Journal of Low Temperature Physics*, vol. 133, pp. 229-238, 2003.
- [15] M. P. A. Jones, C. J. Vale, D. Sahagun, B. V. Hall, and E. A. Hinds, "Spin coupling between cold atoms and the thermal fluctuations of a metal surface," *Physical Review Letters*, vol. 91, pp. 080401-080404, 2003.
- [16] S. Scheel, P. K. Rekdal, P. L. Knight, and E. A. Hinds, "Atomic spin decoherence near conducting and superconducting films," *Physical Review A*, vol. 72, pp. 042901-042904, 2005.
- [17] L. Degiorgi, I. Blatter-Morke, and P. Wachter, "Magnetite: Phonon modes and the Verwey transition," *Physical Review B*, vol. 35, pp. 5421-5424, 1987.

INTRODUCTION

- [18] V. A. M. Brabers, F. Walz, and H. Kronmuller, "Impurity effects upon the Verwey transition in magnetite," *Physical Review B*, vol. 58, pp. 14163-14166, 1998.
- [19] J. Garcia and G. Subias, "The Verwey transition - a new perspective," *Journal of Physics: Condensed Matter*, vol. 16, pp. R145-R178, 2004.
- [20] F. Walz, "The Verwey transition - a topical review," *Journal of Physics: Condensed Matter*, vol. 14, pp. R285-R340, 2002.
- [21] A. Pratt, M. Kurahashi, X. Sun, D. Gilks, and Y. Yamauchi, "Direct observation of a positive spin polarization at the (111) surface of magnetite," *Physical Review B*, vol. 85, pp. 180409-180412, 2012.
- [22] Y. Peng, C. Park, and D. E. Laughlin, "Fe₃O₄ thin films sputter deposited from iron oxide targets," *Journal of Applied Physics*, vol. 93, pp. 7957-7959, 2003.
- [23] W. B. Mi, E. Y. Jiang, and H. L. Bai, "Fe³⁺/Fe²⁺ ratio controlled magnetic and electrical transport properties of polycrystalline Fe₃(1-d)O₄ films," *Journal of Physics D: Applied Physics*, vol. 42, pp. 1-7, 2009.
- [24] J. Ding, D. Zhang, M. Arita, Y. Ikoma, K. Nakamura, K. Saito, *et al.*, "Growth and characterisation of Fe₃O₄ films," *Materials Research Bulletin*, vol. 46, pp. 2212-2216, 2011.
- [25] P. B. Jayathilaka, C. A. Bauer, D. V. Williams, M. C. Monti, J. T. Markert, and C. W. Miller, "Impact of ultrathin transition metal buffer layers on Fe₃O₄ thin films," *Journal of Applied Physics*, vol. 107, pp. 09B101-09B103, 2010.
- [26] D. T. Margulies, F. T. Parker, M. L. Rudee, F. E. Spada, J. N. Chapman, P. R. Aitchison, *et al.*, "Origin of the anomalous magnetic behaviour in single crystal Fe₃O₄ films," *Physical Review Letters*, vol. 79, pp. 5162-5165, 1997.

- [27] W. Eerenstein, T. T. M. Palstra, T. Hibma, and S. Celotto, "Origin of the increased resistivity in epitaxial Fe_3O_4 films," *Physical Review B*, vol. 66, pp. 201101-201104, 2002.

INTRODUCTION

2. Theory

This chapter will provide a brief introduction to the basic theory of magnetic materials and a summary of the structure and magnetic properties of iron oxides. A more detailed survey of contemporary literature investigating the properties of Fe₃O₄ thin films can be found in Chapter 3.

2.1. Introduction to magnetism

In the 1750's, both Michell and Coulomb independently discovered the law of interaction between magnetic poles. Analogous to Coulomb's law for electric charges, this interaction shows a proportional relationship between the force, F , between two magnetic poles and the product of their pole strengths, p_i . The force is also inversely proportional to the square of the pole separation, r . This relationship is shown in equation (2.1) using the SI unit system:

$$F = \frac{\mu_0 p_1 p_2}{4\pi r^2} \quad (2.1)$$

The field that is created by a magnetic pole produces the force acting on the second pole, and this force is directly related to the pole strength and the magnetic field strength, H :

$$F = \frac{\mu_0}{4\pi} p H \quad (2.2)$$

THEORY

Combining equations (2.1) & (2.2) gives a relationship for the strength of the field from a pole (equation (2.3)):

$$H = \frac{p_1}{r^2} \quad (2.3)$$

The units of field strength are Oersted (Oe) in cgs units and Ampere per metre (Am^{-1}) in SI units. To give an idea of the strength of these fields, the magnetic field from the Earth is less than 0.5 Oe (40 A/m) whereas the field from the end of a bar magnet is around 5000 Oe (400 kA/m) [1, 2].

Convention dictates that the magnetic field lines originate at the north pole of a magnet, and terminate at the south pole. A schematic diagram indicating the magnetic field lines around a typical bar magnet is shown in Figure 2.1.

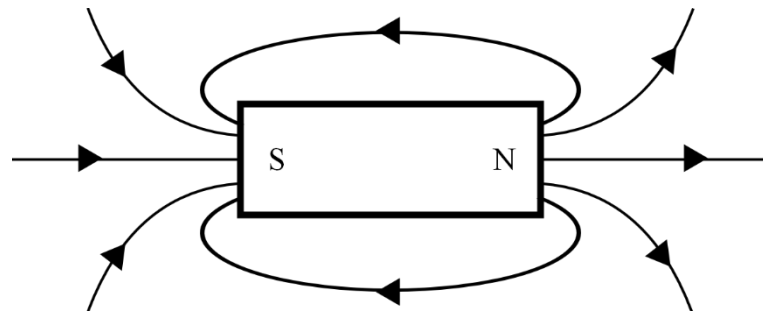


Figure 2.1. Illustration showing the magnetic field lines around a bar magnet where the field lines originate at the north pole and terminate at the south pole.

When a magnet is placed at an angle, σ , in a magnetic field, a torque acts on the magnet to align it parallel with the applied field. The torque is proportional to the magnet's magnetic moment, m , which is the product of its pole strength and the magnet length, l :

$$\mathbf{m} = pl \quad (2.4)$$

The torque of the magnet can be given by:

$$\boldsymbol{\tau} = mH \sin \sigma \quad (2.5)$$

A medium's response when a magnetic field is applied is called its magnetic induction or magnetic flux density, \mathbf{B} . In free space, \mathbf{B} and \mathbf{H} are directly proportional but inside a material another term is included in the relationship: the material's magnetisation, \mathbf{M} . This property is defined as the magnetic moment per unit volume, and is dependent on the material's individual magnetic moments and how these dipole moments interact with each other.

$$\mathbf{B} = \mu_0(\mathbf{H} + \mathbf{M}) \quad (2.6)$$

A material's magnetic properties are defined not only by the magnitude of the magnetisation but also by its susceptibility, χ , which is how the magnetisation varies with applied field.

$$\chi = \frac{\mathbf{M}}{\mathbf{H}} \quad (2.7)$$

A closely related parameter is the magnetic permeability, which reflects the ability of a material to support the formation of a magnetic field inside itself.

$$\mu = \frac{\mathbf{B}}{\mathbf{H}} \quad (2.8)$$

The susceptibility and other magnetic properties of a material are strongly dependent on the types of magnetism it exhibits. The main classes of magnetic materials will be described below.

2.2. Classes of magnetic materials

2.2.1. Diamagnetism

The weakest of the magnetic effects is diamagnetism and it is present in all atoms. As it is so weak it is dominated by stronger interactions like paramagnetism and ferromagnetism in materials that exhibit these phenomena, and so only materials in which atoms that have no net magnetic moment (i.e. they have full electron shells) are typically classified as diamagnetic materials.

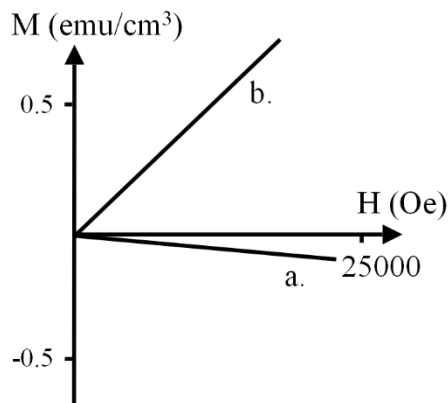


Figure 2.2. Schematic magnetisation curves for (a) diamagnetic, and (b) paramagnetic and anti-ferromagnetic materials. For the diamagnetic material, an applied magnetic field produces a negative magnetisation and a small, negative susceptibility, whereas a paramagnetic or anti-ferromagnetic material would produce a positive magnetisation and a positive susceptibility.

The diamagnetic effect is due to induced change in the orbital motion of electrons when a magnetic field is applied. As it is an induced effect the magnetic moment

created opposes the field creating it which give diamagnetic materials a small, negative susceptibility. A common example of a diamagnetic material is water which has a susceptibility of -9.1×10^{-6} [3]. A schematic illustrating the how the magnetisation of a diamagnetic material is affected when a magnetic field is applied is illustrated in Figure 2.2a.

2.2.2. Paramagnetism

Paramagnetism occurs in materials where the atoms carry magnetic moments, but where there is no intrinsic ordering of the moments. In the absence of applied fields the moments are thus randomly aligned (Figure 2.3) due to thermal energy. Applying a magnetic field competes against the thermally induced disorder and causes the magnetic moments to partially align with the field direction (for all practical field strengths). This leads to a susceptibility which is small, positive and approximately constant at low applied fields. An example of a paramagnetic material is aluminium, which has a susceptibility of 2.2×10^{-5} at 20 °C [4]. A schematic illustrating the how the magnetisation of a paramagnetic material is affected when a magnetic field is applied is illustrated in Figure 2.2b.

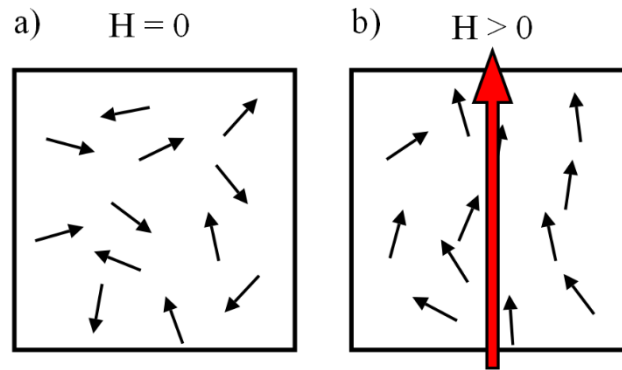


Figure 2.3. Schematic illustrating the random alignment of magnetic moments in a paramagnetic material when no external magnetic field is applied (a) and the partial alignment of magnetic moments in a paramagnetic material when an external magnetic field is applied (b).

Langevin created a localised-moment model to describe how the susceptibility of paramagnetic materials decreases with temperature. The assumption in this model is that the atoms have the same non-interacting magnetic moments and that they are randomly oriented due to their thermal energy in the absence of a magnetic field. By using Boltzmann statistics to find the probability of a magnetic moment (m) lying at an angle θ to the applied magnetic field (H) and averaging over a sphere of the paramagnetic material, the magnetisation (M) of a paramagnetic material can be described in terms of the Langevin function, $L(\alpha)$. A graphical representation of the Langevin function is shown in Figure 2.4.

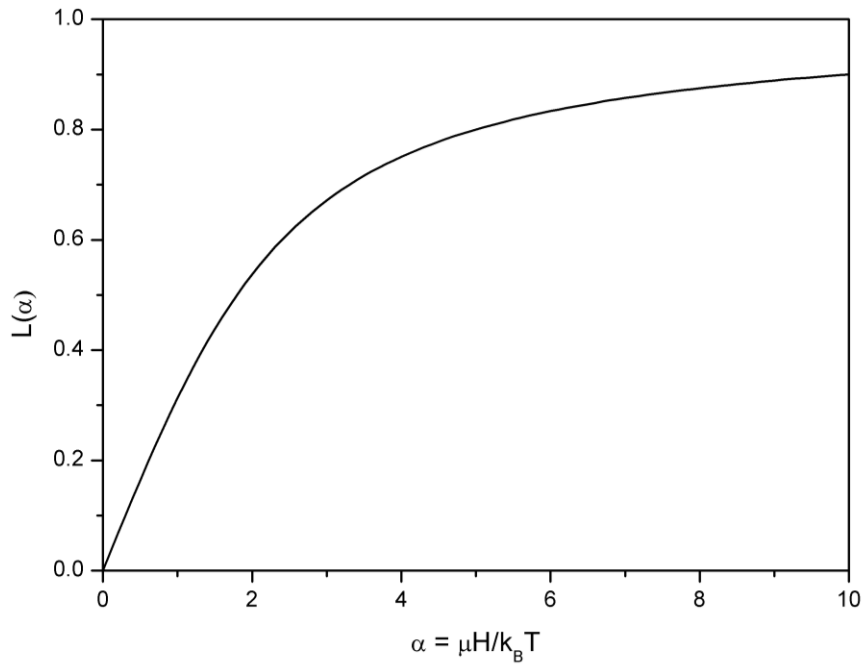


Figure 2.4. Graphical representation of the Langevin function.

$$\mathbf{M} = NmL(\alpha) \quad (2.9)$$

$$\alpha = \frac{mH}{k_B T} \quad L(\alpha) = \coth(\alpha) - \frac{1}{\alpha} \quad (2.10)$$

Where N is the number of atoms per unit volume, k_B is the Boltzmann constant and T is the temperature. By expanding the Langevin function as a Taylor series, the inverse proportionality between χ and T is clearly seen. This series expansion produces Curie's law (equation (2.11)).

$$\chi = \frac{Nm^2}{3k_B T} = \frac{C}{T} \quad (2.11)$$

Although Langevin's theory is phenomenologically correct, it does not produce qualitatively correct results as it neglects the quantisation of angular momentum. The

THEORY

Brillouin function ($B_J(\alpha)$) is used to incorporate quantisation into the derivation of the magnetisation giving a susceptibility of:

$$\chi = \frac{Ng^2J(J+1)\mu_B^2}{3k_B T} = \frac{C}{T} \quad (2.12)$$

Where J is the total angular momentum quantum number and g is the Landé g-factor.

2.2.3. Ferromagnetism

A ferromagnetic material can be defined as having a spontaneous magnetisation in the absence of an external magnetic field. The cause of this spontaneous magnetisation will be explained in this section.

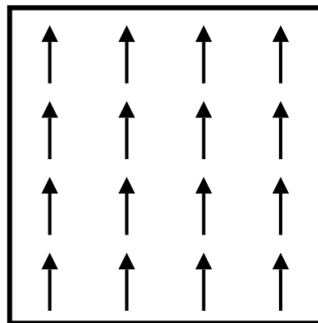


Figure 2.5. Schematic illustrating the parallel alignment of magnetic moments in a ferromagnetic material.

Langevin's theory only accounts for the effects of external fields and thermal agitation on the magnetic moments. It neglects the interaction between neighbouring moments which is why paramagnetic materials that have a ferromagnetic transition do not follow the Curie law. The Curie-Weiss law describes the susceptibility of

ferromagnetic materials that are heated into the paramagnetic region. The Curie-Weiss law follows a more general temperature dependence of:

$$\chi = \frac{C}{T - \theta} \quad (2.13)$$

Weiss explained the extra term (θ) in this relationship by postulating that there is an internal field (equation (2.14)) that acted in addition to the applied magnetic field. This is called the “molecular field” (H_W), where γ is the molecular field constant, and causes ordering of the material’s magnetic moments in the absence of applied fields.

$$H_W = \gamma M \quad (2.14)$$

When this extra field is included in the Curie law (equation (2.11)), it can be seen that $\theta (= C\gamma)$ is a measure of the strength of the molecular field.

Above a certain temperature, ferromagnetic materials become paramagnetic and it follows the Curie-Weiss law with a large value of θ , corresponding to a large molecular field. Weiss proposed that the molecular field acts on the material below this temperature as well, and that this field is so strong that it is capable of ordering magnetic moments in the absence of a magnetic field, causing spontaneous magnetisation.

The variation of spontaneous magnetisation with temperature can be explained by replacing the external field, H , in the classical Langevin description for magnetisation, equation (2.9), with the Weiss molecular field, equation (2.14), at a constant temperature and with zero applied field.

$$M = \left(\frac{k_B T}{m\gamma} \right) \alpha \quad (2.15)$$

THEORY

Plotting these two functions for M as a function of α produce two solutions at their intersection (Figure 2.6): $M = 0$ which is unstable, and a second temperature dependent value, which represents the spontaneous magnetisation, M_{spont} .

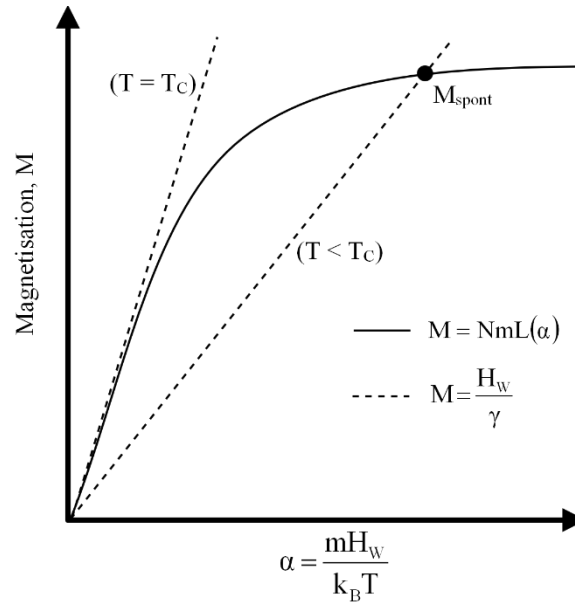


Figure 2.6. Illustration of spontaneous magnetisation using the Langevin function (solid line) and the Weiss molecular field (dashed lines) for constant temperature and zero applied field.

As the temperature increases, so does the gradient of equation (2.15) and when the gradient is the same as the tangent of the Langevin function at the $\alpha = 0$ limit the spontaneous magnetisation disappears. This temperature is called the Curie temperature (T_C) and is the transition temperature between ferromagnetism and paramagnetism. Below T_C the magnetisation increases as the intersection point rolls back along the curve. As mentioned before, a more accurate result can be calculated by using the Brillouin function instead of the Langevin function which can be seen in Figure 2.7 that illustrates the variation of the spontaneous magnetisation with

temperature. This is due to the Langevin function qualitatively predicting the variation of M with T , but not quantitatively.

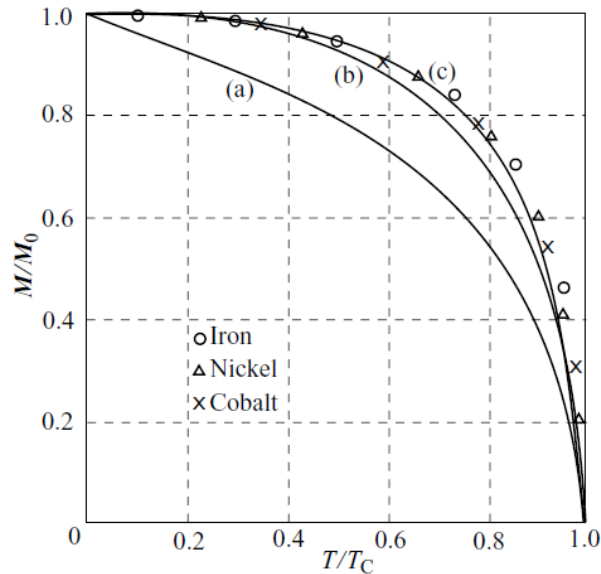


Figure 2.7. The relative spontaneous magnetisation of iron, nickel and cobalt as a function of relative temperature calculated using a) the classical Langevin function, b) the Brillouin function with $J = 1$ and c) $J = 1/2$. Taken from [1].

The molecular field is a phenomenological construct, and to physically understand why ferromagnetic materials exhibit a spontaneous magnetisation we are required to consider a quantum mechanical effect called the exchange interaction, which acts to locally align the magnetic moments of ferromagnetic moments. The exchange interaction has its origin in the Pauli exclusion principle which states that two electrons cannot share the same quantum numbers and hence they must have opposite spins to share the same orbital. This causes the electrons spatial component of the wavefunctions to overlap which in turn causes an increase in the Coulomb repulsion between them. Alternatively, the electrons occupying separate orbitals and having parallel spins can reduce the Coulomb interaction. This couples together the spatial

THEORY

and spin degrees of freedom such that in some materials the exchange interaction promotes ferromagnetic alignment of magnetic moments.

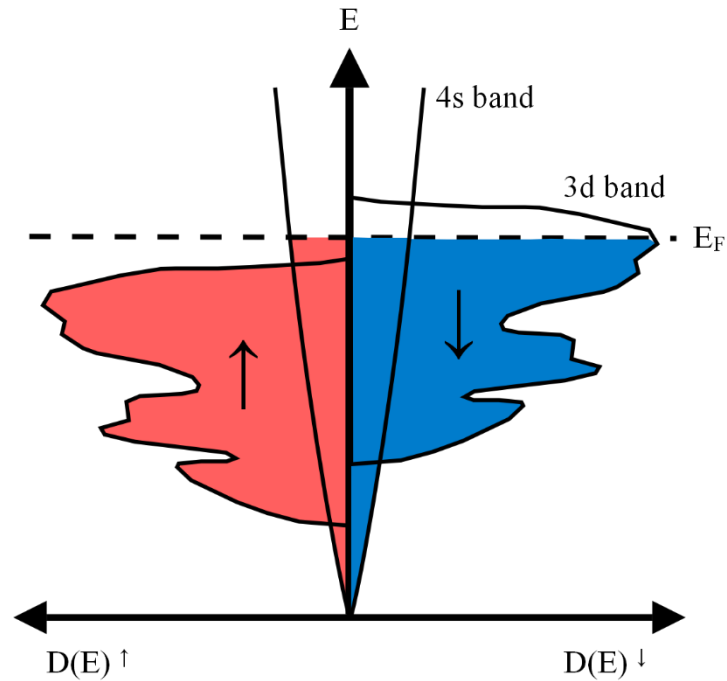


Figure 2.8. Schematic showing the density of states for the spin up and spin down 3d and 4s bands, with the exchange interaction included producing a full 3d spin up band and a partially filled 3d spin down band as shown by the Fermi level, E_F .

To produce a quantitative understanding of the ferromagnetism of 3d metals, a band-based model of the electronic structure is needed. This approach uses a rigid band approximation, that assumes that the shape of the overlapping 3d and 4s bands do not change for the first transition series elements. The 4s band covers a large energy range but has a low density of states as the atomic s orbital can only carry 2 electrons. Conversely, the 3d band has a narrow energy range and a large density of states as the atomic d orbital can carry 10 electrons. The larger the density of states, the less energy

is needed to reverse the spin of an electron, and therefore it is easier to flip the spin of an electron in the 3d band than the 4s band. The exchange interaction can be pictured as shifting the energy of the 3d band of one spin direction relative to the opposite spin direction (Figure 2.8). If the Fermi level lies within the 3d band, then this shift of the energy levels leads to more electrons of one spin direction than the other, thus causing a spontaneous magnetic moment in the ground state.

This shift is not an integer value, which causes the non-integer values for the magnetic moment of ferromagnetic materials. It also explains why Fe, Co and Ni are ferromagnetic and Cu and Zn are not, as their Fermi levels lie above the 3d band. Mn is not ferromagnetic as it appears that the exchange energy is not strong enough to keep one spin band full, whilst the other spin band is less than half full [1].

In ferromagnetic materials, the magnetic moments align parallel to each other (Figure 2.5). This produces a large net magnetisation, which in turn gives a very large and positive susceptibility that is a function of the applied field. The magnetisation does not follow a linear relationship with applied field and follows a hysteretic behaviour, which is illustrated in Figure 2.9. At the highest applied fields, the moments all align to the field giving the highest possible magnetisation, the saturation magnetisation M_S . The hysteretic behaviour means that when the applied field is removed, the material still retains a degree of magnetisation which is called the remanence, M_r . Another important value of a magnetisation graph is the coercivity, H_c , which is the magnetic field needed to reduce the net magnetisation to zero once the sample has been magnetised.

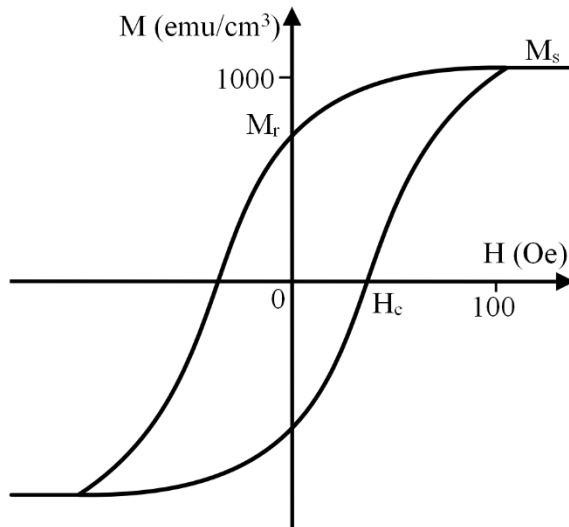


Figure 2.9. Schematic of an M - H loop from a ferromagnetic material showing the saturation magnetisation (M_s), coercivity (H_c) and the remanence (M_r).

2.2.4. Anti-Ferromagnetism

In an anti-ferromagnetic material adjacent spins align anti-parallel, and the material can be thought to have two identical and interpenetrating sublattices. Below the Néel temperature, T_N , one lattice is spontaneously magnetised in one direction and the other lattice is also magnetised but in the opposite direction (Figure 2.10). As these two lattices are identical and have opposite spins, this gives no net spontaneous magnetisation. Anti-ferromagnetic materials respond to an external magnetic field in a similar behaviour to paramagnetic materials, although unlike paramagnetic materials the susceptibility increases with temperature until T_N where it then decreases. This is because above T_N the anti-ferromagnetism vanishes and the material becomes paramagnetic, as in a ferromagnet.

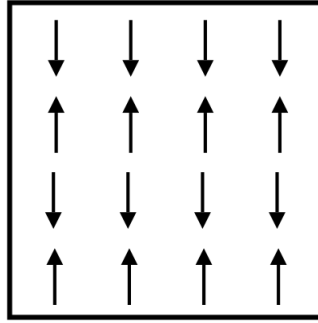


Figure 2.10. Schematic illustrating the anti-parallel alignment of magnetic moments between two parallel sublattices in an anti-ferromagnetic material.

The Weiss localised-moment theory can be used again to describe the relationship between temperature and susceptibility in anti-ferromagnets. Above T_N the susceptibility follows the Curie-Weiss law, but with a negative value of θ . This represents a negative molecular field, thus causing adjacent moments to be anti-parallel. The interaction between the nearest neighbour atoms on different lattices produces two molecular fields, where the field that acts on the first lattice (A) is equal and opposite to the field acting on the second lattice (B). Below T_N , the susceptibility is dependent on the angle between the applied magnetic field and the direction of the spontaneous magnetisations in the sublattices.

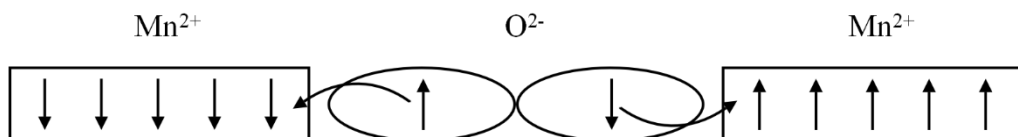


Figure 2.11. Illustration showing the superexchange mechanism seen in MnO where the spin orientation of one Mn^{2+} ion dictates the spin orientation of the second through the O^{2-} ion.

THEORY

The negative molecular field can be explained using the superexchange mechanism, where the interaction between the lattices of opposite spin is mediated through an intermediate ion. An example of this is in the antiferromagnet MnO, where the Mn^{2+} cations form the two magnetic lattices [3]. Figure 2.11 shows how the spin of one Mn^{2+} determines the spin of the next Mn^{2+} . The Mn^{2+} ion on the left has all of its down-spin orbitals occupied, and therefore covalent bonding can only occur if the O^{2-} ion donates an up-spin electron. This leaves a down-spin electron in the O^{2-} p-orbital which it donates to another Mn^{2+} ion. The second bond can only occur if the electrons in the Mn^{2+} ion are spin up.

2.2.5. Ferrimagnetism

Ferrimagnetic materials have similar properties to ferromagnetic materials and have a large positive susceptibility. They are, however, similar to anti-ferromagnetic materials at an atomic scale as the structure is composed of two lattices of anti-parallel moments (A & B). The presence of spontaneous magnetisation is due to one of the sublattices exhibiting larger magnetic moments than the other, thus producing a net magnetisation. To calculate the magnetisation for anti-ferromagnetic materials only the A-B exchange interaction is taken into account as the A-A and B-B exchange interactions were equal in magnitude. For a ferrimagnetic material, the A-A and B-B exchange interactions are no longer equal and are needed to reproduce the experimentally observed behaviour. The A-B exchange interaction between nearest-neighbours tends to align the moments of the two sublattices anti-parallel, and the A-A and B-B exchange interactions align the moments parallel on the sublattices.

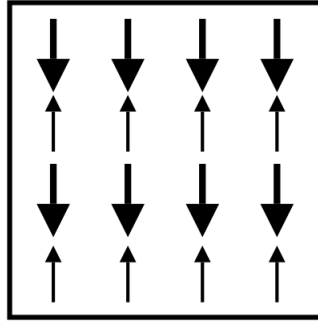


Figure 2.12. Schematic diagram illustrating the anti-parallel alignment of magnetic moments between two unequal, anti-parallel sublattices in a ferrimagnetic material.

Examples of ferrimagnetic materials include cubic ferrites which have the general formula $MO \cdot Fe_2O_3$ where M is a divalent metal ion [5]. These cubic ferrites have a spinel crystal structure comprising of two sublattices: tetrahedral (A) and octahedral (B). Magnetite ($Fe^{2+}O \cdot Fe^{3+}_2O_3$) has an inverse spinel structure where the Fe^{3+} ions are spread equally across the A & B lattices whereas the Fe^{2+} ions are located only on the B lattice. The dominant interaction for magnetite is the antiferromagnetic A-B interaction, where the spins of the Fe^{3+} ions on the A & B lattices are opposite and cancel each other. The Fe^{2+} ions on the B lattice are aligned parallel to each other and it is these ions that cause the net magnetisation.

2.3. Free Energy of Ferromagnetic Materials

This section describes the magnetic energy terms that govern the magnetisation configurations adopted by ferromagnetic materials. The main energy contributions are the exchange energy E_{ex} , the magneto-crystalline anisotropy E_K , the Zeeman energy E_Z , the magneto-static energy E_d and the magneto-elastic energy E_{me} .

$$E_{total} = E_{ex} + E_K + E_Z + E_d + E_{me} \quad (2.16)$$

The magneto-elastic energy term controls how the magnetic material responds when an external stress is applied or when a material is grown in a stressed state, but it will not be discussed further as it is not believed to have a significant effect on the samples studied in this thesis.

2.3.1. Exchange energy

The exchange energy was introduced in Section 2.2.3. and favours parallel alignment of spins across the whole material (i.e. uniformly magnetised configurations). The exchange energy is increased when there is a deviation from parallel alignment of the spins. Within a continuum approximation the exchange energy may be calculated using:

$$E_{ex} = A \int_V (\nabla \mathbf{m})^2 dV \quad (2.17)$$

where A is the material specific exchange stiffness constant and \mathbf{m} is the magnetic direction vector, $\mathbf{m} = \mathbf{M}/M_S$.

2.3.2. Magnetostatic energy

When the internal field lines that are created by the magnet are drawn, they act in the opposite direction to the magnetisation of the magnet. This field is called the demagnetising field, H_d , and it causes the magnetostatic energy, E_{ms} , which can be calculated using:

$$E_{ms} = \frac{1}{2} \mu_0 H_d M \quad (2.18)$$

where M is the magnetisation. A larger demagnetising field therefore produces a larger magnetostatic energy. The demagnetising field is proportional to the samples magnetisation using equation (2.19) and a shape dependent factor called the demagnetising factor, N_d .

$$H_d = -N_d M \quad (2.19)$$

The demagnetising factor can be calculated for different shapes, with N_d being the largest along the short axis, smallest along the long axis and $N_d \leq 1$ for all directions. For a 3-dimensional shape, the sum of the demagnetising factors along the three axes is equal to 1:

$$N_{dx} + N_{dy} + N_{dz} = 1 \quad (2.20)$$

For a rectangle of ferromagnetic material, the short axis will have a larger demagnetising factor which produces a larger magnetostatic energy than along the long axis. Therefore the magnetisation favours alignment along the long axis. This effect of the differing shapes on the magnetostatic energy is called shape anisotropy.

This shape anisotropy produces a larger magnetostatic energy perpendicular to a thin film surface compared to parallel to film surface, with the easy magnetisation direction

THEORY

in the film plane. For a 1-dimensional object (e.g. a nanowire), the easy magnetisation axis would be along the wire length.

One way to further reduce the magnetostatic energy of a rectangular magnet beyond that of the lowest energy uniform configuration, the magnet may split its magnetisation into domains that are anti-parallel to each other. This reduces the demagnetising field for a rectangle of ferromagnetic material as illustrated below in Figure 2.13b. For the lowest magnetostatic energy configuration, the magnet is split into two anti-parallel domains with the addition of closure domains at the ends (Figure 2.13c). The formation of these closure domains removes magnetic poles from the surface and thus the magnetostatic energy is minimised, but at the cost of forming domain walls which increases the exchange and anisotropy energies. Closure domains do not appear in all magnetic materials, only those with a cubic magnetocrystalline anisotropy.

A ring-shaped nanomagnet would have a very large demagnetising energy when in a uniform configuration (Figure 2.13a), which can be reduced by forming an “onion” state (Figure 2.13b) [6, 7] due to the relaxation of moments to lie predominantly parallel to the nanowire. The magnetostatic energy is reduced to zero by forming a vortex state (Figure 2.13c) which is a single domain state. The vortex state minimises the magnetostatic energy as the magnetisation circulates around the ring such that no magnetic poles are created, whereas the onion state still has a relatively large magnetostatic energy due to the stray field created by the head-to-head and tail-to-tail domain walls.

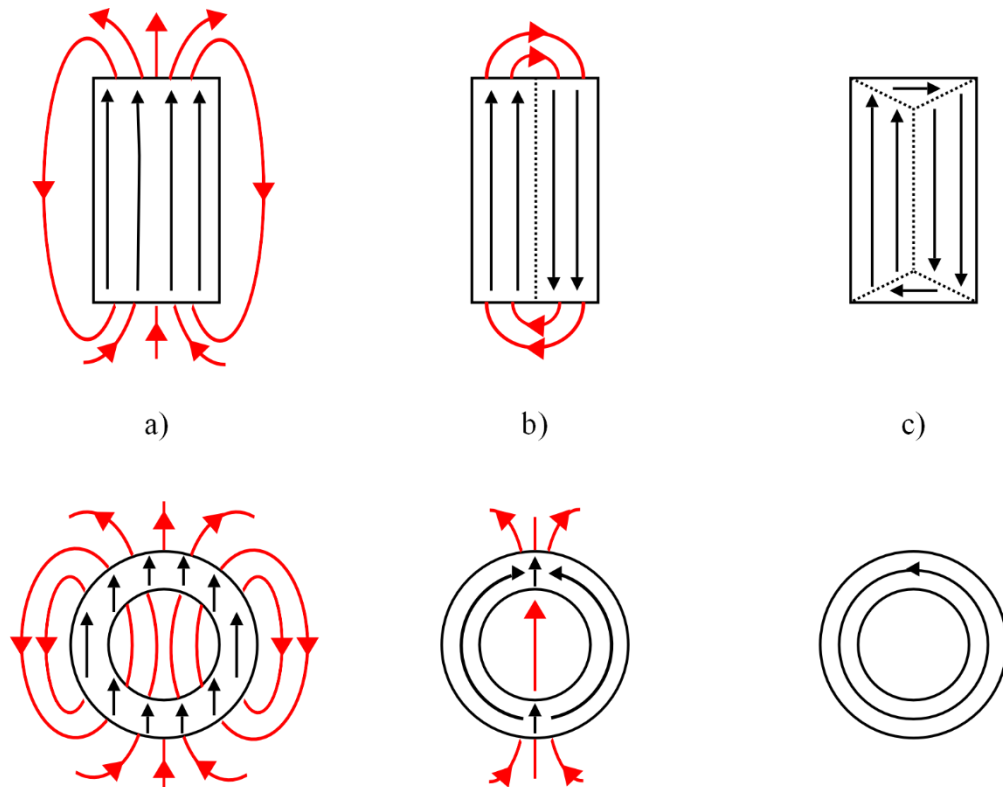


Figure 2.13. Schematic showing how the formation of domains reduces magnetostatic energy in rectangular and ring shaped structure. The magnetostatic energy is maximum in the structures in column a), intermediate in column b) and at a minimum in column c).

2.3.3. Magnetocrystalline anisotropy

The magnetocrystalline anisotropy causes the magnetisation of ferromagnetic materials to align preferentially along certain crystal axes, and is governed by the spin-orbit interaction which couples the material's spins to its crystal lattice. Axes along which it is energetically favourable to align the magnetisation are referred to as "easy" axes, whilst those where it is energetically unfavourable are referred to as "hard" axes.

THEORY

When magnetising a demagnetised sample a much larger field will be required to reach saturation along a hard axis than the easy axis, as is shown schematically in Figure 2.14.

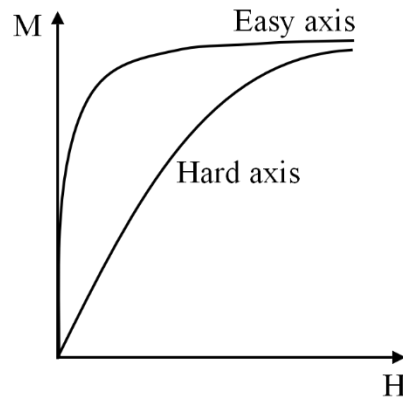


Figure 2.14. Schematic diagram showing M - H curves for magnetising a sample along the easy and hard magnetocrystalline axis.

The magnetocrystalline energy follows the symmetry of the crystal lattice and can be written in terms of a series expansion in directional cosines, α_i , of the saturation magnetisation to the crystal axes. For a cubic crystal structure the magnetocrystalline energy density is approximated by:

$$E_{KC} = K_0 + K_{C1}(\alpha_1^2\alpha_2^2 + \alpha_2^2\alpha_3^2 + \alpha_3^2\alpha_1^2) + K_{C2}(\alpha_1^2\alpha_2^2\alpha_3^2) \quad (2.21)$$

Where K_0 , K_{C1} and K_{C2} are anisotropy constants of the material. The sign of K_{C1} determines the easy axis of the material¹: a negative value prefers alignment along the $\langle 111 \rangle$ direction, whereas a positive value prefers the $\langle 100 \rangle$ direction. As an example, in body-centered cubic iron $K_{C1} = 4.8 \times 10^4 \text{ J/m}^3$ with an easy axis along the $\langle 100 \rangle$

¹The easy axis assignment using the sign of K_{C1} is valid when K_{C2} can be neglected, otherwise the size and sign of K_{C2} can cause different easy and hard axes.

direction whereas for face-centered cubic nickel $K_{CI} = -5 \times 10^3 \text{ J/m}^3$ with an easy axis along the $\langle 111 \rangle$ direction [2].

In a hexagonal crystal structure, the easy axis is along the hexagonal c axis. The symmetry of this structure causes a uniaxial anisotropy which is dependent on the angle ψ between the magnetisation and the hexagonal axis. The uniaxial energy can be approximated to the second order as:

$$E_{KU} = K_0 + K_{U1} \sin^2 \varphi + K_{U2} \sin^4 \varphi. \quad (2.22)$$

2.3.4. Zeeman Energy

The Zeeman energy represents the potential energy associated with applying an external magnetic field to a magnetic material. While the previously described energy terms are governed by the material properties and geometry of a magnet, the Zeeman energy is thus dependent on an *externally* applied magnetic field.

$$E_Z = -\mu_0 \mathbf{M} \cdot \mathbf{H} \quad (2.23)$$

To reduce the Zeeman energy, the moments move to point along the externally applied magnetic field direction. This change can occur via domain wall motion, where the domains parallel with the magnetic field grow in size, or for domains that cannot freely expand or contract and where there are no domain walls, via domain rotation where there is a twisting of the domains to align to the applied field.

2.4. Iron Oxides

There are four major oxides of iron, which vary in both their oxygen content and their crystal structure: wüstite (FeO), magnetite (Fe_3O_4), maghemite ($\gamma\text{-Fe}_2\text{O}_3$), and hematite ($\alpha\text{-Fe}_2\text{O}_3$). Additionally there are other iron oxides, such as $\beta\text{-Fe}_2\text{O}_3$ and $\varepsilon\text{-Fe}_2\text{O}_3$ which are stoichiometrically identical to Fe_2O_3 , but have rarely observed crystal structures and will not be discussed further here. The structure of iron oxides is dominated by the arrangement of the oxygen anions (O^{2-}) in the lattice. This is due to the radius of O^{2-} ions being 0.14 nm which is much larger than the radius of Fe^{2+} and Fe^{3+} (0.082 and 0.065 nm, respectively).

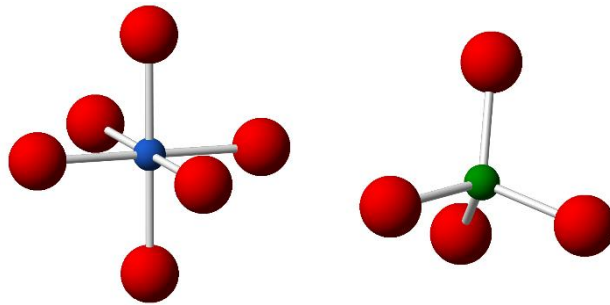


Figure 2.15. Ball and stick model of the two interstitial sites found in magnetite, with the octahedral site on the left and the tetrahedral site on the right. The red balls indicate the oxygen anions and the blue and green balls indicate the iron cations.

The iron cations sit in tetrahedral and octahedral interstitial sites in the oxygen lattice illustrated in Figure 2.15. The following section will introduce the structure and magnetic properties of these four iron oxides [5, 8].

2.4.1. Structure

Wüstite (FeO)

The oxygen anions and the ferrous cations in wüstite form an interpenetrating face centered cubic lattice, similar to the structure of NaCl. A unit cell of wüstite consists of four formula units, but as it is normally found in a cation-deficient phase as Fe_{1-x}O , the cell dimension varies from $a = 4.28 - 4.31 \text{ \AA}$. The Fe_{1-x}O phase is achieved by a proportion of the metal ions being oxidised as well as the creation of cation vacancies. The Fe^{2+} ions are mostly located in the octahedral interstices with a small proportion of Fe^{3+} ions on the usually vacant tetrahedral sites. The ratio of the Fe^{2+} and Fe^{3+} ions is dependent on how far away the iron oxide is from stoichiometry.

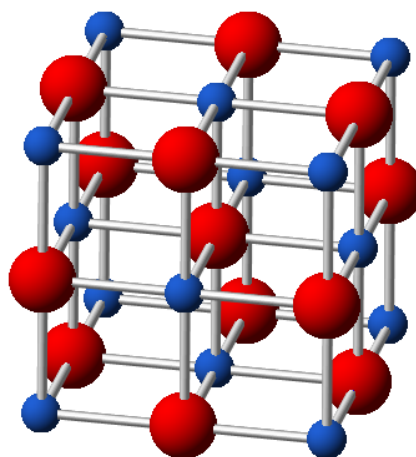


Figure 2.16. Ball and stick model of the crystal structure of wüstite, with the red balls indicating oxygen anions and the blue balls indicating iron cations.

Magnetite (Fe_3O_4)

Magnetite has an inverse spinel structure, which consists of a face centered cubic oxygen lattice with Fe^{2+} and Fe^{3+} cations on the tetrahedral (A) and octahedral (B) interstitial lattice positions. The ratio of the Fe^{2+} ions to the Fe^{3+} ions for stoichiometric Fe_3O_4 is 1:2, with only 1/8 of the 64 tetrahedral sites and 1/2 of the 32 octahedral sites occupied per unit cell. In a normal spinel all of the divalent ions are located on the tetrahedral sites, and all of the trivalent ions located on the octahedral sites. However, for an inverse spinel, such as magnetite, the trivalent ions are equally divided between the tetrahedral and octahedral sites and the divalent ions are located on the octahedral sites. A unit cell of magnetite consists of 8 formula units with a cell dimension of $a = 8.396 \text{ \AA}$.

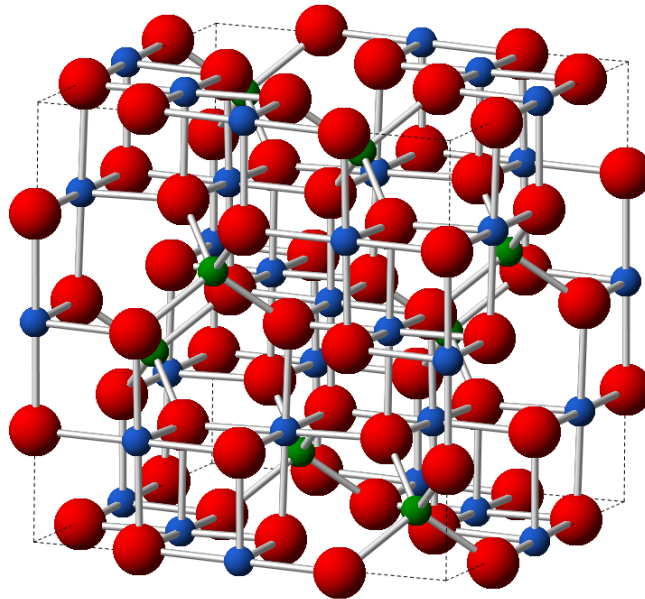


Figure 2.17. Ball and stick model of the crystal structure of magnetite, with the red balls indicating the oxygen anions and the blue and green balls indicating the iron cations. The blue balls are at an octahedral site and the green balls are at a tetrahedral site.

Magnetite undergoes a structural change from a cubic lattice to monoclinic in a transition called the Verwey transition at $T_V = 120$ K, where there is a large drop in magnetisation as well as an increase in the materials resistivity. This topic will be discussed further in Section 3.3.1.

Maghemite (γ -Fe₂O₃)

Maghemite has an iron deficient spinel structure, making it structurally similar to magnetite. The main difference is that whilst magnetite contains mixed valence (Fe²⁺ and Fe³⁺) iron ions, maghemite contains only Fe³⁺ ions. Maghemite can also be written as $(Fe_8^{3+})_A \left[Fe_{\frac{40}{3}}^{3+} \square_{\frac{8}{3}} \right]_B O_{32}$ where \square indicates a vacancy. A unit cell of maghemite consists of 8 formula units with a cell dimension of $a = 8.3474$ Å.

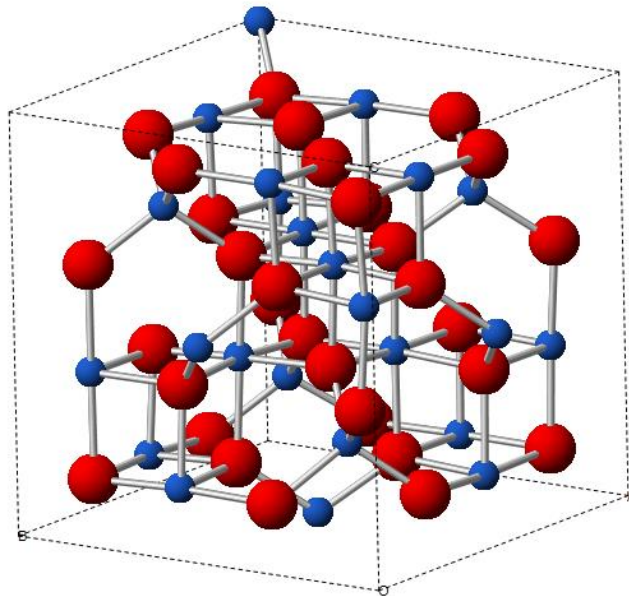


Figure 2.18. Ball and stick model of the crystal structure of maghemite, with the red balls indicating the oxygen anions and the blue balls indicating the iron cations.

THEORY

Hematite ($\alpha\text{-Fe}_2\text{O}_3$)

Hematite is very different to the other iron oxides as the oxygen lattice is not cubic but hexagonal close packed. It has a corundum structure where the Fe^{3+} ions are located on $2/3$ of the 18 octahedral sites per unit cell. A unit cell of hematite consists of 6 formula units with cell dimensions of $a = 5.0356 \text{ \AA}$ and $c = 13.7489 \text{ \AA}$.

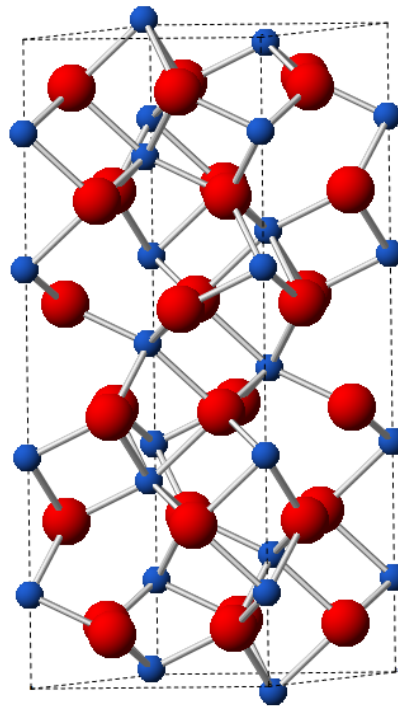


Figure 2.19. Ball and stick model of the crystal structure of hematite, with the red balls indicating the oxygen anions and the blue balls indicating the iron cations.

2.4.2. Magnetism of Iron Oxides

Wüstite (FeO)

Wüstite is antiferromagnetic with $T_N = 203 - 211$ K above which it is paramagnetic [8]. The concentration of defects in the structure has an effect on the value of T_N . When wüstite is anti-ferromagnetic the spins are ferromagnetically ordered along the (111) plane, with the neighbouring (111) planes ordered anti-parallel producing the anti-ferromagnetic properties.

Magnetite (Fe₃O₄)

Magnetite is a ferrimagnetic material with a Curie temperature of 850 K and a saturation magnetisation of $M_S = 471$ kA/m [9]. This ferrimagnetic structure is caused by the two interpenetrating sublattices present in magnetite: tetrahedral (A) and octahedral (B). The spins on the two sublattices are anti-parallel, where the spins from the Fe³⁺ cations on each sublattice are equal. The magnetic moment is produced from the Fe²⁺ cations on the B sites which causes the ferrimagnetic properties. At temperatures below T_V there is a sharp decrease in the magnetisation, which will be discussed further in Chapter 3.

Maghemite (γ -Fe₂O₃)

Maghemite has similar magnetic properties to magnetite in that it is a ferrimagnetic material at room temperature, but with a smaller saturation magnetisation of $M_S = 390$ kA/m [10]. As maghemite transforms to hematite at temperatures above 713 K, the

THEORY

Curie temperature is difficult to measure but has been estimated as $T_C = 820 - 986$ K. Whereas in magnetite the Fe^{3+} ions on the A & B sites were equal and opposite and the Fe^{2+} ions to produce the ferrimagnetic properties, the ferrimagnetic properties in maghemite is produced from the unequal and opposite Fe^{3+} ions on the A & B sites, with the magnetic moment originating from the remaining Fe^{3+} ions on the B sites.

Hematite (α - Fe_2O_3)

At room temperature hematite has weak ferromagnetic properties with a saturation magnetisation of $M_S = 2$ kA/m and a Curie temperature $T_C = 956$ K [10]. Hematite's magnetic properties stem from it exhibiting a canted anti-ferromagnetic ordering. Below 260 K (Morin temperature, T_M) hematite is anti-ferromagnetic with two anti-parallel interpenetrating ferromagnetic sublattices are aligned along the [111] c-axis. Above T_M the spins on these sublattices lie in the (111) plane, but are slightly canted at an angle of 0.1° from the plane with the different sublattices having an opposite sense of rotation, resulting in a weak net magnetisation.

References

- [1] N. A. Spaldin, *Magnetic Materials: Fundamentals and Applications*, 2nd ed.: Cambridge University Press, 2011.
- [2] B. D. Cullity and C. D. Graham, *Introduction to Magnetic Materials*, 2nd ed.: IEEE Press, 2009.
- [3] S. Chikazumi, *Physics of Ferromagnetism*, 2nd ed.: Oxford University Press, 1997.
- [4] H. D. Young and R. A. Freedman, *University Physics with Modern Physics*, 11th ed.: Pearson, 2004.
- [5] J. Smit and H. P. J. Wijn, *Ferrites: Physical Properties of Ferrimagnetic Oxides in Relation to their Technical Applications*: N. V. Philips Gloeilampenfabrieken, 1959.
- [6] M. Klaui, "Head-to-head domain walls in magnetic nanostructures," *Journal of Physics: Condensed Matter*, vol. 20, pp. 1-20, 2008.
- [7] M. Negoita, T. J. Hayward, and D. A. Allwood, "Controlling domain walls velocities in ferromagnetic ring-shaped nanowires," *Applied Physics Letters*, vol. 100, pp. 072405-072409, 2012.
- [8] R. M. Cornell and U. Schwertmann, *The Iron Oxides: Structure, Properties, Reactions, Occurrences and Uses*, 2nd ed.: John Wiley & Sons, 2006.
- [9] D. T. Margulies, F. T. Parker, F. E. Spada, R. S. Goldman, J. Li, R. Sinclair, *et al.*, "Anomalous moment and anisotropy behaviour in Fe₃O₄ films," *Physical Review B*, vol. 53, pp. 9175-9187, 1996.
- [10] T. Tepper and C. A. Ross, "Pulsed laser deposition of iron oxide films," *Journal of Applied Physics*, vol. 91, pp. 4453-4456, 2002.

3. Literature Review

This chapter will introduce, review and summarise the literature written about the main topics associated with the research of this thesis. These topics include trapping neutral atoms, and magnetite thin films and nanostructures.

3.1. Atom Trapping

The manipulation of neutral atoms has a rich history in physics, including the experiments performed by Stern and Gerlach in the 1920's where a beam of silver atoms was sent through an inhomogeneous magnetic field and the resulting deflection providing experimental proof of the quantisation of angular momentum [1].

There are many exciting and interesting applications for trapped ultra-cold atoms, including atomic fountain clocks which are fundamental to the definition of the coordinated universal time standard, and being used to achieve a higher resolution in spectroscopy measurements [2, 3]. Due to their weak interactions with the external world, ultra-cold atoms are also desirable for quantum information processing (QIP) applications [4].

At room temperature, the kinetic energy of neutral atoms is too high to be trapped and therefore the atoms need to be cooled before they can be trapped. A macroscopic cloud of atoms can be cooled by using three counter propagating, mutually orthogonal laser beams that are tuned half a linewidth below a resonance transition (also known

as red-detuning). The laser beam is only absorbed by an atom if the photon energy is up-shifted by the Doppler effect, which occurs when the atom is moving towards the laser source. This applies a friction force to the atom and reduces its energy by $\hbar k$, the energy of the laser photon (\hbar is the reduced Planck constant and k is the photon wavenumber) [5]. After many absorption-emission cycles, the atom cloud is cooled to the milli-Kelvin temperature range. Although this cools the atoms to the mK range, it does not trap them and therefore this principle of laser cooling of neutral atoms was adapted to form a magneto-optical trap (MOT). In a MOT a spatially varying magnetic quadrupole field is applied that causes a Zeeman shift in the magnetic-sensitive energy levels of the atoms that increases with distance from the centre of the trap. Circularly polarised laser beams which are detuned to a frequency below the absorption energy of the atoms, used in combination with the Zeeman shift in energy levels, create a restoring force which concentrates the atoms around the zero magnetic field point [5]. Neutral atoms can be held in traps created by their interactions with magnetic, electric and optical fields [6]. In most cases the trapped atoms can be treated as a quantum harmonic oscillator, and therefore an important parameter associated with atom trapping is the trap frequency, ω_{trap} . In a quantum harmonic oscillator the energy levels are quantised at equally spaced values, so the trap frequency determines the spacing of the energy levels within the trap and the spatial confinement of the trapped atoms [7].

Another important feature of atom traps is the trap depth, U , which defines the minimum energy barrier that an atom must surmount to escape the trap. Therefore, the trap depth strongly influences the atoms trap lifetime with a small trap depth leading to a short trap lifetime.

This review of atom trapping will be covering a few of the types of magnetic trapping experiments and applications that have been performed to illustrate the concepts to aid understanding of a domain wall atom trap, which is the background concept of this research.

3.2. Magnetic Traps

This section follows on from cooling and trapping neutral atoms in a MOT, to firstly explain how atoms react in a magnetic field and then lead into reviews of a few different magnetic atom traps.

It should be noted that to be consistent with the literature, an induction (\mathbf{B}) will be called a field even though this is not scientifically correct.

3.2.1. How atoms react in a magnetic field

A magnetic particle in a magnetic field experiences a potential energy:

$$V_{mag} = -\boldsymbol{\mu} \cdot \mathbf{B} = -g_F \mu_B m_F B \quad (3.1)$$

where $\boldsymbol{\mu}$ ($=g_F \mu_B \mathbf{F}$) is the magnetic moment, g_F is the Landé-factor of the hyperfine state, μ_B is the Bohr magneton, m_F is the magnetic quantum number and \mathbf{F} is the total spin of the particle. The trapping force on an atom is from a magnetic field gradient, which can be best explained by applying the gradient operator to equation (3.1) producing a force of $-g_F \mu_B m_F \nabla |B|$.

Typically in atom trapping experiments an adiabatic approximation can be applied if the Larmor precession of the magnetic moment ($\omega_L = \mu_B B / \hbar$) is much faster than the apparent change of direction of the magnetic field in the rest frame of the moving atom. Then the magnetic moment follows the direction of the field adiabatically with m_F as a constant of motion, with the potential that the atom is moving in being proportional to the modulus of the magnetic field $|\mathbf{B}|$, and the force on the atom being proportional to $\nabla|\mathbf{B}|$.

There are two types of magnetic trap which depend on the orientation of the atomic magnetic moment relative to the direction of the magnetic field as dictated by the value of $g_F m_F$.

- 1) When its magnetic moment points in the same direction as the magnetic field ($m_F g_F < 0$) an atom is in a strong-field-seeking state, meaning that it will be drawn towards increasing fields with the minima of the potential energy being found at the maxima of the magnetic field. However, the maxima of the magnetic field in free space is forbidden by the Earnshaw theorem and therefore traps for high-field seeking atoms are more involved.
- 2) When its magnetic moment points in the opposite direction to the magnetic field ($m_F g_F > 0$) an atom is in a weak-field-seeking state, meaning it will be repelled from the regions of high magnetic field. In this case, the minima of the potential energy are found at the minima of the magnetic field. As the minima of the magnetic field in free space is not forbidden by the Earnshaw theorem, these are the more common neutral atom traps. [6]

The correct atomic state (m_F) can be selected by pumping between atomic transitions with circularly polarised light, thus allowing selection rules to force it towards positive m_F numbers only.

3.2.2. Magnetic microtraps based on current carrying wires

Both strong- and weak-field-seeking traps can be constructed based around current carrying wires.

An example of a strong-field-seeking trap is an atom orbiting around a current (I_ω) carrying wire. This gives an interaction potential of

$$V_{mag} = -\boldsymbol{\mu} \cdot \mathbf{B} = -\left(\frac{\mu_0}{2\pi}\right) I_\omega \frac{1}{r} e_\varphi \cdot \boldsymbol{\mu} \quad (3.2)$$

(e_φ : azimuthal unit vector in cylindrical coordinates) and causes the atom to move in a Keplerian orbit as seen in Figure 3.1.

In the weak-field-seeking case a homogeneous bias field (B_b) is used in addition to the current carrying wire to produce a 2-dimensional field minimum in the form of a quadrupole field. There is then a line at a distance

$$r_0 = \left(\frac{\mu_0}{2\pi}\right) \frac{I_\omega}{B_b} \quad (3.3)$$

parallel to the length of the wire where the bias field and the circular magnetic field from the wire are equal and opposite. From this line the modulus of the magnetic field increases in all radial direction. The atoms in a low-field-seeking state can be trapped in the 2-dimensional quadrupole field and guided along the length of the trap. However, if the bias field is orthogonal to the current carrying wire the two fields

cancel exactly and the trapped atoms could be lost due to Majorana transitions between trapped and untrapped spin states. To prevent this, a small B-field component (B_{ip}) must be added along the wire direction to remove the degeneracy between the trapped and untrapped states. This potential is then known as an Ioffe-Pritchard trap. [6]

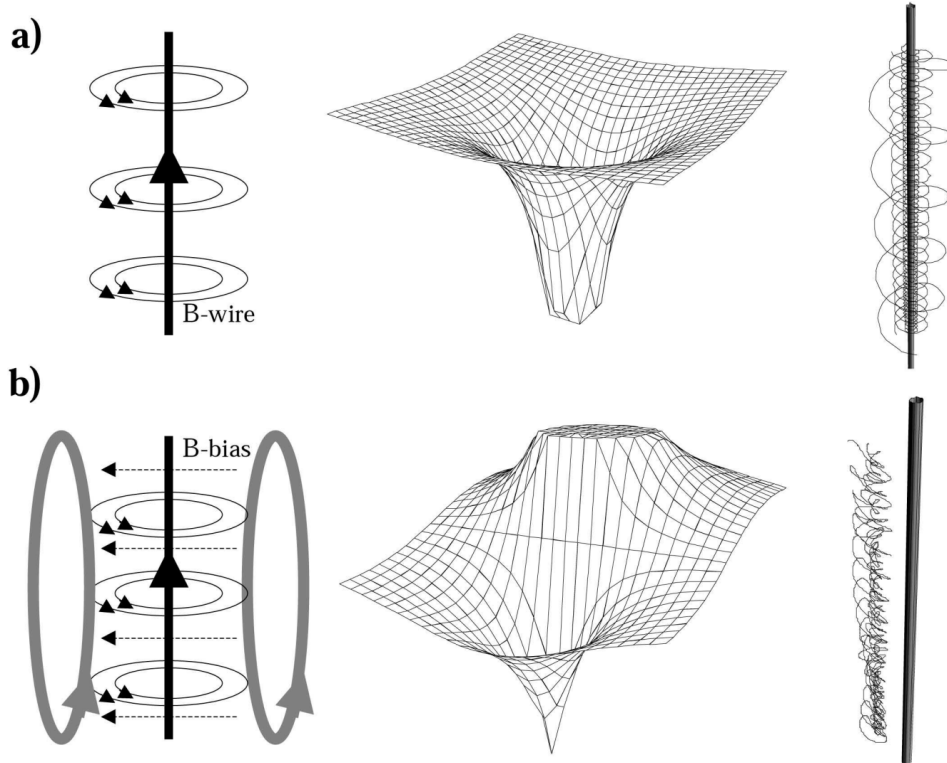


Figure 3.1. Magnetic traps around a wire for an atom in (a) a strong field seeking state and (b) a low field seeking state. Left hand side: illustrates the magnetic field from the current carrying wire and the bias field. Middle: shows the potential landscape for the trapped atom. Right hand side: displays typical classical trajectories for the trapped atom along the current carrying wire. [6]

3.2.3. Free standing wires to atom chips

This section will introduce the concept and advantages of miniaturization of wire based atom traps to the micron scale on atom chips, with experimental evidence of these atom traps on substrates followed by trap loss mechanisms.

Advantages for using atom chips over free-standing current carrying wires include increasing the resolution of the trapping potentials, the substrate acting as a heat-sink which allows larger current densities to be used, and larger current densities in wires with smaller cross-sections producing the highest possible trap gradient.

The resolution of the trapping potential allows the location of the atom cloud relative to other structures on the atom chip to be known to the precision of the fabrication process used. This allows for highly controlled manipulation and measurements to be performed on atom clouds that are very close together.

A limiting factor on the trap gradient is the maximum tolerable current density that can be used for the current carrying wire. The highest possible trap gradient is found at a distance from the wire that is comparable to the width of the wire, d . As the bias field that is required for a trap is proportional to the current density j , the highest trap gradient is given by j/d and therefore the largest trap gradient is found for smaller wires.

One of the first surface mounted atom traps that was miniaturized to the micron scale was achieved experimentally by Folman et al. [8]. The chip design consisted of a 2.5 μm thick patterned Au layer on a 600 μm thick GaAs substrate, with the main elements of the design shown in Figure 3.2a. The wires are defined by 10 μm wide etchings in the gold, which is shown in a SEM image in the inset of Figure 3.2a.

Each of the two 200 μm wide U-shaped current-carrying wires, along with an applied bias magnetic field, can be used to form a MOT as well as a magnetic trap. These U-shaped wires can be used together to form a strong magnetic trap in order to load atoms into the smaller structures, or they can be used as an on-board bias field for traps based on the 10 μm wide wire running between them.

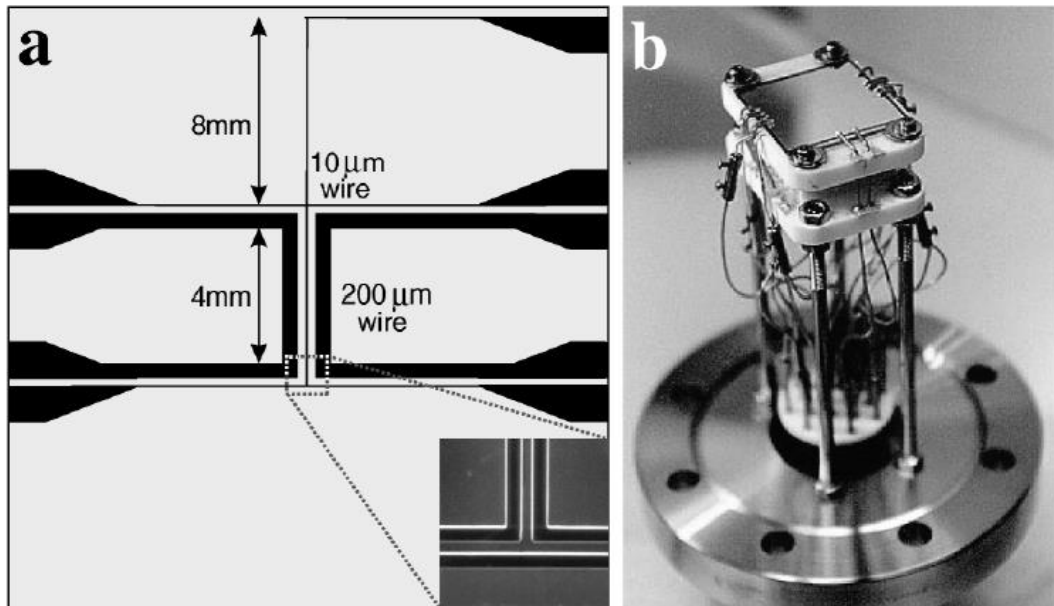


Figure 3.2. (a) A schematic showing the main elements of the chip design, with the inset showing a SEM image of the etched boundary to the wire. (b) Image of the mounted chip prior to being placed in the vacuum chamber. (Taken from [8]).

There are several problems associated with magnetic atom traps based on current carrying wires [6, 9-15], which are briefly described below.

- (1) Majorana spin flips: the spin state of the atom is changed when the magnetic moment of the atom is unable to follow the change in direction of the magnetic field. This can change a weak-field seeking atom into a strong-field seeking atom (or vice versa), and therefore the atom would no longer be trapped. This

occurs at (or near) zeros of magnetic field, and for this reason additional bias fields are applied to remove the zero magnetic field (as mentioned in Section 3.2.2).

- (2) Noise-induced spin flips: there are two main sources of noise-induced spin flips in atom traps, thermally excited currents (Johnson noise) and technical noise in the wire current. These sources of noise cause fluctuations in the magnetic trap fields which can cause the spin state of the atom to change, leading to trap losses. The technical noise in the wire current is caused either by antenna pickup effects or the current source, and if the rf noise that is radiated from the wire is at the Larmor frequency it can induce a spin flip transition. When the atom-wire distance was reduced for a current-carrying wire, there was an increase in trap losses. This was caused by thermal current fluctuations which induce fluctuations in the magnetic field that increase in strength close to the wire surface. These current fluctuations can be reduced by using a material with a larger resistivity.
- (3) Collisional losses: a collision between background gas atoms and the trapped atoms can transfer the trapped atom with enough energy so that it is able to escape from the trap. This loss mechanism can be reduced by using an ultra-high vacuum to reduce collisions.
- (4) Fragmentation of atom cloud: this is not necessarily a trap loss mechanism, but a hindrance to controlled manipulation and measurement of trapped atoms. It has been shown theoretically [14] that geometrical deformations and meanders in the wire can cause distortions in the current flow in the wire. This current flow distortion gives rise to corrugations in the longitudinal potential. It was

also found that as the atom-wire distance is reduced, the atom cloud fragmentation is enhanced.

3.2.4. Mobile domain wall traps

The exciting discovery and development of the concept of using the stray magnetic field from a domain wall to trap atoms above a nanowire is an important background to the research performed and analysed in this thesis.

For the following explanation, the Cartesian co-ordinates are set with the x-direction along the length of the nanowire, the y-direction along the width of the nanowire and the z-direction being perpendicular to the nanowire surface (as shown in Figure 3.3).

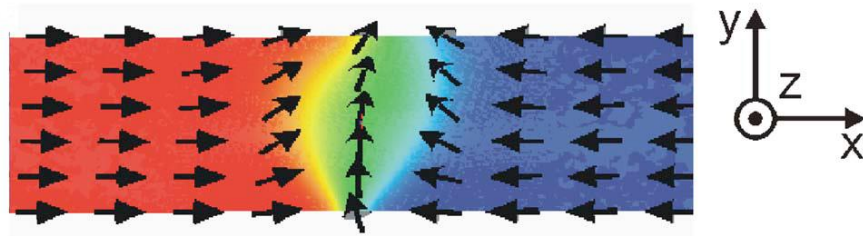


Figure 3.3. Head-to-head magnetic domain wall in a planar magnetic nanowire. (Adapted from [4]).

Allwood et al. [4] proposed a new concept for atom trapping, which involved using a mobile magnetic domain wall (DW) to trap a low-field-seeking atom. A transverse domain wall in a planar magnetic nanowire that has been magnetised along its length (Figure 3.3) will produce a stray field \mathbf{B}_{dw} , that above the DW is dominated by the z component B_{dw}^z . If a low-field-seeking atom was brought near the domain wall it

would be repelled, and therefore to create an atom trap a uniform out-of-plane magnetic field of strength B_{dc} is applied that opposes B_{dw} . B_{dc} compensates B_{dw} such that a 3D surface is created around the DW where $B_{dw}^z = 0$. Furthermore there is a point close to $x = y = 0$ where the x and y components of the magnetic field are also zero, thus creating a global field minimum that can be used to trap atoms. With the atom being in a low-field-seeking state, B_{min} needs to be > 0 as a zero magnetic field would allow majorana spin flips and to achieve this a rotating magnetic field (B_{ac}) is applied similar to a time-orbiting potential (TOP) trap. B_{ac} rotates faster than the trap frequency (ω_{trap}) and therefore the atom effectively sees its time average, creating a smooth bottomed trap with a non-zero field minimum.

Figure 3.4 shows how the combination of B_{dw}^z (circles), B_{dc} (top dashed line) and B_{ac} (bottom dashed line) above the domain wall can be used to create the atom trap.

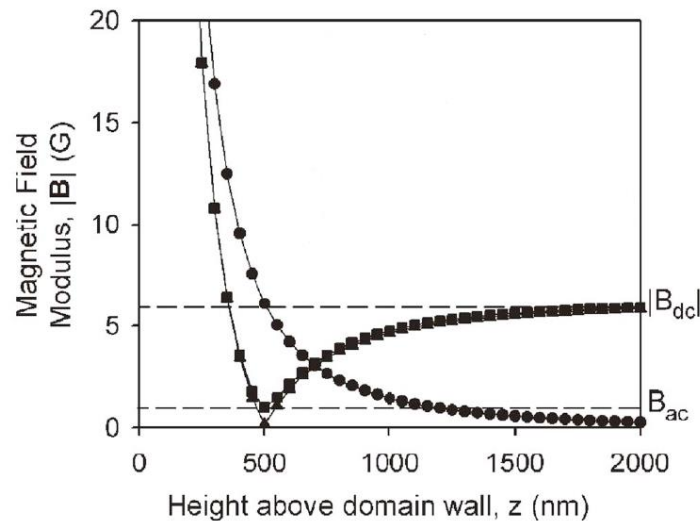


Figure 3.4. The magnetic domain wall stray field as a function of the height above domain wall for zero applied field ($B_{dc} = 0$ G) [circles, ●], and applied fields of $B_{dc} = -6.1$ G and $B_{ac} = 0$ G [triangles, ▲] and $B_{ac} = 1$ G [squares, ■]. The dotted lines show the magnitude of the applied fields. (Adapted from [4]).

LITERATURE REVIEW

As mentioned previously, a domain wall atom trap resembles a quantum harmonic oscillator. The trap frequency thus both defines the spacing of energy levels in the trap, and also may be considered to describe the rate at which the magnetic field changes in the atoms field of reference. An important parameter for an atom trap is the adiabaticity (ω_L/ω_{trap}), where ω_L is the Larmor frequency of the trapped atom. The Larmor frequency (ω_L) describes the rate at which the atom is able to respond to changes in the trap's field direction, and thus the adiabaticity that decides whether or not the atom's magnetic moment can follow the trap's varying magnetic field adiabatically. For successful trapping where atoms respond adiabatically to the time-averaged field modulus of the trap the two following criteria must both be met: $\frac{\omega_L}{\omega_{trap}} \gg 1$ and $\omega_{trap} < \omega_{ac} < \omega_L$ [7].

The trap depth, U , defines the minimum energy barrier that an atom has to overcome to escape from the trap, and thus plays a key role in determining its lifetime. It can be calculated using

$$U = m_F g_F \mu_B (|\mathbf{B}|_\infty - |\mathbf{B}|_{min}) \quad (3.4)$$

Where $|\mathbf{B}|_\infty$ is the magnetic field far above the DW and is equal to

$$|\mathbf{B}|_\infty = \sqrt{|\mathbf{B}_{dc}|^2 + |\mathbf{B}_{ac}|^2} \quad (3.5)$$

The trap depth can also be described as an effective trap temperature, $T = \Delta E/k_B$.

Considering thus, and substituting (3.5) into (3.4):

$$T_\infty = \frac{1}{k_B} m_F g_F \mu_B \left(\sqrt{|\mathbf{B}_{dc}|^2 + |\mathbf{B}_{ac}|^2} - |\mathbf{B}_{ac}| \right) \quad (3.6)$$

While the rotating magnetic field removes the zero point of the magnetic field, it also creates instantaneous zero points in the x-y plane below the trap as it rotates. These zero points are called the "circle of death", and if an atom comes across this then there

is a high chance of it performing a spin-flip to an untrapped state and being lost from the trap.

For DW atom traps to be successfully used for quantum information processing (QIP) DWs need to be moved around a network of nanowires [4]. To do this an additional in-plane field must be applied (B_{app}). This additional field causes the trap depth to increase, as the field at infinity (equation (3.5)) is changed to:

$$|\mathbf{B}|_{\infty} = \sqrt{|\mathbf{B}_{dc}|^2 + |\mathbf{B}_{ac}|^2 + |\mathbf{B}_{app}|^2} \quad (3.7)$$

Furthermore, as an atom trap has a finite depth there is a limit on the acceleration on the DW may undergo before the atom is lost. DWs moving under steady-state conditions usually accelerate to a constant velocity of 10s – 100s m/s in ~ 1 ns. However, for a $\omega_{trap} \sim$ MHz the DW drift velocity is limited to a few cm s^{-1} if atoms are to remain trapped.

A reduction in the DW velocity in permalloy nanowires to $< 1 \text{ cm s}^{-1}$ has been recorded experimentally by Negoita et al. [16, 17]. This was achieved by using alternating rotating applied magnetic fields to move a DW through an undulating nanowire geometry, as illustrated in Figure 3.5. The experimental measurements were performed on a patterned 30 nm thick permalloy nanowire on an oxidised Si substrate, with a wire width of 400 nm and an undulation diameter of 10 μm . Single shot focussed-MOKE signals were measured at different points on the nanowire for field rotation frequencies of 27 Hz (solid lines) and 13.5 Hz (dashed lines), and a rotating magnetic field of $|\mathbf{H}_{rot}| = 110 \text{ Oe}$ (Figure 3.5c). The 13.5 Hz results are shown to take twice as long as the 27 Hz results, which illustrates the feasibility to propagate DWs at a user defined average velocity.

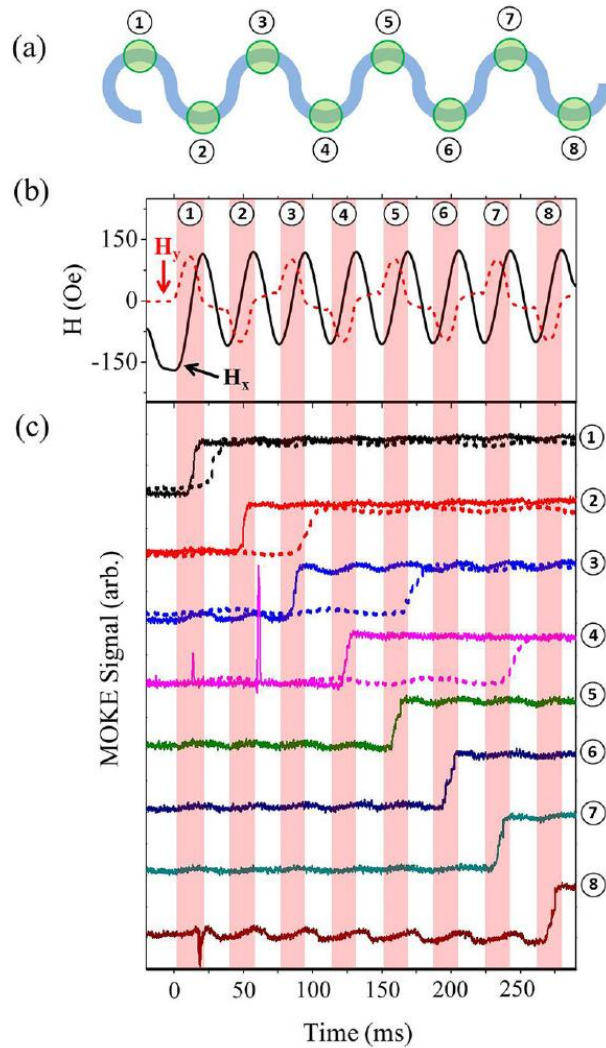


Figure 3.5. (a) Schematic diagram illustrating the different locations along the nanowire where the focused-MOKE laser spot is positioned. (b) The applied field sequence for a field rotation frequency of 27 Hz. The highlighted sections indicate when the DW is expected to pass. (c) Single shot focused-MOKE signals measured at the 8 different locations for field rotation frequencies of 27 Hz (solid line) and 13.5 Hz (dashed line). (Taken from [17]).

For the permalloy nanowire DW atom trap discussed above, the trap lifetime is calculated to be a few hundred milliseconds for atoms that are held 200 nm above the

nanowire. This limitation on the trap lifetime could be reduced by using a non-conducting magnetic material, with a sufficient magnetisation to support the atom trap and a small magneto-crystalline anisotropy to allow the shape anisotropy of the nanowire to dominate. A possible candidate for that meets these criteria is magnetite, Fe_3O_4 , with a saturation magnetisation of 471 kA/m [18] and a conductivity of $250 (\Omega \text{ cm})^{-1}$ [19].

3.3. Magnetite Thin Films

The structure and magnetic properties of bulk magnetite were introduced in the previous chapter (Section 2.4). This section will focus more specifically on a review of the properties of magnetite in thin film form. Two important features of magnetite will be covered initially; the Verwey transition and anti-phase boundaries. The first of these is a material property and has been utilised frequently to assess thin film quality, and the second is a consequence of thin film growth that produces dramatic changes in magnetic and electrical properties from bulk values. This then leads on into a review of the magnetic, electrical and topographical properties of epitaxial and polycrystalline magnetite thin films which will provide a useful reference for the experimental results analysed in this thesis. Lastly, there is a review of different methods that have been used to reduce the anti-phase boundary density in magnetite thin films.

3.3.1. Verwey Transition

At temperatures around 125 K, magnetite undergoes a transition where there is a drop in magnetisation, a specific heat anomaly, a jump in specific resistivity and an expansion in the crystal lattice. This transition has been a large area of interest since its discovery [20-24], and in 1947 Verwey proposed the first model to explain the transition [23]. Verwey determined that above 125 K (T_V), the Fe^{2+} and Fe^{3+} cations are randomly distributed across the B-sites allowing rapid electron hopping between the different valence cations. Below T_V , Verwey proposed a charge ordering where successive $\frac{1}{4}a(100)$ lattice planes would be occupied by Fe^{2+} and Fe^{3+} ions. It was also assumed that magnetite underwent a transition from a cubic to tetragonal structure. Verwey also investigated the effect of stoichiometry on the resistivity drop, and found that introducing octahedral vacancies decreases the transition temperature and the drop amplitude, to a point where the transition disappears.

Since Verwey proposed his model for the transition, a vast amount of research has been performed to either correct or prove the model. Key areas of interest have been the crystal structure of the low-temperature phase, charge transport mechanisms above and below the transition and the ionic ordering in the low temperature phase.

It has been established that the crystal structure of the low temperature phase is not tetragonal as Verwey predicted, or orthorhombic as suggested by Hamilton but actually monoclinic [23]. Twinning of crystal domains has hampered diffraction studies into the low temperature structure to establish any crystal structure changes at the transition [23]. Recent high energy x-ray diffraction measurements [24] from a 40 μm single grain propose an additional interaction producing a new linear three iron

unit called a ‘trimeron’, and the low temperature structure is described by an ordered arrangement of these trimerons. Below the Verwey temperature, the electron density of a Fe^{2+} is significantly delocalised onto two adjacent B-site acceptors (which are usually Fe^{3+} sites) which causes displacements for the acceptor Fe sites and the surrounding oxygen atoms. A trimeron is described as the single delocalised charge over the three Fe sites corresponding to a highly structured small polaron.

Although the Verwey transition will not be addressed experimentally in this thesis, it is popular in literature on magnetite thin films as a measure of film quality and therefore useful to include in a review on the literature covering magnetite thin films.

3.3.2. Anti-Phase Boundaries

The magnetic properties of Fe_3O_4 thin films differ greatly from that of bulk Fe_3O_4 . The magnetic field needed to saturate bulk Fe_3O_4 is ~ 310 Oe whereas it has been reported that Fe_3O_4 thin films are not saturated in magnetic fields of 70 kOe [25]. A difference in the electrical properties between thin films and bulk is also observed, with thin films exhibiting resistivities orders of magnitude higher than the value of $\rho = 0.005 \Omega\text{cm}$ for bulk Fe_3O_4 [26].

Studies by Margulies et al. [18, 25, 27] into the anomalous magnetic behaviour observed in single crystal Fe_3O_4 films lead to the discovery of anti-phase boundaries (APBs), in simple terms boundaries in the films over which the Fe sub-lattice is disrupted. These APBs form as a consequence of the thin film growth mechanism. When Fe_3O_4 is grown as a thin film it initially forms as two dimensional islands on the substrate surface. When these islands meet and coalesce the oxygen lattice is

continuous, but as there are 8 inequivalent unit cell origins the Fe cation sublattice is disrupted [28]. Figure 3.6 shows a schematic illustrating the continuous oxygen lattice with examples of different APB shifts of Fe_3O_4 on an MgO surface.

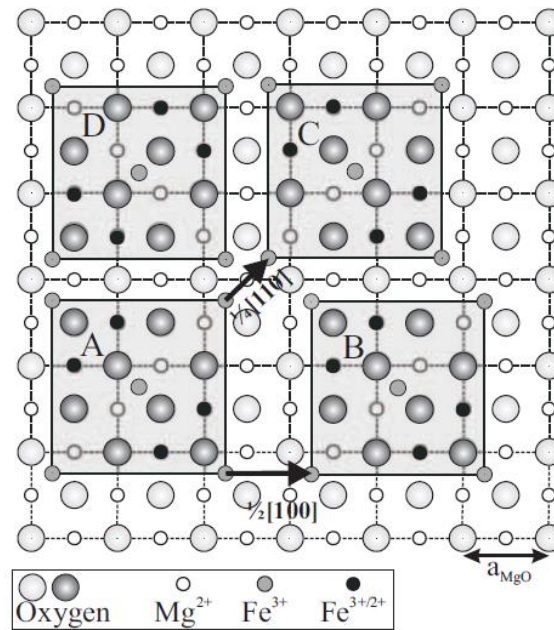


Figure 3.6. Schematic illustrating APB shifts of Fe_3O_4 on a MgO surface caused by translation or rotation relative to the reference A. (Taken from [29]).

In bulk Fe_3O_4 the dominant magnetic interaction is the ($\sim 120^\circ$) anti-ferromagnetic superexchange between the A- and B-sites, where the coupling between cations on the B sites is ferromagnetic. The shift in the structure caused by APBs introduces a new, stronger magnetic coupling between B site cations: a 180° anti-ferromagnetic superexchange [29]. This causes the APB to separate domains that are antiferromagnetically coupled with each other. A useful summary of the different exchange interactions and their relative strength in bulk Fe_3O_4 and across an APB can be found in [29]. This antiferromagnetic coupling across domains is the cause behind the in-plane magnetisation for polycrystalline and epitaxial Fe_3O_4 films to be

unsaturated in fields of 70 kOe, when the film is expected to saturate in a field ~ 310 Oe [25].

A comparison of dark field TEM images of sputter grown nanocrystalline Fe_3O_4 films from [25] to epitaxial Fe_3O_4 films grown using MBE was made by Hibma [28] who reported an average domain size of 300 nm (MBE) compared to 27.5 nm (sputter). This large difference was reported to be due to the very different growth procedures used and although this is likely to make a contribution, the difference in film thickness is overlooked: the MBE film is 200 nm thick, which is four times the thickness of the sputtered film at 50 nm. A study into the effect growth parameters on APB density [30] determined that the domain size, D , increases with film thickness, t , following a $D \propto \sqrt{t}$ relationship. It was also shown that APBs migrate via a thermally activated diffusion process after analysing the effect of postannealing on APB domain size. It is this diffusive nature that lead to studies in the reduction of APB density which is reviewed in Section 3.3.4.

From these journals it can be stated that the density of APBs in Fe_3O_4 thin films is highly dependent on numerous variables, including the growth procedure used, the film thickness and the substrate of choice. Therefore, the magnetic and electrical properties of Fe_3O_4 thin films are complicated, but it also makes them an interesting research area.

3.3.3. Magnetite thin film growths

Fe_3O_4 thin films are an important research area due to their high Curie temperature (860 K) and the predicted 100% spin polarisation which makes Fe_3O_4 an ideal material for applications in spintronic devices. However, due to the presence of APBs in Fe_3O_4 films the half-metallic nature is suppressed along with a large change from bulk values in the magnetic and electronic properties [18, 19, 25, 27, 29]. There are several common themes in the literature regarding the growth of Fe_3O_4 thin films including the cause, effect and reduction of APB density, the Verwey transition, and the materials spin polarisation. However, due to the focus of the research described in this thesis, this section will focus primarily on the effect of growth parameters, film thickness and substrate on the thin films magnetic and basic electrical properties, including their coercivity, grain size and resistivity.

As stated in Section 3.3.2, the resistivity of Fe_3O_4 thin films is orders of magnitude greater than bulk Fe_3O_4 . The resistivity has also been shown to increase with decreasing film thickness. Eerenstein [19] has attributed this to the increase in antiphase domain boundaries for thinner films (Figure 3.7), where the presence of 180° anti-ferromagnetic boundaries at the APBs enhance the resistance in the films.

A series of epitaxial Fe_3O_4 thin films were grown on MgO substrates using MBE with varying film thickness in the range 3 – 100 nm. The increase in the domain size with film thickness was measured from dark field TEM images, where the domain size increases from 5 to 40 nm for 3 and 100 nm thick films, respectively. The effective conductivity was modelled using the effective medium approximation using a function

of the bulk and boundary conductivities, and from this the conductivity of APBs was found to be close to zero.

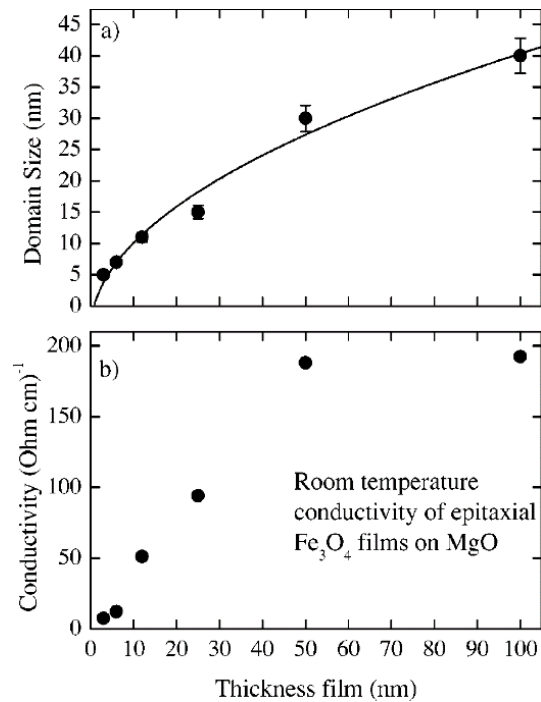


Figure 3.7. Anti-phase domain size and conductivity for various thin film thicknesses for epitaxial Fe₃O₄ thin films on MgO substrates. (Taken from [19]).

The effects of substrate composition and film thickness has also been analysed for epitaxial Fe₃O₄ by Sterbinsky et al [31] with thin films also grown using MBE. The substrates used in this investigation were SrTiO₃ (001) and MgO (001), along with a film grown on a BaTiO₃ surface on MgO (001) substrate. A comparison of the coercivity of Fe₃O₄ films of these films with RMS surface roughness showed an increase in coercivity with surface roughness. This relationship between coercivity and surface roughness is consistent with theoretical predictions of domain rotation for Bloch walls [32].

LITERATURE REVIEW

The explanation of the thin films magnetically isotropic behaviour, however, does not match with their given reference [19]. The lack of in-plane anisotropy in [31] has been attributed to the presence of APBs in the films, and if this explanation was correct then there would be no Fe₃O₄ thin films with an in-plane anisotropy as APBs are inherent in Fe₃O₄ thin film growth. Whilst it has been shown that ultrathin epitaxial Fe₃O₄ films (~ 10 nm) have a vanishing in-plane anisotropy and remnant magnetisation [33], thicker films exhibit anisotropy with [110] as the easy direction, as would be expected from bulk parameters. The reduced in-plane anisotropy is caused due to the large density of APBs producing randomisation of the magnetisation [19]. The films investigated by Sterbinsky had thicknesses in the range of 20 – 190 nm, and although the thinner films might fit the explanation given, the thicker films would not as APB domain size increases with film thickness. The explanation for the isotropic behaviour of the films by having APBs present would be correct if it is also accompanied by a comparison to APB domain size.

Whereas the previous papers were analysing the properties of epitaxial Fe₃O₄ thin films, the following papers will address polycrystalline Fe₃O₄ thin films.

A study by Bollero et al [34] into the influence of film thickness on the coercivity of polycrystalline Fe₃O₄ thin films grown on MgAl₂O₄ and MgO by PLD showed that the largest coercivity values were measured from the thinnest films (Figure 3.8). The thinner films show a homogenous granular distribution with an average grain size of 20 & 50 nm (dependent on substrate), which increases in size and inhomogeneity with increasing film thickness. The larger density of intergranular regions in the thinner films led to an increased density of pinning centres and thus increased coercivity.

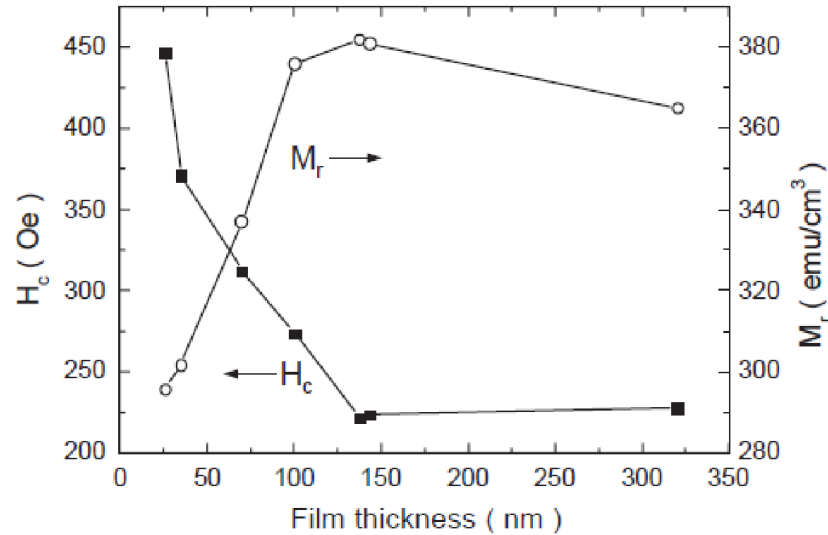


Figure 3.8. Variation in coercivity (H_c , ●) and remanence (M_r , ○) with increasing film thickness for Fe_3O_4 on $MgAl_2O_4$ thin films, measured at 300 K. (Taken from [34])

A comparison of demagnetisation curves (partial hysteresis loops, from +500 Oe to -1000 Oe applied field) for the different substrates for similar film thickness shows a gradual curve with lower normalised remanence for the MgO film compared to the $MgAl_2O_4$ film. This was attributed by the authors to the differing degree of homogeneity of the samples, with APBs acting as pinning centres and the choice of substrate having a strong influence on the APB density. Magnetite films grown on $MgAl_2O_4$ substrates are expected to have a lower APB density than those grown on MgO substrates, due to the closer values of lattice parameter between the film and substrate for $MgAl_2O_4$ than MgO. The thicker the film, the more rectangular the demagnetisation curve became which the authors postulated was related to the critical diameter for transition from single-domain to multi-domain grains in the range 50 – 200 nm.

LITERATURE REVIEW

In contrast to the investigation into the conductivity across APBs in epitaxial films above, Mi et al. [35] have investigated the microstructure and magneto-transport of polycrystalline Fe_3O_4 thin films.

These polycrystalline Fe_3O_4 thin films were grown using DC reactive sputtering on substrates of glass cover slips, cleaved NaCl and kaptonTM. From bright-field TEM images an average grain size of ~ 5 nm was measured for the 20 nm thick film, and ~ 12 nm for the 60 nm thick film. A further high-resolution TEM image of the 20 nm film (Figure 3.9) showed that the grains were surrounded by disordered atoms, which were described as due to the lattice mismatch between neighbouring Fe_3O_4 grains with different lattice orientations. It was also seen that the volume fraction of these disordered atoms decreases with an increase in film thickness due to the particle size increasing with film thickness.

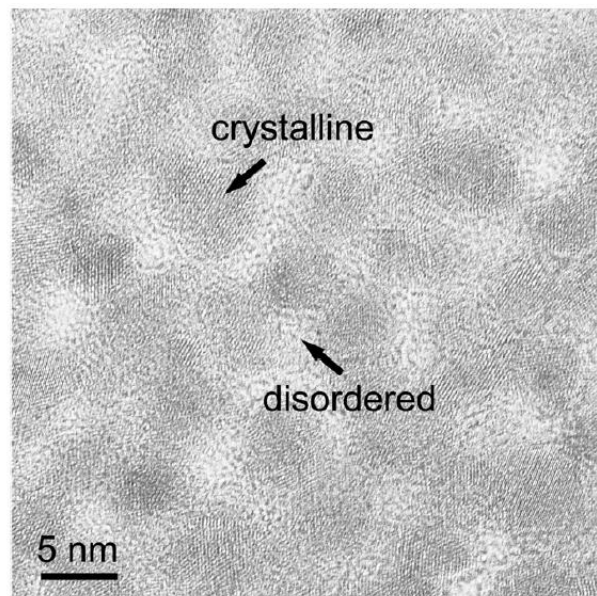


Figure 3.9. High-resolution TEM image of the 20 nm thick polycrystalline Fe_3O_4 film. (Taken from [35]).

The increased resistivity for a 640 nm thick polycrystalline Fe_3O_4 thin film ($\sim 1.58 \times 10^5 \mu\Omega \text{ cm}$ at 300 K) compared to that of epitaxial Fe_3O_4 thin films ($\sim 10^4 \mu\Omega \text{ cm}$) was said to be evidence of the intergrain disordered regions. By investigating the relationship between the resistivity and temperature, it was found that they followed a $\log \rho \sim T^{-1/2}$ relationship which suggests that the transport mechanism through the polycrystalline films is dominated by tunnelling. It was also noted that there was no Verwey transition observed, which was explained due to the large resistivity of the films due to the disordered regions submerging the intrinsic property of the Fe_3O_4 grains.

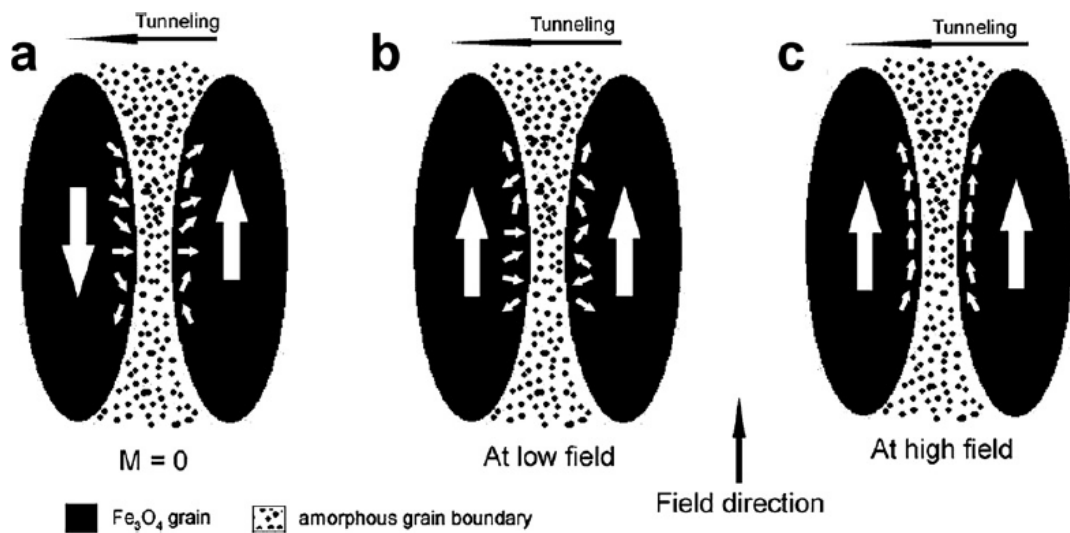


Figure 3.10. Schematic illustration of the tunnelling process between two Fe_3O_4 grains. (Taken from [35])

Analysis of the magnetic and magneto-transport properties using zero-field cooled (ZFC) and field-cooled (FC) curves and magneto-resistance (MR) measurements produced the conclusion that when a magnetic field is applied parallel to the film, the spins in the centre of the grains are oriented first with the spins at the grain edge being

LITERATURE REVIEW

only slightly affected. When the magnetic field is increased above the point when the spins at the grain boundaries start to become aligned with the field, there is a decrease in the resistance. This is illustrated well in Figure 3.10.

A useful comparison illustrating the trends in resistivity and coercivity of epitaxial, textured and polycrystalline Fe_3O_4 thin films is compiled in Table 3.1 from the journals discussed in Section 3.3.3. Other journals are included in Table 3.1 to cover a range of growth techniques and substrates. As a generalisation, the following trends have been found for Fe_3O_4 thin films:

- Resistivity is larger for polycrystalline films than for epitaxial films.
- Resistivity decreases with increasing film thickness.
- Coercivity decreases with increasing film thickness.
- Grain size increases with increasing film thickness.
- Inter-granular disordered region decreases with increasing film thickness (polycrystalline films).
- APB density decreases with increasing film thickness.
- APB density varies with substrate choice, with a smaller lattice mismatch producing a lower APB density.
- Unsaturated in-plane magnetisation in applied magnetic fields of 70 kOe.
- Verwey transition seen in resistivity measurements is either missing or a very small change is seen for polycrystalline films.

Growth technique	Substrate	Thickness (nm)	Coercivity (Oe)	Resistivity (Ω cm)	Ref
PLD (polycrystalline)	MgAl ₂ O ₄ (100)	26	225*		[34]
		320	450*	-	
	MgO (100)	30	380*		
PLD (textured & epitaxial)	Al ₂ O ₃		335	0.023	[36]
	ZnO		380	0.017	
	Si	40 - 60	345	0.015	
	SiO ₂		290	0.017	
	Glass		330	0.013	
MBE (epitaxial)	MgO	3		0.13	[19]
		6		0.082	
		12		0.017	
		25	-	0.008	
		50		0.0053	
		100		0.0052	
MBE (epitaxial)	SrTiO ₃	27 \star	390		[31]
		22 $^\circ$	310		
	MgO	73 $^\circ$	260		
		190 $^\circ$	190	-	
		23 \star	190		
BaTiO ₃ /MgO	23 \star	320			
CVD (polycrystalline)	Si/SiO ₂	24.8		0.017	[37]
		100	-	0.0042	
		12.8	180	-	[38]
		16.1	750	0.145	

		28.9	1860	-	
Reactive sputtering (polycrystalline)	Kapton	300	200*		[39]
	Glass	300	-	0.004	
Reactive sputtering (polycrystalline)	Oxidised Si	17	-	0.07321	[40]
		100		0.04183	
Reactive sputtering (polycrystalline)	Glass	10	-	570	[41]
		1120		0.069	
Reactive sputtering (epitaxial)	MgO (100)	450	85		[27]
		13	150	-	
*Value taken from a graph.		$\diamond pO_2 = 6.9 \times 10^{-7} \text{ Torr}$		$^\circ pO_2 = 2.0 \times 10^{-7} \text{ Torr}$	

Table 3.1. A summary of resistivity and coercivity values of Fe_3O_4 thin films for various film thicknesses, growth techniques and substrates.

3.3.4. APB density reduction methods

The presence of APBs in thin films of magnetite suppress the predicted half-metallic properties which are desired for applications in spintronic devices, and also have a significant impact on the electronic and magnetic properties. Due to the diffusive nature of APBs there have been attempts to reduce the density of APBs in magnetite thin films during and post-growth. Although APBs are present in both epitaxial and polycrystalline films, they have a greater effect on the properties of epitaxial films due

to the intergranular regions in polycrystalline films also acting as a barrier to electronic and magneto-transport.

Creating a soft magnetic material with a small coercivity is an important feature of this thesis so that when nanostructures are fabricated, the shape anisotropy dominates to create domain walls. For this reason, APB reduction methods are relevant to this thesis as APBs have been shown to cause larger coercivity values by acting as pinning sites, and reduce the saturation magnetisation of Fe_3O_4 thin films.

Kumar et al [42] increased the adsorbed atom mobility during thin film growth by applying an electric field across the sample. The films were grown using reactive pulsed DC magnetron sputtering and a comparison was made between films grown with (E10) and without (E0) an in-plane electric field. Two gold contacts spaced 6 mm apart were used to apply the potential difference of 10 V. Glancing angle and locked-coupled XRD measurements were performed, showing that E0 films are polycrystalline but E10 films are highly oriented with [111] texture normal to the film plane. A small increase in the saturation magnetisation is seen for the biased film to 441 emu/cc from 419 emu/cc for the nonbiased film. Along with this increase, the Verwey transition width for the biased film is ~12K whereas the nonbiased film produces a broader transition (~34 K). The saturation magnetisation increase and the narrowing of the Verwey transition has been attributed to the reduction of APB density and structural disorder. There is also a slight increase (~ 50 Oe, estimated from a graph) in the coercivity for the biased film, however the values are not provided.

Peng et al [43] also applied a bias to the substrate during growth, although in this case the polycrystalline films were grown using RF sputtering from a mixed Fe_3O_4 and Fe_2O_3 target and a larger substrate bias of 100 V was used. Films grown at sputter

powers of 200 W were found to be Fe_3O_4 , and a large change in the electronic and magnetic properties can be seen when the film is grown with the substrate bias (Figure 3.11).

The resistivity of the biased film dropped by a factor of 10 and the coercivity and saturation magnetisation both doubled in value. The values of the coercivity (300 Oe) and resistivity ($2.98 \times 10^{-4} \Omega\text{m}$) then lay within the normal range for polycrystalline magnetite thin films. TEM images of nonbiased films showed thicker grain boundaries and a larger density of defects than the biased films. However, although there was a reduction in APB density for the biased film, there were still many APBs present in the film along with the aforementioned thin, amorphous layer at grain boundaries.

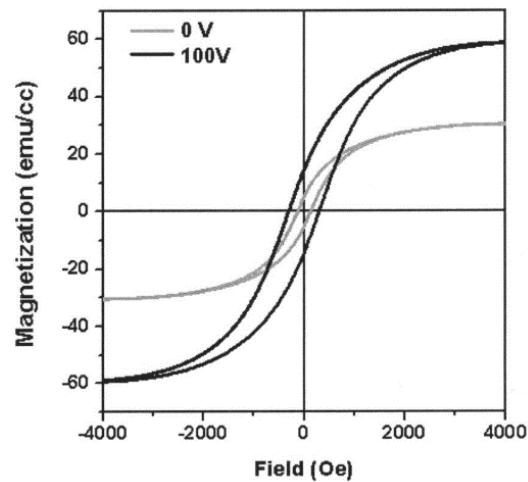


Figure 3.11. Magnetisation loops of sputtered Fe_3O_4 films grown with and without a substrate bias. (Taken from [43]).

Although these two papers produce quantitatively different results when comparing the properties of magnetite thin films grown with and without sample bias, both have

a common result in that, by applying an electric field during deposition, an increase in the saturation magnetisation and a reduction of the density of APBs is observed.

Post-deposition thermal treatment has also been utilised to try and increase the saturation magnetisation of magnetite thin films, for example in the works of Ramay [44] and Zhou [45], who both annealed thin films after growth. In the annealing treatment performed by Ramay the magnetite films were first grown using PLD onto Si (100) substrates at a growth temperature of 450 °C. After the oxygen flow was stopped the films were left at 450 °C for 30, 60 and 90 minutes in a vacuum of 10^{-7} torr. XRD analysis show a preferred [111] orientation for magnetite, but the as grown film and the 30 & 60 minute annealed films also had an additional iron phase. This iron phase was not present in the films annealed for 90 minutes, and for this reason the saturation magnetisation level was lowered however it is attributed to the formation of APBs between the film and substrate. Although the transformation from mixed $\text{Fe}_3\text{O}_4 + \text{Fe}$ films to pure Fe_3O_4 films is discussed, an anomalous increase in saturation magnetisation from 420 emu/cc (30 minutes) to 640 emu/cc (60 minutes) is mentioned but not explained.

This increase in saturation magnetisation at 60 minutes could be caused by a reduction in the APB density present in the Fe_3O_4 as it has been explained that APBs cause a reduction in saturation magnetisation [25] and that they migrate via a thermally activated diffusion process [30], and the drop in saturation magnetisation at 90 minutes purely being due to the Fe in the films being oxidised.

In an alternative approach Zhou et al [45] annealed 100 nm epitaxial Fe_3O_4 films on MgO (100) using a heating stage attached to high resolution XRD chamber. The films were annealed at 250 °C for up to 160 minutes in air. Analysis of the Raman

spectroscopy results pre- and post-annealing shows that no other iron oxide phase other than Fe_3O_4 were present in the films. The Verwey transition temperature was found to be suppressed at longer annealing times, but at 4 minutes the transition is still visible, albeit at a lower temperature and with a minimal change in resistivity. As mentioned in Section 3.3.1, a small deviation from stoichiometry suppresses the Verwey transition and therefore after 4 minutes of annealing it is likely that the films remained in the Fe_3O_4 phase, but with a small change in stoichiometry.

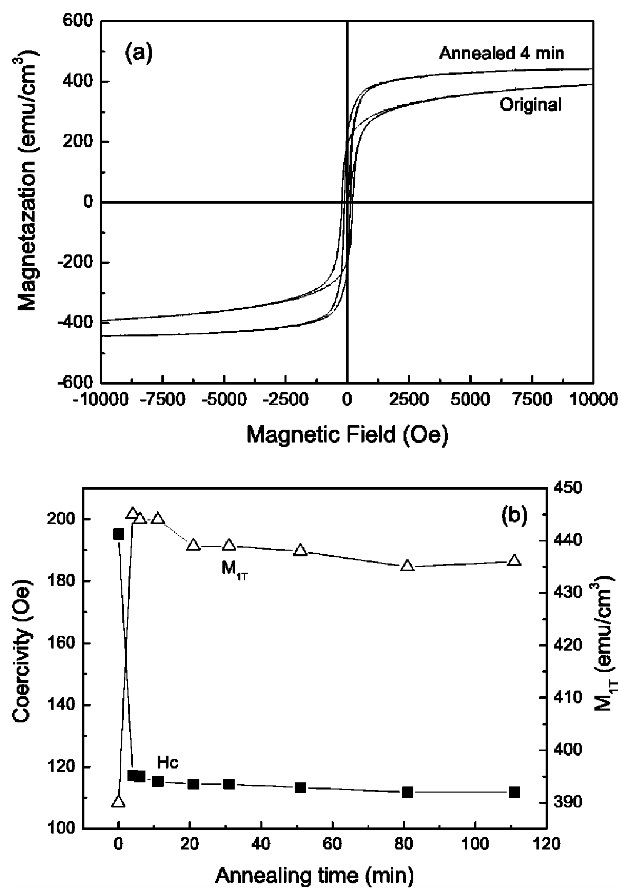


Figure 3.12. (a) Hysteresis loop of original and 4 minute annealed magnetite films. (b) Plot showing the coercivity and magnetic moment in a 1 T applied magnetic field as a function of annealing time. (Taken from [45]).

With this annealing procedure substantial change of the saturation magnetisation (in a 1 T field) and the coercivity are also observed, as illustrated in Figure 3.12. After only 4 minutes the saturation magnetisation can be seen to increase from $\sim 390 \text{ emu/cm}^3$ to $\sim 440 \text{ emu/cm}^3$, and the coercivity drop from $\sim 200 \text{ Oe}$ to 120 Oe . After these initial changes no other variation is observed apart from a slight decrease in the saturation magnetisation. This large change in saturation magnetisation is not attributed to the change in stoichiometry but to the decay of the exchange interaction at APBs. This conclusion is fitting for the dramatic change that is seen in saturation magnetisation, as although a change in stoichiometry in the films would cause a change in saturation magnetisation, it is likely to reduce the saturation magnetisation.

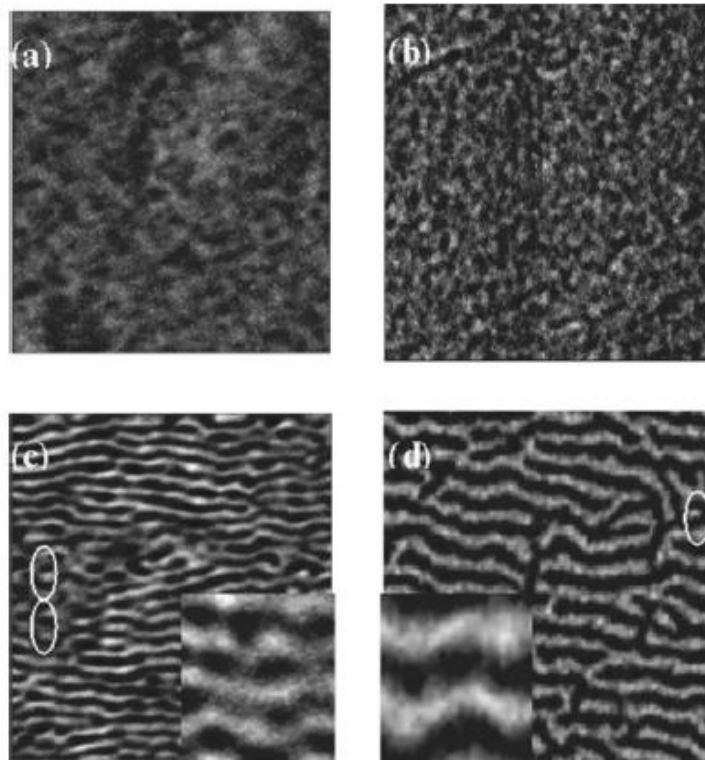


Figure 3.13. MFM images of as-grown $\text{Fe}_3\text{O}_4/\text{MgO}$ films with film thicknesses (a) 100 nm and (b) 400 nm. MFM images for the same films after being annealed for 4 minutes in air at $250 \text{ }^\circ\text{C}$ are shown in (c) 100 nm & (d) 400 nm. Image size: $6 \mu\text{m} \times 6 \mu\text{m}$, inset size: $1 \mu\text{m} \times 1 \mu\text{m}$. (Taken from [45]).

LITERATURE REVIEW

The annealing research by Zhou et al [45] has been continued by Wei et al [46] who have shown a change in the magnetic domain structure for the $\text{Fe}_3\text{O}_4/\text{MgO}$ (100) film after annealing for 4 minutes in air at 250 °C. MFM images of the as-grown Fe_3O_4 thin films with thicknesses of 100 nm and 400 nm show irregular domain structures (Figure 3.13a & b). After the films are annealed, the MFM images show a long-range ordered stripe-like magnetic domain structure (Figure 3.13c & d).

After applying a perpendicular field of +175 mT to the annealed film, the dark stripe domains are partly transformed into dots, with the same occurring for the bright stripes when an opposite field is applied. This can be seen in Figure 3.14a along with a schematic representation of the domain structure. In addition to transforming from the stripe domain structure to dots, it was shown that a majority of these dots are immobile with an example shown in Figure 3.14b. It was concluded from XRD and CEMS data that APBs were the only defect type present with a sufficient density to cause this domain pinning.

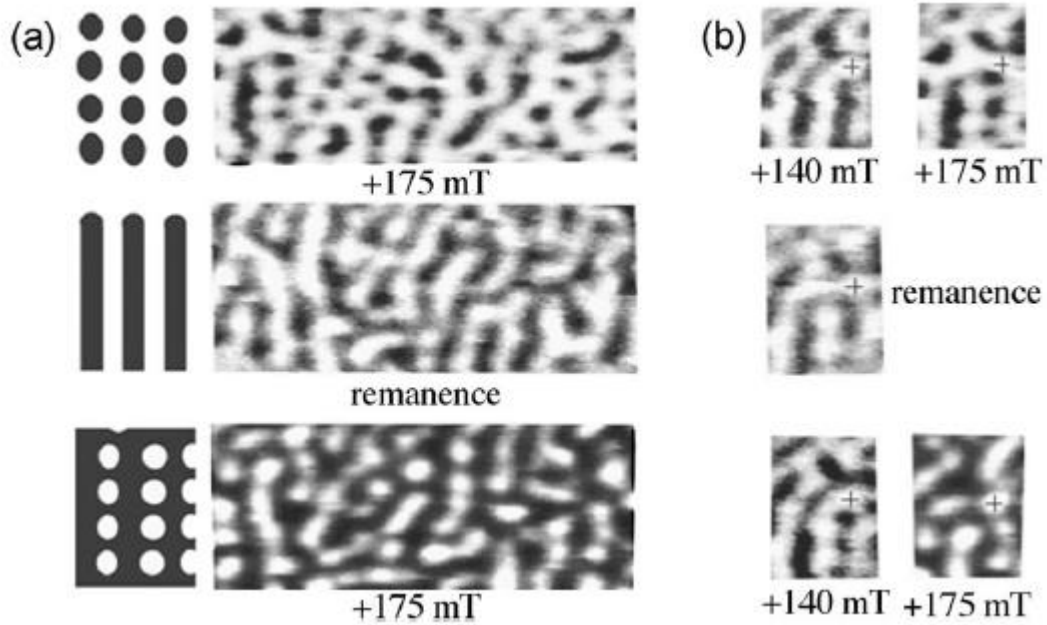


Figure 3.14. (a) MFM images of the annealed Fe_3O_4 thin film with applied perpendicular magnetic fields, with a schematic representation of the domain structure. Image size: $4 \mu\text{m} \times 1.5 \mu\text{m}$. (b) MFM images highlighting a single dot through a field sweep. (Taken from [45]).

Analysis of CEMS data for the p parameter (a measure of in-plane orientation) revealed that the p parameter changed from 1.2 to 0.8 after the film was annealed. As a guide, $p = 2$ corresponds to an in-plane orientation and $p = 0$ is for a perpendicular orientation. The authors suggest that this change in perpendicular anisotropy after annealing the film is possibly attributed to a chemical modification of APBs during the annealing, and that a change in the domain wall energy causing the appearance of the stripe domain pattern.

In combination these three publications provide substantial evidence that post-deposition annealing can improve the properties of as grown magnetite films, with one producing a single phase of magnetite from a mixed phase upon annealing and the

other two causing a large change in magnetic properties after just 4 minutes. This is a positive result for applications based on Fe_3O_4 thin films where the presence of APBs have removed the half-metal properties seen in bulk Fe_3O_4 , and provides evidence of coercivity reduction post growth which is beneficial to this thesis.

3.4. Magnetite Nanostructures

This final section in the literature review ties together the previous sections on atom traps using magnetic domain walls in nanostructures and the properties of magnetite thin films. It covers a review of planar magnetite nanostructures including how the structures were fabricated and their magnetic structure. This review of the magnetic structure of the nanostructures will provide a useful guide and comparison for the experimental results measured and analysed in this thesis.

There are numerous ways of forming magnetite nanostructures. These include using anodic aluminium oxide (AAO) templates with electrodeposition techniques [47-49], utilising the proteins found in magneto-tactic bacteria to form single crystal magnetite nanocrystals [50-52] or using a combination of electron beam lithography and thin film deposition methods to pattern bespoke nanostructures [53, 54]. Although the first two techniques are both interesting, the focus of this section will primarily be on the last method as it produces lithographically patterned planar nanostructures that could be used for atom trapping.

Fonin et al [53] initially grew Fe_3O_4 (100) thin films (thickness = 40 nm) using MBE on MgO (100) substrates. Superconducting quantum interference device (SQUID) magnetometry measurements along different crystal axes shows an in-plane four-fold

anisotropy with the easy axes pointing along the in-plane $\langle 011 \rangle$ directions. Nanostructures of ring arrays with varying outer diameter (D) and linewidth (W) and zig-zag lines were fabricated from these films using focused ion beam milling or argon ion milling through a Cr hard mask, created using electron beam lithography and lift-off procedures. The magnetisation configurations of these structures were analysed using XMCD-PEEM and MFM, and micromagnetic simulations were performed using the object oriented micromagnetic framework (OOMMF) code in order to help interpretation of the experimental results.

Figure 3.15 presents (a) XMCD-PEEM and (c) MFM images obtained from a nanoring ((a) $D = 10 \mu\text{m}$ and (c) $D = 5 \mu\text{m}$, $W = 1135 \text{ nm}$) that were magnetised along their hard axis $[001]$, along with a micromagnetic simulation of the resulting configuration (Figure 3.15b). It can be seen that the magnetocrystalline anisotropy dominates forcing the magnetisation to point along the easy-axes, $\langle 011 \rangle$, creating 4 domains. This forms 90° head-to-head (H-2-H) and tail-to-tail (T-2-T) domain walls located at the top and bottom of the nanoring on the hard axis $[001]$, plus two 90° H-2-T domain walls located at the left and right of the nanoring on the $[010]$ axis. The magnetisation state simulated using OOMMF and following the same initialisation process reproduces the XMCD-PEEM image very well.

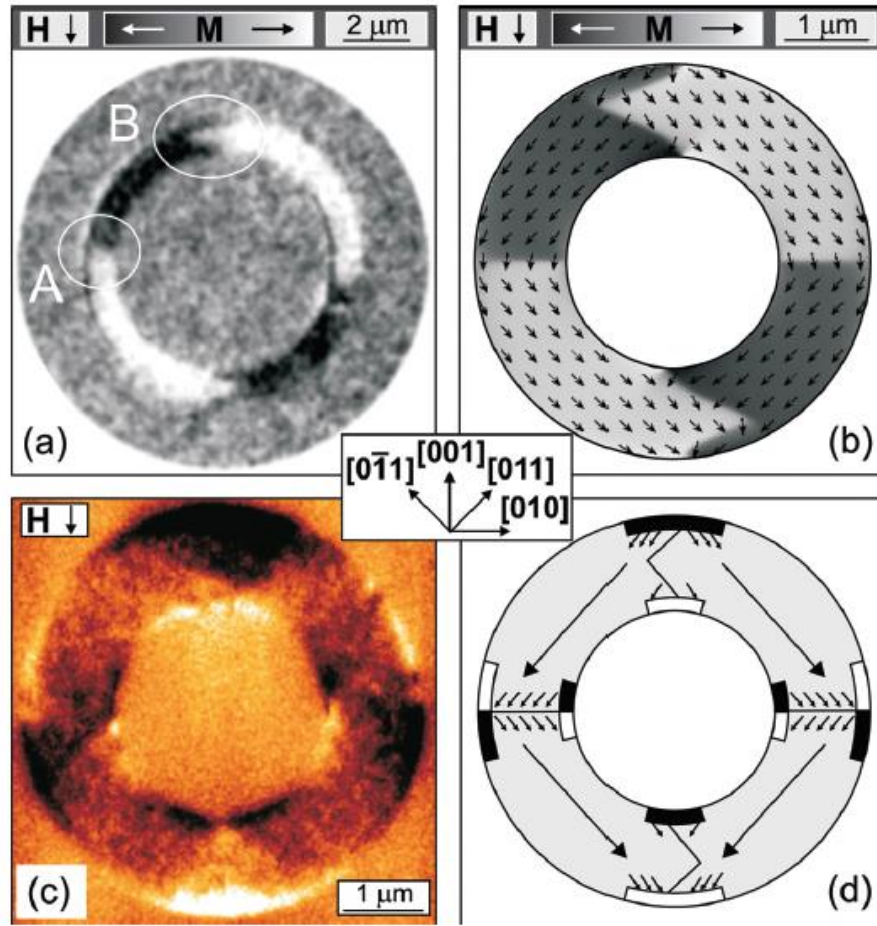


Figure 3.15. (a) A Fe_3O_4 ring with a $10\ \mu\text{m}$ diameter and $1135\ \text{nm}$ width that has been initially magnetised along its hard axis $[001]$ measured using XMCD-PEEM (black and white correspond to magnetisation pointing to the left and right, respectively). For (b-d) a Fe_3O_4 ring with a diameter of $5\ \mu\text{m}$ and $1135\ \text{nm}$ width was used. (b) OOMMF micromagnetic simulation in the remanent state after saturation. (c) MFM image after magnetised along hard axis, and (d) a schematic illustrating the contrast seen in the MFM image. (Taken from [53]).

As a comparison, another ring ($D = 5\ \mu\text{m}$, $W = 530\ \text{nm}$) was magnetised along an easy axis $[01\bar{1}]$ producing a modified onion state (Figure 3.16). Four 90° H-2-T domain walls are formed on the hard axes of the nanoring, with an additional two 180° H-2-H

and T-2-T domain walls formed in the direction of the applied field $[01\bar{1}]$. This produces 6 domains with the magnetisation following the easy axes, $\langle 011 \rangle$.

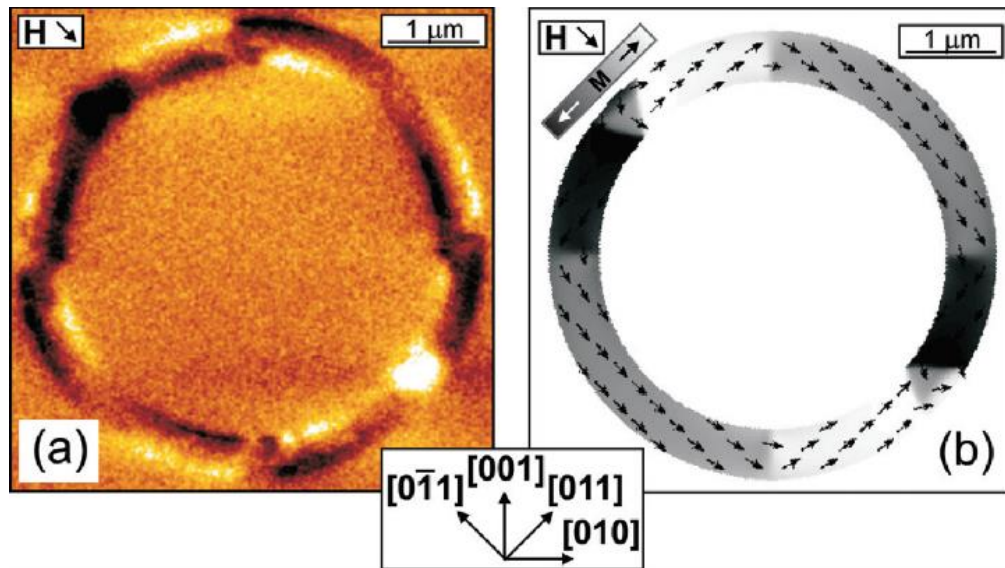


Figure 3.16. A Fe_3O_4 ring with a $5 \mu\text{m}$ diameter and 530 nm width that has been initially magnetised along its easy axis (a) measured using MFM and (b) simulated using OOMMF. (Taken from [53]).

It is clear for the ring geometries in Figure 3.15 & Figure 3.16 that the cubic magnetocrystalline anisotropy dominates the magnetic structure, producing 90° domain walls at the four easy axis directions when the rings are magnetised in both the easy or hard direction. For a Fe_3O_4 ring structure with a large cubic magnetocrystalline anisotropy to be feasible for domain wall motion, the wire width would have to be reduced to allow the shape anisotropy to dominate.

In the same paper, the remanent state of zig-zag nanowires were also imaged after magnetising along the hard axis, producing 90° H-2-H and T-2-T domain wall structures at the kinks. They found that the wider the wire, the more complicated the

LITERATURE REVIEW

domain wall structure with the domain wall featuring a repeated zig-zag folding to reduce the magnetostatic energy, and therefore that the narrower wires would be a better option for achieving domain wall motion.

In contrast to the cubic magnetocrystalline anisotropy present in the Fe_3O_4 nanostructures producing the domain structures in Figure 3.15 & Figure 3.16 [53], nanostructures were patterned by Zhang et al [55] from a ultra-thin $\text{Fe}_3\text{O}_4/\text{GaAs}$ (100) film where the cubic magnetocrystalline anisotropy is negligible.

Post-growth annealing of a 3 nm epitaxial Fe/GaAs (100) thin film grown using MBE produced the Fe_3O_4 thin film. This film is unique in that it exhibits a strong in-plane uniaxial magnetic anisotropy, with a negligible intrinsic cubic magnetic anisotropy. The authors also state that the resistivity of $\sim 0.005 \Omega \text{ cm}$ for the film, which is very close to that of a bulk single crystal, is a result of the lack of APBs in the film. The lack of APBs in the film was attributed to the post-growth annealing of the Fe film, where the oxidation takes place from the film surface down to the substrate by oxygen diffusion [56, 57]. Several arrays of nanowires were formed from the thin film using FIB, with a length of $10 \mu\text{m}$ and widths ranging from $0.5 \mu\text{m} - 1 \mu\text{m}$, so that the long axis was either parallel or perpendicular to the easy axis $[0\bar{1}1]$ of the original Fe_3O_4 film. The inter-wire spacing for all of the arrays were no less than $1 \mu\text{m}$. SEM images of 3 different nanowire arrays are shown in Figure 3.17, with patterns 1 & 2 having a wire width of $1 \mu\text{m}$ and pattern 3 with a width of $0.5 \mu\text{m}$. Patterns 1 & 3 are also aligned with the wires long axis along the $[0\bar{1}1]$ easy axis, whereas pattern 2 is along the $[011]$ hard axis.

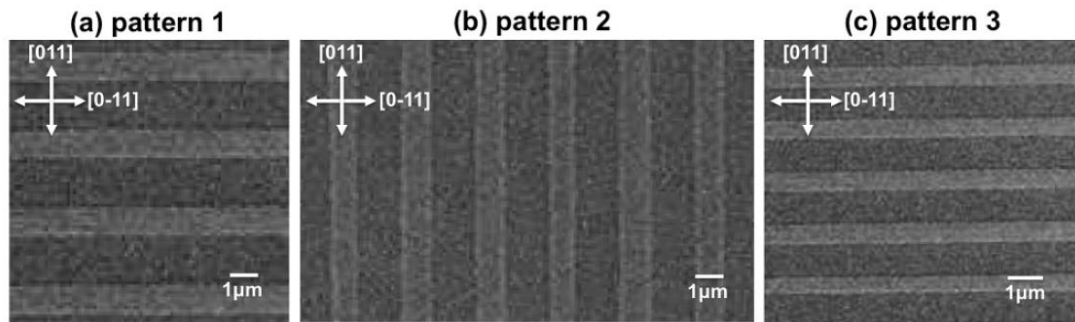


Figure 3.17. SEM images of 3 different nanowire arrays: a) pattern 1, b) pattern 2 & c) pattern 3. Taken from [55].

Interestingly, focussed-MOKE measurements (Figure 3.18) of the nanowires taken with the magnetic field along the easy $[0\bar{1}1]$ and hard $[011]$ directions show that patterns 1-3 all have the same easy and hard magnetisation axes as the original thin film. Even measurements taken of nanowires in pattern 2 which have their long axis along the hard direction, maintain a magnetic easy axis along $[0\bar{1}1]$. The coercivity along the $[0\bar{1}1]$ from nanowires in pattern 3 are smaller than those in pattern 1, which has been attributed to a reduced uniaxial anisotropy in the thinner wires (pattern 3).

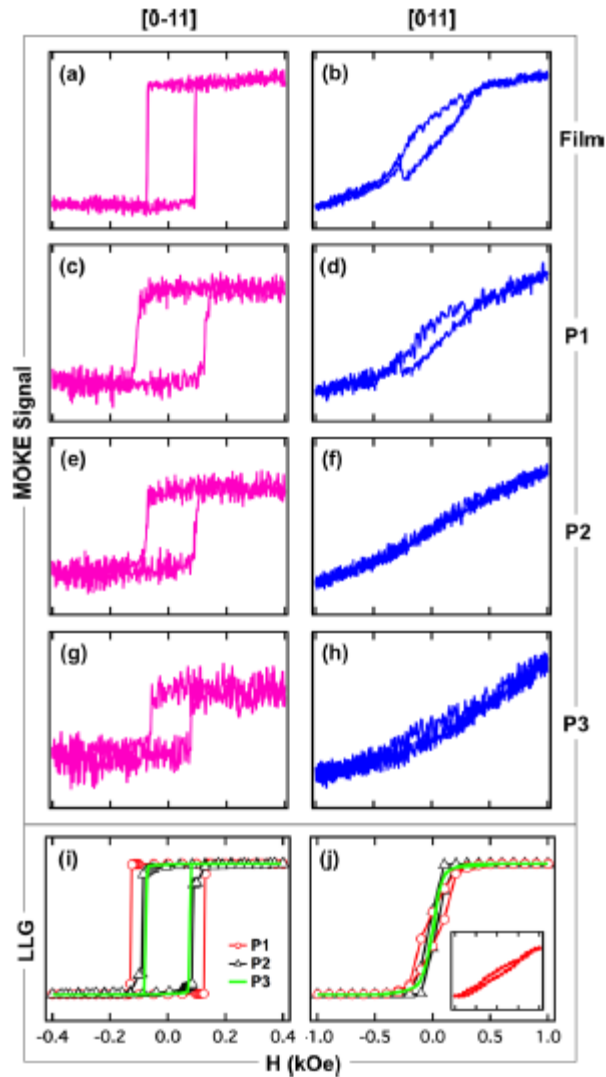


Figure 3.18. Focussed-MOKE hysteresis loops taken along the $[0\bar{1}1]$ (pink) and $[011]$ (blue) axes for the (a)-(b) Fe_3O_4 film, (c)-(d) nanowires in pattern 1, (e)-(f) nanowires in pattern 2, and (g)-(h) nanowires in pattern 3. Hysteresis loop simulations for the nanowire patterns are presented in (i) & (j), with the inset in (j) including interfacial defects. Taken from [55].

Micromagnetic simulations were performed using the LLG Micromagnetics Simulator to reproduce the hysteresis loops in Figure 3.18. Although the hysteresis loops were reproduced well for the loops along the $[0\bar{1}1]$ direction, the experimental loops along

the [011] direction were harder to saturate than the reproduced simulations. The simulations were modified to include interfacial defects, which produced a better fit to the experimental data.

In addition to simulating the hysteresis loops for the nanowires, micromagnetic simulations of Fe_3O_4 rings with a wire width of $1\ \mu\text{m}$ and $0.5\ \mu\text{m}$ were performed. There is no mention of the ring diameter, although a rough estimate using the scale bar in Figure 3.19 is a diameter of $5\ \mu\text{m}$. For these simulations, the rings were saturated along the [011] direction and then relaxed to their remnant state. The $1\ \mu\text{m}$ wide ring produced a four narrow 180° domain walls, with the domains pointing in the easy direction. However, in the $0.5\ \mu\text{m}$ wide ring an onion-state domain formation is produced with the two magnetic domains having their magnetisation following the shape of the ring and the domain walls on the [011] axis. This domain formation was due to the reduced uniaxial anisotropy for the $0.5\ \mu\text{m}$ wire width and the small cubic anisotropy for the film and nanowires.

With a reduce uniaxial anisotropy, the $0.5\ \mu\text{m}$ wire nanoring in Figure 3.19b would be a more suitable option for the domain wall atom trapping concept than the $1\ \mu\text{m}$ wire nanorings or the nanorings produced by Fonin [53]. Reproducing the undulating nanowire configuration by Negoita [17] using the $0.5\ \mu\text{m}$ wide Fe_3O_4 wire would allow for a low DW velocity propagation though a material with a larger resistivity than permalloy and a large saturation magnetisation to support the atom trapping concept.

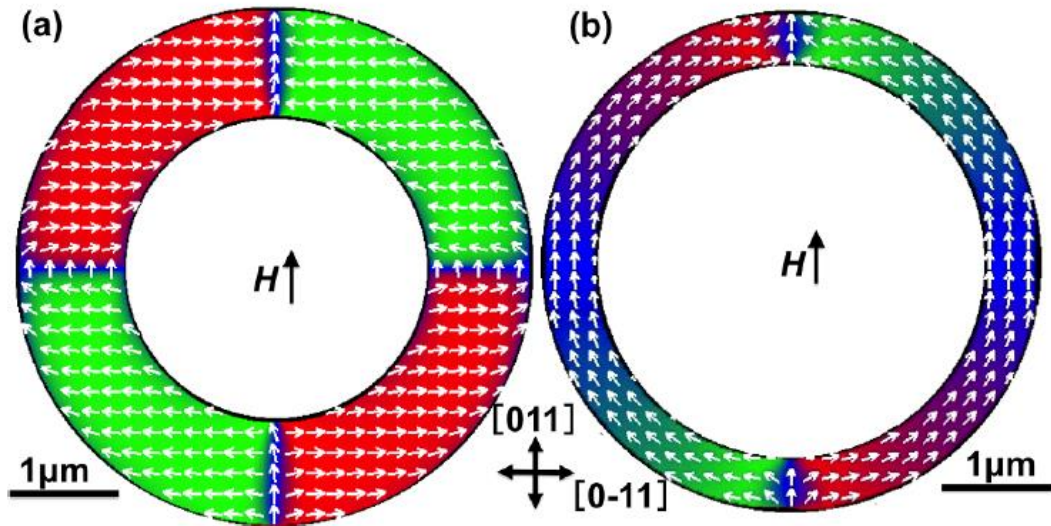


Figure 3.19. Micromagnetic simulations showing the domain structure of Fe_3O_4 nanorings with wire widths of (a) $1 \mu m$ and (b) $0.5 \mu m$ after saturation in $[011]$ direction and relaxation to their remanent state. Taken from [55].

In contrast to the nanostructures with strong magnetocrystalline anisotropy and the uniaxial anisotropy dependent nanorings discussed above, Tsai et al [54] fabricated polycrystalline square islands with dimensions ranging from $1 \times 1 \mu m^2$ to $5 \times 5 \mu m^2$. A nanocrystalline thin film was deposited by reactive magnetron sputtering on to Si/SiO₂ substrates at room temperature followed by annealing at 300 °C for 1 hour. A combination of electron-beam lithography and lift off processing was used to form the structure arrays.

The experimental procedure and analysis of the MFM results given in the paper is short and not entirely clear. The MFM images of these structures show a speckled surface that did not saturate in applied fields of 400 Oe (Figure 3.20). Furthermore, there is no difference in the speckled pattern between the applied field state and remnant state for the $1 \mu m$ dot which was attributed to anti-phase domains present in

the films which pin DWs. No comment is made on the edge contrast in the x-component of the magnetisation reversing for the 5 μm dot with an applied field of 400 Oe.

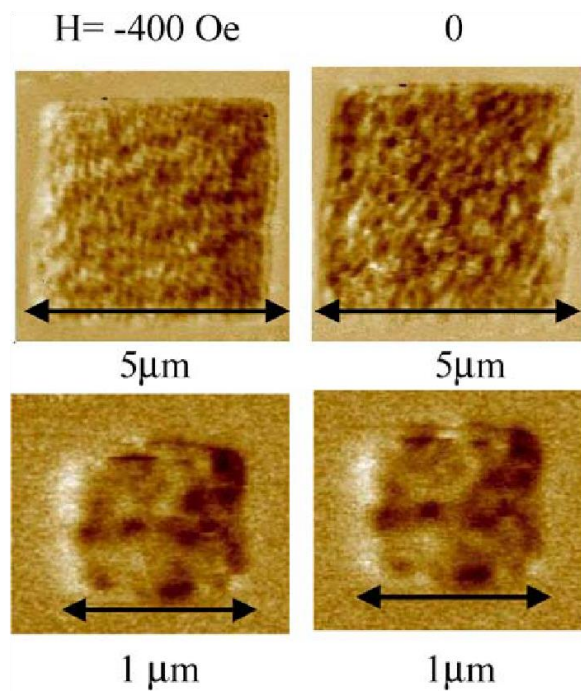


Figure 3.20. MFM images of Fe_3O_4 patterned dots with different widths and applied magnetic field. (Taken from [54]).

Conclusion

It can be seen from the review of the literature in this chapter that there is a large interest in magnetite thin films due to the predicted 100 % spin polarisation and high Curie temperature (860 K). However, there is little research into planar nanostructures of magnetite compared to nanostructures created using magnetotactic bacteria or AAO templates, which is possibly due to the presence of APBs created during magnetite growth on substrates. The presence of APBs in nanostructures could prove

LITERATURE REVIEW

problematic when looking into domain wall motion, as the APBs can act as pinning sites. The density of APBs has been shown to be reduced using annealing treatment due to the diffusive nature of the APBs.

References

- [1] The Editors of Encyclopaedia Britannica. (27/06/2017). *Stern-Gerlach experiment*. Available: <https://www.britannica.com/science/Stern-Gerlach-experiment>
- [2] J. Esteve, "Cold Atoms: Trapped by nanostructures," *Nature Nanotechnology*, vol. 8, pp. 317-318, 2013.
- [3] W. D. Phillips, "Laser Cooling and Trapping of Neutral Atoms," *Reviews of Modern Physics*, vol. 70, pp. 721-741, 1998.
- [4] D. A. Allwood, T. Schrefl, G. Hrkac, I. G. Hughes, and C. S. Adams, "Mobile atom traps using magnetic nanowires," *Applied Physics Letters*, vol. 89, pp. 014102-014104, 2006.
- [5] C. S. Adams and E. Riis, "Laser cooling and trapping of neutral atoms," *Progress in Quantum Electronics*, vol. 21, pp. 1-79, 1997.
- [6] R. Folman, P. Kruger, J. Schmiedmayer, J. Denschlag, and C. Henkel, "Microscopic atom optics: From wires to an atom chip," *Advances in Atomic, Molecular, and Optical Physics*, vol. 48, pp. 263-356, 2002.
- [7] T. J. Hayward, A. D. West, K. J. Weatherill, T. Schrefl, I. G. Hughes, and D. A. Allwood, "Nanomagnetic engineering of the properties of domain wall atom traps," *Journal of Applied Physics*, vol. 110, pp. 123918-123925, 2011.
- [8] R. Folman, P. Kruger, D. Cassettari, B. Hessmo, T. Maier, and J. Schmiedmayer, "Controlling cold atoms using nanofabricated surfaces: atom chips," *Physical Review Letters*, vol. 84, pp. 4749-4752, 2000.

LITERATURE REVIEW

- [9] S. Groth, P. Kruger, S. Wildermuth, R. Folman, T. Fernholz, J. Schmiedmayer, *et al.*, "Atom chips: Fabrication and thermal properties," *Applied Physics Letters*, vol. 85, pp. 2980-2982, 2004.
- [10] M. P. A. Jones, C. J. Vale, D. Sahagun, B. V. Hall, and E. A. Hinds, "Spin coupling between cold atoms and the thermal fluctuations of a metal surface," *Physical Review Letters*, vol. 91, pp. 080401-080404, 2003.
- [11] D. M. Harber, J. M. McGuirk, J. M. Obrecht, and E. A. Cornell, "Thermally induced losses in ultra-cold atoms magnetically trapped near room-temperature surfaces," *Journal of Low Temperature Physics*, vol. 133, pp. 229-238, 2003.
- [12] A. E. Leanhardt, Y. Shin, A. P. Chikkatur, D. Kielpinski, W. Ketterle, and D. E. Pritchard, "Bose-Einstein condensates near a microfabricated surface," *Physical Review Letters*, vol. 90, pp. 1-4, 2003.
- [13] J. Fortagh, H. Ott, S. Kraft, A. Gunther, and C. Zimmermann, "Surface effects in magnetic microtraps," *Physical Review A*, vol. 66, pp. 1-5, 2002.
- [14] D.-W. Wang, M. D. Lukin, and E. Demler, "Disordered Bose-Einstein condensates in quasi-one-dimensional magnetic microtraps," *Physical Review Letters*, vol. 92, pp. 076802-076805, 2004.
- [15] J. Esteve, C. Aussibal, T. Schumm, C. Figl, D. Mailly, I. Bouchoule, *et al.*, "Role of wire imperfections in micromagnetic traps for atoms," *Physical Review A*, vol. 70, pp. 043629-043632, 2004.
- [16] M. Negoita, T. J. Hayward, and D. A. Allwood, "Controlling domain walls velocities in ferromagnetic ring-shaped nanowires," *Applied Physics Letters*, vol. 100, pp. 072405-072409, 2012.

- [17] M. Negroita, M. P. P. Hodges, M. T. Bryan, P. W. Fry, M.-Y. Im, P. Fischer, *et al.*, "Linear transport of domain walls confined to propagating 1-D potential wells," *Journal of Applied Physics*, vol. 114, pp. 163901-163906, 2013.
- [18] D. T. Margulies, F. T. Parker, and A. E. Berkowitz, "Magnetic anomalies in single crystal Fe₃O₄ thin films," *Journal of Applied Physics*, vol. 75, pp. 6097-6099, 1994.
- [19] W. Eerenstein, T. T. M. Palstra, T. Hibma, and S. Celotto, "Origin of the increased resistivity in epitaxial Fe₃O₄ films," *Physical Review B*, vol. 66, pp. 201101-201104, 2002.
- [20] L. Degiorgi, I. Blatter-Morke, and P. Wachter, "Magnetite: Phonon modes and the Verwey transition," *Physical Review B*, vol. 35, pp. 5421-5424, 1987.
- [21] V. A. M. Brabers, F. Walz, and H. Kronmuller, "Impurity effects upon the Verwey transition in magnetite," *Physical Review B*, vol. 58, pp. 14163-14166, 1998.
- [22] J. Garcia and G. Subias, "The Verwey transition - a new perspective," *Journal of Physics: Condensed Matter*, vol. 16, pp. R145-R178, 2004.
- [23] F. Walz, "The Verwey transition - a topical review," *Journal of Physics: Condensed Matter*, vol. 14, pp. R285-R340, 2002.
- [24] M. S. Sem, J. P. Wright, and J. P. Attfield, "Charge order and three-site distortions in the Verwey structure of magnetite," *Nature*, vol. 481, pp. 173-176, 2012.
- [25] D. T. Margulies, F. T. Parker, M. L. Rudee, F. E. Spada, J. N. Chapman, P. R. Aitchison, *et al.*, "Origin of the anomalous magnetic behaviour in single crystal Fe₃O₄ films," *Physical Review Letters*, vol. 79, pp. 5162-5165, 1997.

LITERATURE REVIEW

- [26] W. Eerenstein, T. T. M. Palstra, S. S. Saxena, and T. Hibma, "Spin-polarised transport across sharp antiferromagnetic boundaries," *Physical Review Letters*, vol. 88, pp. 247204-247207, 2002.
- [27] D. T. Margulies, F. T. Parker, F. E. Spada, R. S. Goldman, J. Li, R. Sinclair, *et al.*, "Anomalous moment and anisotropy behaviour in Fe₃O₄ films," *Physical Review B*, vol. 53, pp. 9175-9187, 1996.
- [28] T. Hibma, F. C. Voogt, L. Nielsen, P. A. A. v. d. Heijden, W. J. M. d. Jonge, J. J. T. M. Donkers, *et al.*, "Anti-phase domains and magnetism in epitaxial magnetite layers," *Journal of Applied Physics*, vol. 85, pp. 5291-5293, 1999.
- [29] S. Celotto, W. Eerenstein, and T. Hibma, "Characterization of anti-phase boundaries in epitaxial magnetite films," *The European Physical Journal B*, vol. 36, pp. 271-279, 2003.
- [30] W. Eerenstein, T. T. M. Palstra, T. Hibma, and S. Celotto, "Diffusive motion of antiphase domain boundaries in Fe₃O₄ films," *Physical Review B*, vol. 68, pp. 014428-014434, 2003.
- [31] G. E. Sterbinsky, J. Cheng, P. T. Chiu, B. W. Wessels, and D. J. Keavney, "Investigation of heteroepitaxial growth of magnetite thin films," *Journal of Vacuum Science and Technology B*, vol. 25, pp. 1389-1392, 2007.
- [32] Y.-P. Zhao, R. M. Gamache, G.-C. Wang, T.-M. Lu, G. Palasantzas, and J. T. M. D. Hosson, "Effect of surface roughness on magnetic domain wall thickness, domain size, and coercivity," *Journal of Applied Physics*, vol. 89, pp. 1325-1330, 2001.
- [33] P. A. A. V. D. Heijden, J. J. Hammink, P. J. Bloemen, R. M. Wolf, M. G. V. Opstal, P. J. V. D. Zaag, *et al.*, "Magnetic properties of epitaxial MBE-grown

- thin Fe₃O₄ films on MgO (100)," in *Magnetic Ultrathin Films, Multilayers and Surfaces*, Pittsburgh, Pennsylvania, 1995, pp. 27-32.
- [34] A. Bollero, M. Ziese, R. Hohne, H. C. Semmelhack, U. Kohler, A. Setzer, *et al.*, "Influence of thickness on microstructural and magnetic properties in Fe₃O₄ thin films produced by PLD," *Journal of Magnetism and Magnetic Materials*, vol. 285, pp. 279-289, 2005.
- [35] W. B. Mi, J. J. Shen, E. Y. Jiang, and H. L. Bai, "Microstructure, magnetic and magneto-transport properties of polycrystalline Fe₃O₄ films," *Acta Materialia*, vol. 55, pp. 1919-1926, 2007.
- [36] X. Huang and J. Ding, "The structure, magnetic and transport properties of Fe₃O₄ thin films on different substrates by pulsed laser deposition," *Journal of the Korean Physical Society*, vol. 62, pp. 2228-2232, 2013.
- [37] R. Mantovan, S. Vangelista, S. Cocco, A. Lamperti, and O. Salicio, "Chemical vapor deposition of polycrystalline Fe₃O₄ thin films by using the cyclohexadiene iron tricarbonyl liquid precursor," *Journal of Applied Physics*, vol. 111, pp. 07B107-07B109, 2012.
- [38] R. Mantovan, A. Lamperti, M. Georgieva, G. Tallarida, and M. Fanciulli, "CVD synthesis of polycrystalline magnetite thin films: structural, magnetic and magnetotransport properties," *Journal of Physics D: Applied Physics*, vol. 43, pp. 1-11, 2010.
- [39] J. J. Shen, W. B. Mi, Z. Q. Li, P. Wu, E. Y. Jiang, and H. L. Bai, "Characterisation of facing-target reactive sputtered polycrystalline Fe₃O₄ films," *Journal of Vacuum Science and Technology A*, vol. 24, pp. 390-395, 2006.

LITERATURE REVIEW

- [40] C. Park, Y. Peng, J.-G. Zhu, D. E. Laughlin, and R. M. White, "Magnetoresistance of polycrystalline Fe₃O₄ films prepared by reactive sputtering at room temperature," *Journal of Applied Physics*, vol. 97, pp. 10C303-10C305, 2005.
- [41] H. Liu, E. Y. Jiang, H. L. Bai, R. K. Zheng, and X. X. Zhang, "Thickness dependence of magnetic and magneto-transport properties of polycrystalline Fe₃O₄ films prepared by reactive sputtering at room temperature," *Journal of Physics D: Applied Physics*, vol. 36, pp. 2950-2953, 2003.
- [42] A. Kumar, D. K. Pandya, and S. Chaudhary, "Electric field assisted sputtering of Fe₃O₄ thin films and reduction in anti-phase boundaries," *Journal of Applied Physics*, vol. 112, pp. 073909-073913, 2012.
- [43] Y. Peng, C. Park, and D. E. Laughlin, "Fe₃O₄ thin films sputter deposited from iron oxide targets," *Journal of Applied Physics*, vol. 93, pp. 7957-7959, 2003.
- [44] S. M. Ramay, S. A. Siddiqi, M. S. Anwar, C. Y. Park, and S.-C. Shin, "Effect of annealing time on structural and magnetic properties of laser ablated oriented Fe₃O₄ thin films deposited on Si (100)," *Bulletin of Materials Science*, vol. 35, pp. 501-503, 2012.
- [45] Y. Zhou, X. Jin, and I. V. Shvets, "Enhancement of the magnetization saturation in magnetite (100) epitaxial films by thermo-chemical treatment," *Journal of Applied Physics*, vol. 95, pp. 7357-7359, 2004.
- [46] J. D. Wei, I. Knittel, U. Hartmann, Y. Zhou, S. Murphy, I. V. Shvets, *et al.*, "Influence of the antiphase domain distribution on the magnetic structure of magnetite thin films," *Applied Physics Letters*, vol. 89, pp. 122517-122519, 2006.

- [47] S. P. Ko, J.-Y. Soh, and Y. K. Kim, "Control of magnetic behaviour in Fe₃O₄ nanostructures," *IEEE Transactions on Magnetics*, vol. 41, pp. 3304-3306, 2015.
- [48] L. Zhang and Y. Zhang, "Fabrication and magnetic properties of Fe₃O₄ nanowire arrays in different diameters," *Journal of Magnetism and Magnetic Materials*, vol. 321, pp. L15-L20, 2009.
- [49] L. Y. Zhang, D. S. Xue, X. F. Xu, A. B. Gui, and C. X. Gao, "The fabrication and magnetic properties of nanowire-like iron oxide," *Journal of Physics: Condensed Matter*, vol. 16, pp. 4541-4548, 2004.
- [50] E. T. Simpson, T. Kasama, M. Posfai, R. J. Harrison, and R. E. Dunin-Borkowski, "Magnetic induction mapping of magnetite chains in magnetotactic bacteria at room temperature and close to the Verwey transition using electron holography," *Journal of Physics: Conference Series*, vol. 17, pp. 108-121, 2005.
- [51] J. M. Galloway, J. P. Bramble, A. E. Rawlings, G. Burnell, S. D. Evans, and S. S. Staniland, "Biotemplated magnetic nanoparticle arrays," *Small*, vol. 8, pp. 204-208, 2012.
- [52] L. L. Afremov and A. V. Panov, "Magnetic states and hysteresis properties of small magnetite particles," *The Physics of Metals and Metallography*, vol. 86, pp. 269-275, 1998.
- [53] M. Fonin, C. Hartung, U. Rudiger, D. Backes, L. Heydeman, F. Nolting, *et al.*, "Formation of magnetic domains walls in epitaxial Fe₃O₄ (100) elements (invited)," *Journal of Applied Physics*, vol. 109, pp. 07D315-07D318, 2011.

LITERATURE REVIEW

- [54] J. L. Tsai, K. T. Huang, W. C. Cheng, M. D. Lee, T. S. Chin, S. U. Jen, *et al.*, "Magnetic properties of patterned Fe₃O₄ films," *Journal of Magnetism and Magnetic Materials*, vol. 272, pp. 1664-1665, 2004.
- [55] W. Zhang, P. K. J. Wong, D. Zhang, S. J. Yuan, Z. C. Huang, Y. Zhai, *et al.*, "Magnetic anisotropies in epitaxial Fe₃O₄/GaAs (100) patterned structures," *AIP Advances*, vol. 4, pp. 107111-107116, 2014.
- [56] S. S. A. Hassan, Y. B. Xu, J. Wu, and S. M. Thompson, "Epitaxial growth and magnetic properties of half-metallic Fe₃O₄ on Si (100) using MgO buffer layer," *IEEE Transactions on Magnetics*, vol. 45, pp. 4357-4359, 2009.
- [57] S. S. A. Hassan, Y. B. Xu, J. Wu, J.-G. Zheng, J. Y. Huang, Y. Huang, *et al.*, "The properties and structure relationship of half metallic magnetic materials on GaAs," *IEEE Transactions on Magnetics*, vol. 45, pp. 4360-4363, 2009.

4. Experimental Techniques

In this chapter, the experimental techniques used to grow, pattern and measure iron oxide thin films and nanostructures in this project will be discussed. As many experimental techniques were utilised, this chapter has been split into 5 sections: growth and fabrication techniques, compositional and phase analysis, topology imaging, electrical characterisation and magnetic characterisation.

The growth and fabrication techniques section will cover the use of sputtering and thermal evaporation for thin film growth and the use of electron beam lithography and ion milling for nanostructure formation. X-ray diffraction (XRD), Raman spectroscopy and X-ray photoelectron spectroscopy (XPS) were used to determine the iron oxide phases present in the thin films and these will be explained in the compositional and phase analysis section. The surface morphologies and sample thicknesses were measured using atomic force microscopy (AFM) and spectroscopic ellipsometry respectively and these will be described in the topology imaging section. One of the main aims of this work was to create a higher resistivity analogue of permalloy, and the four-point technique used to measure the resistivity of thin films is explained in the electrical characterisation section. Finally, the magnetic characterisation section describes the magneto-optical Kerr effect (MOKE) magnetometer used for hysteresis loop measurements of thin films, the magnetic force microscope system (MFM) used to image the magnetic states of both thin film and nanostructure, and the magnetic transmission x-ray microscope (M-TXM) at the

Advanced Light Source (ALS) used for high-resolution imaging of iron oxide thin films.

4.1. Growth and fabrication techniques

4.1.1. Sputtering

In the work described in this thesis, thin films of iron and iron oxides were sputtered onto $380 \pm 50 \mu\text{m}$ thick (001) Si substrates with the native oxide and $500 \mu\text{m}$ thick (001) MgO substrates using a Kurt J Lesker sputtering system that was equipped with both a DC and an RF sputtering gun.

Sputtering is a common technique for thin film growth due to its simplicity and versatility [1, 2]. A schematic diagram of the main components of the sputtering system is shown in Figure 4.1.

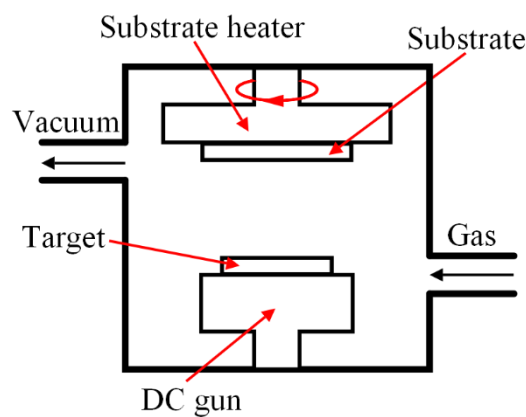


Figure 4.1. Schematic showing the main components of the sputtering system.

The sputtering chamber is first pumped down to a low base pressure (usually around 10^{-6} – 10^{-7} mbar) so as to prevent background gases from reacting with the film, before a process gas (usually argon) is pumped into the chamber to a working pressure of 10^{-2} – 10^{-3} mbar. A large voltage is then applied between the target material (cathode) and the substrate (anode). This applied voltage causes free electrons in the target's surface to be accelerated away from the negatively charged electrode. These electrons collide with neutral atoms of the process gas, causing their ionisation and the initiation of a plasma. The positively charged ions of this plasma are accelerated into the target material with enough kinetic energy to eject target atoms and electrons from the surface. The electrons produce more gas ions and, with the electrons from ionisation events in the plasma, allow the plasma to be sustained. After being ejected, the atoms from the target collide with numerous gas atoms that deflect them and reduce their kinetic energy. This causes the atoms to approach the substrate's surface from partially randomised directions producing conformal growth of a film on the substrate they condense onto it.

To accelerate growth and help sustain the plasma, magnetron sputtering can be used, in which permanent magnets are placed behind the cathode. Here, the magnetic field produced by the magnets traps electrons above the target surface, which enhances the probability of ionisation and also allows the plasma to be formed at a lower working pressure.

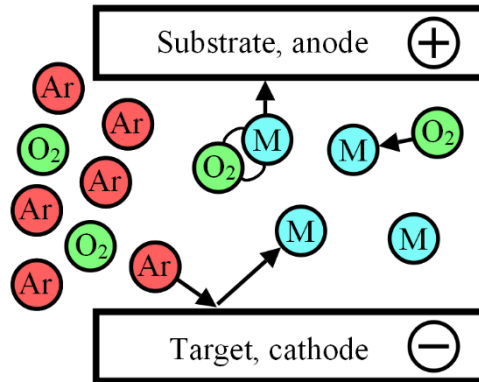


Figure 4.2. Illustration of the reactive sputtering technique where a reactive gas is added to the sputter chamber to react with the sputtered target material. The reactive gas here is oxygen.

The properties of sputtered films can be controlled using several parameters including the substrate temperature, gas pressure, the substrate to target distance and the sputtering power. The substrate temperature effects the mobility of the deposited atoms, and an increased gas pressure increases the rate at which sputtered atoms are thermalized. By reducing the substrate to target distance by half increases the deposition rate by a factor of 4, and the deposition rate is also increased with an increase in sputtering power [3]. Furthermore, although the chamber is pumped down to a low base pressure to prevent contamination from background gases, controlled addition of reactive gases to the chamber can be used to produce films of different chemical composition to the target material (Figure 4.2). Common reactive gases used include oxygen and nitrogen.

In this project, iron targets with 99.95% purity were used as targets, and sputtering was performed using a Hüttinger PFG 1500 DC power supply. To start the growth process, the chamber was pumped down using a Boc Edwards XDS10 roughing pump

and a CTI-cryogenics cryo-torr 8F cryopump to a base pressure of around $10^{-6} - 10^{-7}$ mbar. Once the desired base pressure was reached, argon and oxygen gases were introduced to the chamber via MKS RS-485 mass-flow controllers with a range of 100 sccm and 10 sccm (standard cubic centimetres per minute), respectively. To remove the effects of the stray field from the magnetron gun on the film growth, the sample stage was rotated (at 10 seconds/rev). The substrates were held in place on the substrate holder using clamps on a sheet of copper. A radiative heater was used to control the substrate temperature, with the temperature being measured using a thermocouple placed close to the substrate holder. Maximum substrate temperatures of 800 °C could be obtained.

4.1.2. Nanostructure formation

There are three steps that are used in the lift-off method for nanostructure fabrication: nanostructure patterning of a resist, followed by material growth onto the patterned resist and subsequent resist lift-off. However, as the substrate temperature used to grow magnetite thin films in this project were above the melting point (160 °C) of the polymer resist used (poly(methyl methacrylate) (PMMA)) [4], the nanostructures were instead fabricated by ion milling magnetite films through a nanostructure hard mask, created via electron beam lithography. The steps taken to make the nanostructures are shown in Figure 4.3.

Firstly, an electron sensitive polymer resist (PMMA) was spin coated (step 1) onto the surface of the magnetite thin films in preparation for electron beam lithography (step 2) which was used to pattern the resist. Thermal evaporation (step 3) allowed a bilayer

EXPERIMENTAL TECHNIQUES

of Al & Ti to be grown on top as a hard mask, and the lifting off the resist (step 4) left this hard mask only in the locations of the intended nanostructure pattern. Ion milling (step 5) removed all unwanted magnetite to leave the nanostructures behind, before the hard mask was removed from the magnetite nanostructures (step 6) using a Decon 90 solution which dissolved the aluminium sacrificial layer.

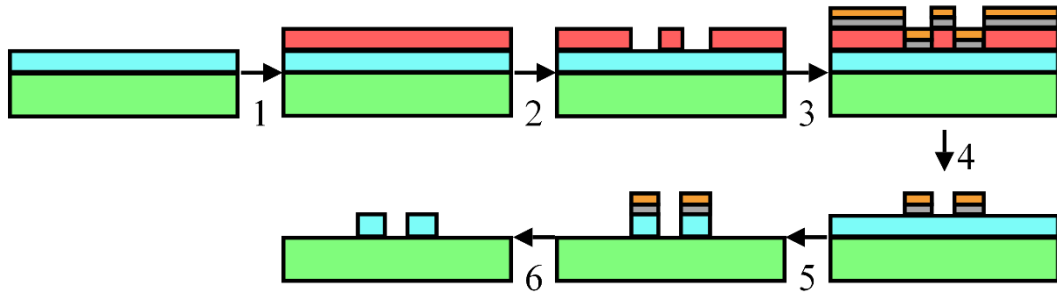


Figure 4.3. A diagram showing the steps used to create nanostructures from Fe_3O_4 thin films (blue) on a Si or MgO (100) substrate (green). Step 1: spin coating of PMMA resist (red). Step 2: electron beam lithography and development of resist template. Step 3: thermal evaporation of Al (grey) and Ti (orange). Step 4: PMMA lift off. Step 5: ion milling. Step 6: Al/Ti hard mask removal using a Decon 90 solution.

4.1.2.1. Electron beam lithography

Electron beam lithography (EBL) is a high-resolution patterning technique used to create a polymer template for nanostructure formation [2]. A growth technique such as thermal evaporation can then be used to grow the nanostructures in the template created.

The electron source, electromagnetic lenses and high vacuum chamber found in a conventional scanning electron microscope (SEM) provides the essential starting point for the development of an EBL system. With the addition of a pattern generator and beam blanker to provide bespoke control of the electron beam exposure, SEMs were originally modified to develop EBL. Purpose built EBL systems are now available that are fully dedicated to nano- and micro-scale patterning and are capable of patterning structures smaller than 10 nm once processes are well-optimised.

Prior to using EBL, a thin layer of polymer resist is spin-coated on the surface of a defect-free substrate (step 1 in Figure 4.3). There are two classes of resist: positive resists that increases in solubility when exposed to an electron beam, and negative resists that decreases in solubility [5]. One popular positive resist, and that used in this research, is poly(methyl methacrylate) (PMMA). Once in the vacuum chamber of the system, the sample is aligned and the electron beam is focussed onto the sample surface. Electron beam parameters such as the beam current, beam dose and the dwell time are set prior to pattern exposure. The electron beam then draws the pattern from a pre-prepared pattern file (step 2 in Figure 4.3).

Once the pattern has been written, the samples are removed from the vacuum chamber and the resist is developed. The developer used in this research was a mixture of methyl isobutyl ketone and isopropyl alcohol (IPA) (1:3 ratio) that dissolves the PMMA resist that has been exposed to the electron beam. The samples are then ready for thermal evaporation growth (step 3 in Figure 4.3). Post growth the remaining PMMA resist and the material above the PMMA is removed by placing the sample in acetone and using an ultrasonic bath. The acetone dissolves the PMMA and the ultrasonic vibrations helped detach the resist from the substrate. Once the resist is

EXPERIMENTAL TECHNIQUES

fully removed the sample is washed in IPA to remove acetone residue and any lift-off debris (step 4 in Figure 4.3).

There are several issues that need to be taken into account when creating a pattern design for EBL. The first is known as the ‘proximity effect’ [6]. This occurs when two patterned areas are placed closely together such that the intermediate area receives a cumulative electron dose due to backscattered electrons. During development, this area of resist is also removed and causes loss of definition of features. To minimise this effect either the structures should be designed to only have features larger than a certain length scale, or the dose should be locally varied in the vicinity of small features. The nanostructures designed in this project were well-spaced so that the proximity effect did not affect the structures greatly other than potentially altering the wire widths.

Another issue involves the ‘write-field’ of the EBL, which is the area that the electron beam can write to via beam deflection, rather than mechanical motion of the sample stage. To write outside this write-field the sample stage is moved. If a structure is drawn across two write-fields, there is a chance that the two sections of the structure will have alignment errors. This error can be removed by ensuring no structures cross write-field boundary. The write-field used to pattern the nanostructures in this project was 100 x 100 μm .

4.1.2.2. Thermal evaporation

Fabrication of structures by ion milling requires the creation of a hard masking layer to protect the parts of the pattern that are to be preserved. In this work this layer was

deposited using a thermal evaporator (step 3 in Figure 4.3). The hard mask consisted of an aluminium/titanium bilayer. Titanium was used to protect the magnetite during ion milling as it is a high strength material and aluminium was used as it can be dissolved in alkali solvents after ion milling to remove the hard mask.

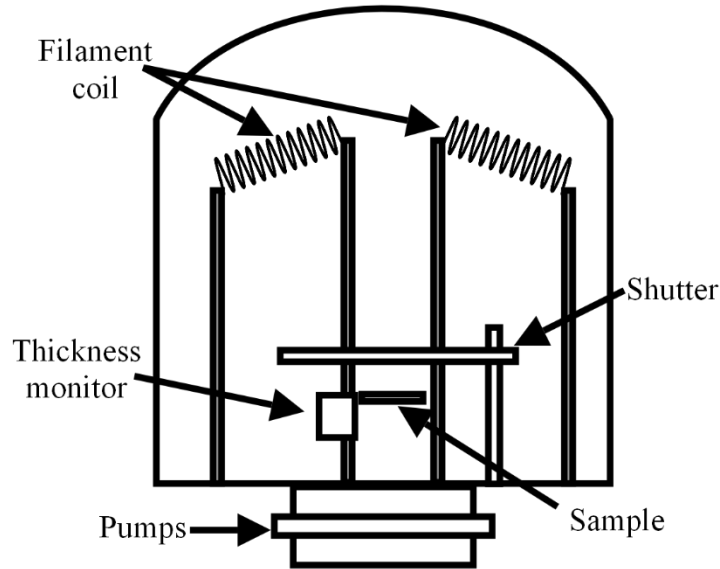


Figure 4.4. Schematic showing the components of the thermal evaporator used to grow the Al/Ti hard masks.

In thermal evaporation thin film growth, the metal evaporant is placed in a refractory metal container, like a tungsten boat or filament coil. The chamber is pumped down to a low base pressure to prevent contamination/oxidation of the films during growth. A high current is then passed through the container. The container heats up due to resistive heating and the metal is evaporated onto the substrate [2].

In this study an Edwards E306A coating system (schematic shown in Figure 4.4) with a base pressure of 1×10^{-6} mbar was used to perform thermal evaporation. A quartz crystal monitor was used to monitor the thickness of the deposited layers. The source

EXPERIMENTAL TECHNIQUES

materials were aluminium wire (99.99+% purity) and titanium wire (99.99% purity) both obtained from Sigma Aldrich. The minimum thickness of titanium needed to protect the magnetite nanostructures was calculated using the calibrated magnetite and titanium etch rates and magnetite layer thickness. In the fabrications performed as part of this project the hard mask composition was Al (10 nm)/ Ti (35 nm).

4.1.2.3. Ion milling

Ion milling was used to remove unwanted material so that only Fe₃O₄ nanostructures were left on the substrate surfaces. In ion milling, Ar ions are accelerated into the sample surface, causing atoms to be ejected. The portions of the sample covered with the EBL defined Al / Ti were protected from being milled as Ti has a lower etch rate than the Fe₃O₄ films. Sample rotation during ion milling ensured uniform removal of material, resulting in straight side walls of the patterned features. The Ar ions were created by flowing Ar gas into a vacuum chamber which had been pumped to a pressure $\sim 10^{-6}$ mbar by a turbo-molecular pump. The Ar atoms were then ionised by electrons emitted from a heated cathode and then accelerated by a pair of optically aligned accelerating grids, to produce a collimated beam of Ar ions. A neutralization filament was used to prevent a positive charge build-up on the sample holder [7]. Figure 4.5 shows a schematic of the main components of an ion miller. In this study ion milling was performed using a custom built ion milling system from Scotech which contained a Veeco 5 cm DW ion source.

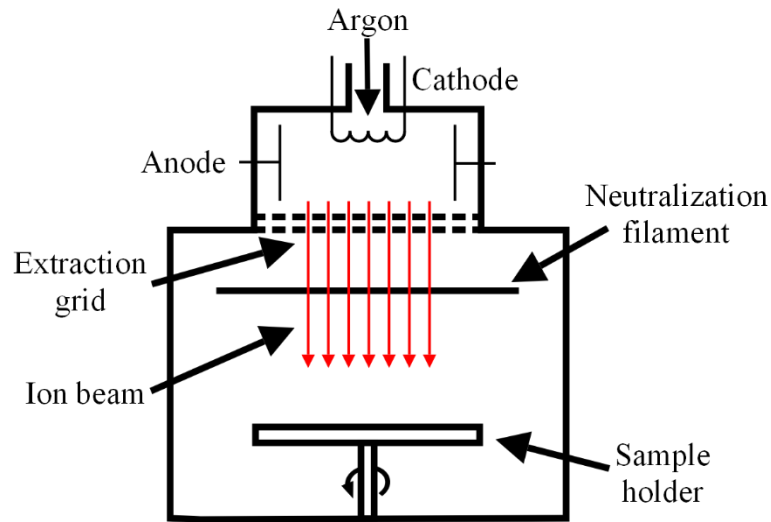


Figure 4.5. Schematic diagram of the main components of an ion milling system.

The etch rate for Fe_3O_4 was calculated by cutting a thin film into sections and creating an array of photoresist lines on the surface using optical lithography. These film sections were then ion milled for 30, 60 and 90 seconds in order to calibrate the etch rate. An Ar ion beam current of 50 mA and beam voltage of 1 kV, a 200V accelerator potential and an Ar flow rate of 5 sccm were used during the milling. Once milled, the resist was removed and the changes in film thickness measured using an atomic force microscope. This indicated an etch rate of 0.61 nm/s for Fe_3O_4 films from which an ion milling time can be calculated for films of a given thickness. The Ti etch rate (0.29 nm/s) was previously measured for the ion miller with the same milling parameters. After ion milling, the hard-masked Fe_3O_4 samples were placed in a 2.75 % Decon 90 / deionised water solution to dissolve the Al layer, thereby removing the hard mask and leaving only the Fe_3O_4 nanostructures on the substrates [8].

4.2. Compositional and phase analysis

4.2.1. X-ray diffraction

X-ray diffraction was used in this work to establish the crystal structure of the deposited films. This aided the determination of the iron oxide phase grown as they have distinct crystal structures, apart from the shared spinel structure of Fe_3O_4 and $\gamma\text{-Fe}_2\text{O}_3$.

In XRD beams of x-rays hit the sample at an angle, θ , and are diffracted by its crystal planes as shown in Figure 4.6. Constructive interference of diffracted beams occurs when the path difference is an integral number of wavelengths, $n\lambda$, such that they are in phase. This leads to Bragg's law [9]:

$$n\lambda = 2d_{hkl} \sin \theta \quad (4.1)$$

Where n is an integral, λ is the x-ray wavelength, d_{hkl} is the spacing between lattice planes and θ are the angles at which an interference fringe are observed. The lattice planes are labelled using Miller indices $(h\ k\ l)$, which represent the reciprocals of intersection with the unit cell edge of planes adjacent to the origin. For example, if the lattice plane intersects the unit cell at values of $(1/2, 1, 1/3)$ then the Miller indices for that plane are $(2\ 1\ 3)$.

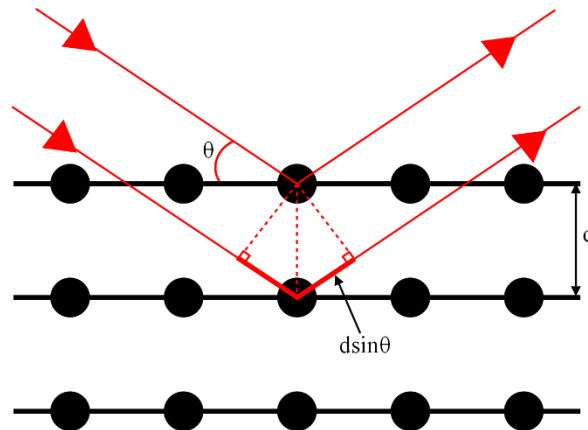


Figure 4.6. Illustration showing the Bragg diffraction of an x-ray beam from lattice planes.

The Siemens D5000 x-ray diffractometer used in this project was arranged in the Bragg-Brentano geometry, where the divergent and diffracted beams are focussed at a fixed radius from the sample. A schematic diagram of this system is shown in Figure 4.7. The Soller, divergence and receiving slits were used to control the divergence of the beam and determine the footprint of the beam on the sample. These were set to 0.5° for all scans. The x-rays used were Cu $K\alpha_1$ and $K\alpha_2$ giving an average $\lambda = 1.54178 \text{ \AA}$. A secondary beam monochromator was used to reduce fluorescence and background noise.

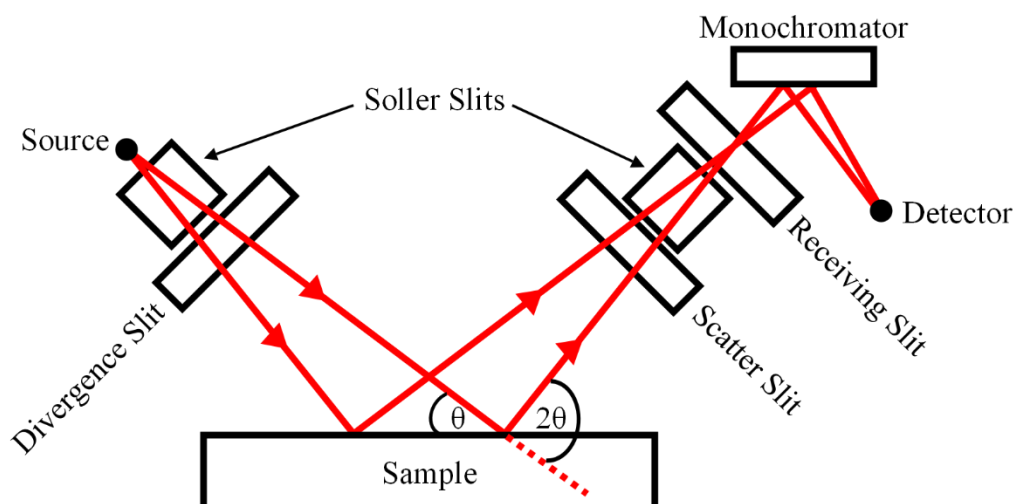


Figure 4.7. Illustration showing the components of an x-ray diffractometer in the Bragg-Brentano geometry.

Two XRD scanning modes were used in this project. These were the “locked-coupled” mode and the “glancing angle” mode. In the locked-coupled mode, the sample is held stationary whilst the source and detector are scanned simultaneously through a chosen angle range. This mode is optimised for powder samples and thick films as the penetration depth of x-rays is on the micrometre scale. In the glancing angle mode the source is held at a small, glancing incidence angle onto the sample and the detector is scanned through a range of angles, as illustrated in Figure 4.8. As thin films on the nanometre scale are measured in this work, the “glancing-incidence” mode was generally used as it is more sensitive to the surface. This is due to the x-ray penetration depth being approximately equal to $\sin(\theta) / 2\mu$, where μ is the linear absorption coefficient. The angle of incidence used in this work is 5° . A feature of the locked-coupled mode is that it is only sensitive to crystal planes that are parallel

to the sample surface (highlighted in Figure 4.8), whereas glancing-incidence probes crystal planes oriented in all directions.

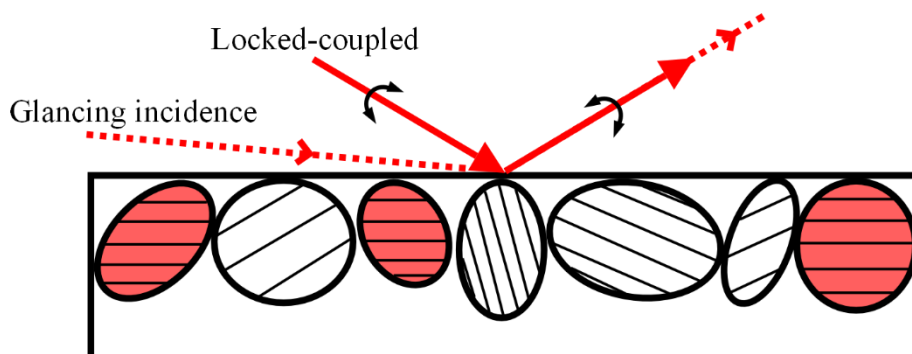


Figure 4.8. Comparison between the Bragg-Brentano and glancing angle geometry in x-ray diffraction. The red grains illustrate lattice planes parallel to the sample surface, which would be probed in the locked-coupled geometry.

The data is presented as x-ray intensity against the scanning angle 2θ , and can be compared to a database of diffraction patterns of known materials. The references used in this work were found using the software “PDF-4+” from the ICDD (International Center for Diffraction Data) [10]. The references for iron and its oxides that were used in this project are shown in Figure 4.9. It can be seen that the diffraction pattern for Fe_3O_4 and $\gamma\text{-Fe}_2\text{O}_3$ are very similar due to them having a very similar crystal structure. Fe_3O_4 has a spinel crystal structure and $\gamma\text{-Fe}_2\text{O}_3$ has an iron deficient spinel structure [11].

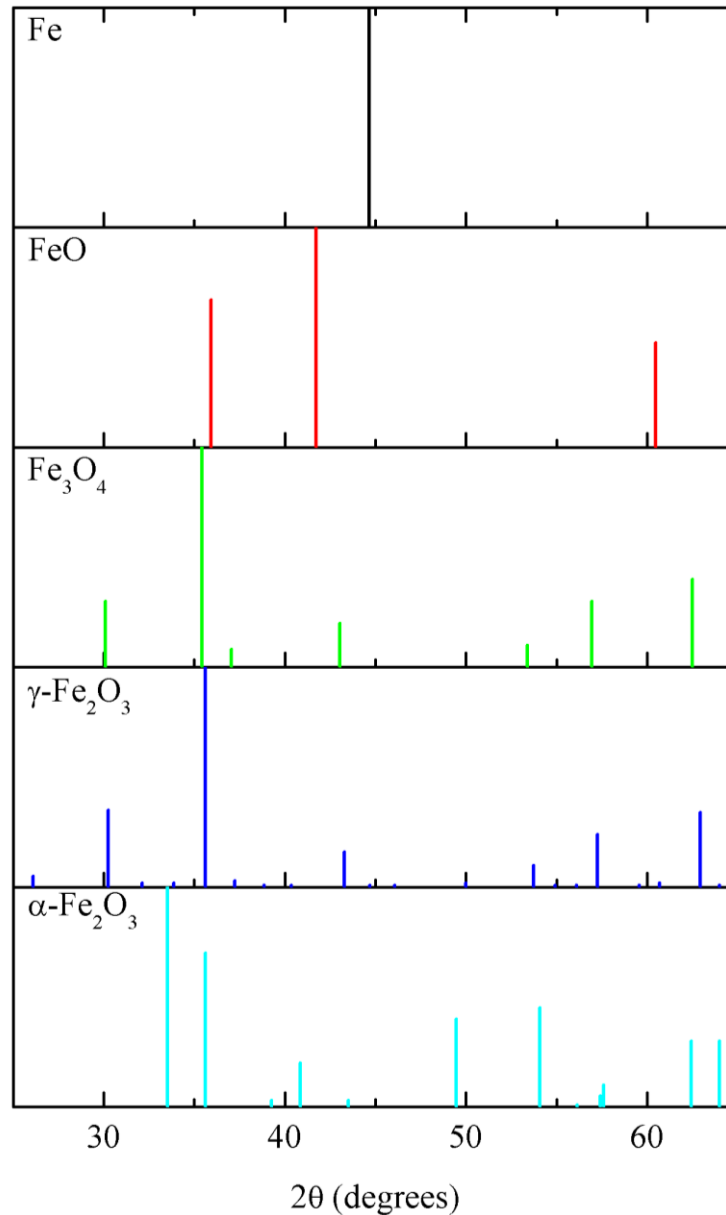


Figure 4.9. The x-ray diffraction standard peak positions and intensities for Fe and its oxides for Cu K α x-rays. [Fe: 00-006-0696, FeO: 01-089-0687, Fe₃O₄: 00-019-0629, γ -Fe₂O₃: 00-039-1346, α -Fe₂O₃: 00-033-0664. Taken from the PDF-4+ database, [10]].

Errors in peak position compared to calculated and reference standards can be seen when samples are strained. For a homogeneous strain peaks are shifted in position

according to Bragg's law as the lattice spacing is changed. However for inhomogeneous strain peak FWHMs are increased, as the non-uniform strain causes non-uniform lattice spacings. A common error with XRD spectra is from sample height displacement where the sample is too low or high in the sample holder which causes shifts in the peak positions.

4.2.2. Raman spectroscopy

A complementary technique to XRD in the determination of the phase of iron oxide films is Raman spectroscopy. This is especially true for establishing whether a material is Fe_3O_4 or $\gamma\text{-Fe}_2\text{O}_3$ as the standard XRD peaks are very similar due to their similar crystal structures, whereas the position and number of Raman peaks are significantly different.

Raman spectroscopy is a spectroscopic technique that relies on inelastic scattering, or Raman scattering, of monochromatic visible light from atoms or molecules. Most photons are elastically scattered (Rayleigh scattering), so that the incoming and outgoing photons have the same energy but a small fraction (approximately 1 in 10 million) of photons are inelastically scattered [12]. Here, a photon excites the molecule from the ground or an excited rovibronic (rotational and vibrational) state to a short-lived 'virtual energy state', before re-emitting a photon with either lower (Stokes) or higher (anti-Stokes) energy such that the molecule occupies a different rotational or vibrational state than it was originally in. Thus, changes in photon energy provides information about the rotational and vibrational modes of the atoms or molecules, which are material specific. An energy level diagram illustrating the

Rayleigh, Stokes Raman and anti-Stokes Raman scattering processes are shown in Figure 4.10.

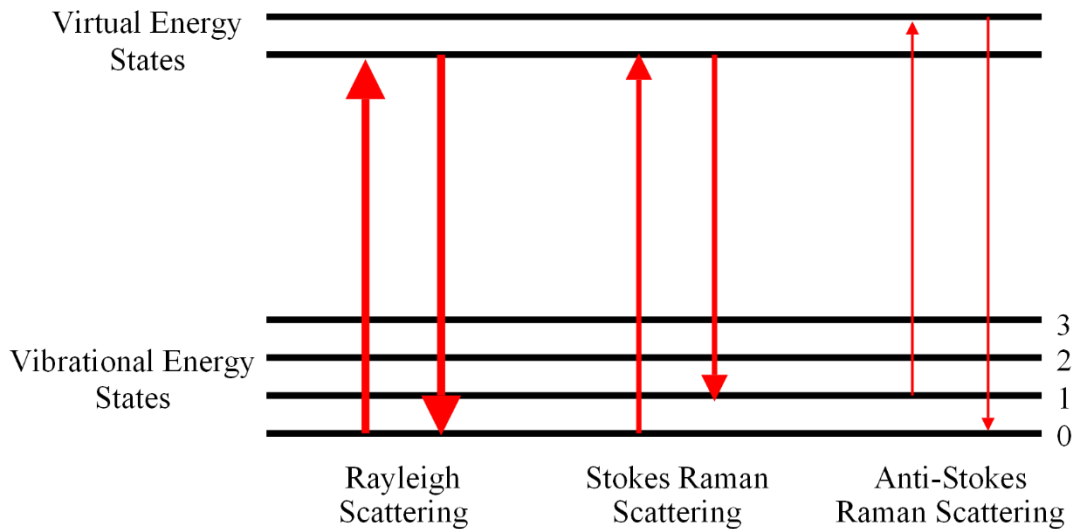


Figure 4.10. Energy level diagram showing Rayleigh scattering, Stokes Raman scattering and anti-Stokes Raman scattering. The line thickness shows the probability of occurrence.

Raman spectroscopy peaks are usually reported as wavenumbers (inverse wavelength) as these are proportional to energy. The change in photon wavenumbers are referred to as the Raman shifts, $\Delta\omega$ (cm^{-1}).

$$\Delta\omega = \frac{1}{\lambda_0} - \frac{1}{\lambda_1} \quad (4.2)$$

A value of 0 cm^{-1} corresponds to the Rayleigh line where there is no change in energy between the incoming and outgoing photons.

A Raman spectrometer consists of a monochromatic light source (usually a laser) that is focussed on the sample surface using an optical microscope which also collects the

scattered light. A filter is then used to attenuate all of the light except the tiny fraction that has been Raman scattered, before a diffraction grating is used to split the scattered light into its component wavelengths. This is then detected by a CCD camera and the data is sent to a computer to be analysed. An illustration of a standard Raman microscope is shown in Figure 4.11. The Raman spectrometer used in this project was a Renishaw inVia Raman Microscope with a $\lambda = 514.5$ nm laser.

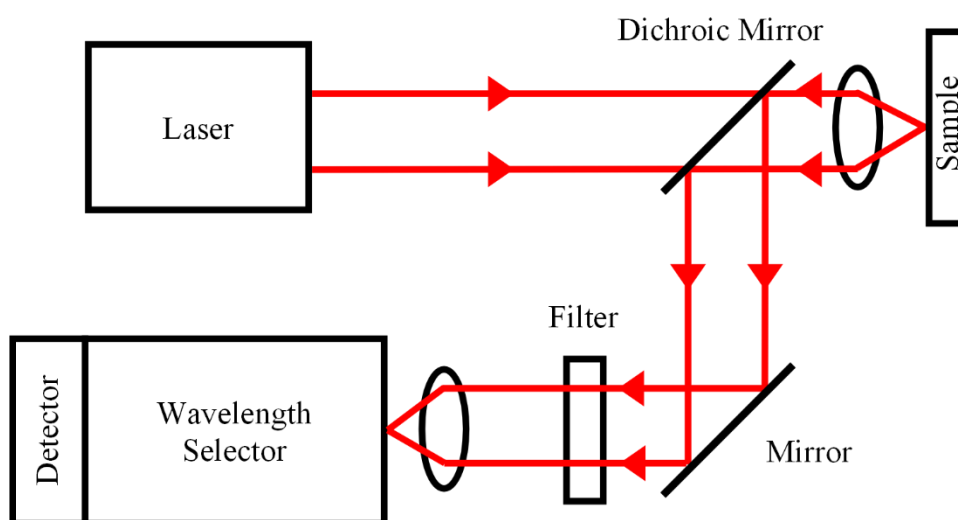


Figure 4.11. Schematic diagram of the main components of a Raman spectrometer.

A vibrational mode is Raman active when the vibration is accompanied with a change in polarizability of the molecule. The energy of the vibrational mode depends on the mass of the atoms, the strength of the bond(s) and the arrangement and symmetry of the atoms. This gives a “fingerprint” for different molecules that can be used to determine the material composition. As an example, diamond only has one Raman peak due to the symmetrical tetrahedral lattice with all the carbon atoms and bonds being equal. Alternatively, polystyrene has multiple Raman peaks from the different

EXPERIMENTAL TECHNIQUES

functional groups and bond strengths [12]. The spectra measured in this project were analysed by comparing peak positions with spectra found in literature.

The peaks in the Raman spectra are assigned labels that correspond to a vibration of a particular irreducible representation in a specific point group using Group theory. There are 4 letters that are used for these labels: A, B, E & T. Both A & B describe singly degenerate wavefunctions, with A being symmetric with respect to the principle axis and B being anti-symmetric. The wavefunctions E & T are doubly and triply degenerate, respectively. These labels have subscripts of either g or u which describe whether the wavefunction is even (g) or odd (u).

For magnetite, a full unit cell has 56 atoms but the smallest Bravais cell has 14 atoms which produces a possible 42 vibrational modes. These are:

$$A_{1g} + E_g + T_{1g} + 3T_{2g} + 2A_{2u} + 2E_u + 5T_{1u} + 2T_{2u}$$

The modes in red are Raman active modes, the modes in green are IR active modes and the modes in blue are silent. As Fe_3O_4 is a centrosymmetric molecule, the rule of mutual exclusion states that the Raman active modes are IR inactive, and vice versa. The description of the Raman active vibrations are given in Table 4.1, along with the measured peak positions from [13].

Raman mode	Raman shift (cm⁻¹) [13]	Description
A_{1g}	668	Symmetric stretch of the O atoms along Fe-O bonds
E_g	306	Symmetric bend of oxygen with respect to Fe
T_{2g} (3)	450 – 490	Asymmetric bend of oxygen with respect to Fe
T_{2g} (2)	538	Asymmetric stretch of Fe and O
T_{2g} (1)	193	Translatory movement of the whole FeO ₄ tetrahedron

Table 4.1. Description of the Raman active modes in Fe₃O₄ along with the measured peak positions from [13].

4.2.3. X-ray photoelectron spectroscopy

X-ray photoelectron spectroscopy (XPS) is a technique that allows the composition of the surface of a sample (depths < 10 nm) to be determined. The probing depth is much smaller than for Raman spectroscopy and GA-XRD (~150 – 200 nm). XPS is performed by irradiating a sample with a beam of x-rays while simultaneously measuring the quantity and kinetic energy of electrons that have escaped the surface via the photoelectric effect [14]. A simple schematic of an x-ray photoelectron spectrometer is illustrated in Figure 4.12.

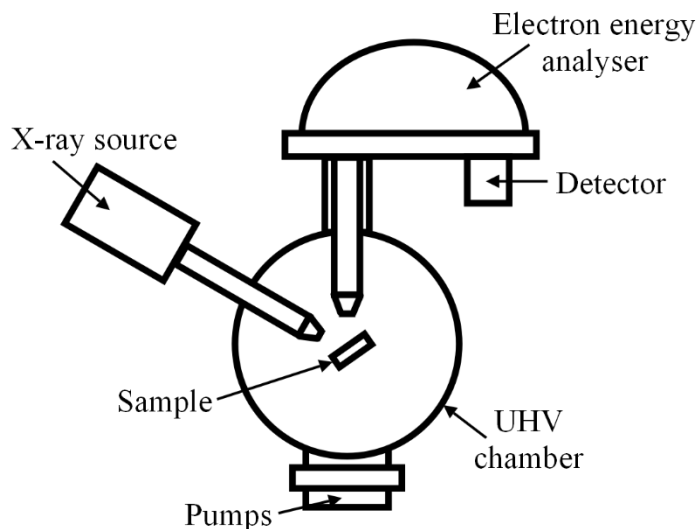


Figure 4.12. Schematic of an x-ray photoelectron spectrometer.

The sample is placed in an ultra-high vacuum chamber to increase the mean free path of the electrons as the detector is usually around a metre from the sample. To measure electrons of a specific energy the emitted electrons pass through an electrostatic lens array. This lens system is set to an energy-specific voltage to focus the electrons onto the analyser's entrance slit and retards their velocity so that their kinetic energy matches the pass energy of the electron energy analyser. To record an electron energy spectrum the lens voltage is then scanned across a pre-set range. The electron energy analyser consists of two concentric hemispheres with potentials applied to them to produce an electrostatic field with a $1/R^2$ dependence, where R is the radial distance from the centre of the analyser. Only electrons with the pass energy follow a path of constant radius to reach the detector. The XPS used in this work was a Thermo Scientific™ K-Alpha™+ X-ray Photoelectron Spectrometer with a micro-focussed monochromated Al K α source.

The binding energy of the electron (E_b) can be calculated from the kinetic energy of the electron (E_{kin}), the energy of the x-ray beam ($h\nu$) and the work function (ϕ) of the spectrometer using:

$$E_b = h\nu - (E_{kin} + \phi). \quad (4.3)$$

This relationship is illustrated using an energy level diagram shown in Figure 4.13.

XPS spectra are generally presented as counts per second versus the binding energy, as calculated using Equation (4.3). These spectra consist of the photoelectron peaks, a background spectra and satellite peaks. The origin of each of these will be described below.

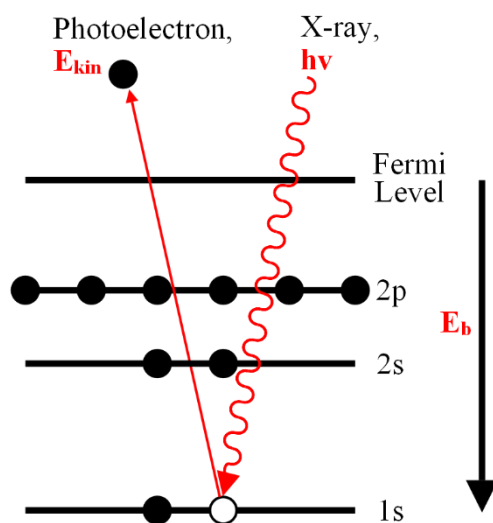


Figure 4.13. Energy level diagram illustrating the photoelectron effect.

Photoelectron peaks correspond to the binding energies of characteristic electron configurations of the elements present in the sample. The position of the peaks can also be used to investigate the chemical environment of the atoms. Multiplet splitting

EXPERIMENTAL TECHNIQUES

occurs when the atom contains an unpaired electron in its outer shell, such that a newly unpaired core level electron may couple it to produce a number of final angular momentum states. These final states form a multi-peak envelope that corresponds to the peak shape seen in the spectra [15]. Furthermore, when samples are non-conducting peak positions are shifted due to a charge build up on the surface causing a potential difference between the sample and detector. This potential difference causes a reduction in the electrons velocity, which changes its kinetic energy. To correct for this the peak position of adventitious carbon (284.8 eV), found as a layer on the surface of most air exposed samples, is used as a reference point [16]. The sample peak corresponding to adventitious carbon is located and compared to the reference value, producing a shift in the binding energy of the spectra.

XPS is a surface sensitive technique: whilst the exciting x-rays penetrate deep into the sample the escape depth of the ejected electrons is small. Those electrons ejected below 10 nm of the surface have a low probability of leaving the surface without losing energy and form the background of the XPS spectra. Another feature of XPS spectra are “shake-up satellite” peaks, which are formed when an outgoing core electron interacts with a valence electron and excites it to a higher energy level. This causes the kinetic energy of the ejected core electron to decrease and produces a peak at a lower kinetic energy (higher binding energy) than the core level peak.

To be able to analyse an XPS peak (Fe2p_(3/2) for example), the background signal needs to be identified and removed. There are three commonly used types of background: a linear background, the Shirley background and the Tougaard background. A Shirley background intensity is proportional to the total peak area intensity above the background for lower binding energies in the peak range. The Tougaard background is based on electron energy losses and has more control of the

background shape than the Shirley background. However, the Tougaard method suffers from practical complications especially with overlapping peaks and therefore the Shirley background is the preferred background method [17]. Gupta and Sen's [18, 19] calculations of the multiplet structure of core p-valence levels of the first row transition metals provide a starting point for peak fitting the multiplet structure. Fe^{2+} and Fe^{3+} ions have different binding energies and multiplet splitting which causes Fe_3O_4 to be distinguished from Fe_2O_3 .

In this work a wide energy spectrum ($E_b = 0 - 1350$ eV) was first measured for all of the samples, before individual scans of the Fe2p ($E_b = 700 - 740$ eV) and O1s ($E_b = 525 - 545$ eV) peaks were performed.

4.3. Surface imaging

4.3.1. Atomic force microscopy

The thicknesses of iron thin films and the grain size distributions of magnetite thin films were measured using an atomic force microscope (AFM). The AFM used in the project was a Veeco Dimension 3100 with OTESPA-R3 tips from Bruker. A schematic diagram of the AFM system is shown in Figure 4.14.

The AFM is from the family of microscopes called scanning probe microscopes (SPMs), and it is very different from optical or electron microscopes as it forms an image by "feeling" the sample surface using a sharp tip on a cantilever instead of focusing light or electrons onto the surface [20]. An AFM is able to create a

topological image of the sample surface using three different modes of operation: contact mode, non-contact mode and Tapping ModeTM. Each of these modes of operation are described below.

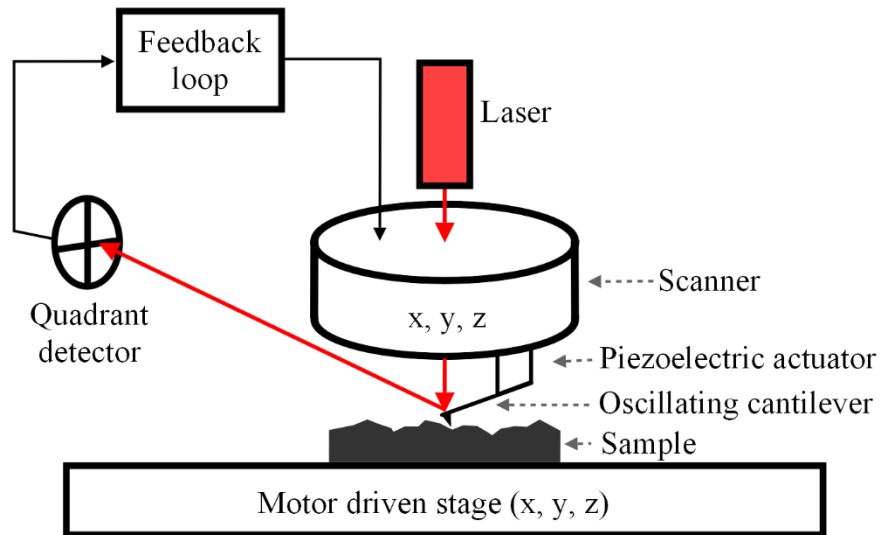


Figure 4.14. Schematic showing the main components of an atomic force microscope.

To understand the different modes of AFM operation it is necessary to consider a van der Waals force-distance curve, as shown in Figure 4.15. When the tip is at a large distance from the sample surface the cantilever has no deflection. As this distance decreases there is an attractive force between the tip and the sample surface and a ‘snap-in’ occurs, where the tip jumps into contact with the surface. When the distance is reduced again the interaction now enters the ‘repulsive’ region which causes the cantilever to bend.

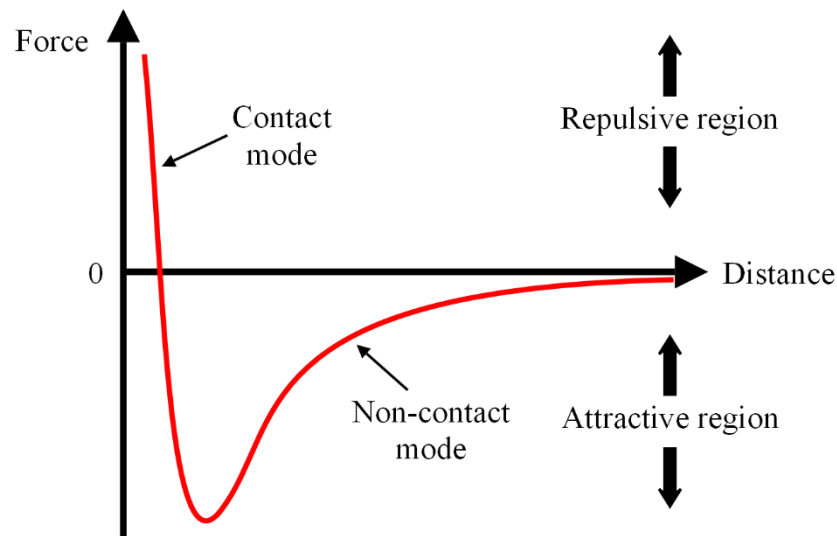


Figure 4.15. A force-distance curve for a tip approaching the sample surface, illustrating the contact and non-contact modes.

Contact mode is the simplest mode of AFM as the deflection of the tip is directly related to the topography of the sample surface. In contact mode the tip is always in contact with the sample surface and is used in the repulsive region of the van der Waals curve. To measure the topography, the cantilever is kept at a certain deflection (constant force), which is maintained via the feedback system and a piezoelectric scanner. The deflection of the cantilever is measured by reflecting a laser off the surface of the cantilever and onto a quadrant detector and the information from the feedback loop is used to give the topography of the surface. Although this is a fast imaging technique it can damage both the tip and the sample during the scanning process due to the repulsive force.

In non-contact AFM the cantilever is oscillated near its resonant frequency whilst it is scanned across the sample surface. Changes in tip-sample distances cause changes in the attractive forces, which in turn affects the resonant frequency of the cantilever.

EXPERIMENTAL TECHNIQUES

The feedback system then detects the changes in the cantilever's resonant frequency or the vibration amplitude of the cantilever and the scanner is lifted up or down to maintain this, thus generating the topography image. As the attractive force is usually smaller than the repulsive force used in contact mode, the signal from non-contact mode is small. Therefore, a sensitive AC detector system is required. However, as the tip is not in contact with the sample surface it is not as damaging as contact mode. Furthermore, a thin layer of liquid forms on most surfaces in ambient air which lowers the resolution of contact mode as the tip gets stuck, unless it is scanned at a very slow speed. This is due to the small oscillation amplitude being of the order of tens to hundreds of Ångstroms. [21]

Tapping ModeTM is a patented technique from Veeco Instruments, and overcomes the problems of both contact and non-contact mode. The cantilever is oscillated near its resonant frequency as in non-contact mode, but the amplitude of oscillation is a magnitude greater. This stops the tip from becoming stuck in the liquid layer on the surface allowing for higher resolution. Tapping ModeTM was the AFM mode used for this research.

4.3.2. Spectroscopic ellipsometry

In this project the thickness of the sputtered magnetite thin films were measured using spectroscopic ellipsometry measurements and modelling. This technique measures the change in polarisation as linear polarised light reflects from the sample surface, which is dependent on the optical properties and the thicknesses of the different layers.

At an interface between two materials incident light can be both reflected and refracted. Thin films and multilayer structures have multiple interfaces, and the total reflected light is a superposition of the light waves that are reflected and transmitted from each of these interfaces as illustrated in Figure 4.16. Interference between the beams depends on their relative phase and amplitudes which can be calculated using Fresnel reflection and transmission coefficients.

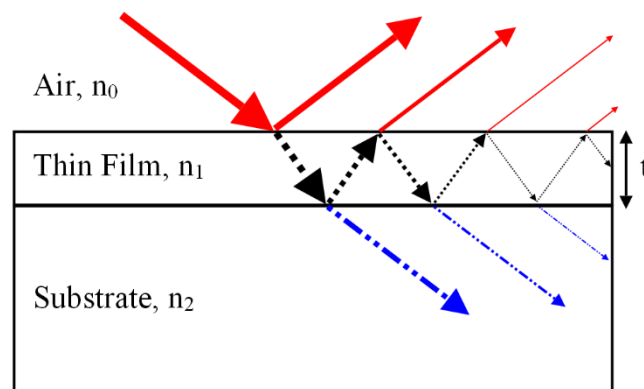


Figure 4.16. Illustration showing light reflecting and refracting at the interfaces of a thin film on a substrate.

Linearly polarised light with both s- and p- components is reflected from the sample surface and the change in polarisation of the reflected light from linear to elliptical is measured using a polarisation analyser and detector. This change in polarisation is represented by an amplitude ratio (ψ) and phase difference (Δ). After a sample has been measured, a model is constructed to describe the sample and then used to calculate the predicted response from Fresnel's equations for linearly polarised light reflecting from the sample surface. When the thickness and optical constants are not known, estimates are given for preliminary calculations. These calculated values are

then compared to the experimental data, and the unknown properties are then varied using regression analysis to improve the match.

For a single measurement, only two parameters are measured (ψ and Δ) from which only two unknown sample properties can be determined. For a single wavelength, several different film thicknesses are calculated for one measurement. To remove this error, spectroscopic ellipsometry is used which over-determines the film thickness. As the film thickness is not wavelength dependent but the refractive index is, a range of wavelengths are used to increase the data volume with less unknown values. This removes the cyclic nature of ellipsometry and produces a single film thickness [22].

The ellipsometer used in this project was a J. A. Woollam VASE® Ellipsometer which has a spectral range of 193 – 3200 nm, a HS-190™ scanning monochromator and a rotating analyser ellipsometer.

4.4. Electrical analysis

4.4.1. Four-point collinear probe method

The resistivity of the thin films were measured using the four-point collinear probe method. This technique involves bringing four equally spaced probes, with a separation s , into contact with the centre of the sample surface thin film's surface. The two outer probes are used to source the current and the two inner probes are used to measure the resulting voltage drop across the sample. An example schematic diagram

of a probe array is shown in Figure 4.17. Using four probes eliminates measurement errors due to contact and lead resistances.

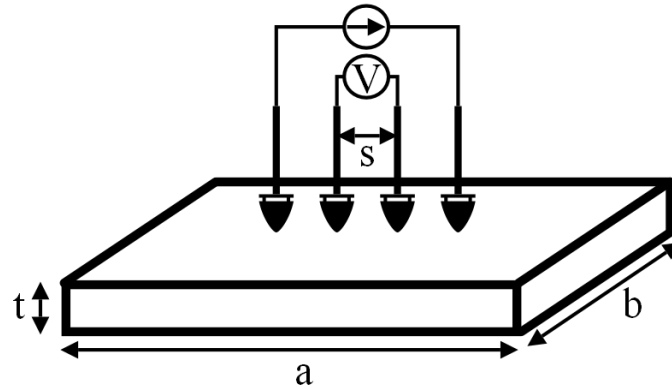


Figure 4.17. Illustration showing the four probe arrangement used to measure thin film resistivity.

By measuring the voltage drop (V) as a function of the applied current (I), the resistivity (ρ) of the sample can be determined using:

$$\rho = \frac{V}{I} t C \quad (4.4)$$

Where t is the film thickness and C is a correction factor that is dependent on the sample shape and dimensions [23]. The correction factor for a thin rectangle with $t < \frac{s}{2}$ (i.e. a thin film) is:

$$\frac{1}{C} = \frac{1}{\pi} \left[\frac{\pi}{b_s} + \ln(1 - e^{-4\pi/b_s}) - \ln(1 - e^{-2\pi/b_s}) + \sum_{m=1}^{\infty} a_m \right] \quad (4.5)$$

For simplicity, substitutions were made: b_s is used for b/s and a_s for a/s . The values of a_m may be calculated using:

EXPERIMENTAL TECHNIQUES

$$a_m = \frac{1}{m} e^{-2\pi(a_s-2)m/b_s} \frac{(1 - e^{-6\pi m/b_s})(1 - e^{-2\pi m/b_s})}{(1 + e^{-2\pi a_s m/b_s})} \quad (4.6)$$

Where using the first term in m in Equation ((4.5) will allow calculations of G that are accurate to 4 significant figures [24].

To perform the resistivity measurements required in this project a custom-built four-point collinear probe rig was constructed using four pointed spring probes with a separation of 1 mm, attached to a Perspex frame shown in Figure 4.18. The current was provided by a Keithley 6221 DC/AC Current Source and voltages were measured using a Keithley 2000 Multimeter.



Figure 4.18. Photograph of the custom built four probe system.

4.5. Magnetic analysis

4.5.1. Magneto-optic Kerr effect magnetometer

Magneto-optic Kerr effect magnetometry is a simple and non-destructive technique that utilises the Kerr rotation of light reflected from a magnetised sample to measure its magnetisation loop [25].

When the electric field of light is polarised parallel (perpendicular) to the plane of incidence it is referred to as p- (s-) polarised light. Linearly polarised light can also be thought as an equal amount of left- and right-handed circularly polarised light. Unequal electric field amplitudes of left- and right-handed circularly polarised light produce elliptically polarised light.

For certain geometries, when s-polarised (p-) light is reflected from a magnetic material the polarisation of the reflected light is slightly rotated from its initial state such that it contains a small p-component (s-). Furthermore, the two components will typically be out-of-phase with each other such that the resultant light will be elliptically polarised. The magnitude of these two effects are typically referred to as the Kerr rotation and the Kerr ellipticity. The cause of this is magnetic circular dichroism, where magnetic materials have different refractive indices for left- and right-circularly polarised light.

There are three main geometries used for magneto-optic Kerr effect measurements, which are identified by the direction of the samples magnetisation with respect to the plane of the sample and plane of incident light [26].

EXPERIMENTAL TECHNIQUES

In the polar Kerr effect the magnetisation is perpendicular to the sample surface and parallel to the plane of incidence. In the transverse Kerr effect the magnetisation is parallel to the sample surface and perpendicular to the plane of incidence. Finally, in the longitudinal Kerr effect the magnetisation is parallel to the sample surface and the plane of incidence. These geometries are shown schematically in Figure 4.19.

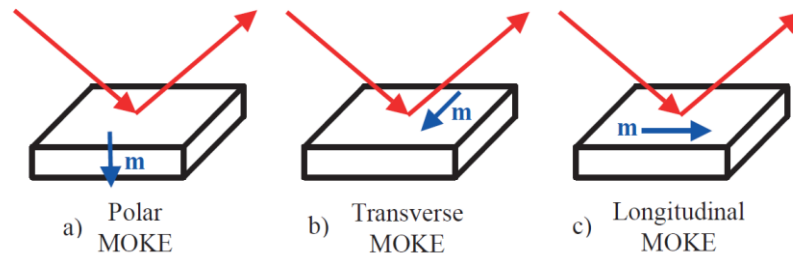


Figure 4.19. Illustration showing how the orientation of the sample magnetisation to the laser direction produces the different MOKE geometries.

The Lorentz force can be used to understand how p- and s-polarised light interact in the three different geometries. When light is incident on a material it causes an oscillation of the surface electrons parallel to the electric field, which gives rise to an electric field component parallel to this in the reflected light. However, in the presence of the sample's magnetisation an additional oscillation occurs due to the Lorentz force which is perpendicular to the electric field and the magnetisation. This additional oscillation produces an electric field component, E_K , which is generally out-of-phase with the reflected parallel electric field. The superposition of these two components gives rise to the magnetisation dependent rotation of the polarisation. When E_K has a component that is normal to the direction of the reflected beam, the resultant polarisation is rotated or the amplitude is varied. For s- and p-polarised light in both polar and longitudinal geometries, E_K causes a rotation of the reflected light

polarisation. However, for the transverse geometry no effects are seen for s-polarised light, due to the electric field and magnetisation being parallel, while for p-polarised light no Kerr rotation is produced but the amplitude of the reflected light varies with the magnetisation direction. This is due to E_K being normal to the reflected beam but also being in the plane of incidence. However, by using a mixture of s- and p-polarised light in transverse geometry the variation of the amplitude of the p-polarised component can be utilised to produce a Kerr rotation which is easily detected [27].

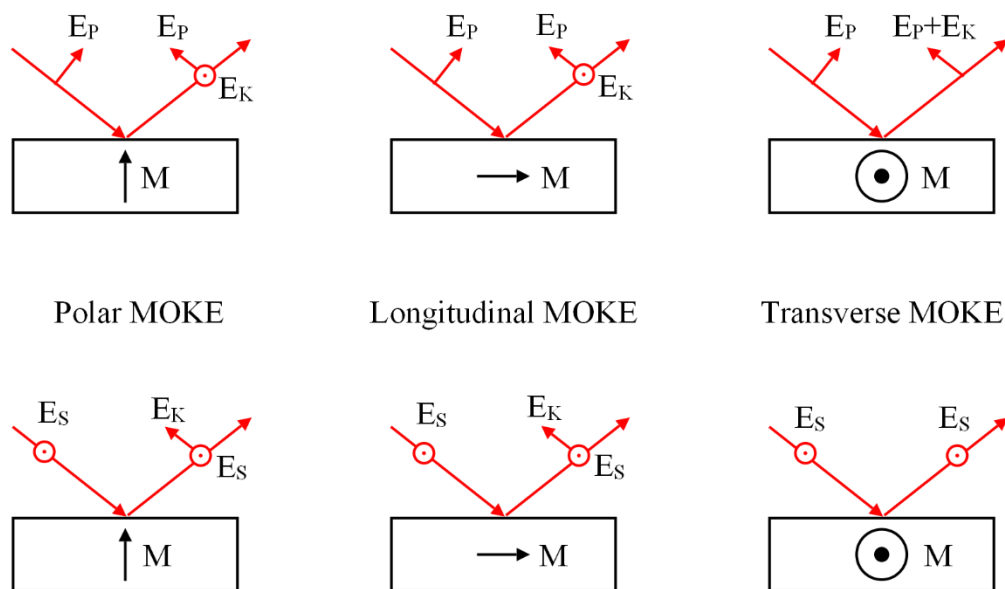


Figure 4.20. Illustration showing the resulting reflected light from incident p- and s-polarised light for polar, longitudinal and transverse MOKE.

The experimental set-up used for this research was an in-house built transverse magneto-optic Kerr effect magnetometer, a schematic of which is shown in Figure 4.21. The setup consisted of a 635 nm diode laser, the beam from which passed through a polariser that was set to produce mixed polarisation light at an angle of 19° degrees from p-polarisation. The beam was then reflected from the surface of the

EXPERIMENTAL TECHNIQUES

samples, which were placed on a rotatable stage. This stage was in between electromagnet pole pieces so that the field is applied parallel to the sample surface and orthogonal to the plane of incidence. The electromagnet was powered by a Kepco bipolar amplifier and could produce maximum field amplitudes of ± 3.5 kOe. The reflected laser beam was then passed through an analyser that was set to a couple of degrees away from extinction, as this provided the greatest signal-to-noise for detecting the Kerr rotation. Lastly, the reflected laser beam intensity was detected using a photodiode and amplifier.

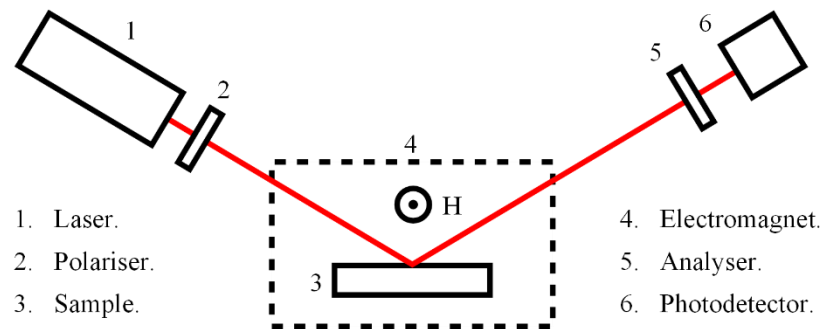


Figure 4.21. Schematic showing the components of a transverse magneto-optic Kerr effect magnetometer.

4.5.2. Magnetic force microscopy

Magnetic force microscopy (MFM) is a secondary imaging mode in AFM that measures the magnetic force gradient acting on a magnetised tip due to demagnetising field above a magnetic sample [21]. The magnetic force gradient is measured using a tip coated with magnetic material that is initially magnetised by a field applied aligned along its length (i.e. perpendicular to the sample surface). For each scanline in the image, two passes are made over the sample surface. The first pass uses tapping mode

to measure the topography of the surface, and the second pass measures the magnetic data and is carried out at a constant “lift height” above the sample surface. This minimises the influence of topography from the magnetic image.

Magnetic force microscopy measurements were performed on a Veeco Dimension 3100 atomic force microscope using Bruker MESP-LM (low moment) probes.

4.5.3. Magnetic Transmission X-ray Microscopy

Magnetic transmission x-ray microscopy (M-TXM) combines element specific x-ray magnetic circular dichroism (X-MCD) effects with the spatial resolution of a transmission x-ray microscope (TXM) to image magnetic contrast in magnetic films and nanostructures. The magnetic contrast is formed from the difference in absorption of circularly polarised x-rays by core level electrons for opposite projections of local magnetisation onto the photon propagation direction [28, 29].

In this research, M-TXM imaging was performed at beamline 6.1.2 at the Advanced Light Source (ALS) synchrotron at the Lawrence Berkeley National Laboratory. The sample imaged using M-TXM was grown on an x-ray transparent Si_3N_4 membrane and was used to understand the magnetisation reversal processes of sputtered Fe_3O_4 thin films.

The experimental setup for M-TXM is analogous to that of a conventional light microscope and consists of: a source, condenser lens, sample, objective lens and a detector. X-rays are emitted from a bending magnet on the storage ring, and directed down the beamline under vacuum. All of the beamline is kept under vacuum apart

EXPERIMENTAL TECHNIQUES

from at the sample position, which is between two x-ray transparent beryllium membranes. The x-ray beam is focussed onto the sample using a Fresnel zone plate (FZP). A zone plate consists of circular gratings with a radially increasing line density, and uses diffraction to focus the x-ray beam. This is necessary as the refractive index of soft x-rays for all materials is close to 1 [30-32]. Two FZPs are used in the experimental setup: a condenser zone plate (CZP) which serves as a condenser lens, and a 'micro' zone plate (MZP) which acts as an objective lens [33]. The CZP, together with a pinhole close to the sample, also act as a linear monochromator due to the MZPs wavelength dependent focal length. This tunes the x-ray beam energy to the desired absorption edge energy, which is Fe L₃ (706 eV) for these measurements. To detect magnetic contrast from samples with in-plane magnetisation the sample is tilted at an angle of 30° to the beam normal and an external magnetic field of up to ±1 kOe can be applied in the sample plane. The MZP focusses the transmitted x-ray image onto a soft x-ray sensitive CCD camera. To enhance the magnetic contrast, the image is divided by a reference image, which may be, for example, taken under the influence of a field strong enough to magnetically saturate the sample.

References

- [1] D. Glocker and S. I. Shah, *Handbook of Thin Film Process Technology* vol. 1: Institute of Physics Publishing, 1995.
- [2] M. J. Madou, *Fundamentals of microfabrication*, 2nd ed.: CRC Press, 2002.
- [3] (2010) Practical Process Tips. *Lesker Tech™*.
- [4] W. F. Smith and J. Hashemi, *Foundations of Materials Science and Engineering*, 4th ed.: McGraw-Hill, 2006.
- [5] T. M. Hall, A. Wagner, and L. F. Thompson, "Ion beam exposure characteristics of resists: Experimental results," *Journal of Applied Physics*, vol. 53, pp. 3997-4010, 1981.
- [6] T. H. P. Chang, "Proximity effect in electron-beam lithography," *Journal of Vacuum Science and Technology*, vol. 12, pp. 1271-1275, 1975.
- [7] Ion Beam Milling Inc. (12/08/2016). *About the ion milling process*. Available: http://www.ionbeammilling.com/about_the_ion_milling_process
- [8] Decon. (12/08/2016). *Decon 90*. Available: <http://www.decon.co.uk/english/decon90.asp>
- [9] B. D. Cullity, *Elements of X-ray Diffraction*, 2nd ed.: Addison-Wesley Publishing Company, 1978.
- [10] T. G. Fawcett, F. Needham, C. Crowder, and S. Kabekkodu, in *National Conference on X-ray Diffraction and ICDD Workshop*, Shanghai, China, 2009, pp. 1 - 3.
- [11] R. M. Cornell and U. Schwertmann, *The Iron Oxides: Structure, Properties, Reactions, Occurrences and Uses*, 2nd ed.: John Wiley & Sons, 2006.
- [12] Renishaw, "What is Raman scattering?," ed.

- [13] O. N. Shebanova and P. Lazor, "Raman spectroscopic study of magnetite (FeFe₂O₄): a new assignment for the vibrational spectrum," *Journal of Solid State Chemistry*, vol. 174, pp. 424-430, 2003.
- [14] N. Fairley, *Introduction to XPS and AES: CasaXPS Manual 2.3.15*: Casa Software Ltd, 2009.
- [15] Surface Science Western laboratories. (2015, 12/08/2016). *Multiplet Splitting*. Available: <http://www.xpsfitting.com/search/label/Multiplet%20Splitting>
- [16] Surface Science Western laboratories. (2015, 12/08/2016). *Adventitious Carbon*. Available: <http://www.xpsfitting.com/search/label/Adventitious>
- [17] Surface Science Western laboratories. (2015, 09/08/2016). *XPS Backgrounds*. Available: <http://www.xpsfitting.com/search/label/Backgrounds>
- [18] R. P. Gupta and S. K. Sen, "Calculation of multiplet structure of core p-vacancy levels," *Physical Review B*, vol. 10, pp. 71-77, 1974.
- [19] R. P. Gupta and S. K. Sen, "Calculation of multiplet structure of core p-vacancy levels. II," *Physical Review B*, vol. 12, pp. 15-19, 1975.
- [20] V. J. Morris, A. R. Kirby, and A. P. Gunning, *Atomic Force Microscopy for Biologists*: Imperial College Press, 1999.
- [21] Veeco, "A Practical Guide to SPM," ed.
- [22] J. A. Woollam. (09/08/2016). *Ellipsometry Tutorial*. Available: <https://www.jawoollam.com/resources/ellipsometry-tutorial>
- [23] H. Topsoe, "Geometric factors in four point resistivity measurement," ed, 1968.
- [24] F. M. Smits, "Measurement of sheet resistivities with the four-point probe," *The Bell System Technical Journal*, pp. 711-718, 1957.

- [25] N. A. Spaldin, *Magnetic Materials: Fundamentals and Applications*, 2nd ed.: Cambridge University Press, 2011.
- [26] D. Jiles, *Introduction to Magnetism and Magnetic Materials*, 2nd ed.: Chapman and Hall, 1998.
- [27] D. A. Allwood, P. R. Seem, S. Basu, P. W. Fry, U. J. Gibson, and R. P. Cowburn, "Over 40% transverse Kerr effect from Ni₈₀Fe₂₀," *Applied Physics Letters*, vol. 92, pp. 072503-072505, 2008.
- [28] P. Fischer, T. Eimuller, G. Schutz, G. Schmahl, P. Guttman, and G. Bayreuther, "Magnetic domain imaging with a transmission x-ray microscope," *Journal of Magnetism and Magnetic Materials*, vol. 198, pp. 624-627, 1999.
- [29] P. Fischer, T. Eimuller, G. Schutz, P. Guttman, G. Schmahl, K. Pruegl, *et al.*, "Imaging of magnetic domains by transmission x-ray microscopy," *Journal of Physics D: Applied Physics*, vol. 31, pp. 649-655, 1998.
- [30] P. Fischer, D.-H. Kim, W. Chao, J. A. Liddle, E. H. Anderson, and D. T. Attwood, "Soft x-ray microscopy of nanomagnetism," *Materials Today*, vol. 9, pp. 26-33, 2006.
- [31] P. Fischer, "Viewing spin structures with soft x-ray microscopy," *Materials Today*, vol. 13, pp. 14-22, 2010.
- [32] S. Mobilio, F. Boscherini, and C. Meneghini, *Synchrotron Radiation: Basics, Methods and Applications*: Springer, 2015.
- [33] The Center for X-ray Optics. (2010, 12/08/2016). *Beamline 6.1.2 (XM-1)*. Available: <http://www.cxro.lbl.gov/BL612/>

5. Growth and initial characterisation of iron oxide thin films

5.1. Introduction

As magnetite, Fe_3O_4 , thin films had not been previously grown using the sputter chamber mentioned in Section 4.1.1 the objective behind this chapter was to vary the reactive sputtering growth parameters to establish the optimum growth method to achieve Fe_3O_4 thin films.

This chapter consists of two sections. The first is the magnetic, electrical and compositional analysis of iron thin films on silicon substrates. Analysis of iron thin films will provide a useful comparison to the iron oxides that will be grown. The second is the characterisation of the substrate temperature dependence on the growth of iron oxide thin films on silicon substrates.

5.2. Analysis of iron thin films on silicon substrates

Iron thin films were grown of varying thickness ($t = 10 - 35$ nm) on silicon substrates using dc magnetron sputtering with the sputterer described in Section 4.1.1. The film thickness range was chosen to be of similar thickness to that used previously by Allwood et al. [1] and Negoita et al. [2] when working theoretically and

experimentally on Ni₈₁Fe₁₉ for domain wall atom trapping. A 2" iron target was cut from a sheet of iron with 99.95% purity using wire erosion, cleaned with acetone and IPA and attached to the DC gun in the sputter chamber. The first section of the growth was to clean the surface of the iron target to prevent any contamination to the thin film. This was achieved by pumping down the chamber to a base pressure of 5×10^{-6} mbar and striking a plasma with an Ar flow rate of 15 sccm and a DC power of 50 W for 30 minutes. During this target cleaning, the substrate shutter remained closed to prevent any unwanted growth on the substrate. After the target cleaning, the substrate shutter was opened to expose the Si substrates and remained open for a set amount of time (5, 10 and 15 minutes). Once the film was grown the shutter was closed and the DC power source and Ar flow turned off.

To establish a growth rate for a set of growth parameters, a corner of the Si substrate was covered with poly(methyl methacrylate) (PMMA). After the thin film growth, this PMMA was removed by putting the samples in a beaker with acetone which was then placed in a sonic water bath to aid the PMMA removal. Once the PMMA was fully removed, the sample was cleaned with propan-2-ol (IPA) to wash the acetone from the sample surface and then dried using nitrogen gas. This process leaves a section of the substrate clean producing a step in the film which was measured using AFM to establish film thickness, and from that the growth rate.

5.2.1. Magneto-optical Kerr effect magnetometry

The magnetic properties of these films were measured using a transverse MOKE magnetometer described in Section 4.5.1. Normalised hysteresis loops for the three film thicknesses are presented in Figure 5.1a. To establish whether an induced anisotropy was present in the films, hysteresis loops were measured as a function of in-plane field angle where a measurement was taken every 30° over a 360° range. A polar plot of the coercivity as a function of field angle for the 35 nm Fe film is presented in Figure 5.1c, which shows what appears to be a very weak uniaxial anisotropy.

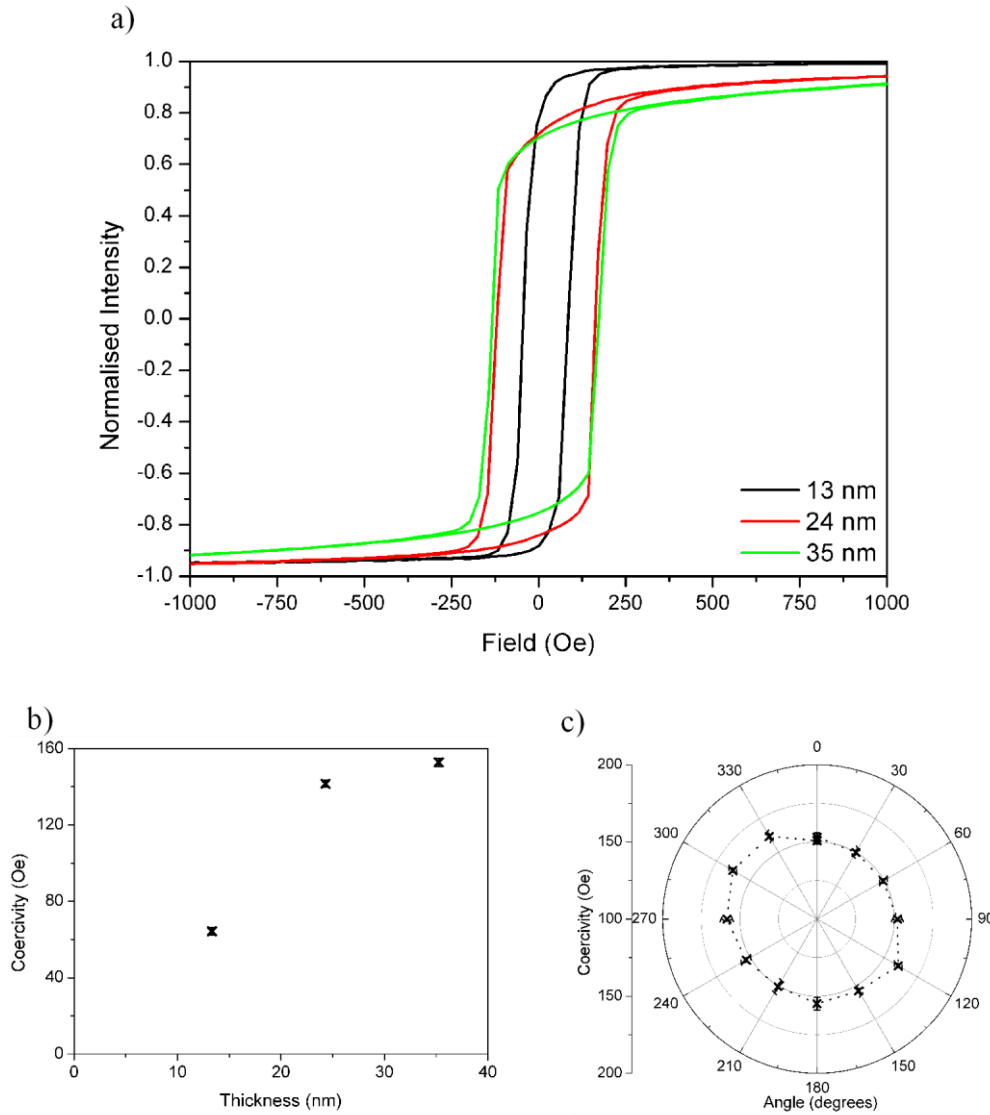


Figure 5.1. a) Normalised hysteresis loops of Fe thin films on Si substrates taken using transverse MOKE for a range of film thicknesses. b) Coercivity values of Fe thin films on Si substrates measured from normalised MOKE hysteresis loops for varying film thickness. c) Polar plot of the coercivity values from rotating a 35 nm Fe on Si thin film in a magnetic field measured using transverse MOKE. The dotted line is a guide.

A comparison of the hysteresis loops for the minimum (30°) and maximum (300°) coercivity values is presented in Figure 5.2, from which it can be seen that both loops

have a similar shape. It was expected that the films would be magnetically isotropic due to the sample rotation during growth, however this small anisotropy could be caused by shape anisotropy of the substrate.

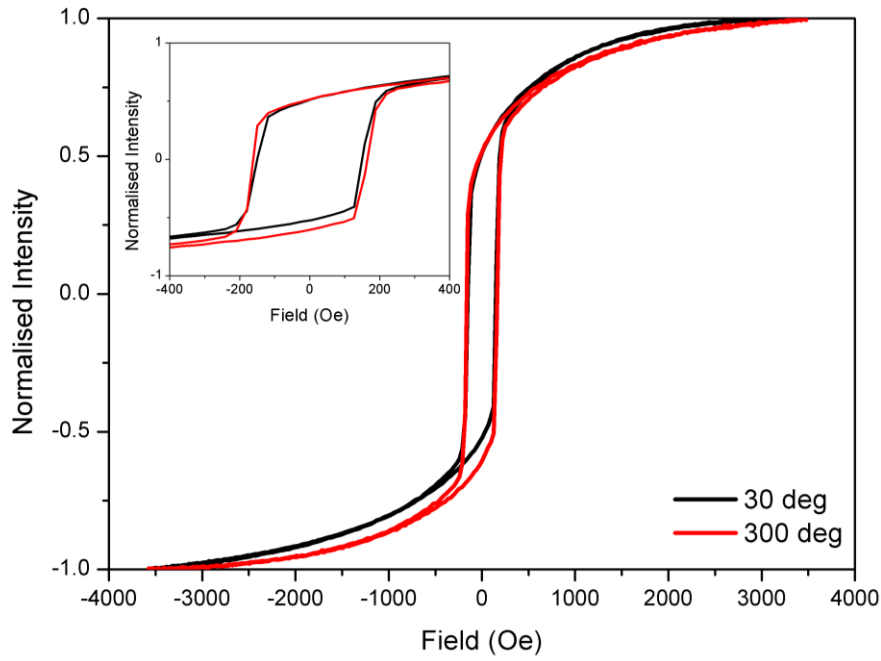


Figure 5.2. Normalised hysteresis loops taken as part of the angular dependency series (30° & 300°) measured using transverse MOKE from a 35 nm Fe on Si film.

Inset: Zoom in of the hysteresis loops.

The coercivity values measured from the hysteresis loops in Figure 5.1a are presented versus the film thickness in Figure 5.1b. This data indicates that there is a substantial increase in the coercivity of the films with thickness. Javed et al. [3] and Kim et al. [4] have also studied the properties of isotropic Fe thin films sputtered onto Si substrates and it was observed that the coercivity values measured on those films are similar to the values measured in this work.

The effect of film thickness on coercivity was also investigated by Kim et al. [4], and it was observed that the coercivity was increased with film thickness up to ~ 20 – 50 nm at which point the coercivity began to decrease in a manner inverse proportionality to the film thickness. The foundation of the resulting peak in coercivity was assigned to the change from Néel wall to Bloch wall at a critical thickness of approximately 40 nm. For Bloch wall motion the coercivity is inversely proportional to the film thickness, whereas for Néel wall motion the coercivity is directly proportional to the film thickness. This could explain the observed increase in coercivity with film thickness seen here, but with only three thicknesses over a small range a more extensive investigation would be needed to establish this. However, this was not the focus of this project and therefore was not pursued further.

5.2.2. Glancing angle x-ray diffraction

Glancing angle x-ray diffraction was utilised to certify that the films grown were iron, and that there were no iron oxides intrinsically present in the samples. The scan range used for these measurements was $2\theta = 40 - 50^\circ$, with a step size of 0.04° . This was chosen both to focus on a strong iron peak located at $2\theta = 44.6732^\circ$ (110) and to also include the positions of peaks for FeO, Fe₃O₄, γ -Fe₂O₃ and α -Fe₂O₃. The angle of x-ray incidence was set to 5° and the samples were not rotated during the measurements. The results of these measurements are presented in Figure 5.3.

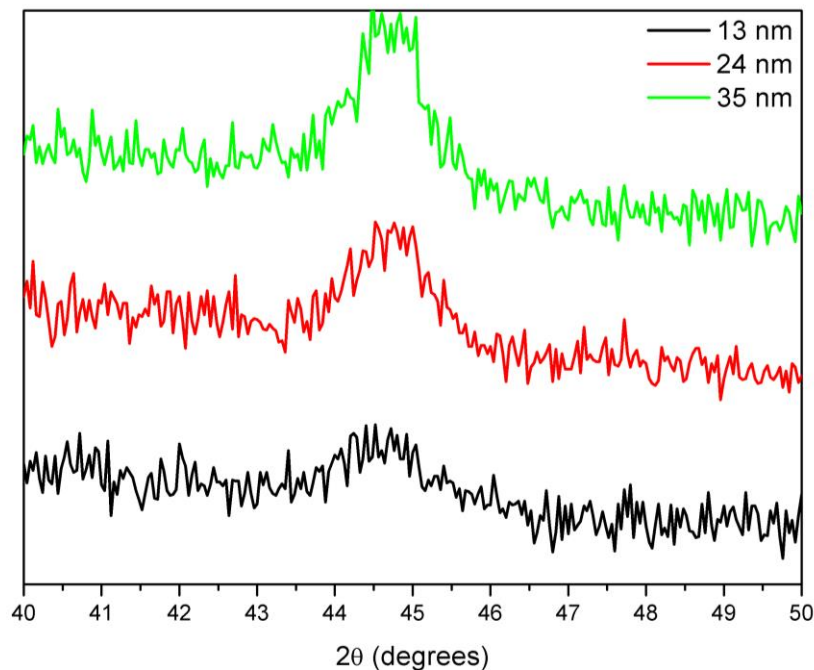


Figure 5.3. Glancing angle XRD spectra of Fe thin films on Si substrates for a range of film thicknesses, taken with an incidence angle of 5° .

For all of three of the XRD spectra in Figure 5.3 a peak is present at $2\theta \approx 44.5^\circ$, which is the Fe (110) peak, with the peak intensity increasing with film thickness, as would be expected. This is the only peak visible above the background signal to noise, and with no peaks seen from any of the iron oxides, these XRD spectra are a useful baseline and comparison for later in the project during the iron oxide compositional analysis.

5.2.3. Resistivity measurements

Measurements of the resistivity of the iron thin films were carried out using the in-house custom built 4 collinear probe assembly described in Section 4.4.1. A current

of 10 μA was applied between the two outer probes and the voltage was measured across the two inner probes. The dimensions of the thin film were measured using Vernier callipers and when combined with the film thicknesses measured by AFM the resistivity was calculated using (4.4 (in Section 4.4.1)). The resistivity values, which are tabulated in Table 5.1, are very similar to the values measured by Kim et al. [4], where for film thicknesses < 50 nm, resistivity values in the range $\sim 1.5 - 3 \times 10^{-4} \Omega \text{ cm}$ were reported. This is a factor of 10 larger than for bulk iron, where the resistivity value at room temperature is $8.57 \times 10^{-6} \Omega \text{ cm}$ [5]. Resistivity measurements on thin films of Permalloy in a similar thickness range typically produce values of $\rho \sim 2 \times 10^{-5} \Omega \text{ cm}$ [6, 7], which is a factor of 10 smaller than thin films of Fe. As oxide materials have a larger resistivity compared to metals, these resistivity measurements on Fe thin films will provide a useful comparison for the iron oxide films.

Film thickness	Resistivity
(nm)	($\times 10^{-4} \Omega \text{ cm}$)
13	2.85 ± 0.78
24	2.43 ± 0.46
35	3.17 ± 0.40

Table 5.1. Resistivity measurements of Fe thin films on Si substrates, measured using a custom-built 4 collinear probe set-up.

5.3. Substrate temperature dependence on iron oxide growth

Having successfully grown pure Fe films attempts were made to modify the process so as to reactively sputter iron oxide films. To grow iron oxide thin films using dc sputtering from iron targets, oxygen is needed to be added to the growth. The ratio of the argon to oxygen flow rates was chosen to be the same as in the work of Margulies et al. [8] where Fe₃O₄ thin films were successfully grown using reactive DC sputtering from an iron target. Thus, the argon flow rate was set to 15 sccm and the oxygen was 0.9 sccm. The substrate temperature was varied to establish the optimal growth temperature to deposit single phase magnetite thin films, i.e. those where no other iron oxide phase was present.

The temperature growth was varied in 100 °C steps from room temperature (RT) to 500 °C which is the growth temperature used by Margulies et al. [8]. Following the procedure used by Margulies, prior to each deposition the substrates were heated to the deposition temperature for 30 minutes under a vacuum $\sim 2 - 5 \times 10^{-6}$ mbar. After this pre-bake, the cryo gate valve was moved from the open to the mid position and a chamber base pressure of 5×10^{-6} mbar was then reached. The dc sputter gun was started in a pure Ar atmosphere, before adding the O₂ gas once the plasma had stabilised. This was left to stabilise for 5 minutes, at which point the substrate shutter was opened for a set amount of time (15 and 60 minutes [45 minutes for RT]) to deposit the films with a deposition pressure of 7×10^{-3} mbar. This is a typical deposition pressure for the flow rates used. Post deposition, the O₂ gas flow was stopped first, then the Ar gas flow before the substrate temperature was set to room

temperature, allowing the system to cool which took ~ 4 – 6 hours depending on the growth temperature used.

For a new growth procedure, the thickness of the films is needed to create a new growth rate. The melting point of PMMA is 160 °C [9], and thus due to the elevated growth temperatures used in this growth series, the previous technique for measuring film thicknesses (i.e. by lifting off a PMMA layer to create a film step) could not be used here therefore ellipsometry was used to measure the film thicknesses. The model used to calculate these is described in Section 4.3.2 and requires the refractive indices of the sample components (i.e. film and substrate). For this reason, the composition of the films is needed prior to the film thickness measurements, which will be addressed in Section 5.3.1.4.

5.3.1. Compositional analysis

As there are multiple available iron oxide phases, compositional analysis was required to establish which iron oxide phase or mixture of iron oxide phases were present in the films grown using the new growth procedure. The compositions of the reactively sputtered films were measured using three techniques: XRD, XPS and Raman spectroscopy. The combination of these techniques allowed the phases present at both surface and in the bulk of the films to be characterised. Furthermore, this multi-technique approach allowed the limitations of each technique (as detailed in Section 4.2) to be overcome so as to build a complete and coherent understanding of the films' phases.

5.3.1.1. Glancing angle x-ray diffraction

Glancing angle XRD measurements were taken at an angle of 5° to the sample surface over the range $2\theta = 25 - 65^\circ$, with a step size of 0.05° . This provides a large range to distinguish between different iron oxides, although Fe_3O_4 and $\gamma\text{-Fe}_2\text{O}_3$ are slightly more difficult to separate due to their similar crystal structures [10].

Figure 5.4 presents the XRD measurements from the films grown at RT, 100°C , 200°C , 300°C , 400°C and 500°C along with the expected peak positions for Fe, FeO, Fe_3O_4 , $\gamma\text{-Fe}_2\text{O}_3$ and $\alpha\text{-Fe}_2\text{O}_3$ films. It can be seen that the films grown at RT and 100°C exhibit crystal structure consistent with $\alpha\text{-Fe}_2\text{O}_3$ and that the films grown at 200°C , 300°C , 400°C & 500°C have a spinel structure. These higher temperature films could either be Fe_3O_4 or $\gamma\text{-Fe}_2\text{O}_3$ as the standard peak positions for these two materials are $\sim 0.3^\circ$ apart, and the extra peaks present in $\gamma\text{-Fe}_2\text{O}_3$ are of such low intensity compared to the main peaks that they would not be visible due to the signal to noise ratio in these measurements. The peaks in the film grown at 200°C are less defined than those grown at 300°C , 400°C & 500°C peaks which could indicate that the transition from $\alpha\text{-Fe}_2\text{O}_3$ to the spinel structure occurs near this temperature, such that there was a mix of oxide phases present.

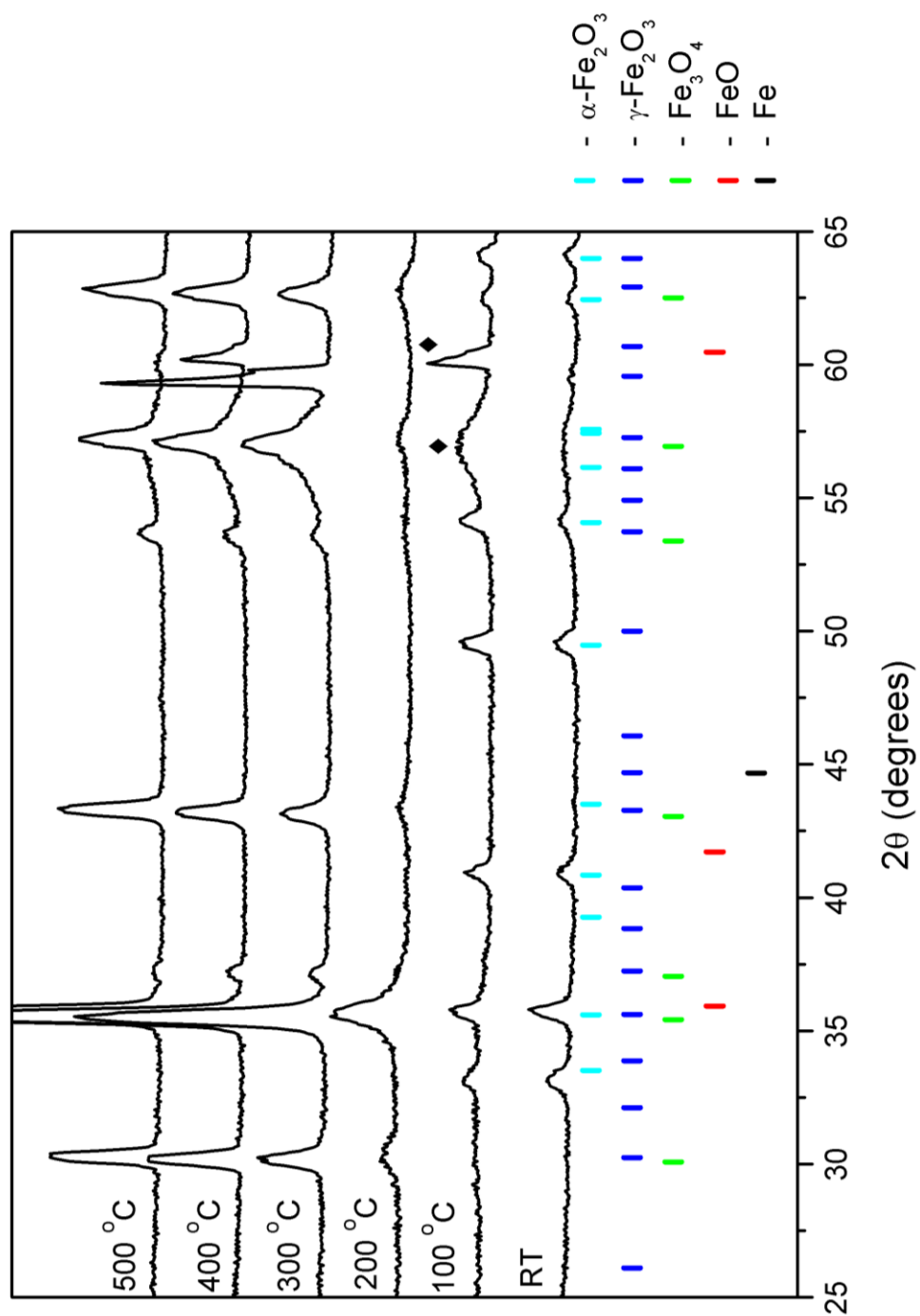


Figure 5.4. Glancing angle XRD of iron oxide thin films with a range of growth temperatures on Si substrates using a glancing angle of 5° , with the XRD peak positions for Fe, FeO, Fe_3O_4 , γ - Fe_2O_3 and α - Fe_2O_3 standards below. ♦ indicates substrate peaks.

There is a wide peak located around 57° and a sharp peak around 60° present in some of the spectra. These two peaks are not present in either the α - Fe_2O_3 or spinel standards and therefore must come from either the Si substrate or contamination on the sample surface. To verify this a scan was taken of a Si substrate over the same range. This is shown in Figure 5.5 and clearly shows the two anomalous peaks. The lack of these peaks in some of the spectra was due to the orientation of the Si (100) substrate.

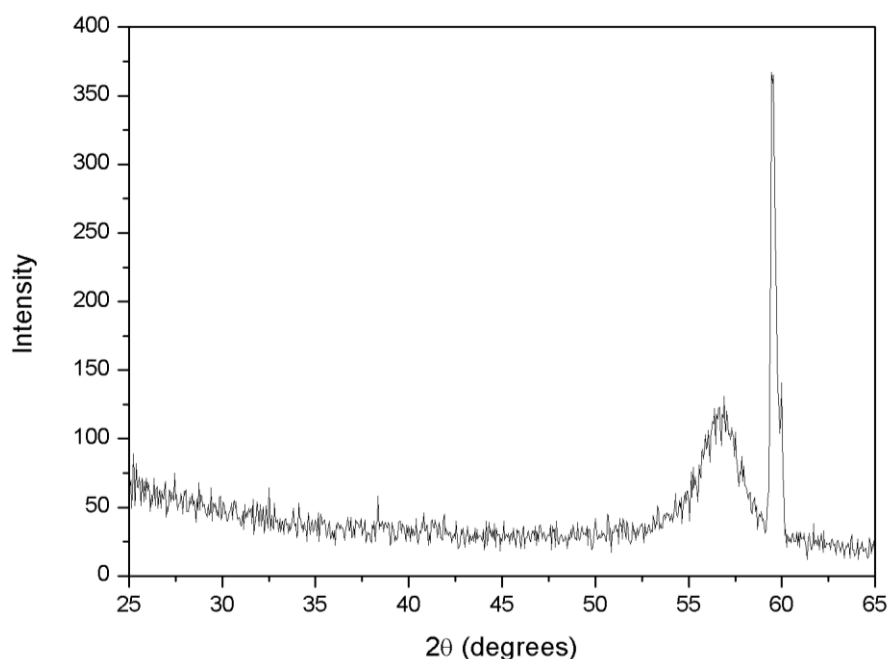


Figure 5.5. Glancing angle XRD of a Si substrate using a glancing angle of 5° .

5.3.1.2. X-ray photoelectron spectroscopy

As it is difficult to distinguish between Fe_3O_4 and γ - Fe_2O_3 using XRD, another technique is needed. XPS was used to measure a film grown at RT and another at 500°C (Figure 5.6) over the Fe2p range (binding energy = $700 - 740$ eV) with a step size

of 0.1 eV. A limitation of using XPS to analyse iron oxides is that the spectra for α - Fe_2O_3 and γ - Fe_2O_3 are very similar, which makes it difficult to distinguish between the two oxides using only XPS. A characteristic of α - and γ - Fe_2O_3 XPS spectra is that shake-up satellite peaks are visible above the Fe 2p peaks (highlighted in Figure 5.6), whereas these satellite peaks are not visible in the Fe_3O_4 spectra. This is due to the mixed valence Fe ions in Fe_3O_4 , which causes two sets of satellite peaks per major peak that merge to look like a background signal. From visibility of satellite peaks it is clear that the RT XPS spectra is Fe_2O_3 and 500 °C XPS spectra is Fe_3O_4 . Another visible sign showing the presence of Fe_3O_4 is the slight hump on the low binding energy side of the Fe 2p^{3/2} peak, which is due to the presence of Fe^{2+} ions which are not found in Fe_2O_3 . Again this is clearly visible and highlighted in Figure 5.6. A feature that is not present in Figure 5.6 is a peak corresponding to pure Fe which would be located at a binding energy of 706.6 eV [11] which indicates that there is no pure Fe at the surface of the films.

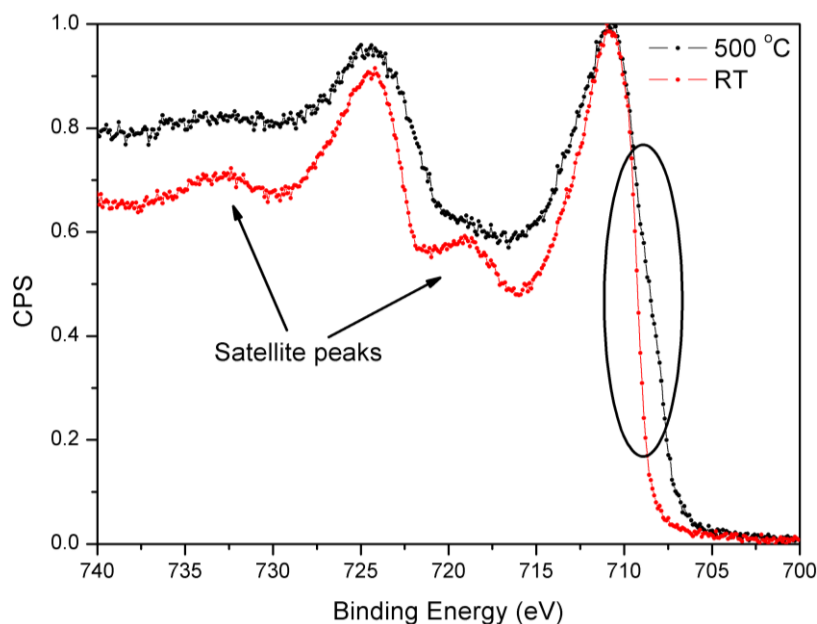


Figure 5.6. Normalised Fe 2p x-ray photoelectron spectra from iron oxide films grown at 500 °C and RT.

To provide a more quantitative analysis of the x-ray photoelectron spectra, the Fe 2p_{3/2} peaks were fitted using the Casa XPS software. A Shirley background was fitted over the binding energy range 705 – 716 eV and a single Gaussian-Lorentzian peak was fitted to the experimental data in this range. The peak fitted to the film grown at 500 °C has a binding energy of 710.6 eV with a FWHM of 4.06 eV (Figure 5.7 a), which corresponds to the binding energy of the Fe 2p_{3/2} peak for Fe₃O₄ [12, 13]. However, fitting a single peak to the RT spectra (Figure 5.7 b) produces a residual standard deviation of 10.58 compared to the residual standard deviation of 3.03 for the 500 °C spectra, which indicates that a more complex peak fitting is needed for the RT spectra to better fit the data.

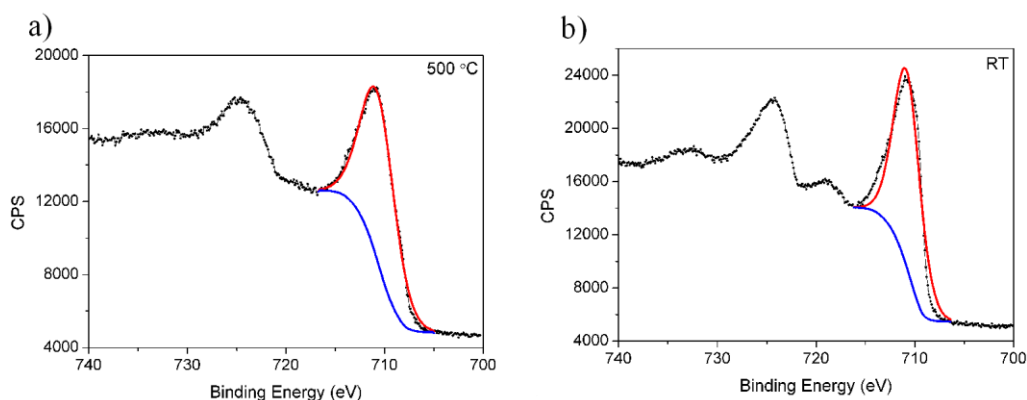


Figure 5.7. Fe 2p x-ray photoelectron spectra from iron oxide films grown at a) 500 °C and b) RT. The Fe 2p_{3/2} is fitted with a Shirley background and a Gaussian-Lorentzian (30:70) peak.

Due to the misfit of a single peak to the experimental data for the RT film, two peaks were fitted with the same background in Figure 5.8. The binding energies and FWHM of these peaks are 710.07 eV [1.82 eV] & 711.56 eV [3.24 eV], producing a residual of 3.42502. The binding energies of these two peaks correspond to Fe₃O₄ & Fe₂O₃

[14], and indicate a mixed iron oxide composition for the surface of the film grown at RT. This mixed phase is not seen in the GA-XRD results where only α -Fe₂O₃ is observed, which could indicate that the Fe₃O₄ is present in small quantities throughout the film.

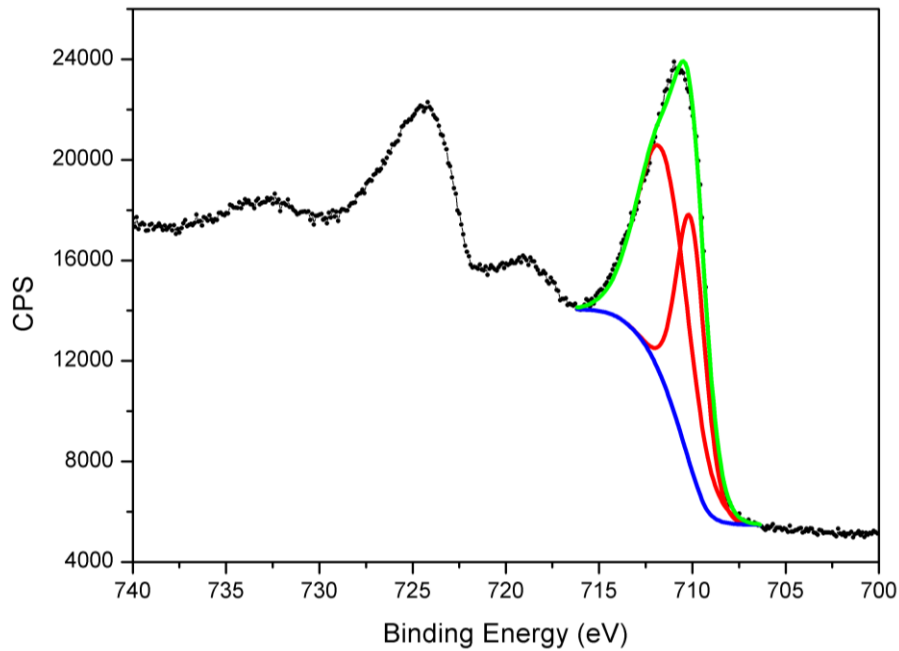


Figure 5.8. Fe 2p x-ray photoelectron spectra from an iron oxide film grown at 500 °C. The Fe 2p_{3/2} is fitted with a Shirley background and two Gaussian-Lorentzian (30:70) peaks.

Even though XPS has shown that iron oxide films grown at 500 °C are Fe₃O₄, it is a surface sensitive technique that only probes ~ 10 nm into the film, and furthermore each measurement took several hours to take. Thus, another quicker technique was required to allow conclusive compositional phase analysis of the whole of a film's thickness.

5.3.1.3. Raman spectroscopy

Raman spectroscopy was used as to rapidly and conclusively characterise the composition of the iron oxide films across the whole of their thickness. Raman spectra were taken over a range of 100 – 1000 cm^{-1} using a $\lambda = 514.5$ nm laser (20 mW) for the films grown at each of the growth temperatures. These are illustrated in Figure 5.9, and a clear difference can be seen between those grown in the RT – 200 °C range and the 300 – 500 °C range. The peak positions of the 300 – 500 °C spectra correlate well with the peak positions tabulated in the overview of Raman mode frequencies for magnetite by Shebanova [15]. These peak positions are compared to the peak positions measured by Shebanova in Table 5.2.

300 °C (cm^{-1})	400 °C (cm^{-1})	500 °C (cm^{-1})	Shebanova (cm^{-1})	Raman Mode
189	189	192	193	T_{2g}
296	313	307	306	E_g
533	532	533	538	T_{2g}
666	665	664	668	A_{1g}

Table 5.2. Peak positions from Raman spectra of iron oxide thin films grown at 300, 400 & 500 °C compared to Fe_3O_4 peak positions and Raman mode assignment by Shebanova [15]. All measured peak positions have an error of $\pm 2 \text{ cm}^{-1}$.

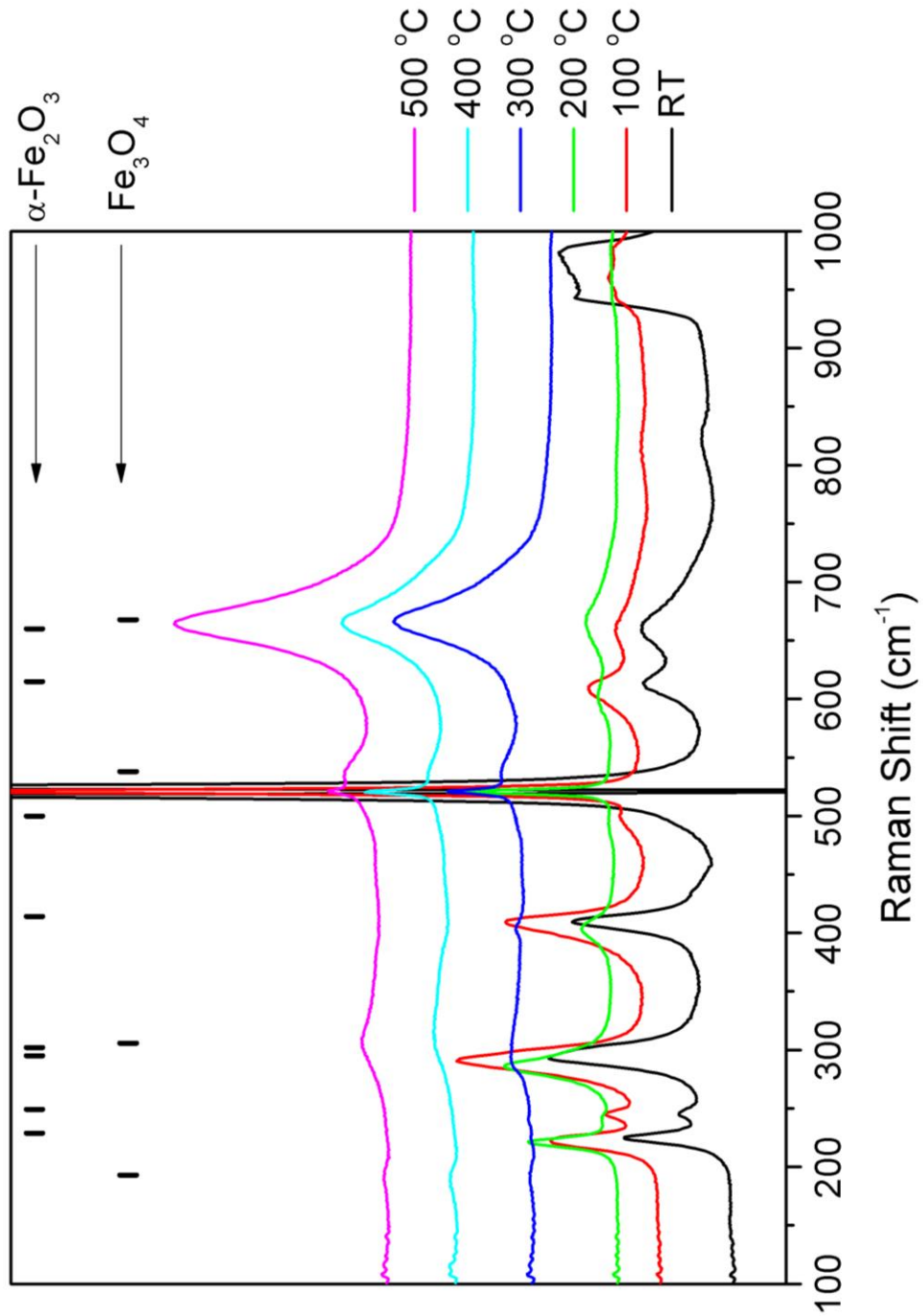


Figure 5.9. Raman spectra from iron oxide thin films grown at different temperatures on Si substrates using a $\lambda = 514.5 \text{ nm}$ laser. The Fe_3O_4 and $\alpha\text{-Fe}_2\text{O}_3$ guides are from the experimental results of Shebanova [15] and Jubb [16], respectively.

The films grown at RT – 200 °C have peaks corresponding to α -Fe₂O₃ which matches with the results from XRD and XPS, except the XRD spectra for the 200 °C film showing peaks for Fe₃O₄ instead of α -Fe₂O₃ which will be discussed later in the chapter. Table 5.3 consists of a comparison of the peak positions from the RT – 200 °C films with the peak positions of Fe₂O₃ measured and assigned by Jubb [16].

RT	100 °C	200 °C	Jubb	Raman
(cm⁻¹)	(cm⁻¹)	(cm⁻¹)	(cm⁻¹)	Modes
224	222	221	229	A _{1g}
245	245	241	249	E _g
292	290	286	295	E _g
-	-	-	302	E _g
409	409	403	414	E _g
-	500	494	500	A _{1g}
613	609	601	615	E _g
660	660	667	660	LO E _u

Table 5.3. Peak positions from Raman spectra of iron oxide thin films grown at RT, 100 & 200 °C compared to α -Fe₂O₃ peak positions and Raman mode assignment by Jubb [16]. All measured peak positions have an error of ± 2 cm⁻¹.

Although Raman spectroscopy is a surface sensitive technique, the penetration depth is large enough (~150 nm) that the whole thickness of these films were analysed. There are peaks in addition to the main iron oxide Raman modes in all of the samples and these were found to be from the Si substrate. A spectra for a Si substrate was

measured and is shown in Figure 5.10, where the main peak around 520 cm^{-1} has saturated the detector causing a drop to zero intensity. The position and strong intensity of the Si peaks in Figure 5.9 affected or even masked most of the iron oxide peaks, with the only Fe_3O_4 peak that is not affected by the Si peaks being the A_{1g} peak located around 666 cm^{-1} . The $\alpha\text{-Fe}_2\text{O}_3$ peak at 500 cm^{-1} is sometimes lost to the strong Si peak around 520 cm^{-1} and the peak that should be at 302 cm^{-1} appears to be seen as a shoulder to the stronger peak at 295 cm^{-1} by Jubb [16]. The film grown at RT has an additional square peak located around $900 - 1000\text{ cm}^{-1}$ which originates from the Si substrate and is more dominant than in the other films as the RT film was thinner (as mentioned at the beginning of Section 5.3).

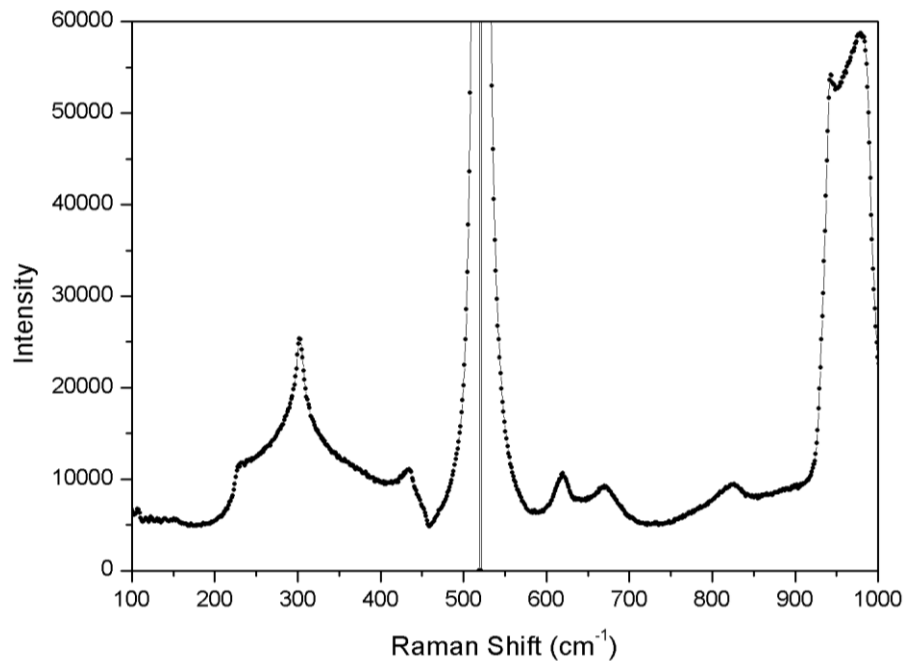


Figure 5.10. Raman spectra from a Si substrate using a $\lambda = 514.5\text{ nm}$ laser.

5.3.1.4. Ellipsometry

Once the composition of the iron oxide thin films was determined using XRD, XPS and Raman spectroscopy the thickness of the films was then calculated using ellipsometry measurements and modelling. The model was fitted with the refractive index of magnetite ($n = 2.42$) and silicon ($n = 3.44$) for the films grown at 300, 400 & 500 °C producing the growth time (t) vs film thickness (T) graph for the different growth temperatures illustrated in Figure 5.11.

As a comparison, a PMMA step was added to the film grown at RT for 15 minutes and had a thickness of 60 nm which is similar to the results in Figure 5.11. As it was possible to measure the thickness of the RT films using the PMMA and complications in the modelling arising from the mixed iron oxide phase indicated by XPS, these films were not measured using ellipsometry. Table 5.4 shows the thin film growth rates for the two iron oxides.

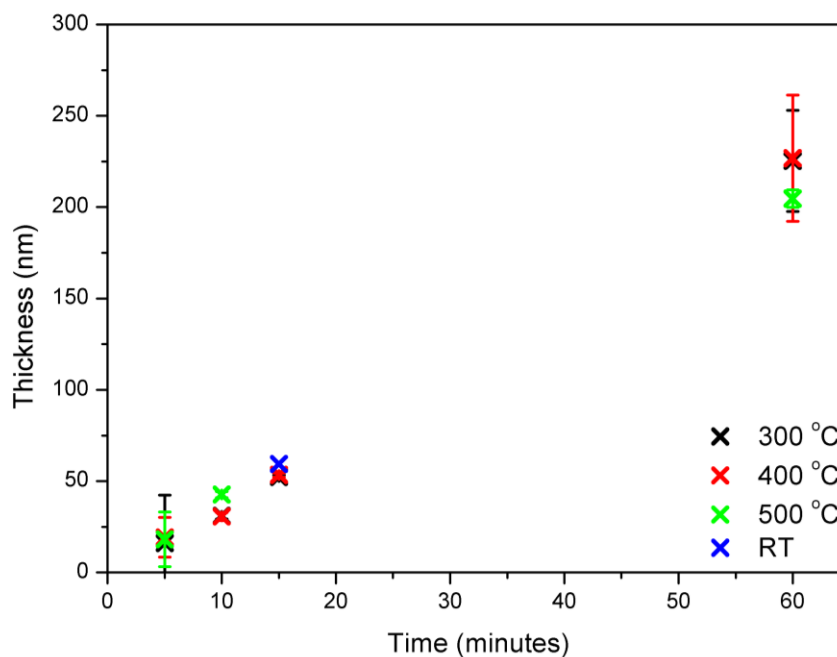


Figure 5.11. Ellipsometry modelling measurements for Fe_3O_4/Si thin films. Film thickness vs time for a range of growth temperatures.

Iron Oxide	Growth Rate ($nm\ min^{-1}$)
Fe_3O_4	$T = 3.52 * t$
$\alpha-Fe_2O_3$	$T = 2.40 * t$

Table 5.4. Growth rate equations for the Fe_3O_4 and $\alpha-Fe_2O_3$ thin films, where T is the film thickness in nm and t is the growth time in minutes.

5.3.2. Magneto-optical Kerr effect Magnetometry

The magnetic properties of the iron oxide thin films were measured using MOKE and analysed to observe the effect of growth temperature. All of the films analysed in this section are 50 nm thick. More in-depth analysis of the effects of film thickness on the films' magnetic properties will be presented in Chapter 6.

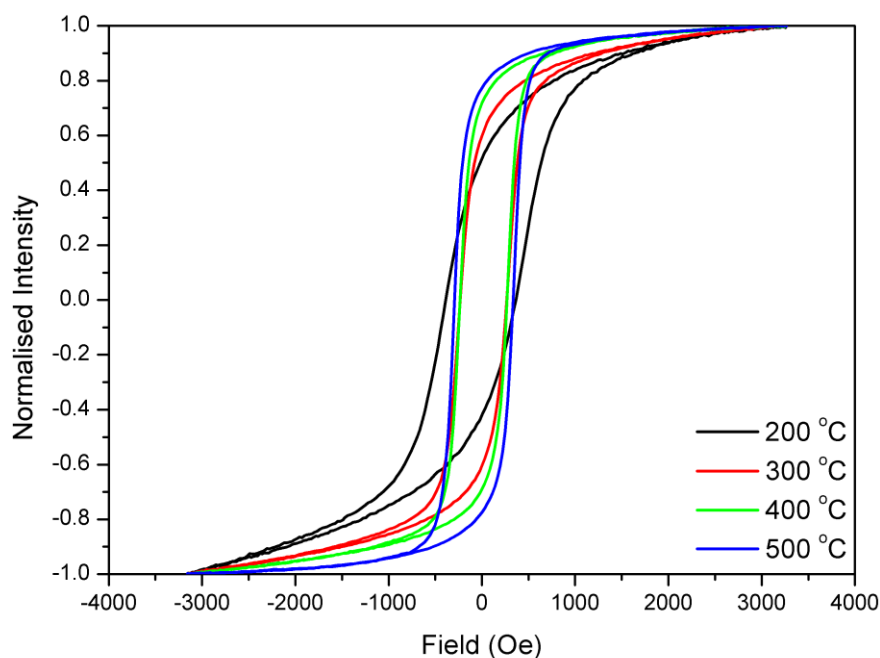


Figure 5.12. Normalised hysteresis loops of 50 nm iron oxide thin films on Si substrates, measured using MOKE.

Even without the compositional analysis presented above, it is clear from the MOKE hysteresis loops presented in Figure 5.12 that adding oxygen and increasing the growth temperature has greatly changed the films' magnetic properties from those of Fe on Si as presented in Section 5.2.1. The coercivity has doubled from ~150 Oe for pure Fe

films to 250 – 300 Oe for iron oxide films grown at 300 – 500 °C. The coercivity of films grown at 200 °C is greater still than this at ~ 350 – 400 Oe. Similar coercivity values have been reported in the literature for polycrystalline Fe₃O₄ thin films [17, 18]. The magnetic isotropic nature of the 50 nm films grown at 200 – 500 °C was investigated by measuring hysteresis loops at a range of in-plane field angles. The measured coercivity values from these hysteresis loops are presented in Figure 5.13 and illustrate that for growth temperatures of 300, 400 & 500 °C the films are magnetically isotropic, however the angular variation of the coercive field is larger but with no obvious pattern for the 200 °C film. Despite this, the variations in the coercivity of all of the films are less than 5% of the average.

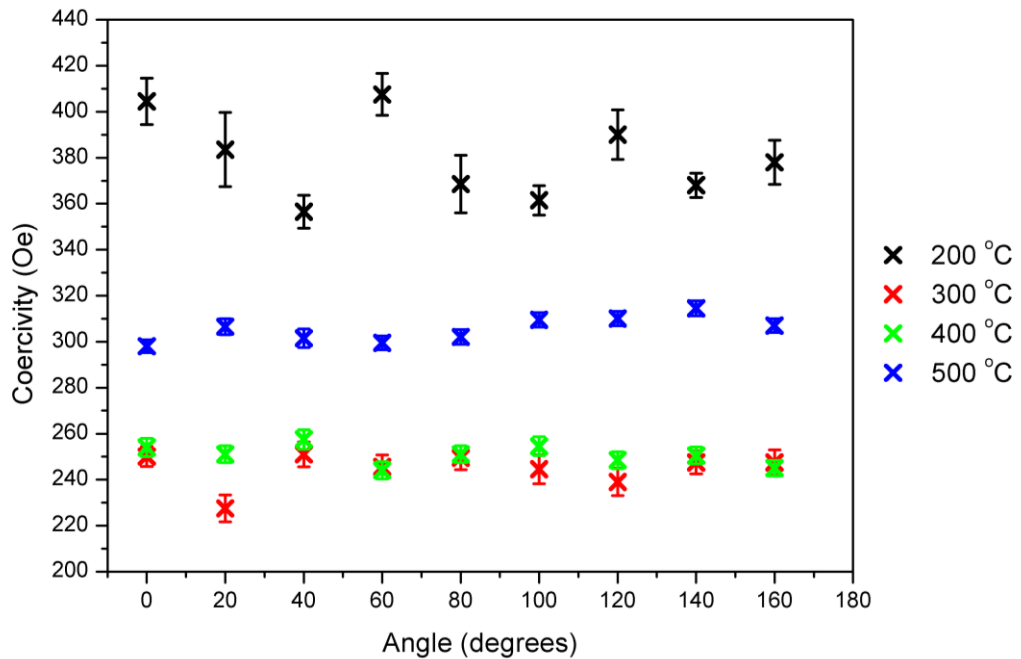


Figure 5.13. Coercivity values from 50 nm iron oxide thin films grown on Si substrates for varying field angle, where 0° is along a sample edge.

A common trait of magnetite thin films is that they have very large saturation fields. This has been reported to be caused by the presence of anti-phase boundaries (APBs). APBs introduce a new strong exchange coupling which favours antiparallel B spins and antiparallel A spins across the boundary. As this exchange coupling is strong, the films may remain unsaturated in fields of 70 kOe [19] and explains the unsaturated hysteresis loops when the MOKE system's maximum 3.5 kOe magnetic field was applied in Figure 5.12.

The films grown at RT and 100 °C were also measured using MOKE. The normalised magnetisation curve for the 100 °C iron oxide film is presented in Figure 5.14. This loop is in stark contrast to the highly hysteretic loops observed for the Fe/Si and Fe₃O₄/Si films. The hysteresis loop appears to resemble that of a superparamagnetic material, and thus the Langevin function as a function of applied field (Equation (5.1)) was fitted to the data.

$$L(H) = \coth(P1 \times H) - \frac{1}{(P1 \times H)} \quad (5.1)$$

$$P1 = \frac{\mu_0 m}{k_B T} \quad (5.2)$$

A value for m at room temperature was calculated from Equation (5.2) using the fitted value of $P1$ ($= 0.0275$ m/A) and the values for μ_0 and k_B , giving $m = 9 \times 10^{-17}$ A/m. From this fit a value for the grain size of cubic and spherical grains was calculated using the saturation magnetisation values for α -Fe₂O₃, γ -Fe₂O₃, Fe₃O₄ and Fe using Equation (5.3). The results of this analysis is presented in Table 5.5.

$$V = \frac{m}{M_S} \quad (5.3)$$

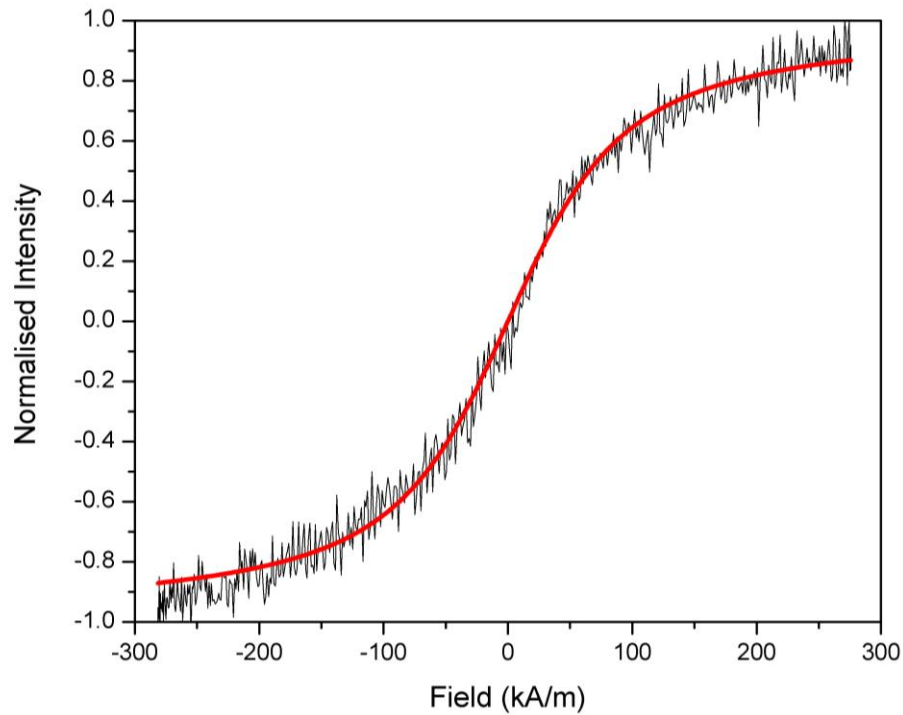


Figure 5.14. Normalised hysteresis loop of a 50 nm iron oxide thin film grown at 100 °C on a Si substrate, measured using MOKE, and fitted using the Langevin function.

Material	Saturation Magnetisation (kA/m) [10, 20]	Grain Size - cube (nm)	Grain Size - sphere (nm)
α -Fe ₂ O ₃	2	355.7 ± 1.5	441.4 ± 0.4
γ -Fe ₂ O ₃	390	61.3 ± 0.3	76.2 ± 0.07
Fe ₃ O ₄	471	57.5 ± 0.2	71.4 ± 0.07
Fe	1717	37.4 ± 0.2	46.4 ± 0.05

Table 5.5. Calculated values for the average grain size from the fitted Langevin function for different iron oxides and iron, using bulk saturation magnetisation value (at room temperature).

Combining the calculated average grain sizes in Table 5.5 and an AFM image (Figure 5.15) of the 100 °C film, it is clear to see that the calculated grain size is far too large compared to the grain size in the AFM image. Therefore, this rules out the possibility of hematite being the origin of the superparamagnetic behaviour observed in Figure 5.14. The average grain size in Figure 5.15 is 28.6 ± 1.6 nm which is a factor of 10 smaller than the calculated values of 355.7 and 441.4 nm for hematite. However, the calculated grain sizes for γ -Fe₂O₃, Fe₃O₄ and Fe are much closer to the measured value. A possible theory that ties the mixed phase XPS results for the RT film with this data is that the film consists of a matrix α -Fe₂O₃ containing isolated superparamagnetic Fe₃O₄ grains, and that the ratio of α -Fe₂O₃ to Fe₃O₄ decreases with increasing growth temperature such that the films grown above 300 °C are dominantly Fe₃O₄. From measurements and calculations performed by Dunlop [21] the grain size range for super-paramagnetic Fe₃O₄ particles at room temperature is from 29 – 36 nm, in which the average grain size of 28.6 ± 1.6 nm in Figure 5.15 fits. This evidence is not conclusive, but it does offer an interesting possible explanation to the observed behaviour.

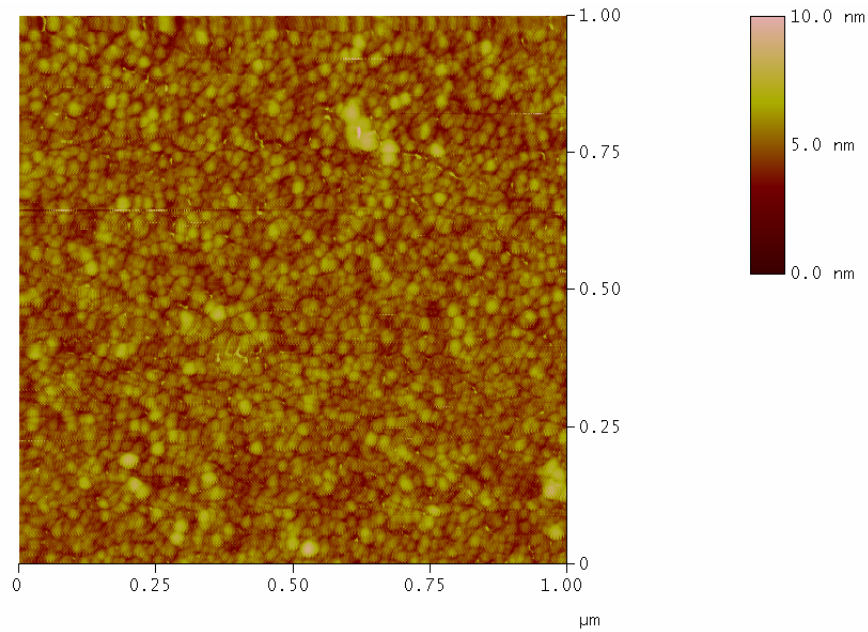


Figure 5.15. AFM image of the 50 nm iron oxide film grown at 100 °C.

The raw MOKE data from the 50 nm iron oxide thin film grown at RT is presented in Figure 5.16. The low MOKE signal and the lack of an obvious hysteresis does agree with the theory that the film is α -Fe₂O₃ which is a canted anti-ferromagnet. The magnetic properties of this film are unclear from the data and further analysis would be needed, possibly using a different measurement technique. However, the focus of this project is on ferrimagnetic Fe₃O₄ thin films and therefore further analysis will not be made on this film here.

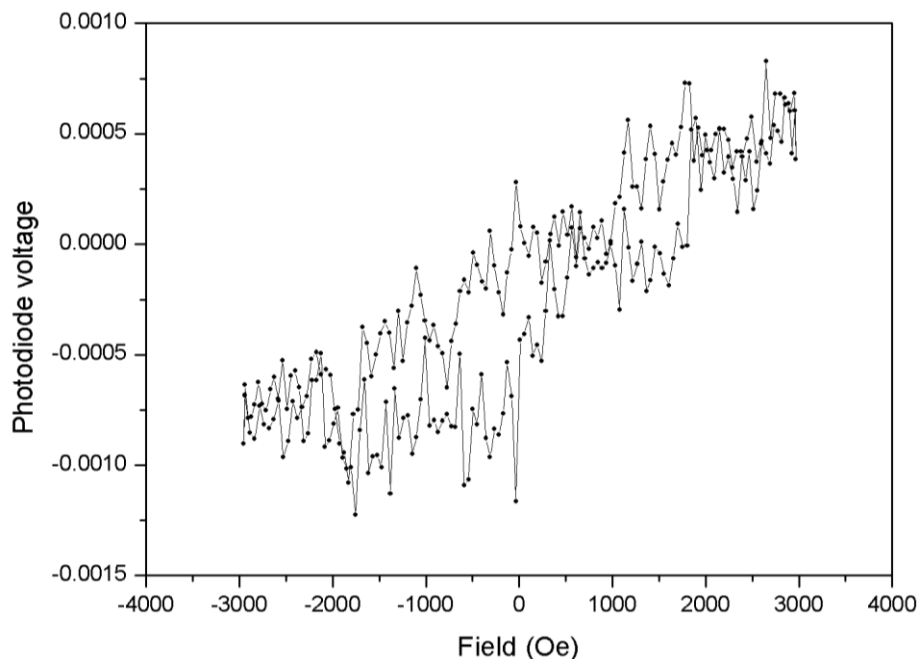


Figure 5.16. Raw MOKE loop of a 50 nm iron oxide thin film grown at RT on a Si substrate.

5.3. Conclusion

In conclusion, Fe_3O_4 thin films on Si substrates have been successfully grown using reactive DC sputtering from a Fe target. It was shown, using a combination of GA-XRD, Raman spectroscopy and XPS, that the iron oxide phase of the thin film can be selected by changing the substrate growth temperature used. Fe_3O_4 thin films are produced for substrate growth temperatures of 300, 400 & 500 °C and a mixed iron oxide phase of $\alpha\text{-Fe}_2\text{O}_3$ and Fe_3O_4 was produced at temperatures of RT, 100 & 200 °C. Comparing the GA-XRD spectra for Fe thin films grown on Si substrates to the spectra from the iron oxide films shows that there is no pure Fe phase present in the

iron oxide films, which is backed up by the lack of a Fe peak in the XPS spectra taken on the RT & 500 °C iron oxide films.

The in-plane magnetisation loops produced using a MOKE magnetometer for 20 – 50 nm Fe films on Si substrates produced a coercivity of ~ 150 Oe, and were shown to possess a small in-plane magnetic anisotropy by varying the in-plane applied field angle. Unsaturated loops were produced in an applied field of 3.5 kOe for the 50 nm iron oxide films grown at 200 – 500 °C, with coercivity values of 250 – 300 Oe for the 300 – 500 °C films and 350 – 400 Oe for the 200 °C film. These were shown to be magnetically isotropic by varying the in-plane applied field angle, within a 5% error of the average coercivity value.

The magnetisation loop produced for the 50 nm iron oxide film grown at 100 °C was in stark contrast to the hysteretic loops produced for the 200 – 500 °C films, and resembled that of a superparamagnetic material. The Langevin function was fitted to the normalised magnetisation loop, which produced a value of $m = 9 \times 10^{-17}$ A/m that was used in combination with the saturation magnetisation values of different iron oxide phases and pure iron to estimate the average grain size of the superparamagnetic material. α -Fe₂O₃ was instantly ruled out as the source of the superparamagnetism as its estimated grain size was a factor of 10 larger than the measured grain size from an AFM image of the 100 °C film. The estimated grain sizes for γ -Fe₂O₃, Fe₃O₄ and Fe were all close enough to the measured grain size value to be possible sources of the superparamagnetism. Using a combination of these calculations and the XPS peak fitting for the RT film, a possible theory is that the films consist of a matrix of α -Fe₂O₃ containing isolated superparamagnetic Fe₃O₄ grains. The ratio of α -Fe₂O₃ to Fe₃O₄ decreases with increasing growth temperature such that the films grown above 300 °C are predominately Fe₃O₄. This theory fits with the raw MOKE data for the RT film,

as its small MOKE signal and lack of obvious hysteresis is due to α -Fe₂O₃ being a canted-antiferromagnet.

The next step to take with these Fe₃O₄ thin films is to investigate the effect of varying the substrate choice and the film thickness over the growth temperature range of 300 – 500 °C. This is with the aim of finding a Fe₃O₄ thin film with a coercivity small enough to allow DWs to form when the films are patterned into nanostructures, and a large resistivity so as to increase the trap lifetime for the domain wall atom trapping application.

References

- [1] D. A. Allwood, T. Schrefl, G. Hrkac, I. G. Hughes, and C. S. Adams, "Mobile atom traps using magnetic nanowires," *Applied Physics Letters*, vol. 89, pp. 014102-014104, 2006.
- [2] M. Negoita, T. J. Hayward, and D. A. Allwood, "Controlling domain walls velocities in ferromagnetic ring-shaped nanowires," *Applied Physics Letters*, vol. 100, pp. 072405-072409, 2012.
- [3] A. Javed, N. A. Morley, and M. R. J. Gibbs, "Effect of growth parameters on the structure and magnetic properties of thin polycrystalline Fe films fabricated on Si <100> substrates," *Applied Surface Science*, vol. 257, pp. 5586-5590, 2011.
- [4] Y. K. Kim and M. Oliveria, "Magnetic properties of sputtered Fe thin films: Processing and thickness dependence," *Journal of Applied Physics*, vol. 74, pp. 1233-1241, 1993.
- [5] Kaye and Laby Online. *Table of Physical & Chemical Constants. 2.6.1 Electrical Resistivities. Version 1.0 (2005).* Available: www.kayelaby.npl.co.uk
- [6] A. F. Mayadas, J. F. Janak, and A. Gangulee, "Resistivity of Permalloy thin films," *Journal of Applied Physics*, vol. 45, pp. 2780-2781, 1974.
- [7] A. Schuhl, F. N. V. Dau, and J. R. Childress, "Low-field magnetic sensors based on the planar Hall effect," *Applied Physics Letters*, vol. 66, pp. 2751-2753, 1995.

- [8] D. T. Margulies, F. T. Parker, F. E. Spada, R. S. Goldman, J. Li, R. Sinclair, *et al.*, "Anomalous moment and anisotropy behaviour in Fe₃O₄ films," *Physical Review B*, vol. 53, pp. 9175-9187, 1996.
- [9] T. M. Hall, A. Wagner, and L. F. Thompson, "Ion beam exposure characteristics of resists: Experimental results," *Journal of Applied Physics*, vol. 53, pp. 3997-4010, 1981.
- [10] R. M. Cornell and U. Schwertmann, *The Iron Oxides: Structure, Properties, Reactions, Occurrences and Uses*, 2nd ed.: John Wiley & Sons, 2006.
- [11] M. C. Biesinger, B. P. Payne, A. P. Grosvenor, L. W. M. Lau, A. R. Gerson, and R. S. C. Smart, "Resolving surface chemical states in XPS analysis of first row transition metals, oxides and hydroxides: Cr, Mn, Fe, Co and Ni," *Applied Surface Science*, vol. 257, pp. 2717-2730, 2011.
- [12] S. Gota, E. Guiot, M. Henriot, and M. Gautier-Soyer, "Atomic-oxygen-assisted MBE growth of α -Fe₂O₃ on α -Al₂O₃ (0001): Metastable FeO (111)-like phase at subnanometer thicknesses," *Physical Review B*, vol. 60, pp. 14387-14395, 1999.
- [13] C. Ruby, B. Humbert, and J. Fusy, "Surface and interface properties of epitaxial iron oxide thin films deposited on MgO (001) studied by XPS and Raman spectroscopy," *Surface and Interface Analysis*, vol. 29, pp. 377-380, 2000.
- [14] K. Wandelt, "Photoemission studies of adsorbed oxygen and oxide layers," *Surface Science Reports*, vol. 2, pp. 1-121, 1982.
- [15] O. N. Shebanova and P. Lazor, "Raman spectroscopic study of magnetite (FeFe₂O₄): a new assignment for the vibrational spectrum," *Journal of Solid State Chemistry*, vol. 174, pp. 424-430, 2003.

- [16] A. M. Jubb and H. C. Allen, "Vibrational spectroscopic characterization of hematite, maghemite, and magnetite thin films produced by vapor deposition," *Applied Materials & Interfaces*, vol. 2, pp. 2804-2812, 2010.
- [17] A. Bollero, M. Ziese, R. Hohne, H. C. Semmelhack, U. Kohler, A. Setzer, *et al.*, "Influence of thickness on microstructural and magnetic properties in Fe₃O₄ thin films produced by PLD," *Journal of Magnetism and Magnetic Materials*, vol. 285, pp. 279-289, 2005.
- [18] X. Huang and J. Ding, "The structure, magnetic and transport properties of Fe₃O₄ thin films on different substrates by pulsed laser deposition," *Journal of the Korean Physical Society*, vol. 62, pp. 2228-2232, 2013.
- [19] D. T. Margulies, F. T. Parker, M. L. Rudee, F. E. Spada, J. N. Chapman, P. R. Aitchison, *et al.*, "Origin of the anomalous magnetic behaviour in single crystal Fe₃O₄ films," *Physical Review Letters*, vol. 79, pp. 5162-5165, 1997.
- [20] M. Kamata, H. Kura, M. Takahashi, T. Ogawa, and T. Tanaka, "Direct Synthesis of Single Crystalline α -Fe Nanoparticles with High Saturation Magnetization by Mixed Surfactant," *IEEE Transactions on Magnetics*, vol. 48, pp. 3944-3946, 2012.
- [21] D. J. Dunlop, "Superparamagnetic and single-domain threshold sizes in magnetite," *Journal of Geophysical Research*, vol. 78, pp. 1780-1793, 1973.

6. Analysis and optimisation of the morphology and magnetic properties of Fe₃O₄/Si and Fe₃O₄/MgO (100) thin films

6.1. Introduction

Where the previous chapter focussed on the development and analysis of growing the correct iron oxide phase thin film by varying the growth temperature, this chapter will investigate the effect of substrate choice, growth temperature and film thickness on the coercivity, resistivity and surface morphology of Fe₃O₄ thin films. This was with the aim of finding the optimum film growth properties to produce Fe₃O₄ films with a coercivity as low as possible, a small surface roughness and large resistivities, compared to the resistivity of Permalloy. These properties are important for the domain wall atom trapping application as the larger resistivity will increase the trap lifetime, and a low coercivity and small surface roughness will aid the formation and controlled movement of domain walls in nanostructures.

6.2. Sample growth

In this chapter there are two different Fe_3O_4 film series, the first of which used the same growth procedure for producing Fe_3O_4 thin films in Section 5.3 and the second is adapted from this in an attempt to overcome repeatability issues.

The second growth procedure differs from the first in two parts. The first was introduced as it was found that the Fe target started to become oxidised during film growth which inhibited the ability to strike and maintain a stable plasma, and therefore to remove this effect a new Fe target was used for each growth. Secondly, a lower pressure was achieved in the sputtering chamber prior to growth to reduce the probability of contamination in the thin film. The pressure reached was 5×10^{-7} mbar compared to the previously used pressure of 5×10^{-6} mbar.

For both film series, the substrate temperatures used were 300, 400 & 500 °C as these were expected to produce the correct phase of iron oxide. The Fe_3O_4 films were grown with nominal thicknesses of 17.5, 35, 52.5 and 105 (± 2) nm, with multiple films grown for each thickness at a growth temperature of 500 °C in order to check repeatability for both film series.

In addition to the Si substrates films were also grown on MgO (100) substrates. MgO (100) substrates were chosen after it was shown by Chen et al in [1] that a smaller coercivity value can be achieved when using a substrate that has a smaller lattice mismatch to Fe_3O_4 . MgO (100) substrates have a lattice parameter (0.4212 nm) that is half that of Fe_3O_4 (0.8397 nm), as well as the oxygen lattice in both MgO and Fe_3O_4 forming a face-centered cubic lattice with a 0.3% lattice mismatch [2].

For the first film series the single crystal MgO (100) substrates used were 5 mm x 5 mm with one side polished. In addition to these substrates, 10 mm x 10 mm MgO (100) substrates were used for the second series due to difficulties with measuring resistivity. This was due to the 4-probe resistivity rig not being capable of measuring samples as small as 5 mm x 5 mm. However, after these films were grown, a new 4-probe resistivity rig was constructed (as mentioned in Section 4.4.1) that was able to measure thin films on the 5 mm x 5 mm substrates. Both substrates were ordered from the same company to ensure that the only difference was the size. In the second series the vast majority of films were grown on the 10 mm x 10 mm substrates, with only the 500 °C films and the 105 nm thick film grown at 300°C being deposited on the smaller substrates.

6.3. Texture analysis of Fe₃O₄/MgO (100) thin films

To establish whether the Fe₃O₄ films grown on MgO (100) substrates were polycrystalline to match the films grown on Si substrates, a combination of locked-coupled (θ - 2θ) and glancing angle XRD was utilised. A Bruker D8 Discover was used for these measurements as its resolution is ~15 arcseconds, which is ~0.004°. This resolution was needed to separate the MgO (200) peak located at $2\theta = 42.91^\circ$ and the Fe₃O₄ (400) peak located at $2\theta = 43.05^\circ$.

Figure 6.1 shows a locked-coupled scan over the range $2\theta = 30 - 45^\circ$ with a step size of 0.005° of a 105 nm Fe₃O₄ thin film grown on an MgO (100) substrate. It can be seen in Figure 6.1 that there is a strong peak at $2\theta = 42.93^\circ$ which is the MgO (200)

peak. There is also a second peak located at $2\theta = 43.21^\circ$ which is from the thin film and is the Fe_3O_4 (400) peak. The inset graph in Figure 6.1 shows the full scale of the MgO (200) peak, and that the Fe_3O_4 (400) peak is ~ 150 times smaller than the MgO (200) peak. Fe_3O_4 has other peaks that would be present in the $2\theta = 30 - 45^\circ$ range, including the Fe_3O_4 (311) peak which is located at $2\theta = 35.42^\circ$ and is $\sim 5x$ larger than the Fe_3O_4 (400) peak. This can be seen in Figure 6.3 for glancing angle (5°) XRD spectra from polycrystalline $\text{Fe}_3\text{O}_4/\text{Si}$ thin films grown at 300, 400 & 500 $^\circ\text{C}$, where the spectra were taken using a Siemens D5000 Diffractometer. In Figure 6.1 there are no other visible peaks above the noise floor except the MgO (200) and Fe_3O_4 (400) peaks, which indicates that the film has a (100) crystal lattice texture.

Texture is used to describe the crystallographic orientations of a polycrystalline material. There are two extreme cases of crystallographic texture: a material with no distinct texture having a random crystallite orientation, and the opposite where the material is a single crystal. When a material has a preferred orientation, it is described as having a crystallographic texture.

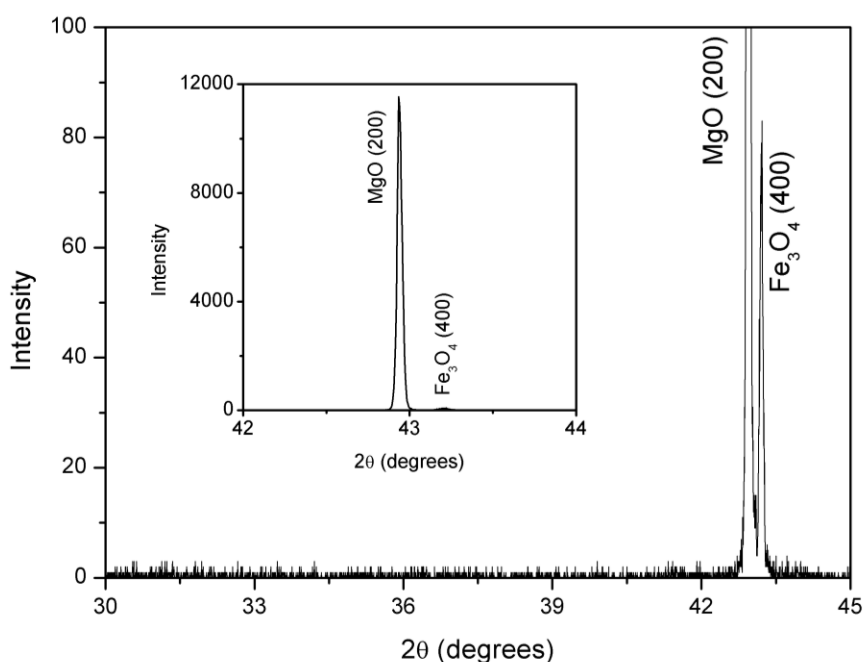


Figure 6.1. A locked-coupled XRD spectra from a 105 nm Fe₃O₄ film on an MgO (100) substrate. Inset: Full-scale XRD spectra, highlighting the intensity difference between the MgO (200) & Fe₃O₄ (400) peaks.

To confirm that the Fe₃O₄ thin film grown on MgO (100) is textured, a glancing angle XRD measurement was taken at an incidence angle of 5° over an angle range of 2θ = 25 – 65° with a step size of 0.02°. This will aid the confirmation that the film is textured as in a glancing angle spectra the thin film peaks should show up more strongly but will still be missing if the film is textured as Bragg's law will not be satisfied. Figure 6.2 presents glancing angle XRD spectra taken from both an empty sample holder (black data) and a sample holder containing the Fe₃O₄ film grown on MgO (100) (red data). The only peaks present in the spectrum of the film are those from the substrate holder, indicating that the Fe₃O₄ film is textured. Together, the

ANALYSIS AND OPTIMISATION OF THE MORPHOLOGY AND MAGNETIC PROPERTIES OF $\text{Fe}_3\text{O}_4/\text{Si}$ AND $\text{Fe}_3\text{O}_4/\text{MgO}$ (100) THIN FILMS

locked-coupled and glancing angle measurements provided strong evidence that the Fe_3O_4 films grown on MgO (100) substrates had a (100) crystal lattice texture.

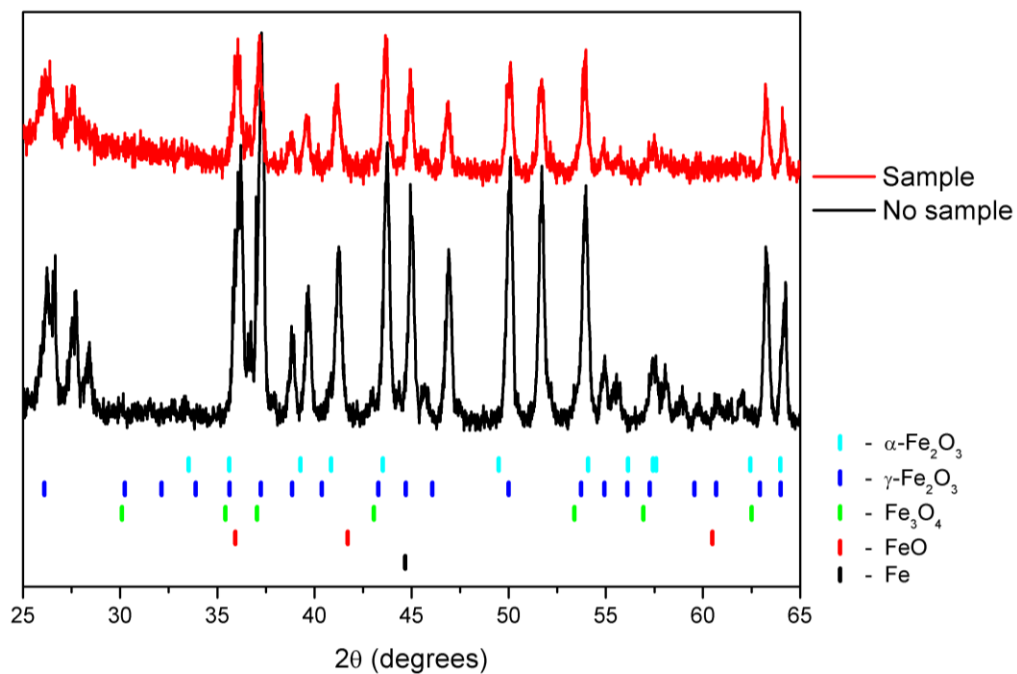


Figure 6.2. Glancing angle (5°) XRD of the sample holder and a 105 nm Fe_3O_4 film on an MgO (100) substrate.

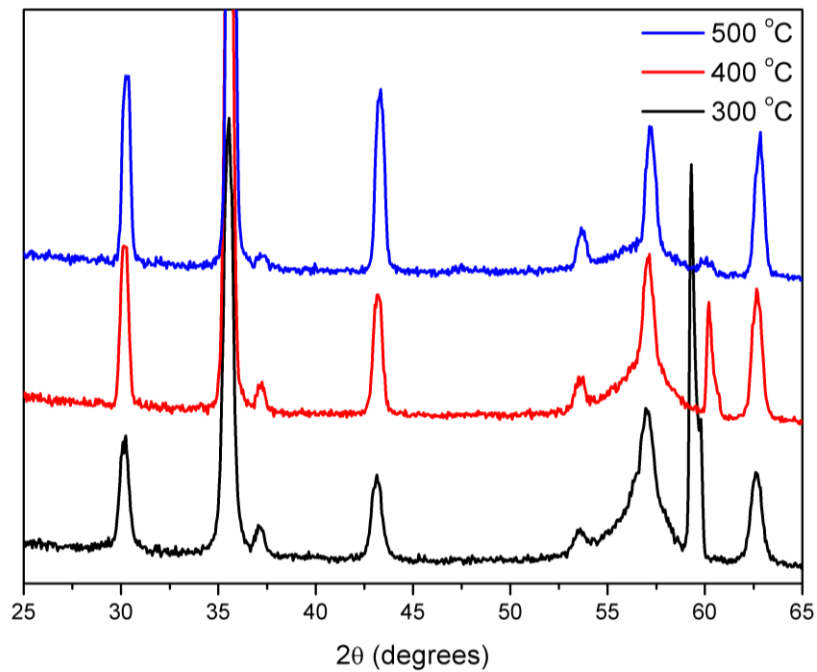


Figure 6.3. Glancing angle (5°) XRD of 105 nm Fe₃O₄/Si grown at temperatures of 300, 400 & 500 °C. (Adapted from Figure 5.4).

From these locked-coupled and glancing angle XRD spectra it can be concluded that Fe₃O₄ thin films grown on MgO (100) substrates are (100) textured, whereas the Fe₃O₄ thin films grown on Si substrates are shown to be fully random with no distinct crystal lattice texture.

For simplicity, through this work the films grown on Si substrates will be described as polycrystalline and the films grown on MgO (100) will be described as textured.

6.4. Study of surface morphologies of $\text{Fe}_3\text{O}_4/\text{Si}$ & $\text{Fe}_3\text{O}_4/\text{MgO}$ (100) thin films

The surface morphology of both of the $\text{Fe}_3\text{O}_4/\text{Si}$ & $\text{Fe}_3\text{O}_4/\text{MgO}$ thin film series were imaged using AFM to measure the grain size and basic morphology. This was to investigate the effect caused by the substrate choice, growth temperature and film thickness on the surface morphology. The $\text{Fe}_3\text{O}_4/\text{Si}$ for both film series will be presented together and analysed first, followed by the analysis from the $\text{Fe}_3\text{O}_4/\text{MgO}$ film series which will be presented separately as the surface morphologies observed for both film series need in-depth discussion and analysis.

6.4.1. Surface morphology of $\text{Fe}_3\text{O}_4/\text{Si}$ thin films

Figure 6.4 presents AFM images from both $\text{Fe}_3\text{O}_4/\text{Si}$ thin film series at a range of growth temperatures (top: 300 °C, middle: 400 °C & bottom: 500 °C) and film thickness with images a – d from the first film series and e – h from the second series.

The AFM images of the $\text{Fe}_3\text{O}_4/\text{Si}$ films exhibits clear grains and grain boundaries, with a large difference in the shape of the grains for different growth temperatures. For the $\text{Fe}_3\text{O}_4/\text{Si}$ films grown at 300 °C the grains are regular and homogenous, whereas the grains in the $\text{Fe}_3\text{O}_4/\text{Si}$ films grown at 500 °C are irregular in shape. This can be seen clearly in Figure 6.5 which compares 105 nm $\text{Fe}_3\text{O}_4/\text{Si}$ thin films grown at 300 °C, 400 °C and 500 °C.

ANALYSIS AND OPTIMISATION OF THE MORPHOLOGY AND MAGNETIC PROPERTIES OF
 Fe_3O_4/Si AND Fe_3O_4/MgO (100) THIN FILMS

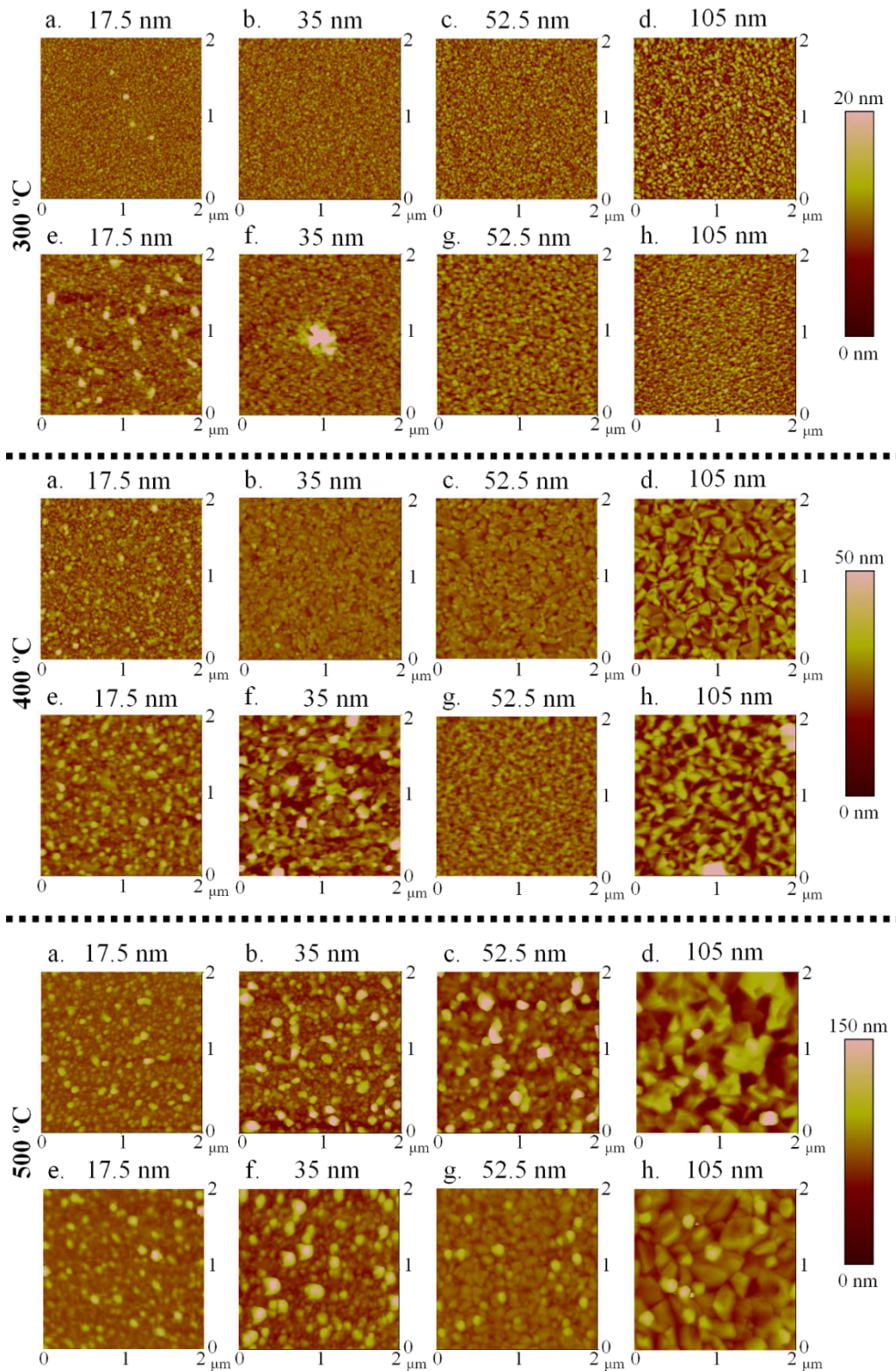


Figure 6.4. AFM images ($2 \mu m \times 2 \mu m$) from both Fe_3O_4/Si thin film series grown at different growth temperatures with different film thicknesses. a) – d): first film series, e) – h): second film series.

ANALYSIS AND OPTIMISATION OF THE MORPHOLOGY AND MAGNETIC PROPERTIES OF $\text{Fe}_3\text{O}_4/\text{Si}$ AND $\text{Fe}_3\text{O}_4/\text{MGO}$ (100) THIN FILMS

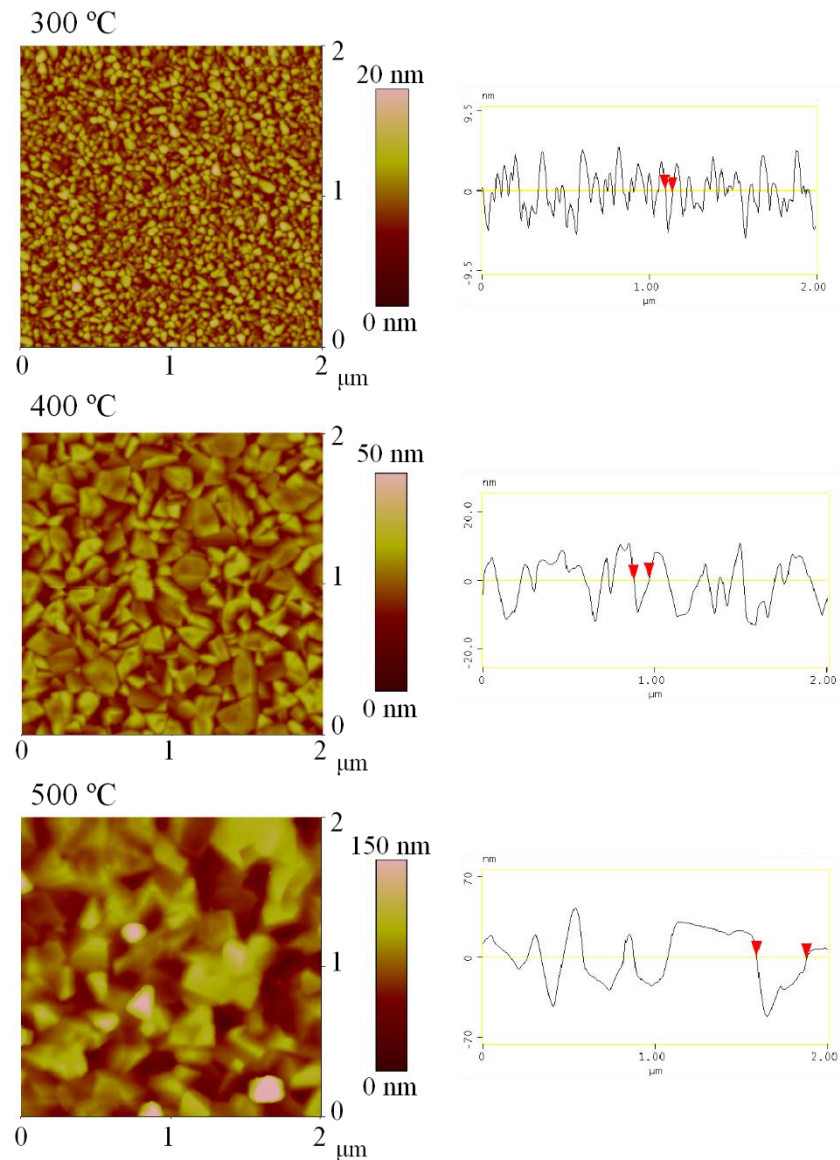


Figure 6.5. AFM images from 105 nm $\text{Fe}_3\text{O}_4/\text{Si}$ thin films grown at 300 °C, 400 °C and 500 °C along with the line section graphs.

The average grain size of the $\text{Fe}_3\text{O}_4/\text{Si}$ films was measured by counting the number of grains on 10 lines of known width across the AFM image, and then dividing the line length by the number of grains it intersects. The average grain size vs. film thickness is presented for each growth temperature in Figure 6.6.

An increase in average grain size is seen with an increase in the film thickness for all the growth temperatures used, with the rate of increase with thickness being higher for higher growth temperatures. It can be seen that the grain size increases across the thickness range used from 41 nm to 57 nm for the 300 °C films and from 65 nm to 230 nm for the 500 °C films. The increase in grain size with substrate temperature can be explained as follows: when the substrate temperature is increased there is also an increase in the surface mobility of atoms during the growth of the film. This additional surface mobility allows the formation of larger grains when compared to films of the same thickness grown at a lower temperature.

The RMS surface roughness was measured for each of the AFM images and plotted against the film thickness for each of the growth temperatures in Figure 6.6. The surface roughness has a similar trend to the grain size with growth temperature, where there is a greater increase in the RMS surface roughness data with increasing film thickness for the higher growth temperatures. This increase is caused by the larger intergranular regions seen for the higher growth temperatures and the larger grains. Cross-sections of the AFM images illustrate this in Figure 6.5.

Although both the average grain size and roughness for the two different film series have similar values, it can be seen in Figure 6.6 that the first film series shows an increase in both the grain size and roughness with film thickness, whereas the second film series has a more varied trend with film thickness. This indicates that the surface morphology of the Fe₃O₄/Si thin films is sensitive to small changes in the growth conditions.

ANALYSIS AND OPTIMISATION OF THE MORPHOLOGY AND MAGNETIC PROPERTIES OF Fe_3O_4/Si AND Fe_3O_4/MGO (100) THIN FILMS

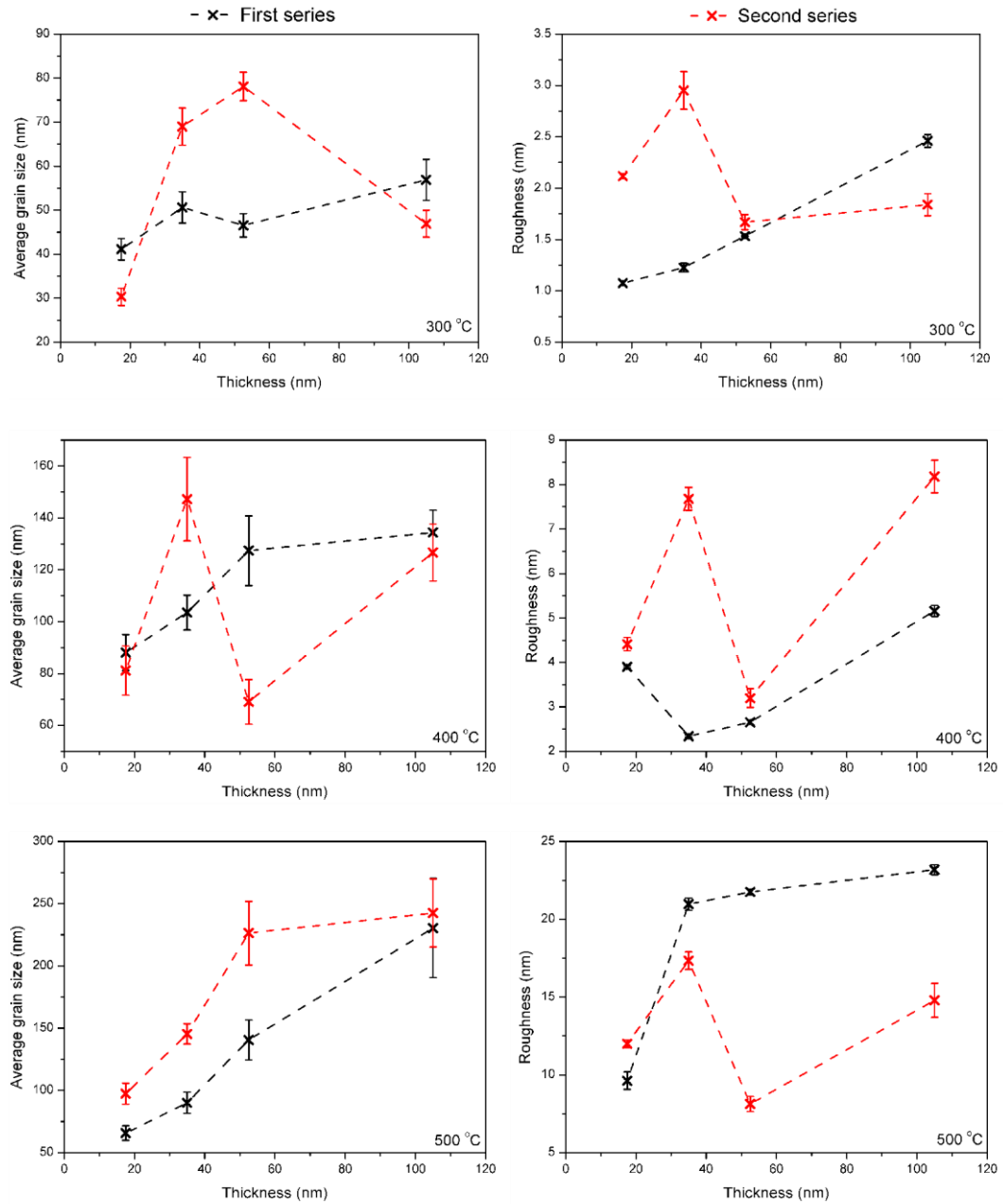


Figure 6.6. Average grain size vs film thickness (left) and surface roughness vs film thickness (right) for both the first (black) and second (red) Fe_3O_4/Si thin film series grown at different growth temperatures. Top: 300 °C, middle: 400 °C & bottom: 500 °C.

6.4.2. Surface morphology of Fe₃O₄/MgO (100) thin films

The AFM images taken from the first series Fe₃O₄/MgO (100) films are presented in Figure 6.7, with the film thickness increasing from left to right (a. 17.5 nm, b. 35 nm, c. 52.5 nm & d. 105 nm) and increasing growth temperature from top to bottom (top: 300 °C, middle: 400 °C & bottom: 500 °C).

There are large differences between the surface morphologies of these Fe₃O₄/MgO thin films and those observed previously for Fe₃O₄/Si, which can be seen when comparing Figure 6.4 & Figure 6.7.

Where the films grown on Si substrates had clear grains and grain boundaries, with the average grain size ranging from 41 nm to 230 nm, the films grown on MgO substrates are flat with a very small grain size. The grain size of these AFM images were not measurable using the technique used for the Fe₃O₄/Si films due to the nanocrystalline grain size. Although the grain size on these AFM images is too small to be measured, the RMS roughness was measured to be < 2 nm for all films.

Another feature in a couple of the films is the appearance of holes in the sample surface. These are seen in the 35 nm 400 °C film, and the 17.5 nm and 105 nm 500 °C films. The holes are irregular in shape, with widths of ~ 100 nm, and varying densities for each film. The film with the largest density of holes present is the 17.5 nm 500 °C film, followed by the 35 nm 400 °C film and the 105 nm 500 °C film with the least. The presence of holes in only a couple of the Fe₃O₄/MgO films in Figure 6.7 show that the surface morphology is highly sensitive to variations in the growth

ANALYSIS AND OPTIMISATION OF THE MORPHOLOGY AND MAGNETIC PROPERTIES OF $\text{Fe}_3\text{O}_4/\text{Si}$ AND $\text{Fe}_3\text{O}_4/\text{MGO}$ (100) THIN FILMS

procedure, but this sensitivity does not seem to correlate systematically to the thickness or growth temperature.

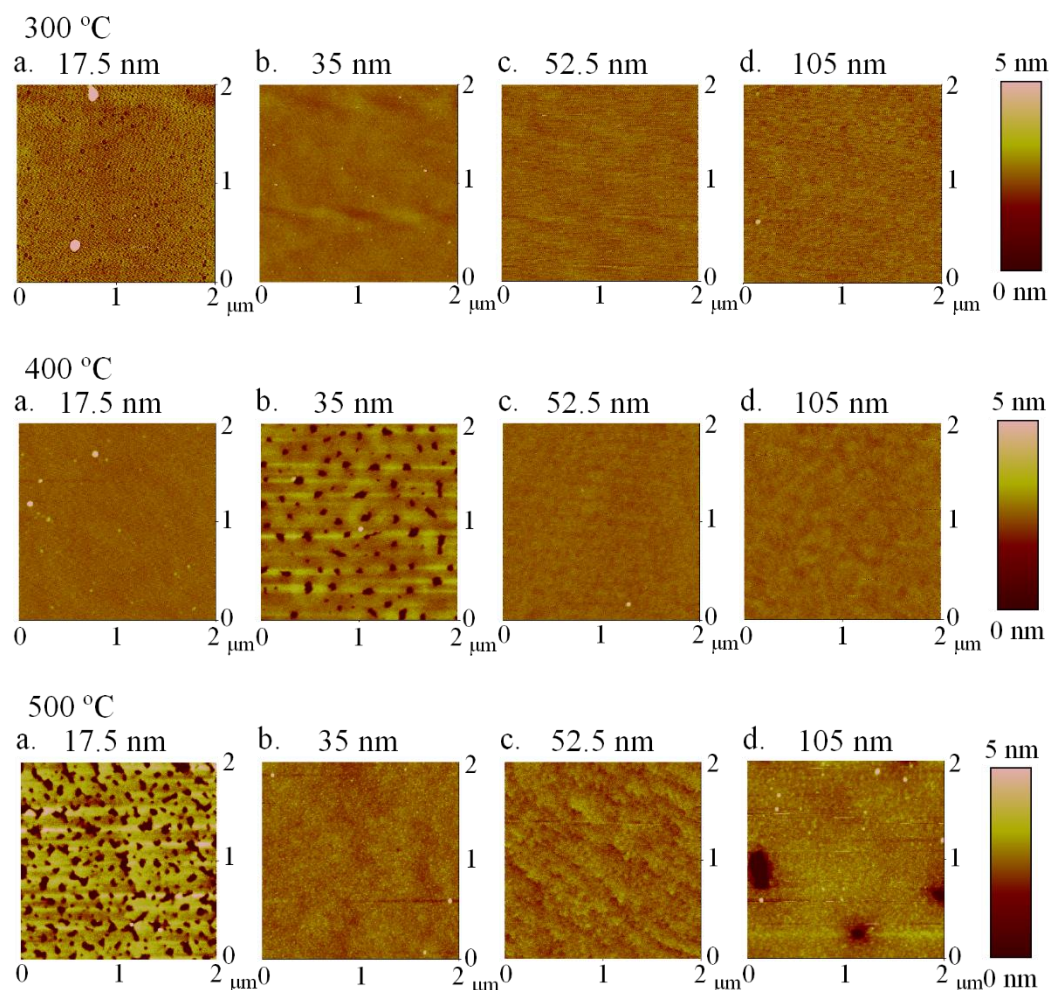


Figure 6.7. AFM images ($2 \mu\text{m} \times 2 \mu\text{m}$) from the first $\text{Fe}_3\text{O}_4/\text{MgO}$ (100) thin film series grown at different growth temperatures with different film thicknesses: a) 17.5 nm, b) 35 nm, c) 52.5 nm & d) 105 nm.

Holes in the film surface have previously been observed by Sala et al. [3] on Fe_3O_4 thin films grown on Pt (111) substrates. For growths above room temperature, the Fe grows on the Pt (111) substrate via the Volmer-Weber island growth mode where the substrate temperature strongly dictates the island size and density. It was shown that

heating the Fe_3O_4 films caused dewetting, where the FeO underlayer became visible through holes in the film surface. Figure 6.8 illustrates the holes in the Fe_3O_4 film showing the FeO layer underneath using bright- and dark-field LEEM, LEED and XPEEM. In the bright-field LEEM image (Figure 6.8a) and the dark-field LEEM image (Figure 6.8d), the dark regions are Fe_3O_4 and the white regions are FeO, whereas the opposite is used in the dark-field LEEM images (Figure 6.8b & c).

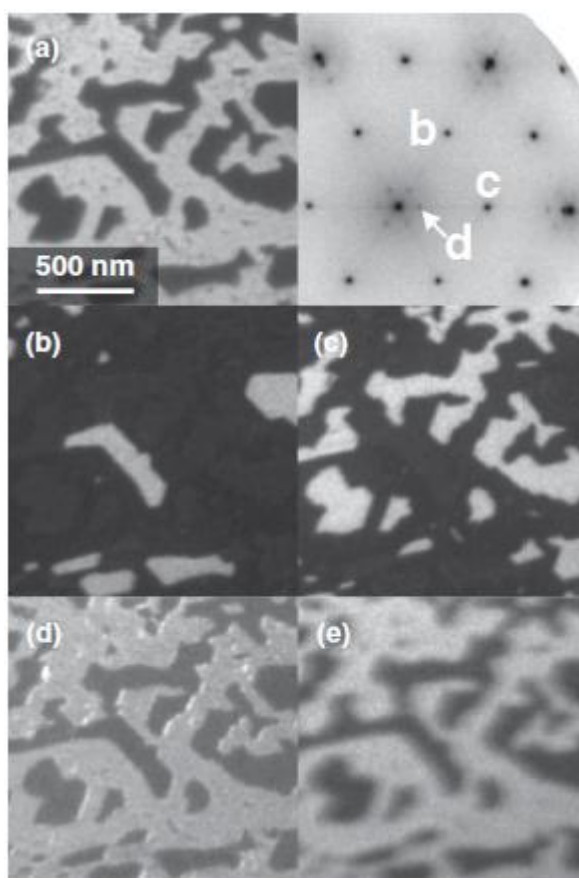


Figure 6.8. Strongly dewetted $\text{Fe}_3\text{O}_4/\text{FeO}/\text{Pt}$ (111) film analysed using bright- and dark-field LEEM, LEED and XPEEM. a) Fe_3O_4 (dark) & FeO (white) structures shown using bright-field LEEM image and the corresponding LEED pattern, where the labels mark the diffraction spots used for the dark-field LEEM images in b) Fe_3O_4 ($1/2;0$), c) Fe_3O_4 ($0;1/2$) & d) FeO ($0,0$). e) An XPEEM image of the Pt 4 $f_{7/2}$ photoemission line. (Adapted from [3])

Although the films grown on Si substrates for both film series produced similar trends in morphology and comparable values for grain size, the AFM images in Figure 6.9 for the films grown on MgO substrates from the second film series show a very different surface morphology to the first $\text{Fe}_3\text{O}_4/\text{MgO}$ film series.

The films on the 5 mm x 5 mm substrates² have small to non-visible grains, and are very smooth with RMS surface roughness values of < 1 nm which is similar to the first $\text{Fe}_3\text{O}_4/\text{MgO}$ film series (< 2 nm). However, the films grown on the 10 mm x 10 mm substrates exhibit 3-dimensional square islands protruding from the film surface. The AFM images show that these islands are not all the same shape on a film but a combination of squares and rectangles (from a top view), and have a range of sizes and heights that do not appear to correlate with the film thickness or growth temperature. These islands range in size from 70 nm (52.5 nm 300 °C) to 480 nm (17.5 nm 400 °C), and vary in height in the range of 7 nm (52.5 nm 300 °C) to 73 nm (17.5 nm 400 °C). The films were all measured with the <100> substrate direction parallel to the image edges and in all of the images the islands are aligned in the same direction which is roughly 45° to the film edge.

For ease, these features will be referred to as “nano-towers”.

A line scan across the nano-towers from the 35 nm film grown at 400 °C (Figure 6.10) illustrates that their shape is not rounded at the top but flat with straight vertical sides. In general, the surface between the nano-towers is flat and resembles that of the $\text{Fe}_3\text{O}_4/\text{MgO}$ (100) films grown on the 5 mm x 5 mm substrates, however the 17.5 nm and 52.5 nm films grown at 400 °C have a different surfaces. In these samples the

² All of the films (a - d) grown at 500 °C and the 105 nm film (d) grown at 300 °C were grown on 5 mm x 5 mm MgO (100) substrates.

surface appeared to comprise of numerous lower nano-towers that protrude slightly from the surface. This is illustrated in Figure 6.11.

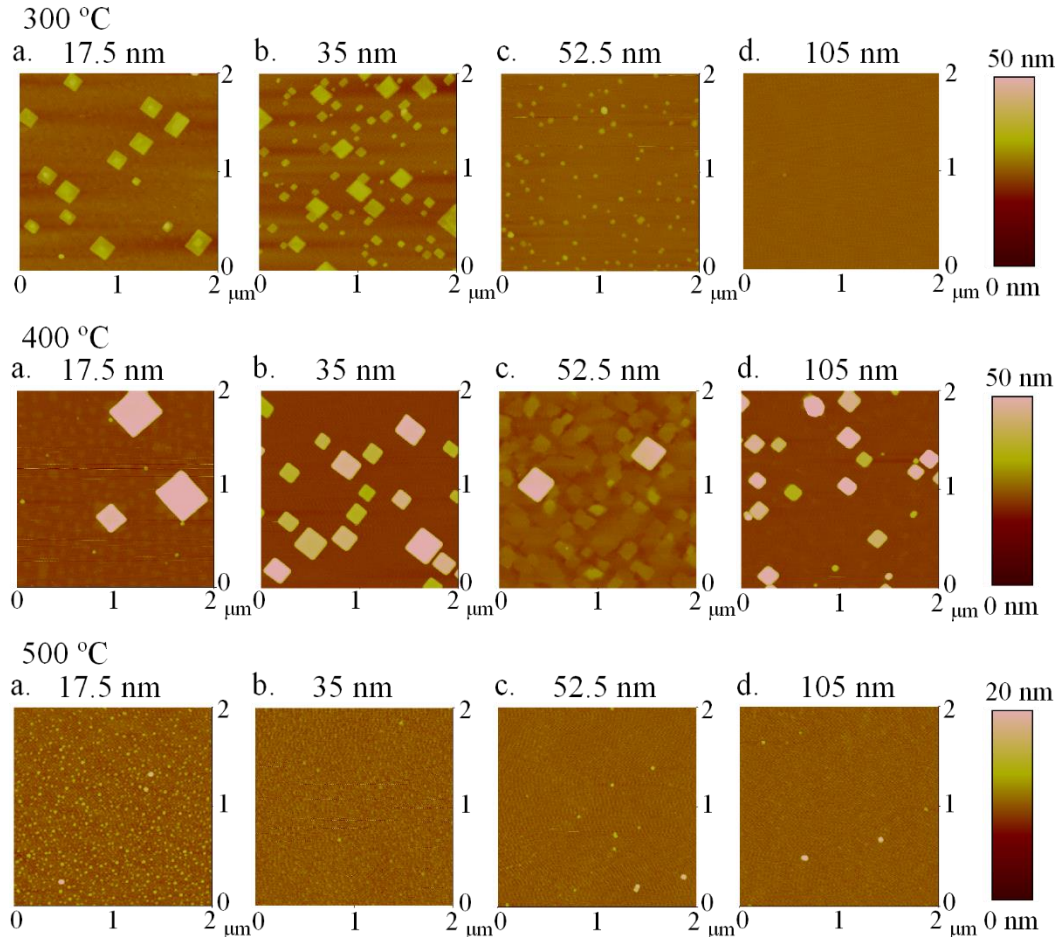


Figure 6.9. AFM images ($2 \mu\text{m} \times 2 \mu\text{m}$) from the second Fe₃O₄/MgO (100) thin film series grown at different growth temperatures with different film thicknesses. a) 17.5 nm, b) 35 nm, c) 52.5 nm & d) 105 nm.

ANALYSIS AND OPTIMISATION OF THE MORPHOLOGY AND MAGNETIC PROPERTIES OF Fe_3O_4/Si AND Fe_3O_4/MgO (100) THIN FILMS

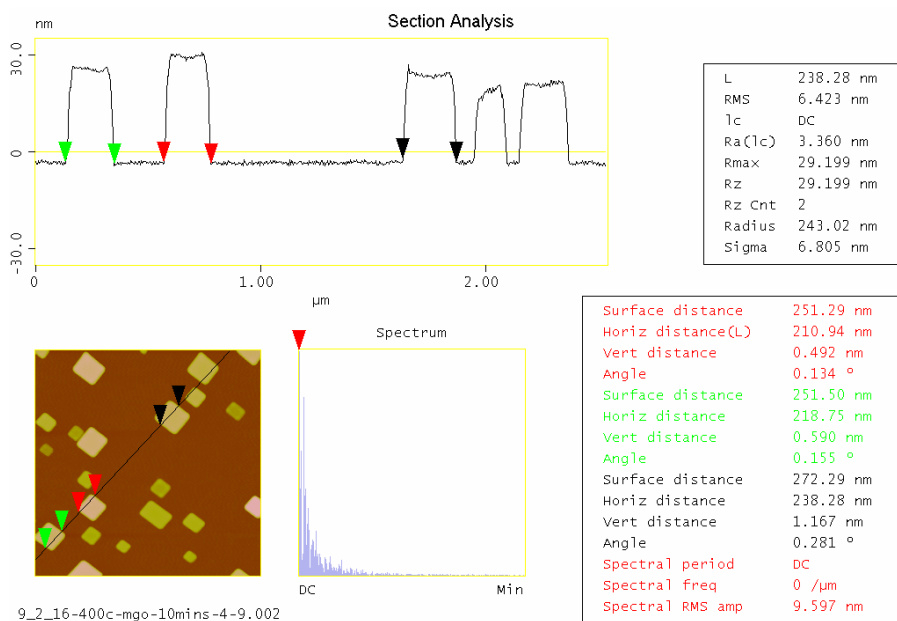


Figure 6.10. Section image from a 35 nm Fe_3O_4/MgO (100) film grown at 400 °C, illustrating the straight vertical sides to the nano-towers with a flat surface.

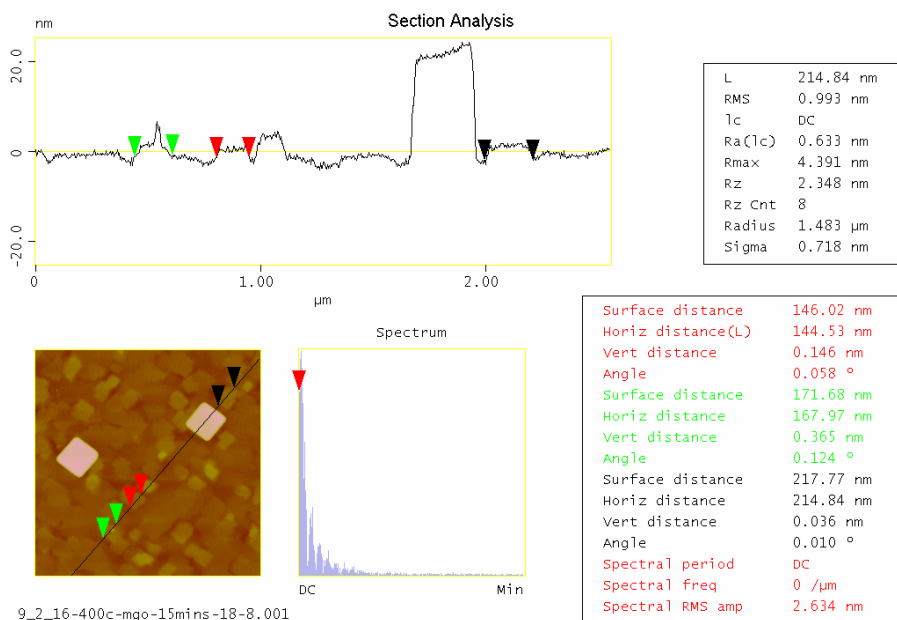


Figure 6.11. Section image from a 52.5 nm Fe_3O_4/MgO (100) film grown at 400 °C, illustrating the lower nano-tower surface.

To establish whether these nano-towers were an artefact of the AFM scanning (for example, from a dirty AFM tip), images were taken with two different scan angles. Figure 6.12 presents AFM images taken with scan angles of 0° and 45° from the 35 nm thick Fe₃O₄/MgO (100) film grown at 400 °C. If the nano-towers were an artefact from the scanning then they would not be expected to rotate with the scan angle. However, as can be seen in Figure 6.12 they clearly did rotate which can be seen by considering the outlined nano-towers in both images: in the 45° image the nano-towers are aligned with the image edges, but they are aligned at a diagonal in the 0° image. This provides a strong indication that the nano-towers are a feature of the sample surface.

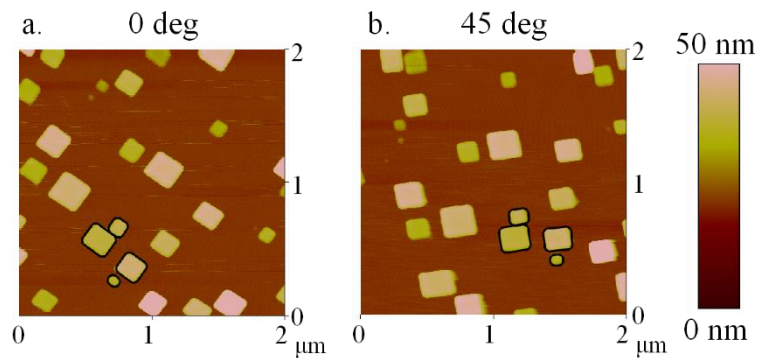


Figure 6.12. AFM images (2 μm x 2 μm) of the 35 nm Fe₃O₄/MgO (100) film surface taken with a 0° scan angle (a.) and a 45° scan angle (b.). The nano-islands outlined in black are a guide to the rotation.

Similar island features have been seen previously by Hartig et al. [4] for Ag thin films grown on Mo (100). After heat treatment to remove oxygen contamination from the Mo substrates, the surface was left with an undulating surface with seemingly flat (100) “plains”. Ag was then thermally evaporated onto the substrate surface, and from

UHV-SEM images it can be seen that flat-topped pyramids of Ag formed on the surface. These crystals are an example of the Stranski-Krastanov growth mode where island growth is favoured after an initial continuous layer was grown [5].

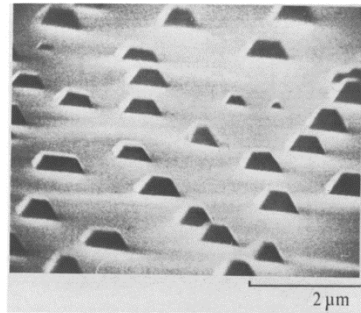


Figure 6.13. SEM image taken at an incidence of $\sim 10^\circ$ of Ag clusters grown on a Mo (100) substrate at 550 °C. 20 ML of Ag was deposited. Taken from [4].

In another study, Reisinger et al [6] grew TiN islands on Si (001) substrates by using pulsed laser deposition (Figure 6.14). In this case the island's formation were described using the Volmer-Weber growth mode which differs from the Stranski-Krastanov mode in that islands grow from the start, and are not preceded by the formation of a continuous layer. Another feature observed by Reisinger et al [6] was that these islands formed at a substrate temperature of 650 °C, whereas at a substrate temperature of 600 °C a smooth two-dimensional film was grown which illustrates that the surface morphology is dependent on growth temperature.

Purely from the AFM images, it is difficult to sure which of these two growth modes, Stranski-Krastanov or Volmer-Weber, produced the nano-towers seen in Figure 6.9.

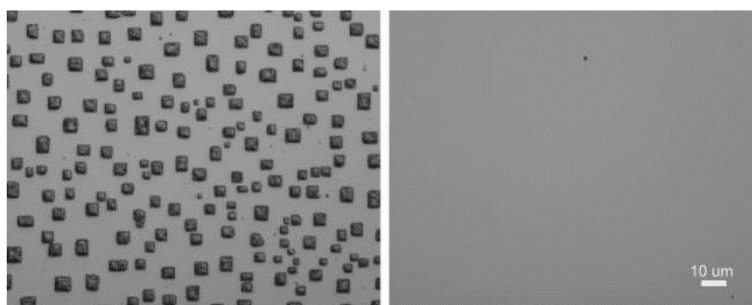


Figure 6.14. Optical micrographs of the surface of TiN films grown on Si (001) by pulsed laser deposition. The left film was grown at a substrate temperature of 650 °C and displays island growth, whereas the right film was grown at a substrate temperature of 600 °C and has a two-dimensional growth. (Taken from [6]).

To investigate whether the presence of nano-towers is substrate size specific, 35 nm Fe₃O₄ thin films were grown at 400 °C on a 5 mm x 5 mm and a 10 mm x 10 mm MgO (100) substrate simultaneously. This was repeated to produce four Fe₃O₄/MgO (100) films in total, using the same growth procedure as the second film series.

These films were then imaged using AFM and a comparison to the 35 nm Fe₃O₄/MgO (100) film with the nano-towers present and grown on the 10 mm x 10 mm substrate from the second film series is made in Figure 6.15. The first thing to note from the AFM images is that the substrate size does not appear to have an effect on the surface morphology of the thin films. For both growth runs the surface morphology presented in Figure 6.15 is very similar for the different substrate sizes, however the surface morphology is very different for each growth run. There are three different surface morphologies in Figure 6.15, with the initial film from the second film series having the nano-towers present and two separate morphologies without nano-towers. A variation on the first surface morphology has been seen previously in Figure 6.9 where

the film consisted of nano-towers with what appears to be a flattened tower background. The films imaged in Figure 6.15 have the flattened tower background but no nano-towers. The second surface morphology resembles that of the $\text{Fe}_3\text{O}_4/\text{MgO}$ (100) films in Figure 6.7 and the films grown on the 5 mm x 5 mm MgO (100) substrates in Figure 6.9. These show a smooth surface with no presence of nano-towers, normal or flattened.

These results show that the size of the MgO substrate did not cause the nano-towers to grow but that the surface morphology of the films is highly dependent on variations during the film growth.

ANALYSIS AND OPTIMISATION OF THE MORPHOLOGY AND MAGNETIC PROPERTIES OF
Fe₃O₄/Si AND Fe₃O₄/MgO (100) THIN FILMS

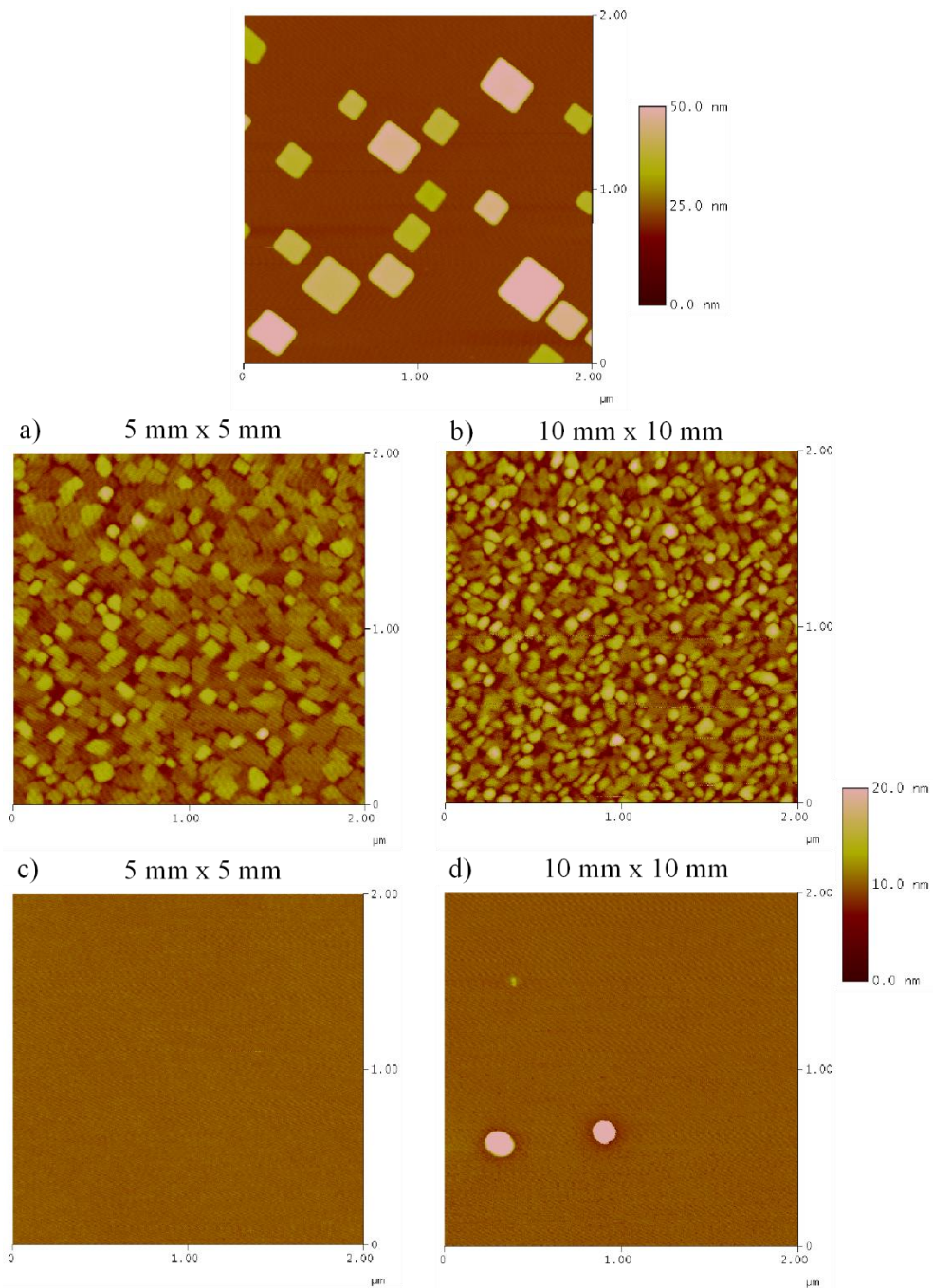


Figure 6.15. AFM images from 35 nm Fe₃O₄/MgO (100) thin films grown at 400 °C, with the original film from Figure 6.9 shown at the top for comparison. Films a) & c) were grown on 5 x 5 mm MgO (100) substrates and films b) & d) were grown on 10 x 10 mm MgO (100) substrates. Films a) & b) were grown together and films c) & d) were grown together.

AFM analysis of $\text{Fe}_3\text{O}_4/\text{Si}$ and $\text{Fe}_3\text{O}_4/\text{MgO}$ thin films has shown that the surface morphology is highly dependent on variations during the film growth and the substrate used. The films on Si substrates produced clear grains and grain boundaries, whereas the films on MgO substrates produced a variety of different morphologies including smooth films with a roughness < 1 nm, to films with oriented 3D islands protruding from the surface. A positive correlation was found between the grain size of the films grown on Si substrates and both the growth temperature and film thickness.

6.5. Analysis of magnetic properties of $\text{Fe}_3\text{O}_4/\text{Si}$ and $\text{Fe}_3\text{O}_4/\text{MgO}$ thin films

To investigate the effect of film thickness and substrate choice on the magnetic properties of the Fe_3O_4 thin films, magnetisation loops were measured using a MOKE magnetometer. From these normalised hysteresis loops the coercivity was measured and plotted against the film thickness in Figure 6.19 for both film series. Furthermore, multiple films of the same thickness were measured for the same growth temperature of 500 °C in order to establish whether or not the growth process was repeatable. This was motivated by the variability seen in the surface morphology.

To establish whether the Fe_3O_4 thin films grown on MgO (100) substrates had an in-plane magnetic anisotropy, magnetisation loops at varying field angles along the sample surface were measured. The coercivity values from these measurements on a 105 nm thick film are presented in Figure 6.16 for the varying magnetic field angles. It can be seen that there is little variation in coercivity with magnetic field angle illustrating an isotropic nature for the Fe_3O_4 films grown on MgO (100) substrates.

The Fe_3O_4 films grown on Si substrates were previously shown to be isotropic in Section 5.3.2. The magnetically isotropic nature of the Fe_3O_4 thin films grown in this project is to be expected as the rotating sample holder prevents the magnetron field from inducing a magnetic anisotropy in the film.

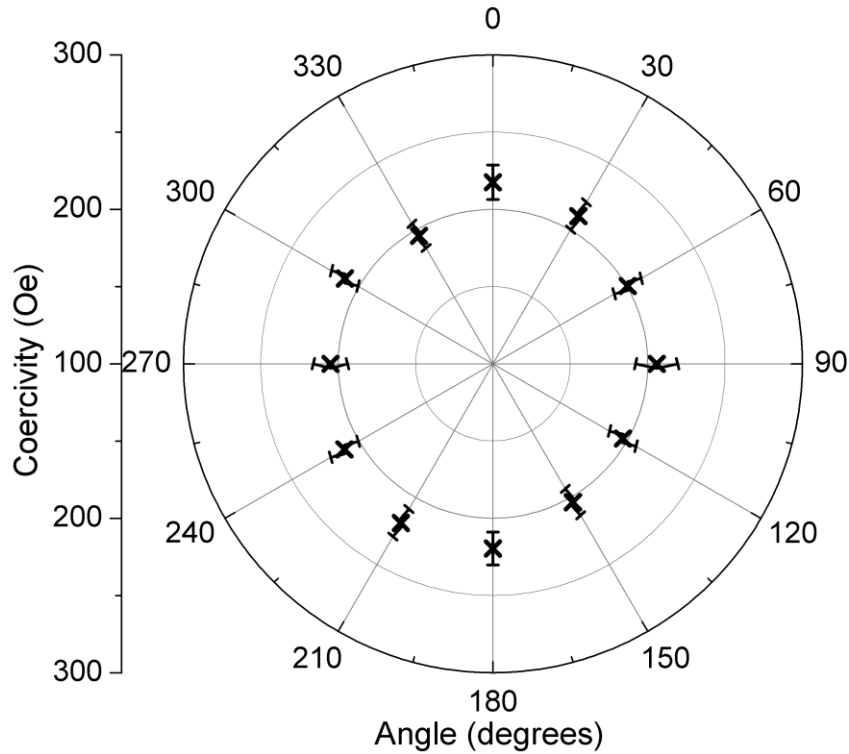


Figure 6.16. Coercivity values from 105 nm Fe_3O_4 thin films grown on MgO (100) substrates for varying field angle, where 0° is along a sample edge.

Figure 6.17 shows a comparison of the normalised MOKE hysteresis loops between the two different film series for both substrates with a film thickness of 35 nm. This film thickness was chosen for comparison as the AFM analysis for the films grown on MgO substrates produced a variety of different morphologies. All of these

morphologies (smooth surface, holes & nano-towers) are present for the 35 nm films across all of the growth temperatures (Table 6.1).

Growth temperature (°C)	Morphology	
	1 st film series	2 nd film series
300	Smooth	Nano-towers
400	Holes	Nano-towers
500	Smooth	Smooth

Table 6.1. A guide to the different surface morphologies of the 35 nm $\text{Fe}_3\text{O}_4/\text{MgO}$ thin films.

A clear feature of the normalised hysteresis loops in Figure 6.17 is that there is little difference between the two film series. Also, it can be seen that none of the films are saturated in the 3.5 kOe in-plane magnetic field which is to be expected for Fe_3O_4 thin films [7].

The biggest difference in the hysteresis loop shapes for Figure 6.17 is seen for the 300 °C Si and 400 °C MgO films. The difference in the 300 °C Si film hysteresis loops originates from the 1st series loop being off-centre along the y-axis, which is likely to be an artefact from a misalignment of the MOKE setup. However, the difference in the hysteresis loops for the 400 °C MgO films illustrates that the second series film is harder to reach saturation³ than the first series. A possible reason behind this loop variation could originate from the difference in surface morphology between the two

³ This term is used loosely as none of the Fe_3O_4 thin films in this project reach magnetic saturation with the in-plane magnetic field of 3.5 kOe.

ANALYSIS AND OPTIMISATION OF THE MORPHOLOGY AND MAGNETIC PROPERTIES OF
Fe₃O₄/Si AND Fe₃O₄/MgO (100) THIN FILMS

films: the first series film has a smooth surface whereas the second series film has a nano-tower surface.

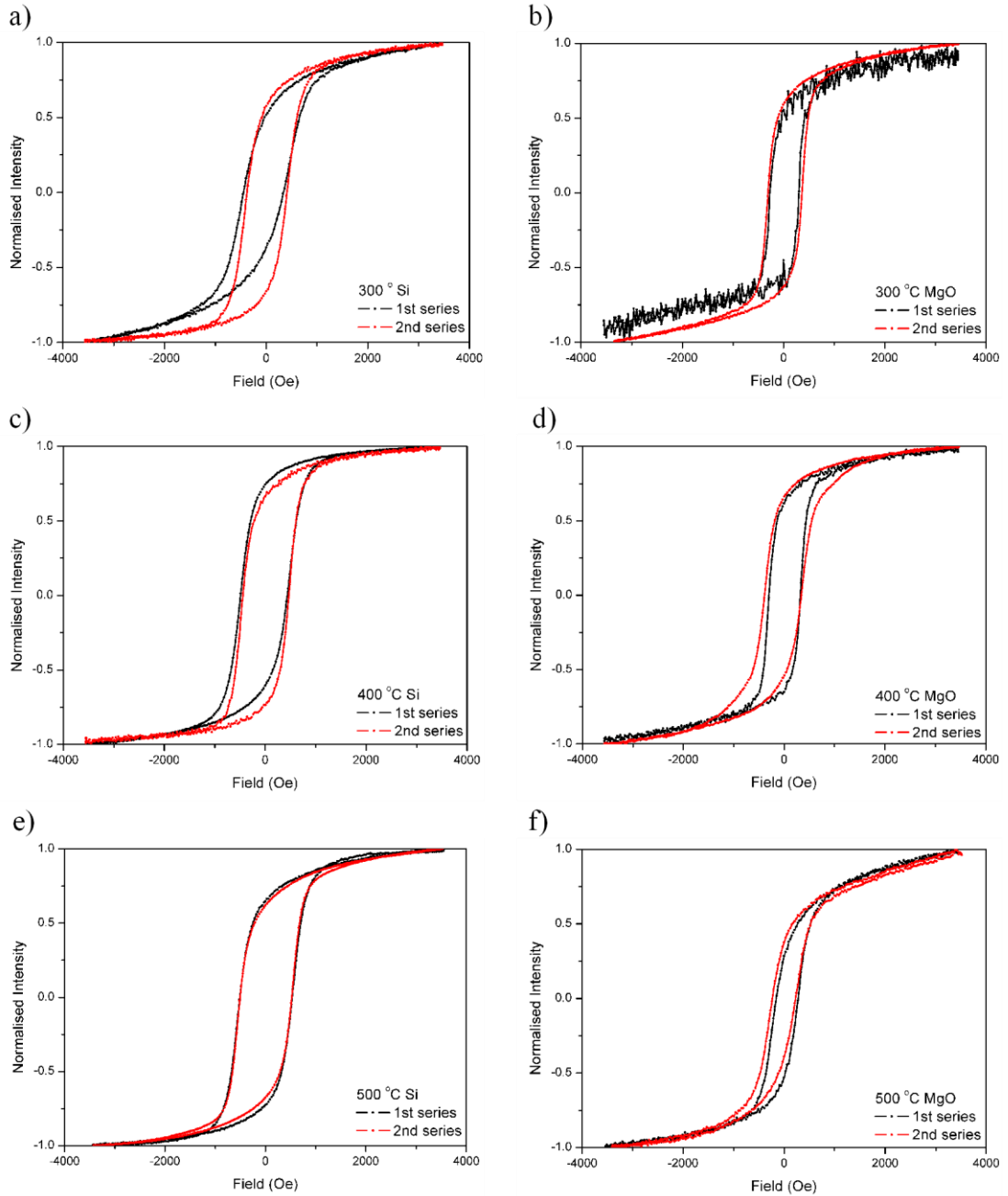


Figure 6.17. Normalised MOKE hysteresis loops for 35 nm Fe₃O₄ thin films on Si and MgO substrates and growth temperatures of 300 °C, 400 °C and 500 °C, comparing both film series.

Magnetic hysteresis loops were measured for the 35 nm $\text{Fe}_3\text{O}_4/\text{MgO}$ films grown at 400 °C used to investigate the repeatability of the nano-tower surface (where three separate surface morphologies were measured). The normalised magnetisation loops for these films are presented alongside the coercivity values measured from these hysteresis loops in Figure 6.18. The magnetisation loops for the 35 nm $\text{Fe}_3\text{O}_4/\text{MgO}$ films grown at 400 °C from both film series are presented as a comparison in Figure 6.18a where the surface morphology of the first series film is smooth and the second series film has nano-towers. The magnetisation loops in Figure 6.18b correspond to the AFM images in Figure 6.15b & c with a flattened nano-tower surface, and the magnetisation loops in Figure 6.18c correspond to the AFM images in Figure 6.15d & e with a smooth surface.

An interesting feature of the coercivity values is that all of the films grown for this investigation into the effect of surface morphology produce very similar coercivity values that are within error of each other. These coercivity values are, however, smaller than that measured from the film with nano-towers present by ~ 50 Oe.

From these measurements and analysis, it is clear that the presence of nano-towers on the $\text{Fe}_3\text{O}_4/\text{MgO}$ film surface produces a higher coercivity value than the other surface morphologies observed. These other surface morphologies (smooth, holes and flattened nano-tower) produce coercivity values that are very similar and are within error of each other.

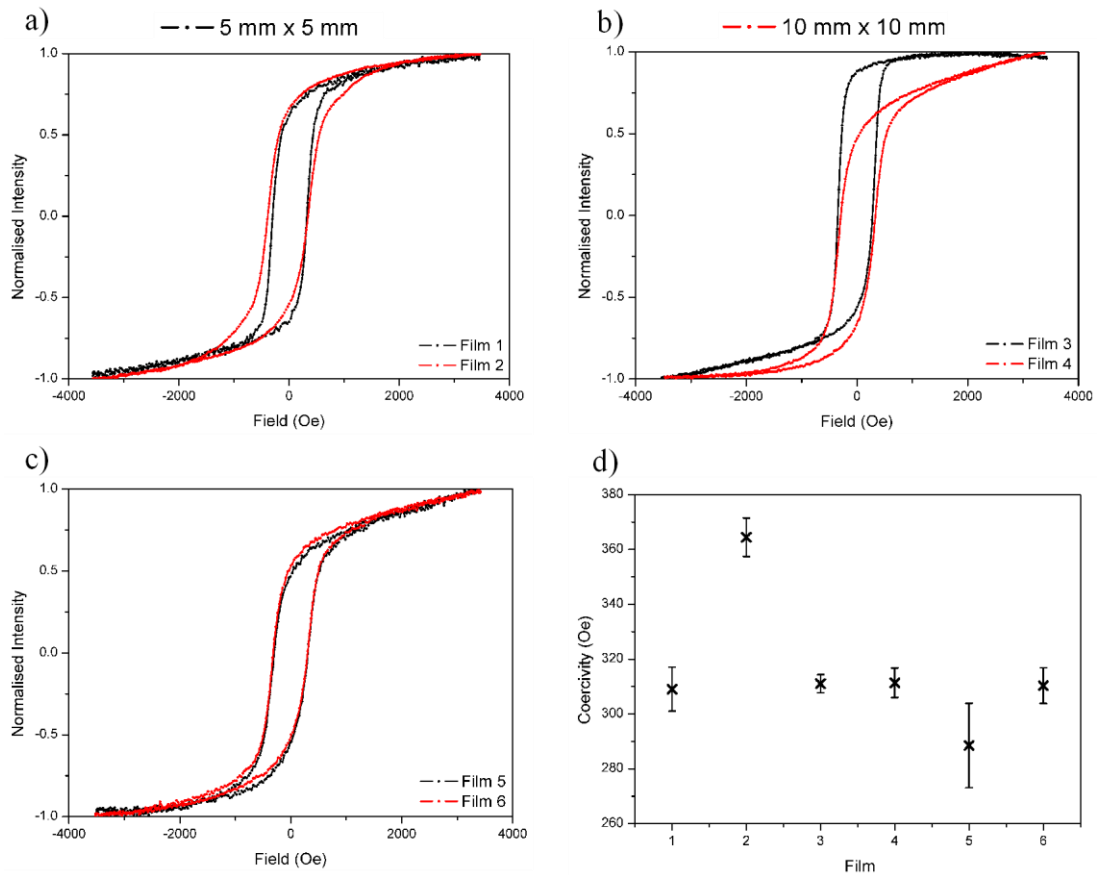


Figure 6.18. Normalised magnetisation loops for 35 nm $\text{Fe}_3\text{O}_4/\text{MgO}$ films grown at 400 °C on 5 mm x 5 mm (black) & 10 mm x 10 mm (red) substrates. a) Film 1: first series film (smooth surface), Film 2: second series film (nano-tower surface). b) Film 3 & 4: grown simultaneously with a flattened nano-tower surface. c) Film 5 & 6: grown simultaneously with a smooth surface. d) A comparison of the coercivity values measured for these films.

To investigate whether there is a dependence on growth temperature and the film thickness on the coercivity, the coercivity values for the two film series were measured from normalised hysteresis loops. The similarity between the two film series can be seen in the coercivity values presented against the film thickness for the different

growth temperatures and substrates in Figure 6.19. In this figure, the same coercivity data scale was used for each growth temperature to allow an easier comparison between the two film series. The error bars on the coercivity values are from a single film, with the multiple films grown at 500°C for each thickness plotted along with the mean coercivity value for these films plotted as \blacktriangle . The dashed lines are for a visual guide, and also connect the mean coercivity values of the films grown at 500°C .

The coercivity values for the films grown at 500°C have values ranging over 100 Oe for some film thicknesses, which is in contrast to the multiple films grown at 400°C to investigate the repeatability of the nano-tower morphology. For all of those films, the coercivity values produced were within error of each other apart from the film with the nano-tower morphology. A possible cause for this variation in coercivity value could originate from the thermal contact of the substrate to the substrate holder. Although great care was taken to have the substrates lie flat on the substrate holder, the clamping mechanism combined with a slight curvature to the copper substrate holder caused variation between different film growths.

A decrease in coercivity of ~ 100 Oe was observed for Fe_3O_4 films grown on MgO (100) substrates compared to Fe_3O_4 films on a Si substrate. This was to be expected due to the work by Chen et al [1] which showed that a smaller coercivity can be achieved when using a substrate with a smaller lattice mismatch to the film.

The coercivity value of the $\text{Fe}_3\text{O}_4/\text{MgO}$ films are roughly in the 200 – 300 Oe region for all growth temperatures and film thicknesses, across both film series. A general trend can be seen for most of the graphs in Figure 6.19 where the coercivity decreases with increasing film thickness. However, there is no apparent trend between the growth temperature and coercivity.

ANALYSIS AND OPTIMISATION OF THE MORPHOLOGY AND MAGNETIC PROPERTIES OF $\text{Fe}_3\text{O}_4/\text{Si}$ AND $\text{Fe}_3\text{O}_4/\text{MgO}$ (100) THIN FILMS

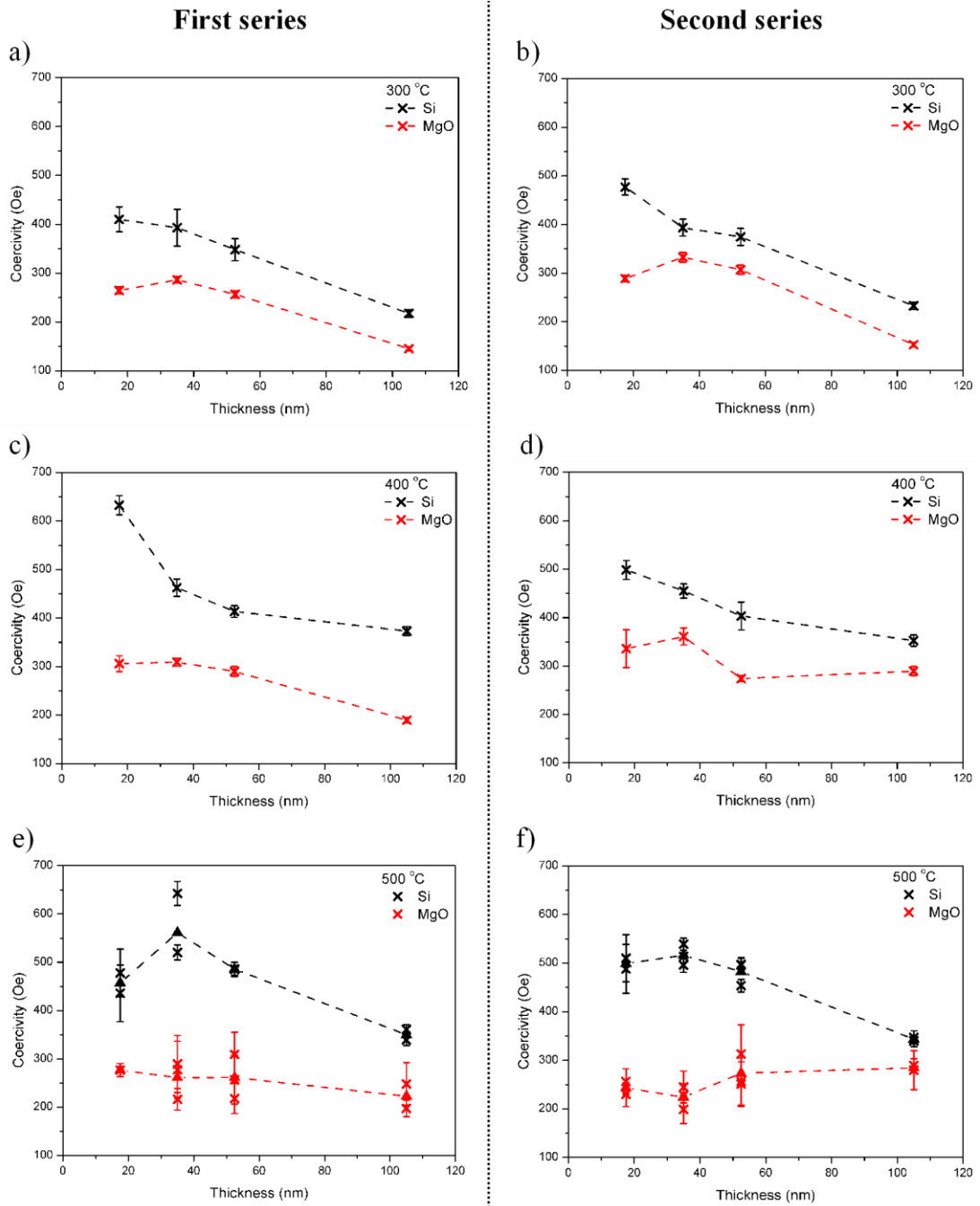


Figure 6.19. Coercivity values versus film thickness for $\text{Fe}_3\text{O}_4/\text{Si}$ (black) and $\text{Fe}_3\text{O}_4/\text{MgO}$ (100) (red) films grown at different temperatures for both film series. \blacktriangle : mean coercivity value for the films grown at 500 °C. The lines are visual guides.

A possible explanation behind the decrease in coercivity with increasing film thickness could be associated with the increasing grain size for increasing film thickness seen by AFM surface morphology analysis (Section 6.4). An increase in coercivity is to be expected with a decrease in grain size towards the multi-domain to single-domain transition [8, 9]. To establish whether there is a relationship between the average grain size of Fe_3O_4 films grown on Si substrates and their coercivity value, the coercivity was plotted against the corresponding grain size in Figure 6.20 for both film series. It is clear to see that there is no trend correlating the coercivity value with the average grain size for either film series. There is also no evidence of grain size dependence for the films grown on MgO substrates, however a similar trend for a decrease in coercivity with increasing film thickness is seen for these films. Another theory for the increase in coercivity with decreasing film thickness is that the APB density increases with decreasing film thickness and that APBs act as pinning sites [10]. Although it is unlikely that the Fe_3O_4 thin films grown here do not contain APBs as it has been shown to be part of Fe_3O_4 thin film growth [7, 11-15], this can only remain a possible theory for these films as there is no conclusive evidence for or against the presence of APBs.

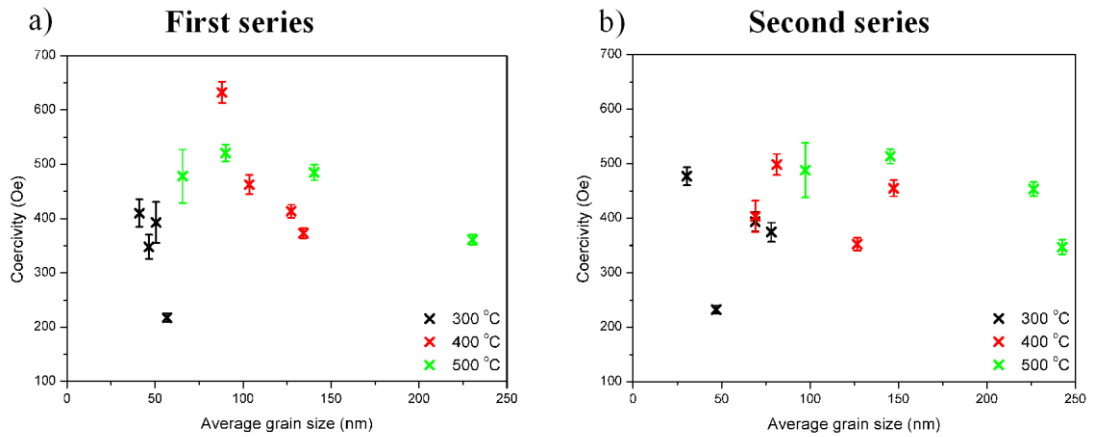


Figure 6.20. Coercivity values plotted against the average grain size for both film series.

Fe_3O_4 thin films grown on MgO (100) substrates have been shown to be magnetically isotropic, as well as producing smaller coercivity values than corresponding films grown on Si substrates. The origin for this lower coercivity is due to the smaller lattice mismatch between Fe_3O_4 and MgO . It has been shown that there is no variation in coercivity of $\text{Fe}_3\text{O}_4/\text{MgO}$ thin films for the different surface morphologies observed, apart from a slightly elevated coercivity value for the nano-tower surface. However, a spread of over 100 Oe between coercivity values for films grown at the same temperature and film thickness on the same substrate have been measured. This is possibly caused due to variations in thermal contact between the substrate and copper plate during the film growth. The coercivity of $\text{Fe}_3\text{O}_4/\text{Si}$ & $\text{Fe}_3\text{O}_4/\text{MgO}$ thin films has also been shown to decrease with an increase in film thickness caused by the decrease in APB density with increasing film thickness.

6.6. Investigation into the magnetic switching mechanism for $\text{Fe}_3\text{O}_4/\text{Si}_3\text{N}_4$

One of the aims of this project was to make planar Fe_3O_4 nanostructures and to image domain walls in these structures. Before nanostructures are made from these Fe_3O_4 thin films, it is beneficial to investigate and understand how the magnetisation is reversed so as to aid the investigation into the magnetic structure of the nanostructures.

To investigate the magnetisation reversal mechanism in these reactively sputtered Fe_3O_4 thin films, M-TXM measurements were performed on a Fe_3O_4 thin film grown on an x-ray transparent Si_3N_4 membrane. These measurements were taken at beamline 6.1.2 at the Advanced Light Source (ALS) synchrotron at the Lawrence Berkeley National Laboratory by Dr Tom Hayward, Mr Jonathan Wood and Mr Tom Broomhall. The film analysed in this section had a film thickness of 105 nm and was grown at 500 °C using the growth method described in Section 6.2.

As there was a large variation in surface morphologies observed in this project, especially between the two different substrates, it was important to know what the surface morphology of the $\text{Fe}_3\text{O}_4/\text{Si}_3\text{N}_4$ film looked like. An AFM image of the surface of the film is shown in Figure 6.21. Although the surface does not feature a smooth surface like the $\text{Fe}_3\text{O}_4/\text{MgO}$ films or distinct grains like the $\text{Fe}_3\text{O}_4/\text{Si}$ films, similarities to both can be seen. The surface features a number of holes which have been seen before in Figure 6.7 on some of the $\text{Fe}_3\text{O}_4/\text{MgO}$ films. The RMS surface roughness value of 8.1 nm and granular structure of the film is more comparable to the films grown on Si substrates to those on MgO substrates.

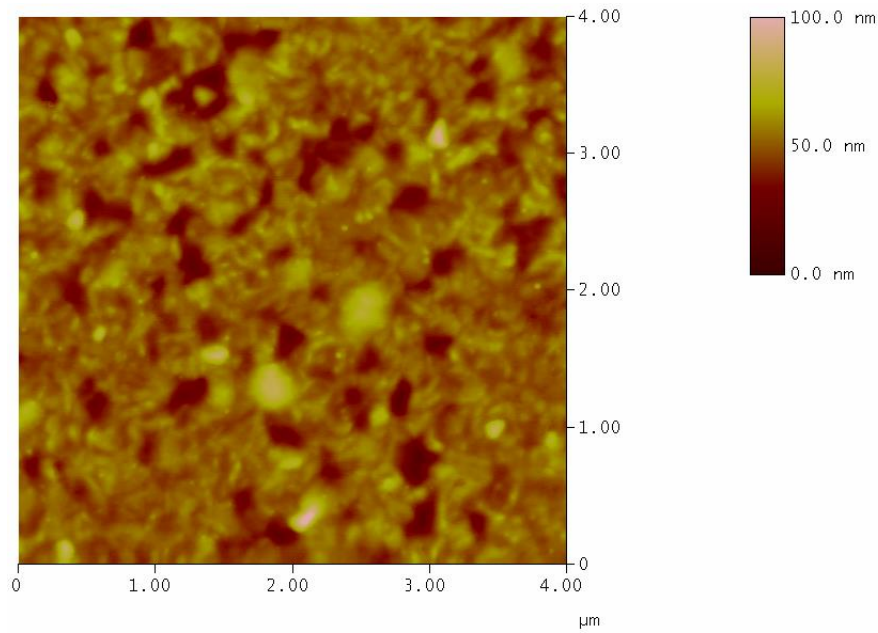


Figure 6.21. AFM image of Fe₃O₄/Si₃N₄ membrane film.

To aid the analysis of the M-TXM results a magnetisation loop (Figure 6.22) was measured from the Fe₃O₄/Si₃N₄ film using a MOKE magnetometer, from which a coercivity value of 338 ± 24 Oe was measured. This value is within error of the coercivity value measured for the Fe₃O₄/Si film (343 ± 17 Oe) of the same thickness from Section 6.5 and close to the coercivity value for the Fe₃O₄/MgO film (284 ± 35 Oe). This, along with the surface morphology, indicates that the film grown on Si₃N₄ will have a comparable switching mechanism to the films grown on Si substrates.

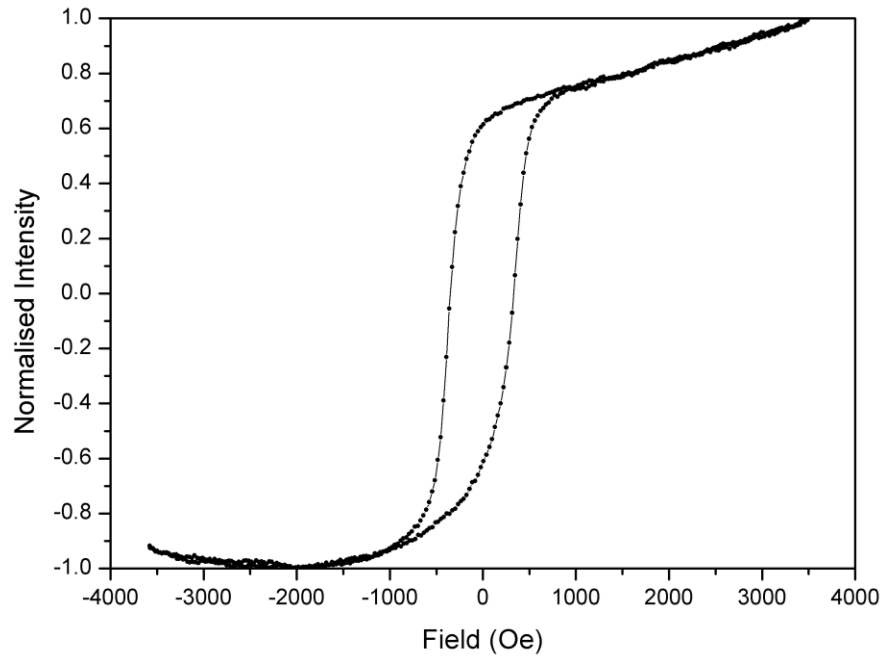


Figure 6.22. Normalised hysteresis loop from $\text{Fe}_3\text{O}_4/\text{SiN}$ membrane film.

To investigate the switching mechanism of the $\text{Fe}_3\text{O}_4/\text{Si}_3\text{N}_4$ film, a series of images were taken using M-TXM where the magnetic contrast in the image is formed due to the difference in absorption of circularly polarised x-rays for +x and -x local magnetisation directions.

To enhance the magnetic contrast in the images taken, each image was divided by a reference image. This reference image was taken after an in-plane magnetic field of +1000 Oe was applied and then removed, leaving the film in a remnant state. A series of images were then taken at increasing negative applied magnetic fields to provide a macroscale view of the magnetisation reversal process in the thin film. The negative magnetic fields applied were: -100 Oe, -200 Oe, -300 Oe, -400 Oe, -500 Oe, -600 Oe, -800 Oe and -1000 Oe. Figure 6.23 shows the M-TXM difference images taken of the $\text{Fe}_3\text{O}_4/\text{Si}_3\text{N}_4$ thin film for the negative magnetic fields applied.

ANALYSIS AND OPTIMISATION OF THE MORPHOLOGY AND MAGNETIC PROPERTIES OF
Fe₃O₄/Si AND Fe₃O₄/MGO (100) THIN FILMS

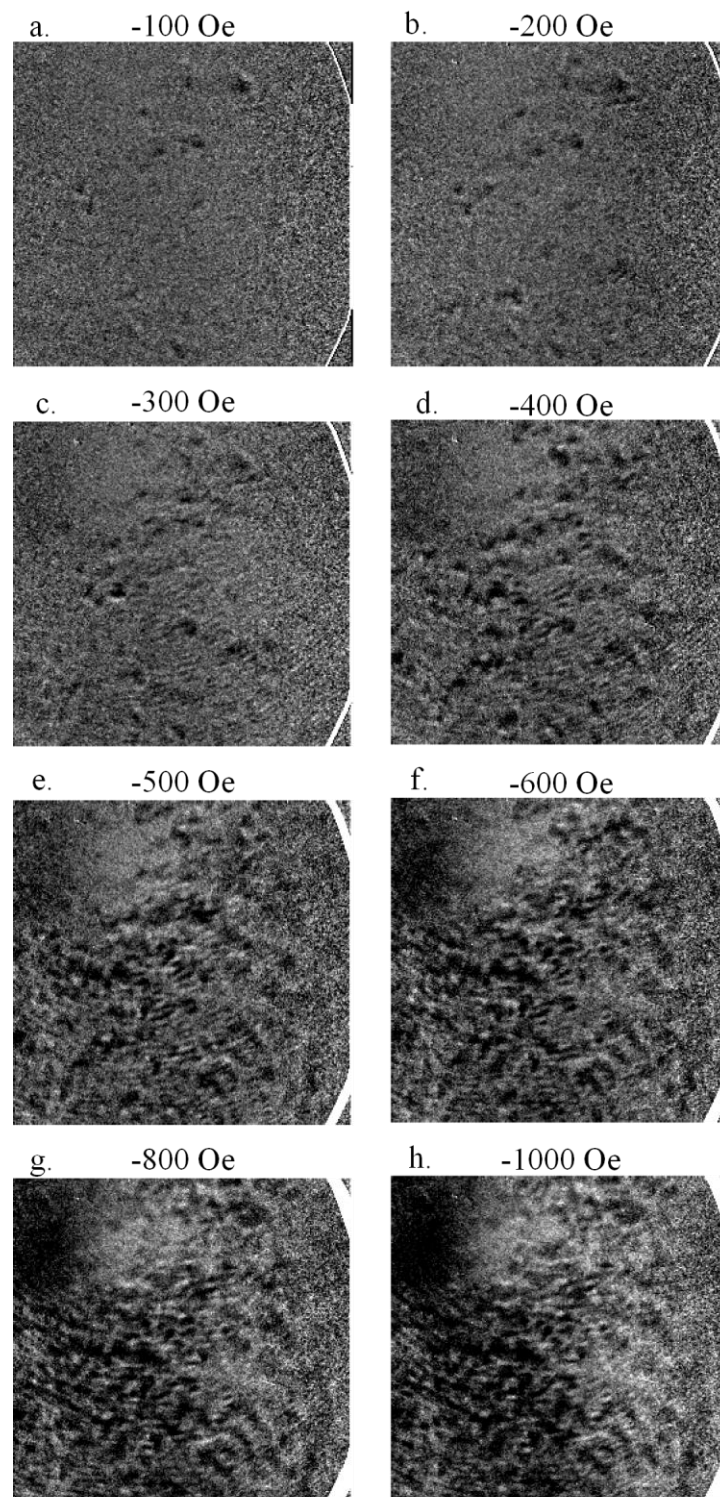


Figure 6.23. M-TXM difference image series from Fe₃O₄/Si₃N₄ membrane where the reference image was taken at 0 Oe after a +1000 Oe in-plane field is applied.

The images in Figure 6.23 are difference images, and therefore the contrast (dark regions) that is seen originates from a change in the magnetisation direction in the negative magnetic field images compared to the positive magnetic field reference image. As the magnetic field was increased, the amount of contrast in the images can be seen to increase which is to be expected. After -100 Oe was applied (Figure 6.23a) the difference image shows little contrast, and when compared to the magnetisation loop in Figure 6.22 it can be seen that the film is close to the remnant state at -100 Oe. However, it is just above -100 Oe when the magnetisation starts to drop off towards the coercive point (338 Oe) which can be seen in the M-TXM images as a greater increase in the contrast regions between Figure 6.23c & d. The significant amount of contrast in the final image in Figure 6.23 indicates that most of the film is magnetised in the opposite direction to the initial +1000 Oe applied magnetic field.

After comparing the AFM image (Figure 6.21) and the M-TXM images it can be seen that these images show that the switching mechanism in the $\text{Fe}_3\text{O}_4/\text{Si}_3\text{N}_4$ thin film is not likely to be via domain wall motion but by what appears to be individual grain switching. This is where the grains are not strongly exchange coupled, and thus domain wall motion from grain to grain doesn't seem to occur. Thus each grain exhibits a field induced reversal that does not generally correlate with those of its neighbours.

Due to the similarities between the $\text{Fe}_3\text{O}_4/\text{Si}_3\text{N}_4$ and $\text{Fe}_3\text{O}_4/\text{Si}$ films in this project the switching mechanism in these films is likely to be via individual grain switching.

6.7. Resistivity measurements

A custom built 4 collinear probe rig was used to measure the resistivity of the Fe₃O₄ thin films to establish how they compared to the resistivity of Permalloy. The same technique was used for the Fe thin films in Section 5.2.3, with an applied current of 10 μ A being applied across the outer two probes and the voltage being measured across the inner two probes. The error values for the resistivity measurements are calculated from combined equipment and measurements errors.

The resistivity values are presented against the film thickness in Figure 6.24, with values of ρ generally in the range $1 - 10 \times 10^{-3} \Omega \text{ cm}$. This is a factor of 10 larger than the resistivity of the Fe thin films in Section 5.2.3 and a factor of 100 larger than Permalloy thin films of similar thicknesses [16, 17]. These larger resistivity values will increase the domain wall atom trap lifetime due to the decrease in Johnson noise for higher resistivity materials.

The measured values of resistivity in Figure 6.24 are comparable to those reported in Table 3.1 and the films grown on MgO show a similar trend with decreasing resistivity with increasing film thickness, although two films vary from this (105 nm 300 °C & 35 nm 400 °C). This trend was attributed by Eerenstein [10] to be caused by a decrease in APB density with increased film thickness. There also appears to be no systematic difference in resistivity for the different growth temperatures used or different substrate sizes.

In contrast to the Fe₃O₄/MgO films, the resistivity of the Fe₃O₄/Si films appears to increase with film thickness. As the film thickness increases so does the grain size,

ANALYSIS AND OPTIMISATION OF THE MORPHOLOGY AND MAGNETIC PROPERTIES OF
Fe₃O₄/Si AND Fe₃O₄/MgO (100) THIN FILMS

which decreases the grain boundary density. This would cause a decrease in resistivity, however the opposite is observed. A possible cause for the increase in resistivity could be from the larger, boulder like grains having a different packing than those that are smoother. This could influence the conduction paths through the material.

ANALYSIS AND OPTIMISATION OF THE MORPHOLOGY AND MAGNETIC PROPERTIES OF
Fe₃O₄/Si AND Fe₃O₄/MgO (100) THIN FILMS

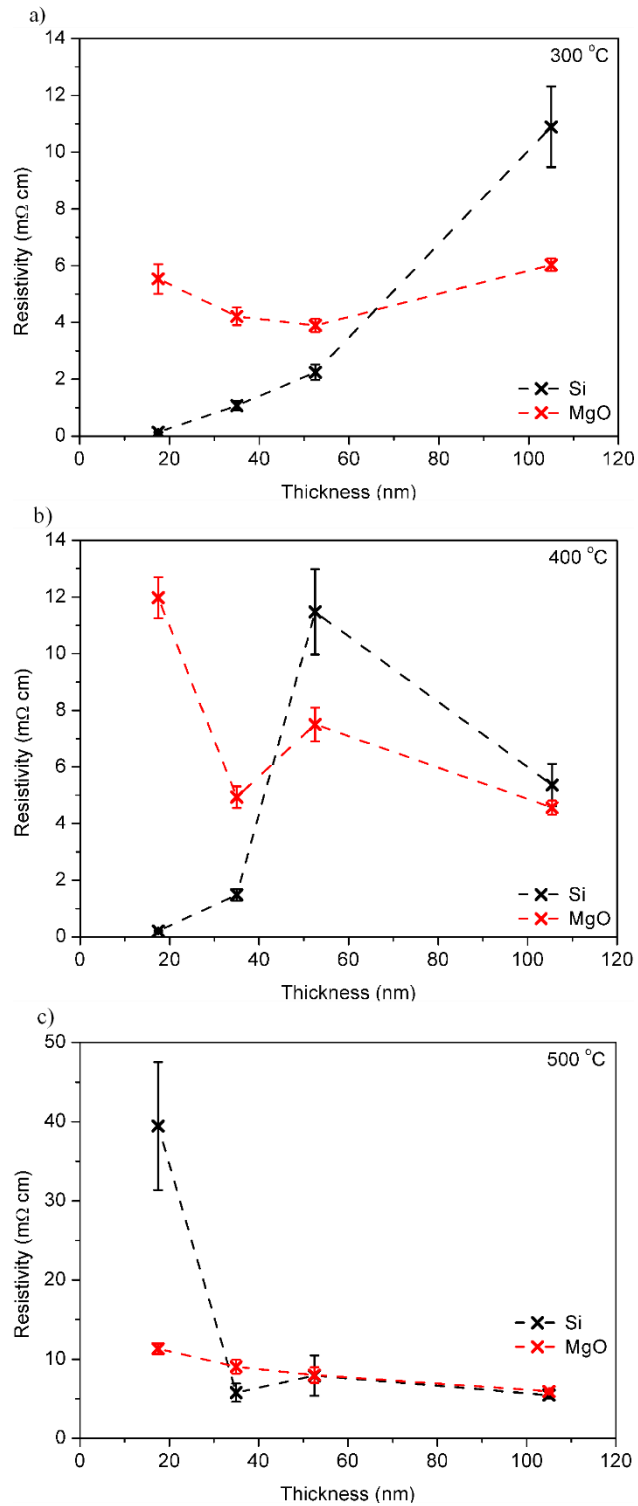


Figure 6.24. Resistivity vs film thickness for Fe₃O₄/Si and Fe₃O₄/MgO (100) films grown at different growth temperatures.

6.8. Conclusion

In this chapter, the effect of film thickness, growth temperature and substrate choice on the magnetic, electrical and morphological properties of Fe_3O_4 thin films was investigated.

The two substrates chosen were Si, which was previously used for the iron oxide phase investigation in Section 147, and MgO (100) which is frequently used for studies of Fe_3O_4 thin films [7, 12, 18] as it has a fcc oxygen lattice similar to the Fe_3O_4 oxygen lattice and its unit cell is approximately half the size of the Fe_3O_4 unit cell. The $\text{Fe}_3\text{O}_4/\text{Si}$ thin films were previously shown to be polycrystalline, and the $\text{Fe}_3\text{O}_4/\text{MgO}$ (100) thin films grown here were shown to be textured using a combination of locked-coupled and glancing-angle XRD.

The surface morphology of the Fe_3O_4 film on the two substrates (Si & MgO) are very different from each other. The Si substrate films are granular with clear grain boundaries, with the grain size and surface roughness both increasing with growth temperature and film thickness. The MgO substrate films produce a variety of surface morphologies, from smooth films with no visible grains (from the AFM images taken) and a RMS surface roughness of < 2 nm to films with oriented square towers protruding up to 70 nm from a smooth surface (Stranski-Krastanov or Volmer-Weber growth mode). It was shown that the surface morphology of these films was highly sensitive to variations during the film growth.

The $\text{Fe}_3\text{O}_4/\text{MgO}$ films display an isotropic magnetic behaviour with applied in-plane magnetic fields, and also show a decreased coercivity value with a drop of ~ 100 Oe compared to the same thickness $\text{Fe}_3\text{O}_4/\text{Si}$ film. Repeatable coercivity values were

found for Fe₃O₄/MgO films grown at 400 °C even with different surface morphologies, although a larger coercivity was found for the nano-tower surface. However, variations in coercivity for films of the same thickness have been measured for some films grown at 500 °C on both Si and MgO substrates. A possible cause of variations during the film growths was from variations in the thermal contact of the substrate to the substrate holder. Variation in the substrate temperature was shown in the previous chapter to produce different iron oxide phases, although this was over a large temperature range. It has also been shown by Sala et al. [3] that small variations in the substrate temperature greatly alter the surface morphology of the thin film. This difference in thermal contact is a possible origin for the coercivity variation observed for films of the same thickness.

The magnetic reversal mechanism for these reactively sputtered Fe₃O₄ thin films was investigated using M-TXM on a Fe₃O₄/Si₃N₄ thin film. The images taken using M-TXM illustrate that the reversal mechanism for this film was via individual grain switching, and from AFM and MOKE analysis, it was found that this film closely resembled a Fe₃O₄/Si film.

From all the results analysed in this chapter, the substrate choice that is most likely to produce domain walls in nanostructures made from the thin films are Fe₃O₄ thin films grown on MgO (100). This is due to the reduced coercivity values compared to Fe₃O₄/Si for the same film thickness, and the smooth thin films grown on MgO substrates compared to the granular films on the Si substrates.

References

- [1] Y. Z. Chen, J. R. Sun, Y. N. Han, X. Y. Xie, J. Shen, C. B. Rong, *et al.*, "Microstructure and magnetic properties of strained Fe₃O₄ films," *Journal of Applied Physics*, vol. 103, pp. 07D703-07D705, 2008.
- [2] A. Bollero, M. Ziese, R. Hohne, H. C. Semmelhack, U. Kohler, A. Setzer, *et al.*, "Influence of thickness on microstructural and magnetic properties in Fe₃O₄ thin films produced by PLD," *Journal of Magnetism and Magnetic Materials*, vol. 285, pp. 279-289, 2005.
- [3] A. Sala, H. Marchetto, Z.-H. Qin, S. Shaikhutdinov, T. Schmidt, and H.-J. Freund, "Defects and inhomogeneities in Fe₃O₄ (111) thin film growth on Pt (111)," *Physical Review B*, vol. 86, pp. 155430-155439, 2012.
- [4] K. Hartig, A. P. Janssen, and J. A. Venables, "Nucleation and growth in the system Ag/Mo (100): A comparison of UHV-SEM and AES/LEED observations," *Surface Science*, vol. 74, pp. 69-78, 1978.
- [5] J. A. Venables, G. D. T. Spiller, and M. Hanbucken, "Nucleation and growth of thin films," *Reports of Progress in Physics*, vol. 47, pp. 399-459, 1984.
- [6] D. Reisinger, M. Schonecke, T. Brenninger, M. Opel, A. Erb, L. Alff, *et al.*, "Epitaxy of Fe₃O₄ on Si (001) by pulsed laser deposition using a TiN/MgO buffer layer," *Journal of Applied Physics*, vol. 94, pp. 1857-1863, 2003.
- [7] D. T. Margulies, F. T. Parker, F. E. Spada, R. S. Goldman, J. Li, R. Sinclair, *et al.*, "Anomalous moment and anisotropy behaviour in Fe₃O₄ films," *Physical Review B*, vol. 53, pp. 9175-9187, 1996.
- [8] B. D. Cullity and C. D. Graham, *Introduction to Magnetic Materials*, 2nd ed.: IEEE Press, 2009.

- [9] N. A. Spaldin, *Magnetic Materials: Fundamentals and Applications*, 2nd ed.: Cambridge University Press, 2011.
- [10] W. Eerenstein, T. T. M. Palstra, T. Hibma, and S. Celotto, "Origin of the increased resistivity in epitaxial Fe₃O₄ films," *Physical Review B*, vol. 66, pp. 201101-201104, 2002.
- [11] W. Eerenstein, T. T. M. Palstra, S. S. Saxena, and T. Hibma, "Spin-polarised transport across sharp antiferromagnetic boundaries," *Physical Review Letters*, vol. 88, pp. 247204-247207, 2002.
- [12] S. Celotto, W. Eerenstein, and T. Hibma, "Characterization of anti-phase boundaries in epitaxial magnetite films," *The European Physical Journal B*, vol. 36, pp. 271-279, 2003.
- [13] D. T. Margulies, F. T. Parker, and A. E. Berkowitz, "Magnetic anomalies in single crystal Fe₃O₄ thin films," *Journal of Applied Physics*, vol. 75, pp. 6097-6099, 1994.
- [14] D. T. Margulies, F. T. Parker, M. L. Rudee, F. E. Spada, J. N. Chapman, P. R. Aitchison, *et al.*, "Origin of the anomalous magnetic behaviour in single crystal Fe₃O₄ films," *Physical Review Letters*, vol. 79, pp. 5162-5165, 1997.
- [15] T. Hibma, F. C. Voogt, L. Nielsen, P. A. A. v. d. Heijden, W. J. M. d. Jonge, J. J. T. M. Donkers, *et al.*, "Anti-phase domains and magnetism in epitaxial magnetite layers," *Journal of Applied Physics*, vol. 85, pp. 5291-5293, 1999.
- [16] A. F. Mayadas, J. F. Janak, and A. Gangulee, "Resistivity of Permalloy thin films," *Journal of Applied Physics*, vol. 45, pp. 2780-2781, 1974.
- [17] A. Schuhl, F. N. V. Dau, and J. R. Childress, "Low-field magnetic sensors based on the planar Hall effect," *Applied Physics Letters*, vol. 66, pp. 2751-2753, 1995.

- [18] S. M. Thompson, V. K. Lazarov, R. C. Bradley, T. Deakin, B. Kaeswurm, G. E. Sterbinsky, *et al.*, "Using the infrared magnetorefractive effect to compare the magnetoresistance in (100) and (111) oriented Fe₃O₄ films," *Journal of Applied Physics*, vol. 107, pp. 09B102-09B104, 2010.

7. Coercivity modification of Fe_3O_4 thin films using annealing treatment

In Chapter 6 it was found that the coercivity values measured for Fe_3O_4 thin films grown on MgO (100) substrates are lower than those grown on Si substrates. The best candidate thin film for the domain wall atom trapping application was determined to be Fe_3O_4 films grown on MgO substrates due to the lower coercivity values. Although these films were the best candidate, the coercivity was still very large ($\sim 200 - 300$ Oe) and therefore steps were taken to investigate reducing the coercivity.

Previous studies of Fe_3O_4 films by Zhou et al. [1] and Wei et al. [2] have shown that annealing epitaxial $\text{Fe}_3\text{O}_4/\text{MgO}$ (100) thin films for 160 minutes at 250°C in air produces a dramatic change in the films magnetic properties. It was shown that only after annealing for 4 minutes there was a large drop in coercivity from 200 Oe to 120 Oe, along with a substantial change in saturation magnetisation (in a 1 T field) from ~ 390 emu/cm³ to ~ 440 emu/cm³. After the initial change in the films magnetic properties after 4 minutes of annealing, there were no other variations observed apart from a slight decrease in the saturation magnetisation. Analysis of the Raman spectroscopy results pre- and post-annealing shows that no other iron oxide phase other than Fe_3O_4 were present in the films. A more in depth review of this work can be found in Chapter 3 (Literature Review). With the aim of reducing the coercivity value of sputtered Fe_3O_4 thin films, the films in this study were annealed using the same procedure reported by Zhou et al. [1].

In this chapter, Fe₃O₄ thin films grown on Si and MgO (100) substrates were annealed for 4 minutes at 250 °C in air. These films were analysed using XRD, XPS and Raman spectroscopy to determine any compositional changes post annealing. To establish whether the coercivity reduction was successful, magnetisation loops were measured from the films prior to and post annealing. Also, the surface morphology was imaged using AFM to investigate whether the annealing produced any change in the films' surface.

7.1.Oxidation methodology

To perform oxidation of the Fe₃O₄ films two different furnaces were utilised: a Lenton LTF 14/75/610 tube furnace & an Elite BCF 11/8 box furnace. The furnace used will be stated for each sample.

The furnaces were heated to 250 °C ± 10 °C and a ceramic boat with a half-cylinder shape was used as a sample holder. The ceramic boat was placed in the furnace to reach 250 °C prior to the sample annealing treatment. The sample(s) were then placed in the ceramic boat and annealed in the furnace for 4 minutes. The annealing temperature and time were chosen for this study after it was shown that this combination produced the desired drop in coercivity for epitaxial Fe₃O₄/MgO films [1, 2]. Once removed from the furnace, the ceramic boat and samples were left to cool in air before the samples were removed. A consequence of this is that the films remained at an elevated temperature in air for longer than the set 4 minutes, however all of the films were cooled to RT in under 2 minutes.

7.2. Initial oxidation

To establish whether this technique would produce a drop in coercivity for the polycrystalline Fe₃O₄ thin films grown in this research, a Fe₃O₄/Si and a Fe₃O₄/MgO film (both 50 nm) from Chapter 6 were annealed using the methodology described above. The composition of these films were analysed using XRD, XPS and Raman spectroscopy, both prior and post annealing. Magnetisation loops were measured using MOKE and surface morphology images were taken using AFM. The Lenton tube furnace was used for these samples.

7.2.1. Compositional analysis

A combination of compositional analysis techniques were used to analyse the films prior to and post annealing. Glancing angle XRD, XPS and Raman spectroscopy were used as the combination of these techniques allowed the phases present at both surface and in the bulk of the films to be characterised. Each of these techniques has a limitation on identifying the composition of iron oxides; Fe₃O₄ and γ -Fe₂O₃ have similar crystal structures and so their XRD spectra are difficult to distinguish one from the other, determining α -Fe₂O₃ from γ -Fe₂O₃ in XPS spectra is complex as they have almost identical peak positions and requires expert peak fitting, and the Raman spectra from a Si substrate produces a large quantity of peaks that obscure the iron oxide peaks in the range used. By using multiple techniques allowed for the limitations of each to be overcome and provide a clear understanding of the films composition post annealing.

7.2.1.1. Glancing angle x-ray diffraction

Glancing angle XRD measurements were taken at an incidence angle of 5° to the sample surface over the range $2\theta = 25 - 40^\circ$, with a step size of 0.05°. This range was chosen as it contains peaks for Fe, FeO, Fe₃O₄, γ -Fe₂O₃ and α -Fe₂O₃, allowing for detection of secondary iron oxide phases in the film post annealing. The spectra taken prior to annealing (black) and post annealing (red) of the Fe₃O₄/Si film are presented in Figure 7.1. XRD spectra was only taken for the Fe₃O₄ thin films on Si substrates as the x-ray diffractometer available at the time was not capable of distinguishing between the MgO & Fe₃O₄ peaks in locked coupled mode. Also, as it was shown in Figure 6.2, the Fe₃O₄/MgO thin films do not produce any peaks in the glancing angle mode as the films are textured.

The peak positions in Figure 7.1 illustrate that the film has a spinel structure both before and after annealing, with no other peaks appearing after annealing. However, the peak positions had a positive shift of $2\theta \approx 0.3^\circ$ in the annealed spectra compared to the non-annealed results. This shift could be a systematic error caused by a slight variation in sample height in the diffractometer (as discussed in Section 4.2.1) or could be caused by the presence of γ -Fe₂O₃ which has an iron-deficient spinel structure and a smaller lattice constant than Fe₃O₄ ($a_{\text{Fe}_3\text{O}_4} = 8.396 \text{ \AA}$, $a_{\gamma\text{-Fe}_2\text{O}_3} = 8.3474 \text{ \AA}$) [3]. The standard Bragg peak positions for Fe₃O₄ and γ -Fe₂O₃ are shown in Figure 7.1 which highlight that the γ -Fe₂O₃ peaks are at a marginally higher 2θ value than Fe₃O₄.

The XRD spectra taken post-annealing produces an inconclusive result as the variation observed could have been caused by experimental error or by the presence of γ -Fe₂O₃.

However, the XRD spectra from the annealed film does show a spinel structure similar to the pre-annealed film.

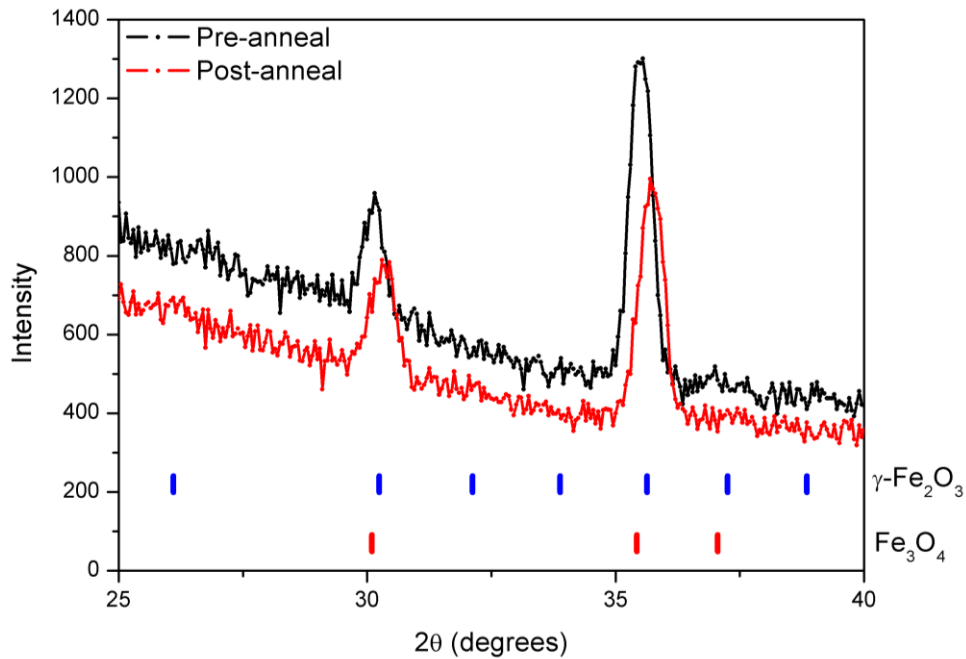


Figure 7.1. Glancing-angle XRD spectra of $\text{Fe}_3\text{O}_4/\text{Si}$ thin film taken prior to annealing treatment (black) and post annealing treatment (red) using a glancing angle of 5° . The standard Fe_3O_4 (red) and $\gamma\text{-Fe}_2\text{O}_3$ (blue) Bragg peak positions are presented under the spectra as a guide.

7.2.1.2. X-ray photoelectron spectroscopy

The $\text{Fe}_3\text{O}_4/\text{Si}$ and $\text{Fe}_3\text{O}_4/\text{MgO}$ thin films were analysed using XPS over the $\text{Fe}2p$ range (binding energy = 700 – 740 eV) with a step size of 0.1 eV. Figure 7.2 shows XPS measurements for the $\text{Fe}_3\text{O}_4/\text{Si}$ and $\text{Fe}_3\text{O}_4/\text{MgO}$ thin films both prior to and post annealing.

The spectra (Figure 7.2) have been normalised to the Fe 2p_{3/2} peak to aid comparison between the non-annealed (black) and annealed films (red). By visual comparison, the shake-up satellites became more prominent in the annealed films than non-annealed which indicates that there was a secondary iron oxide present in the films. Another notable feature which became diminished in size after annealing was the hump present on the lower binding energy side of the Fe 2p_{3/2} peak. This hump is characteristic of the presence of Fe²⁺ ions in Fe₃O₄ as the binding energy of the Fe²⁺ ions in Fe₃O₄ has been shown to be ~708 eV (Table 7.1, [4]), and the reduction in this suggests a decrease of Fe₃O₄ in the sample. This decrease could be caused by a conversion of Fe₃O₄ to γ -Fe₂O₃, as γ -Fe₂O₃ only contains Fe³⁺ ions.

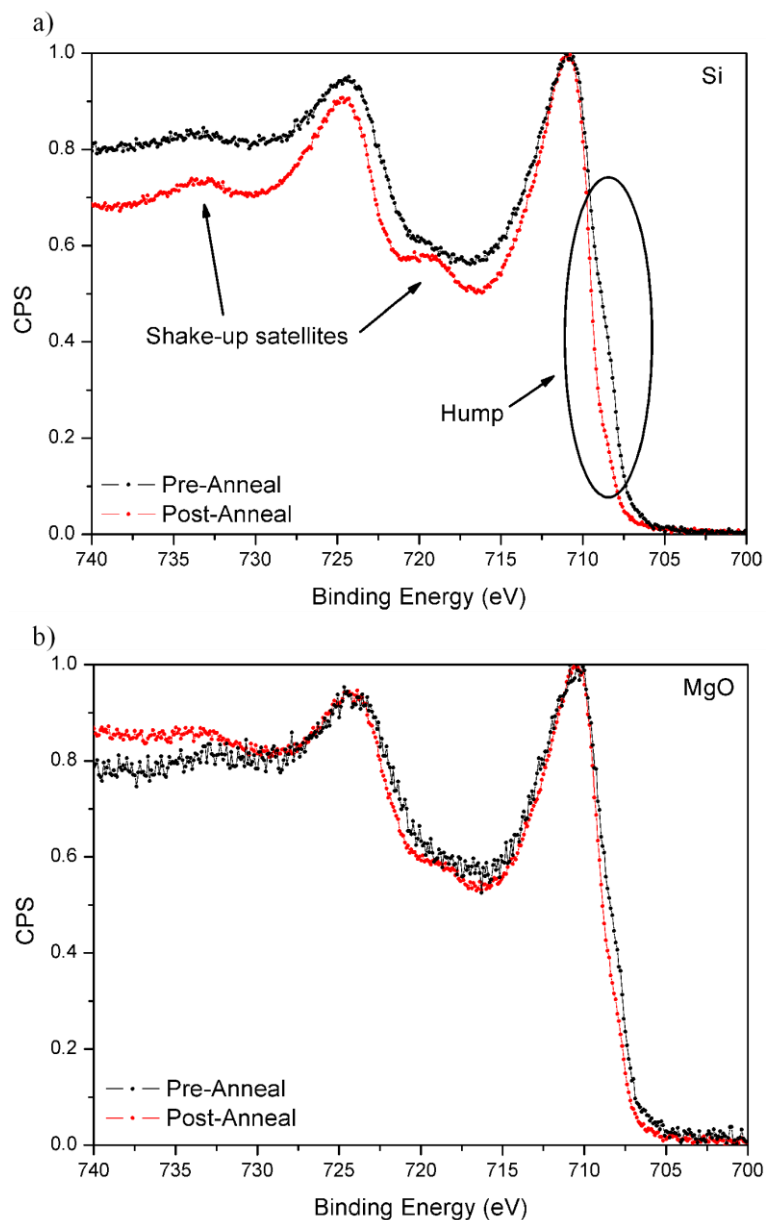


Figure 7.2. Normalised Fe 2p x-ray photoelectron spectra from $\text{Fe}_3\text{O}_4/\text{Si}$ and $\text{Fe}_3\text{O}_4/\text{MgO}$ (100), taken prior to annealing treatment (black) and post annealing treatment (red).

To extrapolate more information about the secondary iron oxide indicated by the XPS data, the Fe $2p_{3/2}$ peak was fitted with Gaussian-Lorentzian (30:70) peaks and a Shirley

background. Figure 7.3 presents the Fe 2p_{3/2} peak fitting to the Fe₃O₄/Si and Fe₃O₄/MgO films prior to and post annealing.

The pre-annealed Fe₃O₄ films (Figure 7.3a & b, Si & MgO) were fitted with a single peak at a binding energy of 710.6 with a FWHM of 3.89 eV (Fe₃O₄/Si) and 710.3 eV with a FWHM of 4.11 eV (Fe₃O₄/MgO). The peak fitting produces a residual standard deviation of 5.307 for the Fe₃O₄/Si spectra and 2.374 for the Fe₃O₄/MgO spectra. These peak positions match with the Fe 2p_{3/2} peak positions for Fe₃O₄ of 710.6 eV given in Table 7.1.

Iron Oxide	Fe 2p _{3/2} peak (eV)	
	[4]	[5]
Fe	706.9 ± 0.1	706.5 ± 0.2
FeO	709.5 ± 0.2	709.6 ± 0.2
Fe ₃ O ₄ (Fe ²⁺)	708.3 ± 0.15	710.8 ± 0.2
Fe ₃ O ₄ (Fe ³⁺)	710.6 ± 0.2	
α - & γ -Fe ₂ O ₃	711.0 ± 0.15	711.6 ± 0.2

Table 7.1. Binding energies of the Fe 2p_{3/2} peaks for Fe and its oxides. [4, 5]

For the annealed films (Figure 7.3c – f) the spectra were fitted twice, once with a single peak and also with two peaks. The initial fitting with a single peak did not fit closely to the experimental spectra, which is clearly observed in the annealed Si film (Figure 7.3c). This suggests that there is a secondary iron oxide which in combination with the Fe₃O₄ present produces a different peak shape to the non-annealed spectra. Introducing a secondary peak greatly improves the fit of the experimental data. The

binding energies and FWHM of the Si peaks are 710.33 eV [FWHM = 1.75 eV] & 711.37 eV [3.69 eV] and the MgO peaks are 709.94 eV [1.75 eV] & 710.59 eV [4.08 eV]. The residual standard deviation for the films on Si and MgO substrates was reduced when two peaks are fitted compared to the single peak. For the film on Si the residual standard deviation was 10.310 for the single peak fit and reduced down to 3.367 for the two peak fit. Similarly, the residual standard deviation for the film on MgO was reduced from 4.438 to 2.756. The peak positions for the annealed films match with the Fe 2p_{3/2} peak positions for Fe₃O₄ and α - & γ -Fe₂O₃.

With the XPS results suggesting the presence of a secondary iron oxide and the XRD results showing spinel structure, it seems likely that the annealed films are a mixture of Fe₃O₄ and γ -Fe₂O₃. However, XPS is a surface sensitive technique (~ 10 nm) and does not give any indication on how the iron oxide phases are distributed through the whole film.

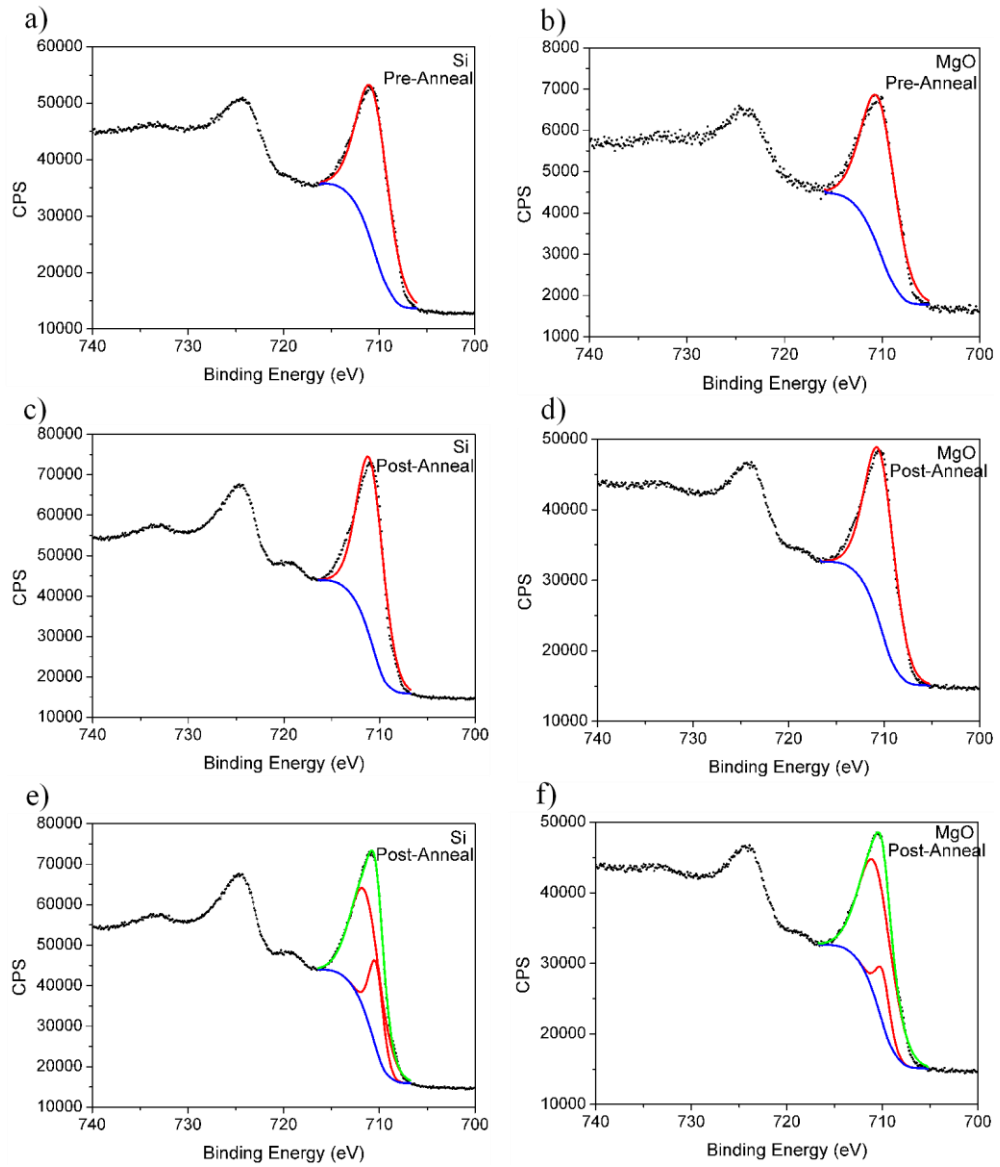


Figure 7.3. *Fe 2p x-ray photoelectron spectra from pre-annealed [a) & b)] and post-annealed [c) – f)] Fe_3O_4 thin films on Si [left] & MgO (100) [right] substrates. The $\text{Fe } 2p_{3/2}$ is fitted with a Shirley background (blue) and Gaussian-Lorentzian (30:70) peak(s) (red). The overall peak envelope is shown in green.*

7.2.1.3. Raman spectroscopy

As the XRD spectra was inconclusive as to whether the annealed film contained a secondary iron oxide and the XPS only probing the surface of the films, Raman spectroscopy was utilised to analyse the whole film thickness. Raman spectroscopy is also capable of distinguishing between the different Fe₂O₃ phases and Fe₃O₄.

To clarify that the secondary iron oxide is γ -Fe₂O₃, Raman spectra were taken over a range of 100 – 1000 cm⁻¹ using a $\lambda = 514.5$ nm laser (20 mW) before and after the annealing treatment. As with the XPS spectra, the Raman spectra were normalised to the Fe₃O₄ A_{1g} peak at 666 cm⁻¹. The normalised Raman spectra for both the pre- and post-annealed Fe₃O₄/Si and Fe₃O₄/MgO films are presented in Figure 7.4.

Additional peaks appear in the annealed films (red) that are not present in the non-annealed films in the normalised spectra in Figure 7.4. The only peaks present in the non-annealed films are from Fe₃O₄ (& Si), and in the annealed films there are additional peaks around 700, 450 and 350 cm⁻¹. The Raman shift peak positions for FeO, Fe₃O₄, γ -Fe₂O₃, α -Fe₂O₃, α -FeOOH and γ -FeOOH from various references [6-9] are displayed in Table 7.2, with the strongest peak for each oxide underlined. Fe is not included in this table as there are no Raman peaks in the experimental range measured. Goethite (α -FeOOH) and lepidocrocite (γ -FeOOH) are included in Table 7.2 to rule out the formation of iron oxyhydroxides during the annealing treatment. Comparing the additional Raman peaks in Figure 7.4 to the binding energy values in Table 7.2 indicates that the additional peaks are from γ -Fe₂O₃.

Iron Oxide		Raman Shift (cm ⁻¹)
FeO	Wüstite	<u>595</u>
Fe ₃ O ₄	Magnetite	193, 310, 554, <u>672</u>
γ-Fe ₂ O ₃	Maghemite	365, 511, <u>700</u>
α-Fe ₂ O ₃	Hematite	229, 249, <u>295</u> , 302, 414, 500, 615, 660
α-FeOOH	Goethite	241, 299, <u>387</u> , 480, 549
γ-FeOOH	Lepidocrocite	<u>248</u> , 301, 348, 528, 653

Table 7.2. Peak positions of Raman spectra from iron oxides, with the strongest peak underlined. [6-9]

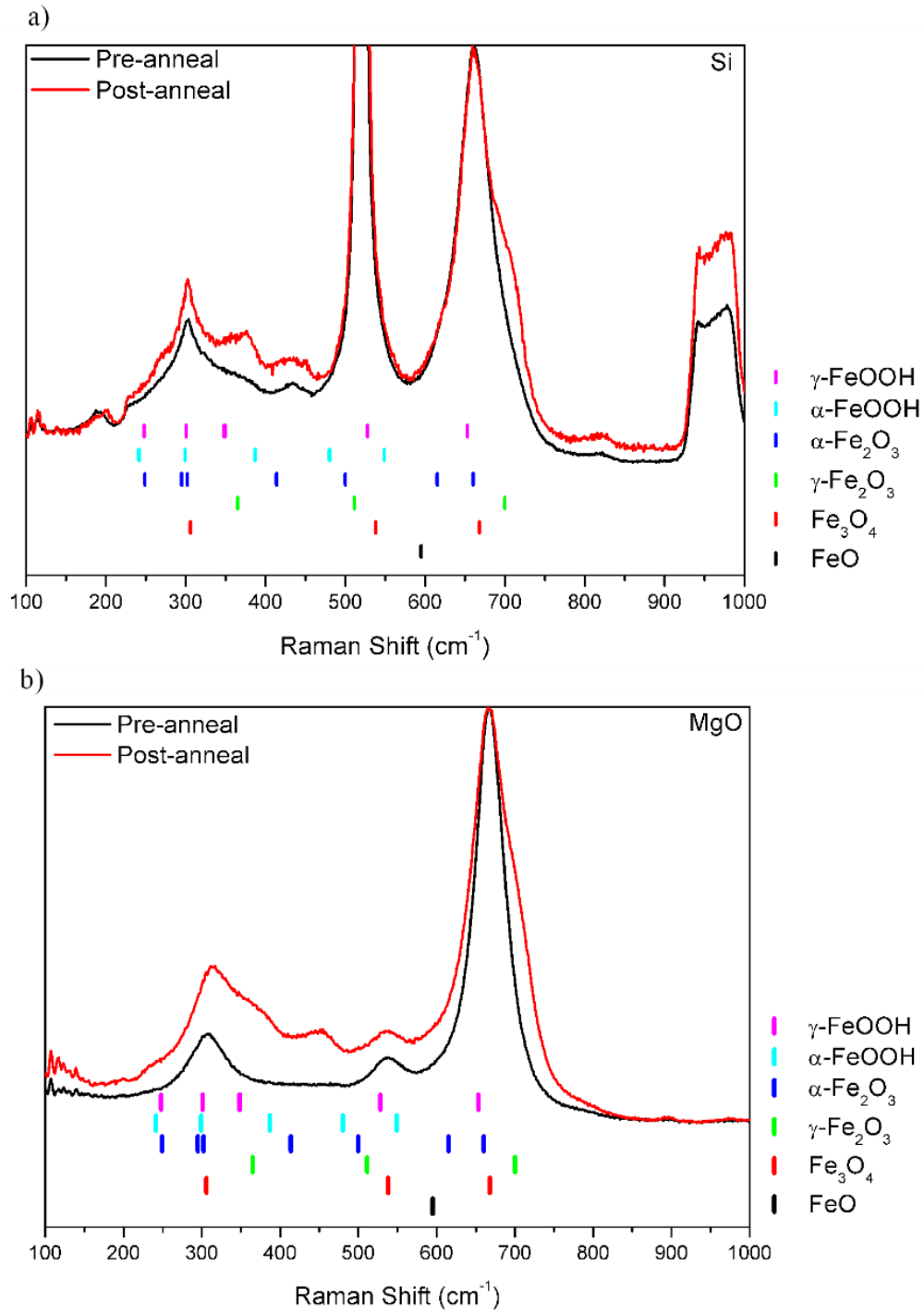


Figure 7.4. Raman spectra from $\text{Fe}_3\text{O}_4/\text{Si}$ and $\text{Fe}_3\text{O}_4/\text{MgO}$ (100) before (black) and after (red) annealing treatment using a $\lambda = 514.5$ nm laser. Peak positions for FeO (black), Fe_3O_4 (red), $\gamma\text{-Fe}_2\text{O}_3$ (green), $\alpha\text{-Fe}_2\text{O}_3$ (blue), $\alpha\text{-FeOOH}$ (cyan) and $\gamma\text{-FeOOH}$ (magenta) are shown as a guide [6-9].

From the combination of glancing angle XRD, XPS and Raman spectroscopy measurements, the annealed films were deduced to have a mixed iron oxide composition of Fe₃O₄ and γ -Fe₂O₃.

7.2.2. Surface morphology

The surface morphology of the films were imaged using AFM to establish whether the annealing treatment modified the grain size and surface roughness. Typical AFM images are presented in Figure 7.5 and from a visual comparison there is no difference after the Fe₃O₄/Si film have been annealed, however there is a slight difference for the Fe₃O₄/MgO film. In the annealed MgO film there are small grains across the surface, whereas in the pre-annealed image the film surface is smooth. The surface changes to the film on MgO are explored in detail later on. The RMS surface roughness of the annealed films (Si & MgO, respectively) are 16.0 ± 0.7 & 0.3 ± 0.3 nm which are comparable to the pre-annealing surface roughness values of 15.3 ± 0.5 & 1.1 ± 0.4 nm. The larger roughness value for the pre-annealed MgO film is due to a larger amount of debris on the film surface.

After annealing the Fe₃O₄/Si and Fe₃O₄/MgO thin films for 4 minutes, there was no major morphological changes seen.

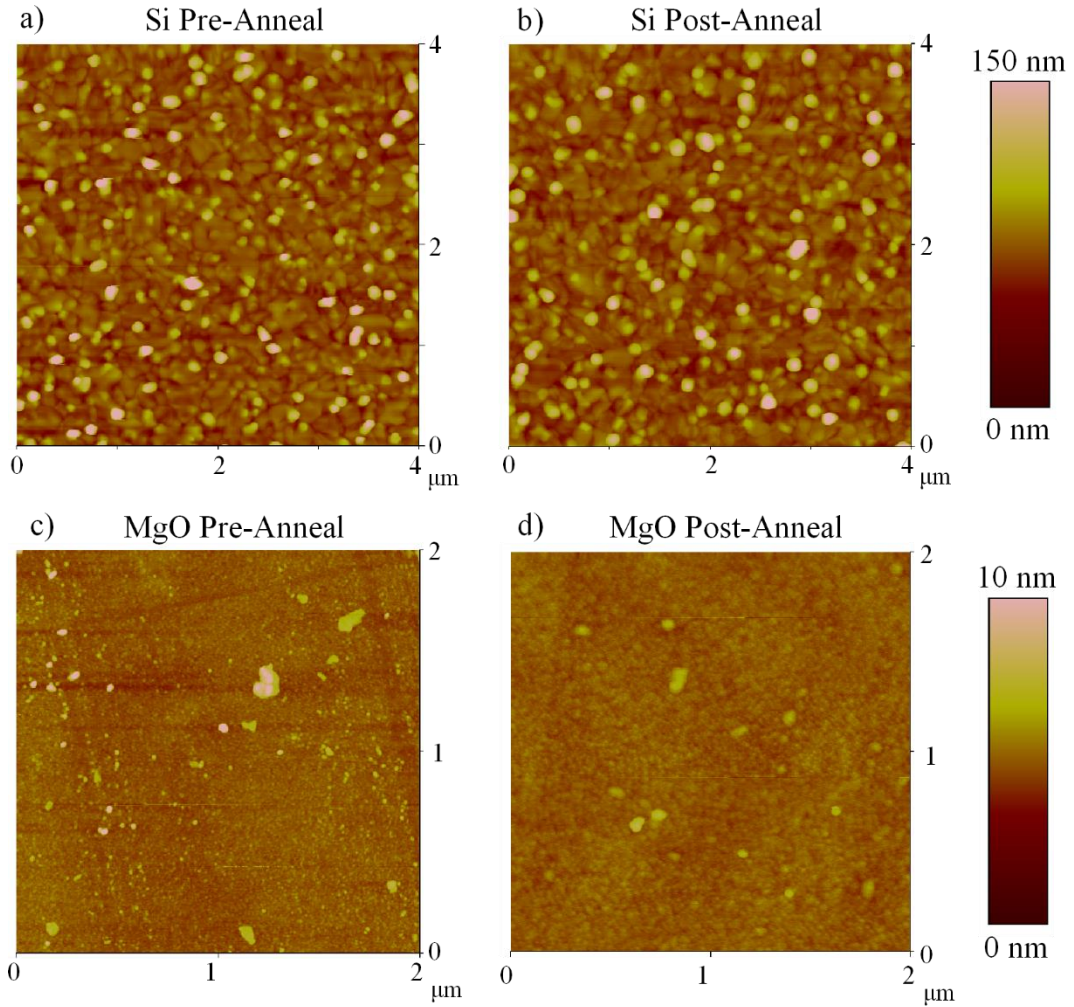


Figure 7.5. AFM images from Fe_3O_4/Si ($4 \mu m \times 4 \mu m$) and $Fe_3O_4/MgO(100)$ ($2 \mu m \times 2 \mu m$) taken pre- and post-annealing treatment.

7.2.3. Magnetic analysis

To establish whether the coercivity of the Fe_3O_4 thin films was reduced by the annealing treatment magnetisation loops were measured using MOKE both before and after annealing. Normalised hysteresis loops for films grown on Si and MgO (100) are presented in Figure 7.6.

The MOKE results showed that annealing produced dramatic differences in the magnetic responses of both the Si and MgO films, with the former producing a loop with a greater coercivity and the latter exhibiting a large drop in coercivity and change in loop shape. The coercivity of the pre-annealed film on Si was 473 ± 14 Oe, and increased to 827 ± 26 Oe after the annealing treatment. In contrast to this, the coercivity of the film on MgO (100) was 269 ± 50 Oe prior to annealing, and decreased to 123 ± 3 Oe after the annealing treatment. This drop in coercivity is in agreement with the work by Zhou et al. where a drop in coercivity from 200 Oe to 120 Oe was reported.

The change in loop shape for the film on MgO can be seen in the average relative remenance values (measured from the normalised loops) which dramatically change from 0.305 prior to annealing to 0.805 post annealing. A smaller change in average relative remenance is seen for the film on Si, with an increase from 0.705 to 0.725 post annealing.

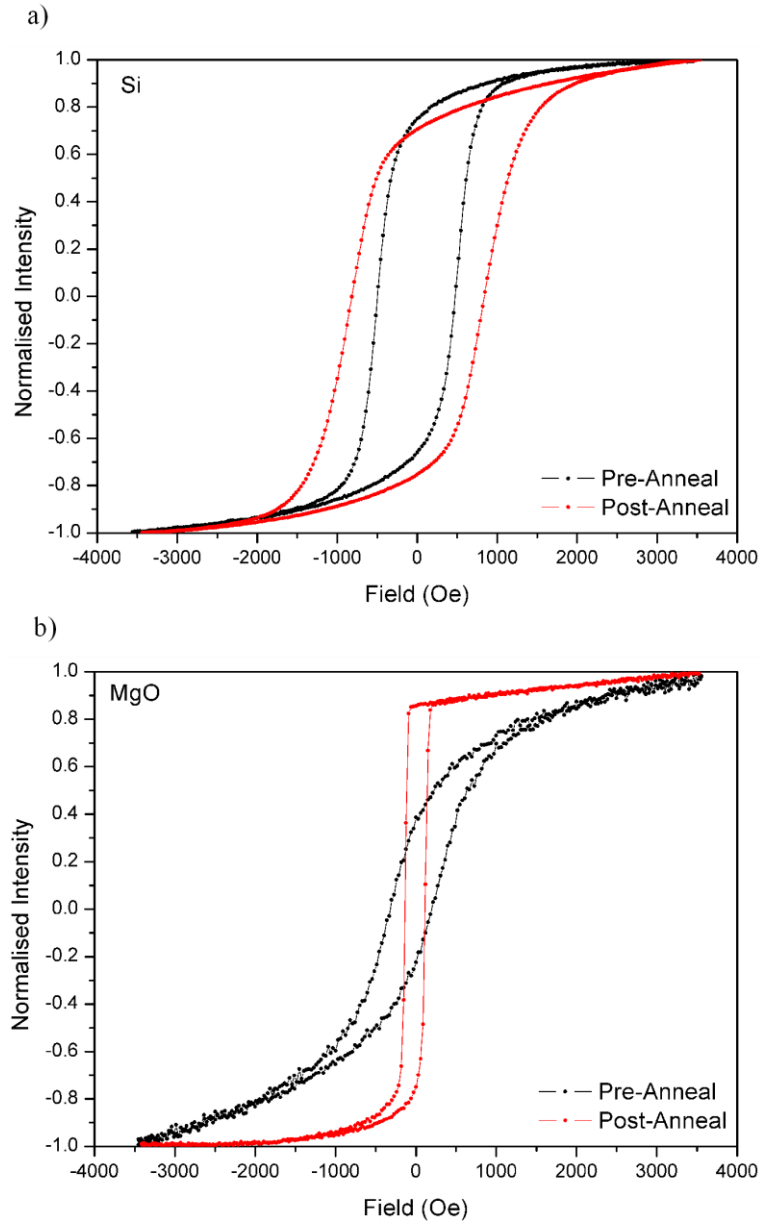


Figure 7.6. Normalised hysteresis loops of $\text{Fe}_3\text{O}_4/\text{Si}$ and $\text{Fe}_3\text{O}_4/\text{MgO}$ (100) measured using MOKE. Results taken prior to annealing treatment (black) and post annealing treatment (red).

A possible reason behind the increase in coercivity seen for the annealed film on Si is the presence of $\gamma\text{-Fe}_2\text{O}_3$ in the films. Coercivity values of 2100 Oe have been recorded by Chang et al. [10] after annealing $\text{Fe}_3\text{O}_4/\text{Si}$ thin films at 320 °C and 360 °C in air for

10 to 90 minutes. In these measurements, the Fe_3O_4 films were found to be fully converted to $\gamma\text{-Fe}_2\text{O}_3$.

The explanation provided by Zhou et al. [1] for the reduction in the coercivity of epitaxial $\text{Fe}_3\text{O}_4/\text{MgO}$ (100) thin films after annealing was associated with the strong anti-ferromagnetic exchange interaction across APBs. As APBs are meta-stable defects, the decrease in coercivity was due to a change in stoichiometry of the APB which causes a decay of the anti-ferromagnetic exchange interaction. The films in this study on MgO substrates are textured not epitaxial, and the annealed film contains a mixed iron oxide phase. Two of the major differences between the Fe_3O_4 films on Si and MgO substrates is that the films on Si are polycrystalline and granular, and those on MgO are textured and smooth. Both of these films contain the mixed iron oxide phase after annealing, however have very contrasting magnetic responses. The increase in coercivity for the annealed film on Si has been explained due to the presence of $\gamma\text{-Fe}_2\text{O}_3$, though the presence of $\gamma\text{-Fe}_2\text{O}_3$ in the annealed films on MgO does not produce the same effect. This indicates that further investigation is needed to establish why and how the coercivity is reduced for the annealed film on MgO.

7.3. Repeatability of annealing treatment

Following the success of a reduction in coercivity of the $\text{Fe}_3\text{O}_4/\text{MgO}$ (100) film after annealing, new $\text{Fe}_3\text{O}_4/\text{Si}$ and $\text{Fe}_3\text{O}_4/\text{MgO}$ (100) films were grown using the method described in Section 6.2 to establish whether the coercivity reduction was repeatable. This is due to the repeatability issues seen for surface morphology and coercivity values of the $\text{Fe}_3\text{O}_4/\text{MgO}$ films grown in Chapter 6.

For each thin film growth, two of each substrate (Si & MgO (100)) were used which provided a comparison after annealing that isolates any annealing repeatability differences from the growth repeatability issues discussed in Chapter 6. These films were then annealed together as a Si and MgO (100) pair, with each pair notated by a letter (a, b, c ...). From 3 growths there were 6 Si & MgO (100) annealing pairs (a – f) and an additional pair of Si films (g & h) from a 4th growth. The films (a & b), (c & d), (e & f), (g & h) were grown simultaneously.

The Elite box furnace was utilised to anneal films a – d, and the Lenton tube furnace was used for films e – h.

7.3.1. Magnetic analysis

To establish whether the change in coercivity following the annealing treatment for the Fe₃O₄/Si and Fe₃O₄/MgO thin films was repeatable, magnetisation loops were measured both prior to and post annealing for all of the films.

The magnetisation loops were measured using a transverse MOKE magnetometer with a maximum applied magnetic field of ± 3.5 kOe. The coercivities measured from the normalised hysteresis loops from each of the films are shown in Figure 7.7.

It is clear that there is a large difference between the annealed films from this series of experiments compared to those measured in the initial study in Section 7.2. In the initial study, the coercivity of the film grown on MgO was shown to decrease dramatically from 269 ± 50 Oe to 123 ± 3 Oe, whereas those in this more extensive study retained values to within ± 20 Oe of the pre-annealed coercivity.

In contrast to those on MgO substrates, the annealed films on Si substrates show a substantial change in coercivity following annealing, and significant variations in the size of this change from sample to sample. The change in coercivity between pre- and post-annealed films on Si substrates varied from 436 ± 11 Oe to 1609 ± 60 Oe for film a, to a negligible change in coercivity for film c.

An interesting feature is the large difference in coercivity between the annealed films g & h, as these films were grown together but unlike the other films were annealed on separate days. The humidity and ambient temperature during the annealing treatment for the two films was 30% and 17 °C for film g and 31% and 16 °C for film h. This small variation between the two films is unlikely to have caused the vast difference in post-annealed coercivity values.

Possible causes for this variation in coercivity for the post-annealed films will be discussed later in the chapter (Section 7.3.4) after the compositional and surface morphology analysis. However, it has been shown that the reduction in coercivity observed in Section 7.2.3 for the Fe₃O₄/MgO film post annealing was not repeatable.

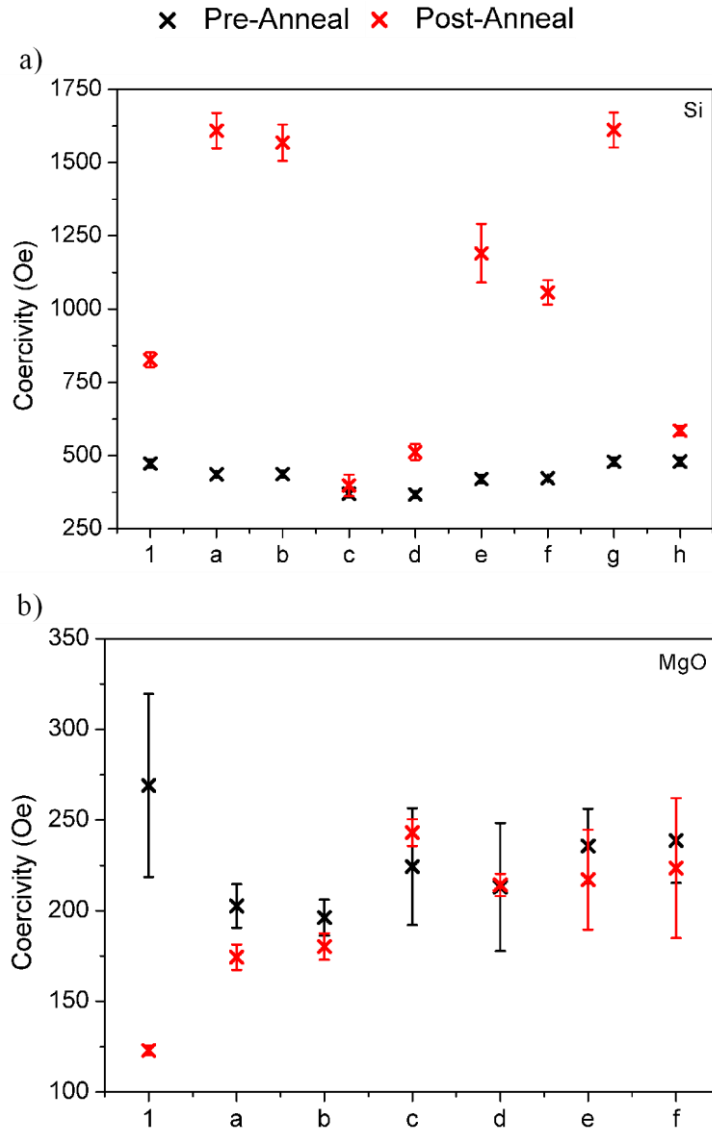


Figure 7.7. Coercivity values measured from normalised magnetisation loops for a) $\text{Fe}_3\text{O}_4/\text{Si}$ and b) $\text{Fe}_3\text{O}_4/\text{MgO}$ (100) thin films both pre-annealing (black) and post-annealing (red) treatment. Coercivity values of the films from Section 7.2.3 are included as “1”.

7.3.2. Raman spectroscopy

Raman spectroscopy was chosen for the extended compositional study here rather than XRD or XPS. XRD was not chosen due to the difficulty in separating the responses from Fe₃O₄ and γ -Fe₂O₃ due to their similar crystal structures, and XPS only probes the top surface of the film and presents difficulties when distinguishing between the different Fe₂O₃ phases. Raman spectroscopy provides a measurement of the whole film thickness and there are clear differences in the spectra from the different iron oxide phases, providing an easier method for film composition analysis.

All of the films were measured using Raman spectroscopy post-annealing, with the spectra presented in Figure 7.8 & Figure 7.9. These spectra were vastly different to those measured from Fe₃O₄/Si and Fe₃O₄/MgO (100) films and annealed films previously, with the intensity of the additional peaks being greater than those seen in Figure 7.4. This implies that the composition of the annealed films in this study are different to annealed films in Section 7.2.1.3.

From the variation between the spectra it is clear that there are differing concentrations of secondary iron oxide present in the films post-annealing. To aid identification of the iron oxide phases present in the annealed films, Lorentzian peaks were fitted to the annealed Fe₃O₄/MgO (100) spectra. The centre of the peaks in the spectra were selected, from which the Origin software fitted the Lorentzian peaks to best fit the data. The annealed Fe₃O₄/Si spectra were not fitted with Lorentzian peaks due to the presence of Si peaks which complicate the fitting process. The fitted peak positions from the annealed films on MgO substrates are tabulated in Table 7.3, and are notated on the annealed Fe₃O₄/Si spectra as a reference.

The fitted Raman spectra have peaks corresponding to both Fe_3O_4 and $\gamma\text{-Fe}_2\text{O}_3$ present which is the same as in Figure 7.4, however there are also additional peaks in Figure 7.8 that are from neither of these iron oxides. There is a peak at 454 cm^{-1} that has been assigned to Fe_3O_4 in Table 7.3 even though it is not mentioned in Table 7.2. This peak was mentioned by Shebanova et al. [9] in a review of Fe_3O_4 Raman spectra in the literature to be the third predicted Fe_3O_4 T_{2g} mode and expected to be between $450 - 500\text{ cm}^{-1}$. There is a peak located at $\sim 115\text{ cm}^{-1}$ which is not from any of the iron oxides in Table 7.2, and it is also present in previous Raman spectra (Figure 5.9) although it is very small. As to what this peak comes from and why it is more pronounced in these spectra is unknown.

Another peak that does not correspond to any peaks from Table 7.2 is found at 250 cm^{-1} , and although $\alpha\text{-Fe}_2\text{O}_3$ does have a peak 249 cm^{-1} there are no other peaks to justify assigning it to $\alpha\text{-Fe}_2\text{O}_3$. A possible explanation for this peak is that the rule of mutual exclusion is broken and that it is a T_{1u} IR-active mode for Fe_3O_4 . This has been observed previously by Jacintho et al [11] for nanoparticles of Fe_3O_4 with diameters in the 10-15 nm range, who explained the breakdown of the rule of mutual exclusion as being due to quantum size effects.

Langevin peak positions (cm ⁻¹)						Iron
a	b	c	d	e	f	Oxide
716.5	716.7	719.9	718.8	716.7	714.2	γ -Fe ₂ O ₃
672.1	671.9	668.6	666.9	676.5	671.6	Fe ₃ O ₄
578.6	579.3	554.6	567.3	545.9	565.8	Fe ₃ O ₄
515.1	515.8	510.2	511.5	511.9	514.4	γ -Fe ₂ O ₃
454.1	454.8	462.3	459.1	456.4	454.2	Fe ₃ O ₄
373.8	374.0	374.5	376.2	376.4	372.9	γ -Fe ₂ O ₃
320.7	320.5	331.3	330.3	320.5	316.1	Fe ₃ O ₄
249.0	250.7	268.9	268.9	257.9	251.0	Fe ₃ O ₄ (T _{1u} IR)
185.7	186.8	142.7	137.8	184.3	181.2	Fe ₃ O ₄
116.0	116.7	114.8	115.2	115.9	110.2	?

Table 7.3. Peak locations of the Lorentzian peaks fitted to the annealed Fe₃O₄/MgO (100) Raman spectra.

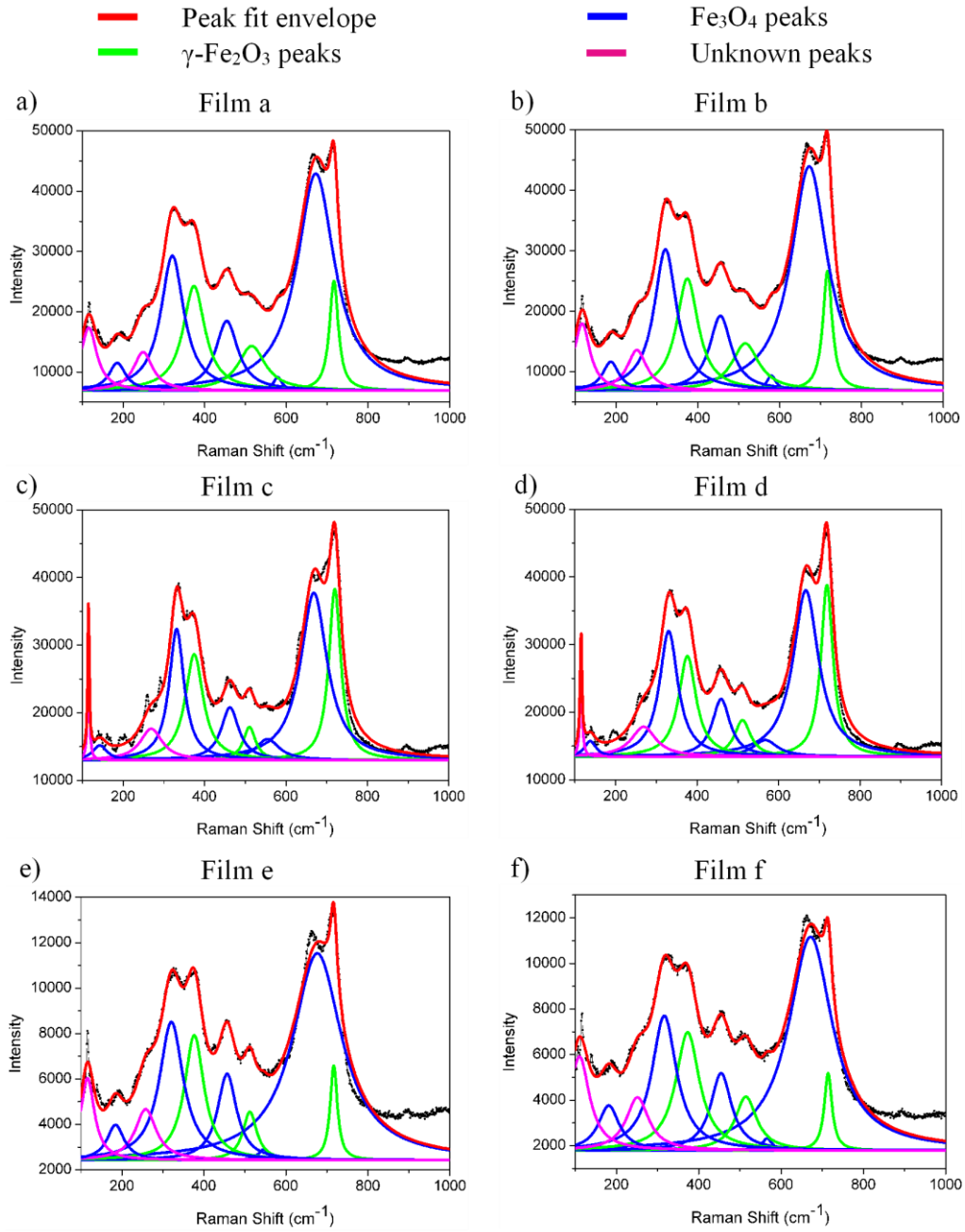


Figure 7.8. Raman spectra from $\text{Fe}_3\text{O}_4/\text{MgO}$ (100) post-annealing treatment using a $\lambda = 514.5 \text{ nm}$ laser. The spectra is fitted with multiple Lorentzian peaks (Fe_3O_4 blue, $\gamma\text{-Fe}_2\text{O}_3$ green, unknown magenta) producing an overall peak envelope (red).

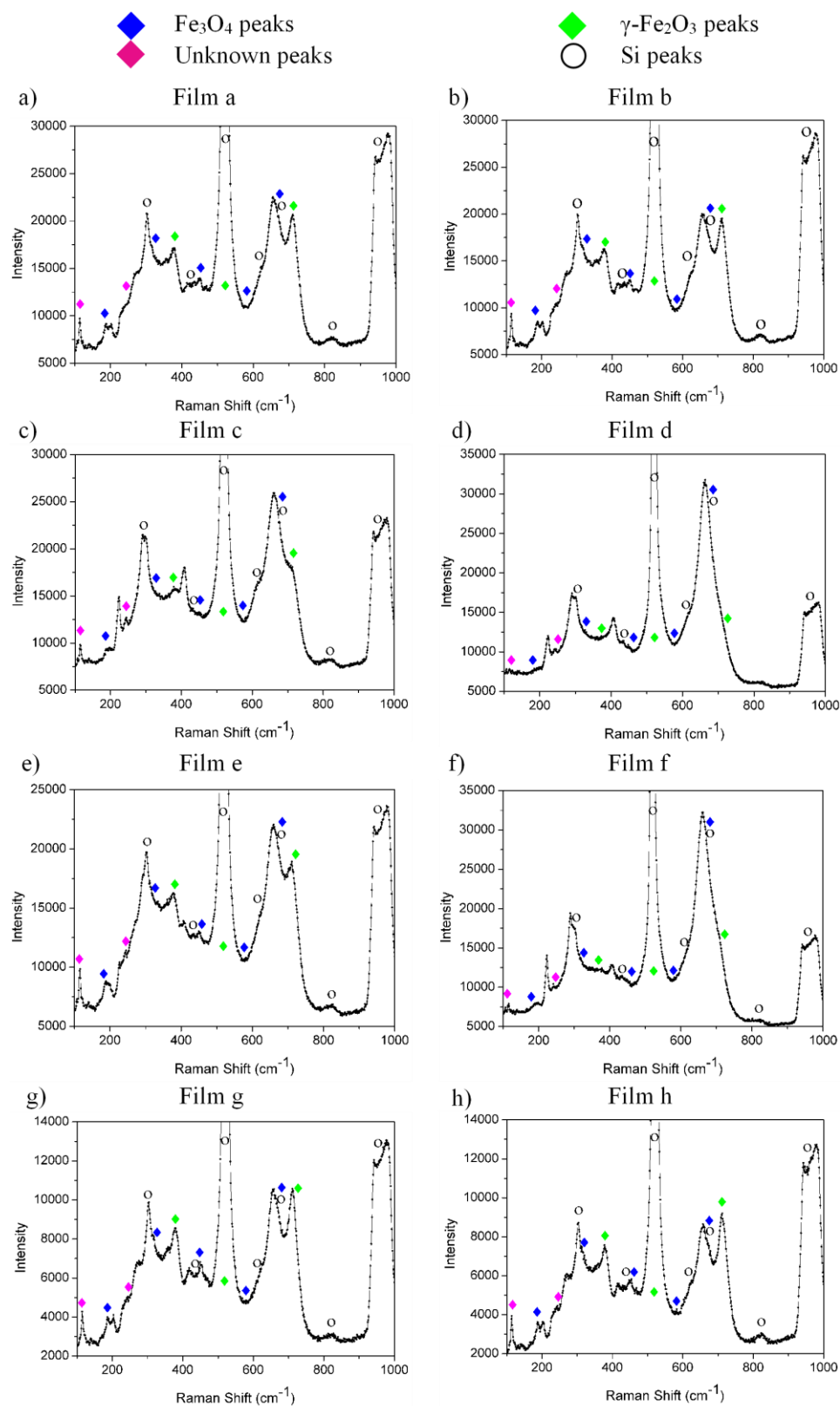


Figure 7.9. Raman spectra from $\text{Fe}_3\text{O}_4/\text{Si}$ post-annealing treatment using a $\lambda = 514.5$ nm laser. ◆: Lorentzian peak positions from annealed MgO (100) films (Fe_3O_4 blue, $\gamma\text{-Fe}_2\text{O}_3$ green, unknown magenta). o: Si substrate peak positions.

The peak intensities (I) for the Fe₃O₄ peak at $\sim 661\text{ cm}^{-1}$ and the γ -Fe₂O₃ peak at $\sim 711\text{ cm}^{-1}$ were measured, and the ratio ($I_{\gamma\text{-Fe}_2\text{O}_3} / (I_{\text{Fe}_3\text{O}_4} + I_{\gamma\text{-Fe}_2\text{O}_3})$) calculated to indicate how the composition varied from film to film. These values are presented in Figure 7.10 along with the difference in coercivity values of the pre- and post-annealed films on Si. A comparable trend can be seen for most of the films between the coercivity and Raman peak ratio, however this is broken by films c & h. A possible explanation for this is given below.

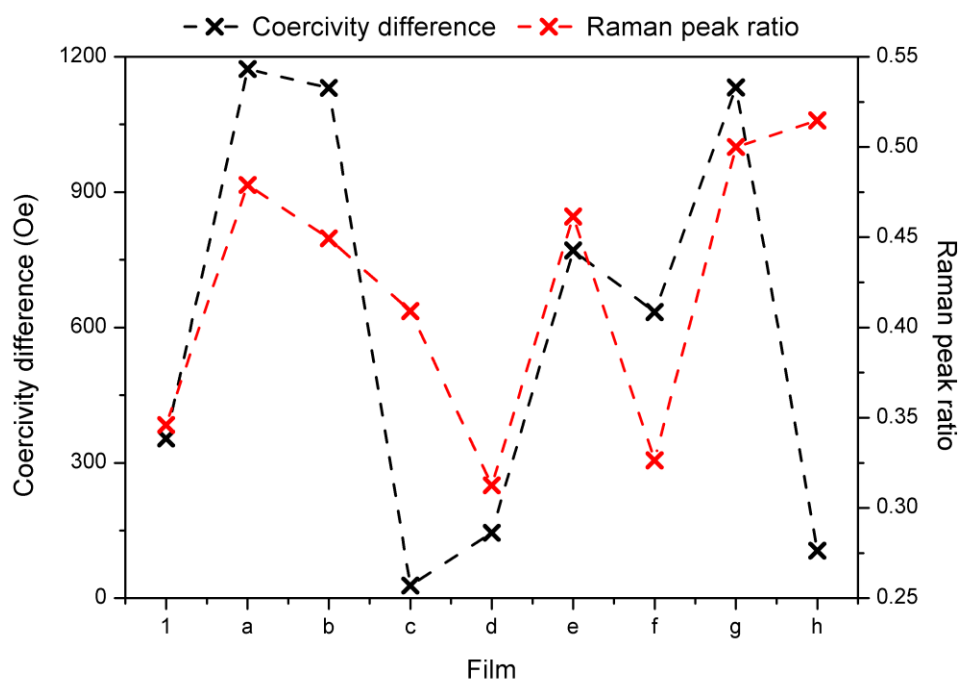


Figure 7.10. A comparison between the difference in coercivity values (black) of the pre- and post-annealed films on Si substrates with the ratio of the γ -Fe₂O₃ Raman peak at $\sim 711\text{ cm}^{-1}$ to the Fe₃O₄ Raman peak at $\sim 661\text{ cm}^{-1}$ (red). Dashed lines are used as a guide.

An interesting feature of the films was that the Fe₃O₄ films pre-annealing were dark and close to black whereas post-annealing these films become lighter and slightly

brown in colour. On three of the annealed films on Si substrates (c, d & h), small spots (1 – 2 mm in diameter) were observed on the surface that were the original dark colour.

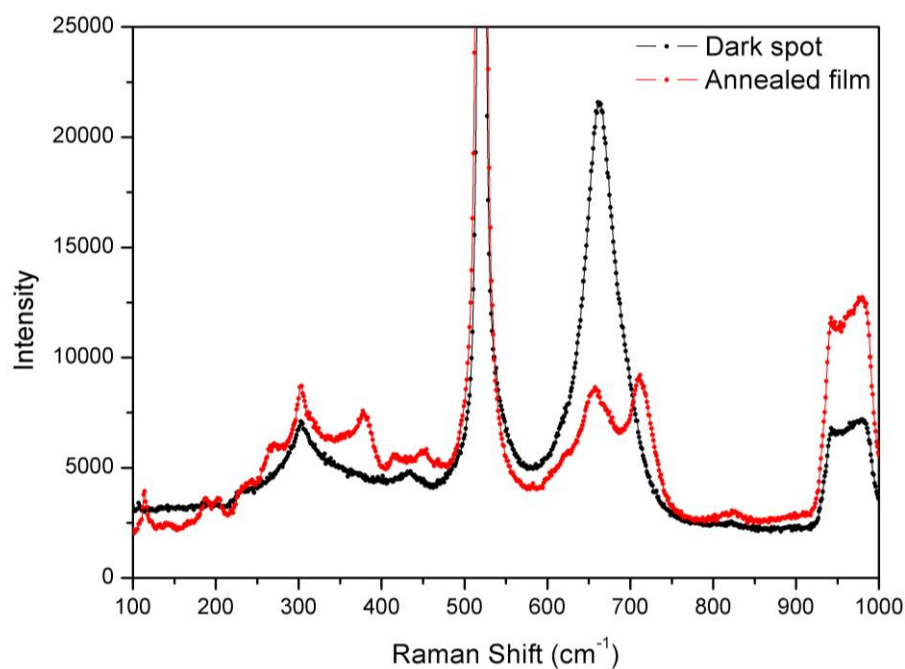


Figure 7.11. Raman spectra from the dark spot on the surface of film h on a Si substrate (black) and from the annealed surface of film h (red).

The Raman spectra from the spot on film h is presented in Figure 7.11 and it is clear that there is a large difference from the previously measured spectra in Figure 7.9h. The spectra above resembles the $\text{Fe}_3\text{O}_4/\text{Si}$ Raman spectra seen in Figure 7.4a (black) and does not contain any of the additional peaks observed in Figure 7.9. This indicates that there are regions in the post-annealed film that are still Fe_3O_4 instead of the mixed iron oxide phase seen in the Raman spectra in Figure 7.9. Even though all of the spectra in Figure 7.8 & Figure 7.9 show a mixed iron oxide phase of Fe_3O_4 and $\gamma\text{-Fe}_2\text{O}_3$, only three of the films have spots of Fe_3O_4 that are visible to the naked eye on the film surface. The other films may have areas that are Fe_3O_4 only, however this

could vary from film to film as to the area and number of spots. The presence of these regions of Fe₃O₄ in the annealed films provides a reason for the difference seen for some of the films when comparing the Raman peak ratio to the coercivity difference in Figure 7.10. The Raman spectra in Figure 7.9 are taken from regions of the film where there is a mixed iron oxide phase and does not represent the film as a whole, whereas the coercivity of the films is measured for the whole film and therefore also includes the mixed iron oxide phase and Fe₃O₄ regions. Two of the biggest differences in Figure 7.10 are for films c & h, which both contain regions of Fe₃O₄ visible to the eye. How the presence of Fe₃O₄ regions could affect the magnetic properties of the thin films is discussed in Section 7.3.4.

A possible explanation for the variable presence of these Fe₃O₄ regions on the annealed films could be due to variations in the thermal contact between the film and the ceramic crucible during the annealing treatment. It was suggested in Chapter 6 that the thermal contact between the substrate and substrate holder was a source of the variability seen for surface morphology and coercivity. The same argument can be used here for the presence of Fe₃O₄ regions in the annealed films.

7.3.3. Surface morphology

It should be noted that there are no AFM images prior to annealing due to equipment failures, and thus conclusions drawn about changes in the surface morphology are purely on observations from previous films in Chapter 6 and Section 7.2.2.

The initial annealing study in Section 7.2.2 showed that the surface morphology of the annealed films was not affected by the annealing treatment. For the films grown on

Si substrates which were annealed in this study, the roughness values (Table 7.4) and morphology is varied for the different films. Films g & h have clear grains and the lowest roughness values which is in contrast to films c & d where the grains are unclear, with the largest roughness values. There are a couple of reasons as to why there was variation across the different films, the first being that the original pre-annealed films had differing surface morphologies and that they were not altered from the annealing treatment. Another contrasting explanation is that all of the films had similar surface morphologies originally and that the annealing treatment produced the variations observed. However, the most likely of these two explanations is that the films had differing surface morphologies prior to the annealing treatment and that there was minimal variation post annealing. This can be deduced from the fact that annealing was found to have little effect on surface morphology in the initial study (Figure 7.5) and that films grown under nominally identical conditions have already been shown to exhibit substantial variations in morphology (Chapter 6).

Film	Roughness (nm)	Film	Roughness (nm)
a	13.2 ± 0.3	e	15.8 ± 0.3
b	14.3 ± 0.3	f	14.9 ± 0.5
c	22.5 ± 0.8	g	7.7 ± 0.3
d	18.1 ± 0.6	h	7.6 ± 0.3

Table 7.4. RMS roughness values for the post-annealed Fe₃O₄/Si thin films from AFM images.

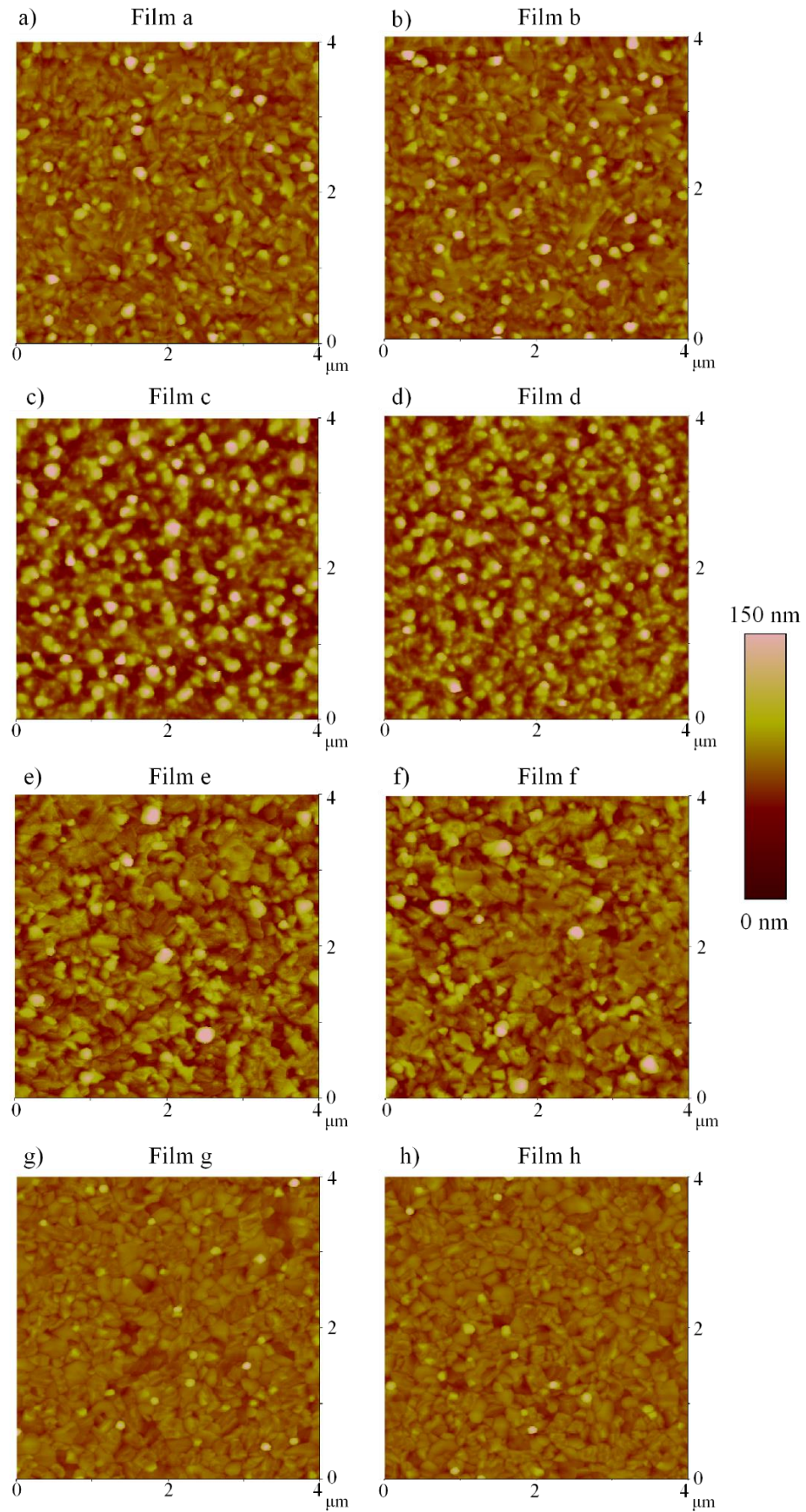


Figure 7.12. AFM images (4 x 4 μm) of $\text{Fe}_3\text{O}_4/\text{Si}$ thin films post-annealing treatment.

AFM data from the post-annealed Fe₃O₄/MgO films are shown in Figure 7.13. The MgO (100) substrates used in this section were 10 mm x 10 mm in size and from the same batch of substrates onto which the films grown in Chapter 6 were deposited (i.e. those Fe₃O₄ films that featured the nano-towers on their surface). In the annealed samples on MgO substrates two distinct surface morphologies were observed. The AFM images of MgO films a & b have a similar surface morphology to films grown in Chapter 6, with a surface of stacked square grains that are aligned together. In contrast to these samples, the AFM images taken from films c – f grown on MgO are different to anything else measured in this work, although it does have similarities to the nano-towers of Chapter 6. On first examination, these surfaces resemble a grid of ragged features that are 500 nm in size on a flat surface.

Although these features stand out on the AFM images, when a line section is taken across these features they are not obvious from the background surface (Figure 7.14). The features actually appear to be regions of film that are lower than the rest of the film surface, with a drop of ~ 2 nm which makes them darker than the rest of the film in the AFM image. This is in contrast to the nano-towers which protruded from the surface with heights ranging from 7 nm to 73 nm. The larger nano-towers from Chapter 6 were in the region of 250 – 300 nm in size which is much smaller than the islands in Figure 7.13, and were also spread across the whole film surface with no order except the ordering of their orientation. The islands in Figure 7.13 are aligned along straight lines that are perpendicular to each other, and do not form straight edged squares but squares with ragged edges. This is again another difference between the features and nano-towers as the nano-towers have straight edges and form cubes. One feature that all of the annealed MgO films have in common though is that the surface roughness is less than 2.5 nm.

As there are no AFM images from prior to annealing the films showing whether these films had nano-towers, no definite statement can be made as to what caused these features to form. However, the surface morphology of $\text{Fe}_3\text{O}_4/\text{MgO}$ films was shown in Chapter 6 to be highly variable and the different surface morphologies seen in Figure 7.13 could be a further manifestation of this.

Without the AFM images of the $\text{Fe}_3\text{O}_4/\text{Si}$ & $\text{Fe}_3\text{O}_4/\text{MgO}$ thin films prior to annealing, no definitive conclusion can be made about the effect of annealing on the surface morphology. A comparison to the surface morphology prior to and post annealing in Section 7.2.2 and the AFM images in Chapter 6 provides guidance on what is likely to be concluded for the films in this study. The variation in surface morphology seen for the annealed films on both Si and MgO is most likely caused by variations in the surface morphology prior to annealing. This is due to the highly variable surface morphologies seen in Chapter 6 as well as there being no change in surface morphology for the annealed films in Section 7.2.2 compared to the films prior to annealing. How the surface morphology might affect the magnetic data is discussed in Section 7.3.4.

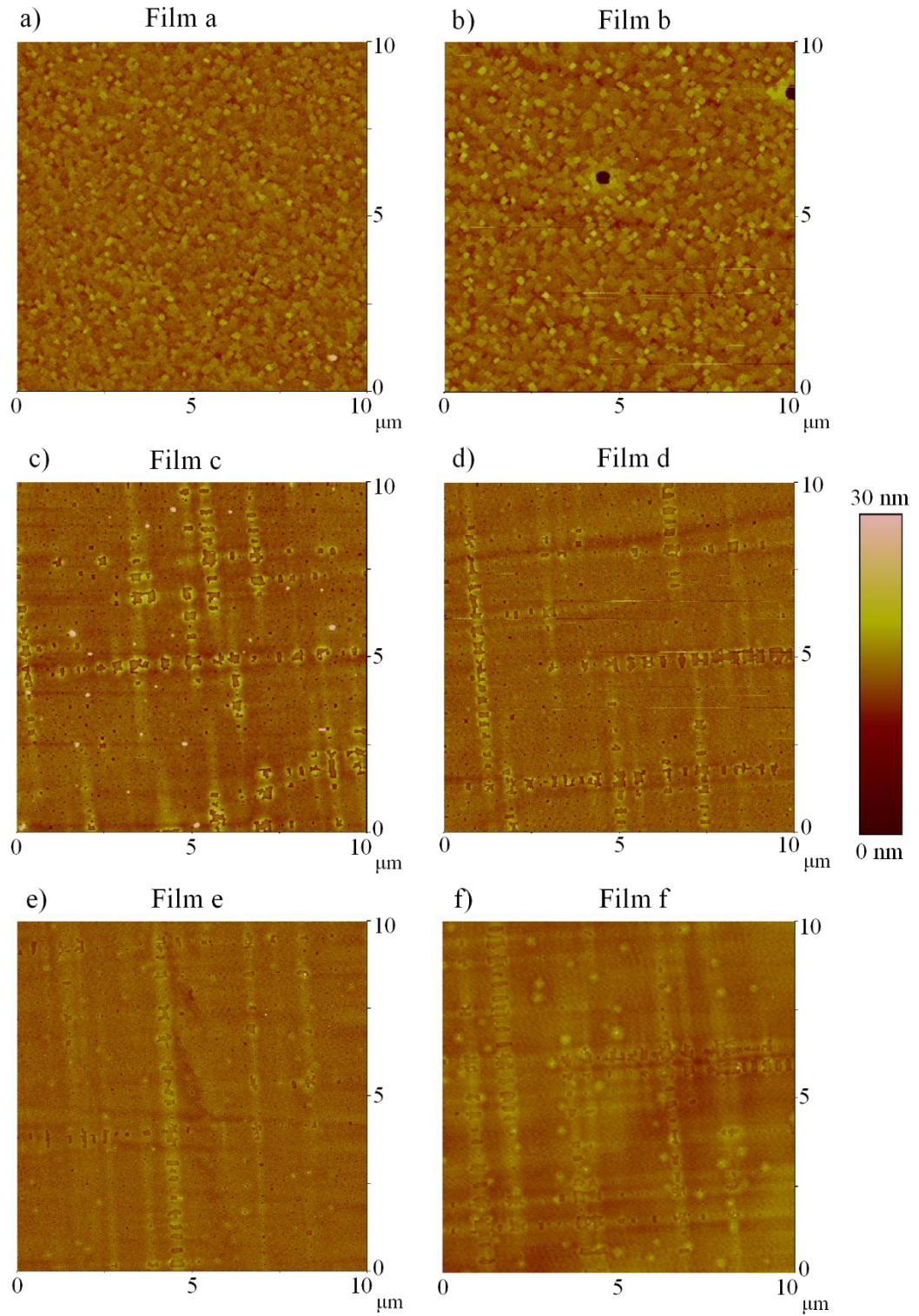


Figure 7.13. AFM images ($10 \times 10 \mu\text{m}$) of $\text{Fe}_3\text{O}_4/\text{MgO}$ (100) films post-annealing treatment.

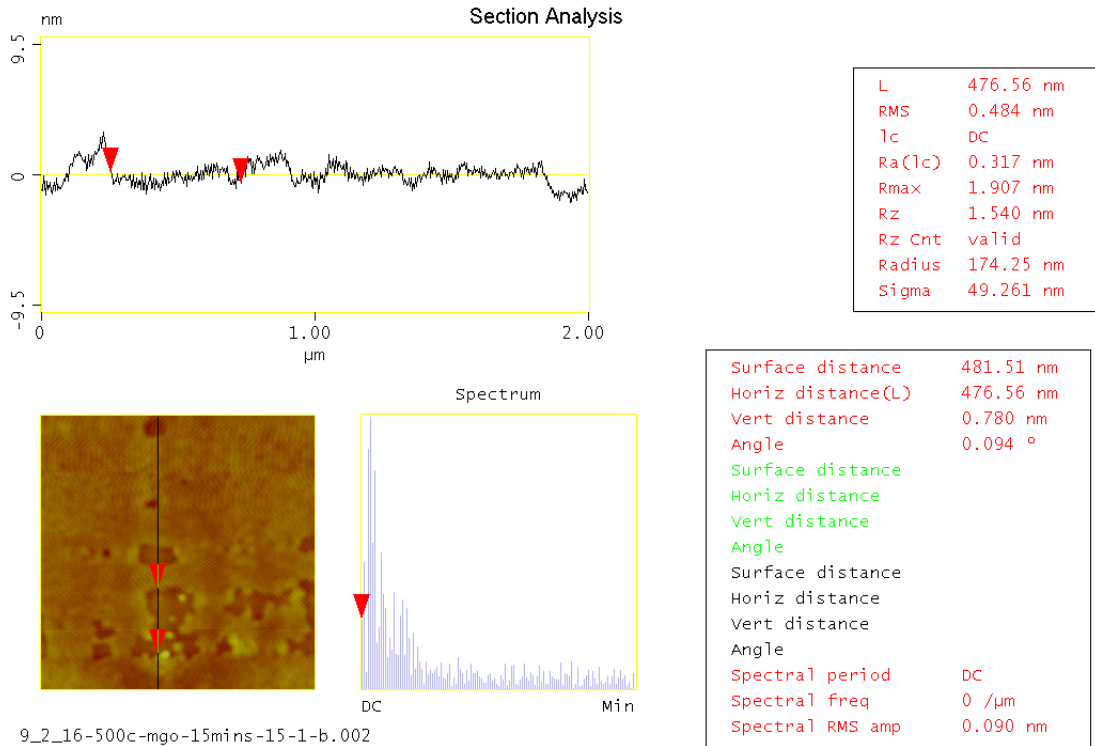


Figure 7.14. Section image from film d on an MgO (100) substrate illustrating the size of the features.

7.3.4. Discussion

The main difference between the films in this study and those measured initially in Section 7.2 is the surface morphology. Although it was shown in Chapter 6 that the different surface morphologies observed had little effect on the coercivity of the films, it appears that they cause differences in the way the samples respond to annealing. It appears that the drop in coercivity observed by Zhou et al. [1] and in Section 1 is only possible for Fe₃O₄/MgO films with a smooth and artefact-free surface, although this has not been reproduced for this work. Without the surface morphology of the films

prior to annealing, no firm conclusion can be made about the effect surface morphology has on the differing magnetic responses post annealing.

In contrast to those on MgO substrates, the annealed films on Si substrates show a substantial change in coercivity following annealing, and significant variations in the size of this change from sample to sample. The change in coercivity between pre- and post-annealed films on Si substrates varied from 436 Oe to 1609 Oe for film a, to negligible change in coercivity for film c.

A possible reason that could explain the large difference between the coercivity of films g & h is the presence of a spot of Fe₃O₄ on the surface of film h. This theory also explains the small to negligible change in coercivity seen for films c & d, as both of these films had visible spots on the film surface. Film c had a larger Fe₃O₄ region than film d, which correlates with the larger coercivity change seen for film d than film c. The large area of Fe₃O₄ is likely to switch magnetisation at a lower magnetic field than the rest of the mixed iron oxide due to the larger coercivity of γ -Fe₂O₃ thin films [10], which leads to a lower coercivity measured for film h than film g. The Si film series most likely contain regions of Fe₃O₄ in differing volumes and quantity which caused the large variation in coercivity observed.

Further investigation into the localised composition across the surface of a film would be needed to confirm this explanation for the variation in coercivity post-annealing.

7.4. Conclusion

Fe_3O_4 thin films on Si and MgO (100) substrates were annealed at 250 °C for 4 minutes in atmosphere. The initial annealing test produced thin films with a mixed iron oxide phase containing Fe_3O_4 and $\gamma\text{-Fe}_2\text{O}_3$. For the film on the MgO substrate, the annealing treatment produced a drop in coercivity from 269 Oe to 123 Oe and an increase in coercivity for the film on the Si substrate from 473 Oe to 827 Oe. The reduction in coercivity for the annealed film on MgO is possibly caused by a decay of the anti-ferromagnetic exchange interaction across APBs as explained and proposed by Zhou et al. [1]. The increase in coercivity for the annealed film on Si is likely to be due to the presence of $\gamma\text{-Fe}_2\text{O}_3$ as it has been shown by Chang et al. [10] that coercivity values of up to 2100 Oe can be achieved when Fe_3O_4 thin films are annealed to produce $\gamma\text{-Fe}_2\text{O}_3$. The surface morphology of the $\text{Fe}_3\text{O}_4/\text{MgO}$ (100) thin films is very likely to have an effect on the annealed coercivity value, with the only film producing a reduction in coercivity having a smooth and artefact free surface. Further annealing of $\text{Fe}_3\text{O}_4/\text{Si}$ and $\text{Fe}_3\text{O}_4/\text{MgO}$ films was performed to establish repeatability as it has been shown previously in Chapter 6 that the surface morphology and coercivity was highly variable.

All other annealed films on MgO had little or no variation in coercivity post annealing, which is probably due to the differing surface morphologies measured post-annealing from the smooth surface seen for the initial annealing study. Without information on the surface morphology prior to annealing, no firm conclusion can be made about the exact origin of the variation in coercivity. The opposite was found for the annealed Si films, where there was a huge variation in the annealed coercivity values. $\text{Fe}_3\text{O}_4/\text{Si}$

films grown simultaneously but annealed on separate days have been shown to vary drastically in their post annealing coercivity values despite having similar surface morphologies. This indicates that the surface morphology of the Fe₃O₄ thin films on Si is unlikely to be cause of the coercivity variation. The humidity and ambient temperature were measured during the annealing treatment, and with little variation between the two days it was determined that the humidity and ambient temperature were not the cause of the large coercivity difference. The origin of this variation is most likely to have been caused by the presence of spots on one of the two simultaneously grown films surface after annealing which was shown using Raman spectroscopy to be purely Fe₃O₄. Visible regions of Fe₃O₄ were found on two other annealed films, and it was these films that produced little to negligible changes in coercivity after annealing. The variation in the volume and number of these regions in the films is most likely to be the cause of the coercivity variation with the larger Fe₃O₄ regions switching at lower magnetic fields.

References

- [1] Y. Zhou, X. Jin, and I. V. Shvets, "Enhancement of the magnetization saturation in magnetite (100) epitaxial films by thermo-chemical treatment," *Journal of Applied Physics*, vol. 95, pp. 7357-7359, 2004.
- [2] J. D. Wei, I. Knittel, U. Hartmann, Y. Zhou, S. Murphy, I. V. Shvets, *et al.*, "Influence of the antiphase domain distribution on the magnetic structure of magnetite thin films," *Applied Physics Letters*, vol. 89, pp. 122517-122519, 2006.
- [3] R. M. Cornell and U. Schwertmann, *The Iron Oxides: Structure, Properties, Reactions, Occurrences and Uses*, 2nd ed.: John Wiley & Sons, 2006.
- [4] N. S. McIntyre and D. G. Zetaruk, "X-ray photoelectron spectroscopic studies of iron oxides," *Analytical Chemistry*, vol. 49, pp. 1521-1529, 1977.
- [5] P. Mills and J. L. Sullivan, "A study of the core level electrons in iron and its three oxides by means of x-ray photoelectron spectroscopy," *Journal of Physics D: Applied Physics*, vol. 16, pp. 723-732, 1983.
- [6] A. M. Jubb and H. C. Allen, "Vibrational spectroscopic characterization of hematite, maghemite, and magnetite thin films produced by vapor deposition," *Applied Materials & Interfaces*, vol. 2, pp. 2804-2812, 2010.
- [7] M. Hanesch, "Raman spectroscopy of iron oxides and (oxy)hydroxides at low laser power and possible applications in environmental magnetic studies," *Geophysical Journal International*, vol. 177, pp. 941-948, 2009.
- [8] S. Li and L. H. Hihara, "A micro-Raman spectroscopic study of marine atmospheric corrosion of carbon steel: The effect of akaganeite," *Journal of the Electrochemical Society*, vol. 162, pp. C495-C502, 2015.

- [9] O. N. Shebanova and P. Lazor, "Raman spectroscopic study of magnetite (FeFe_2O_4): a new assignment for the vibrational spectrum," *Journal of Solid State Chemistry*, vol. 174, pp. 424-430, 2003.
- [10] W. D. Chang and T. S. Chin, "Undoped maghemite thin films with coercivity up to 2100 Oe for magnetic recording," *IEEE Transactions on Magnetics*, vol. 32, pp. 3620-3622, 1996.
- [11] G. V. M. Jacintho, A. G. Brolo, P. Corlo, P. A. Z. Suarez, and J. C. Rubim, "Structural investigation of MFe_2O_4 (M=Fe,Co) magnetic fluids," *Journal of Physical Chemistry C*, vol. 113, pp. 7684-7691, 2009.

8. Study of Fe_3O_4 nanostructures on Si & MgO (100) substrates

8.1. Introduction

This chapter consists of a comparison between nanostructures of Fe_3O_4 on Si and MgO (100) substrates with the aim of forming a domain wall or a nanoscale field source that could potentially be used for atom trapping [1-3]. The previous chapters have analysed reactively sputter grown Fe_3O_4 thin films on Si and MgO (100) substrates to find the best candidate film for domain wall formation in nanostructures. It was found that $\text{Fe}_3\text{O}_4/\text{MgO}$ thin films produce a lower coercivity and smoother surface morphology than $\text{Fe}_3\text{O}_4/\text{Si}$ thin films.

The nanostructures that are analysed in this chapter were created from the best candidate film which was a 50 nm thick $\text{Fe}_3\text{O}_4/\text{MgO}$ film grown at 300 °C & 500 °C, which will be compared to nanostructures on a Si substrate. Magnetic force microscopy was used to image the magnetic structure of the nanostructures after an in-plane magnetic field was applied.

8.2. Design and fabrication of nanostructures

Fe_3O_4 thin films grown on Si & MgO (100) substrates were transformed into a nanostructure array using EBL to pattern a resist, thermal evaporation of the Al/Ti hard mask, ion milling to remove unwanted Fe_3O_4 followed by the hard mask removal. This process is described in more detail in Section 4.1.2. The design of the nanostructure array is shown in Figure 8.1. Each nanoring was centred in an individual $100\ \mu\text{m}$ square write-field.

The structures were described using the grid notation 'letter' 'number'. The wire width of the structures increases with increasing 'letter': 100 (A), 300 (B), 500 (C), 800 (D), 1000 (E) & 2000 (F) nm, and the radius of the nanorings increases with increasing 'number': 5 (1), 7.5 (2), 10 (3), 15 (4), 20 (5) & 25 (6) μm . For example, a nanoring with a radius of $10\ \mu\text{m}$ and a wire width of 300 nm would have the notation B3.

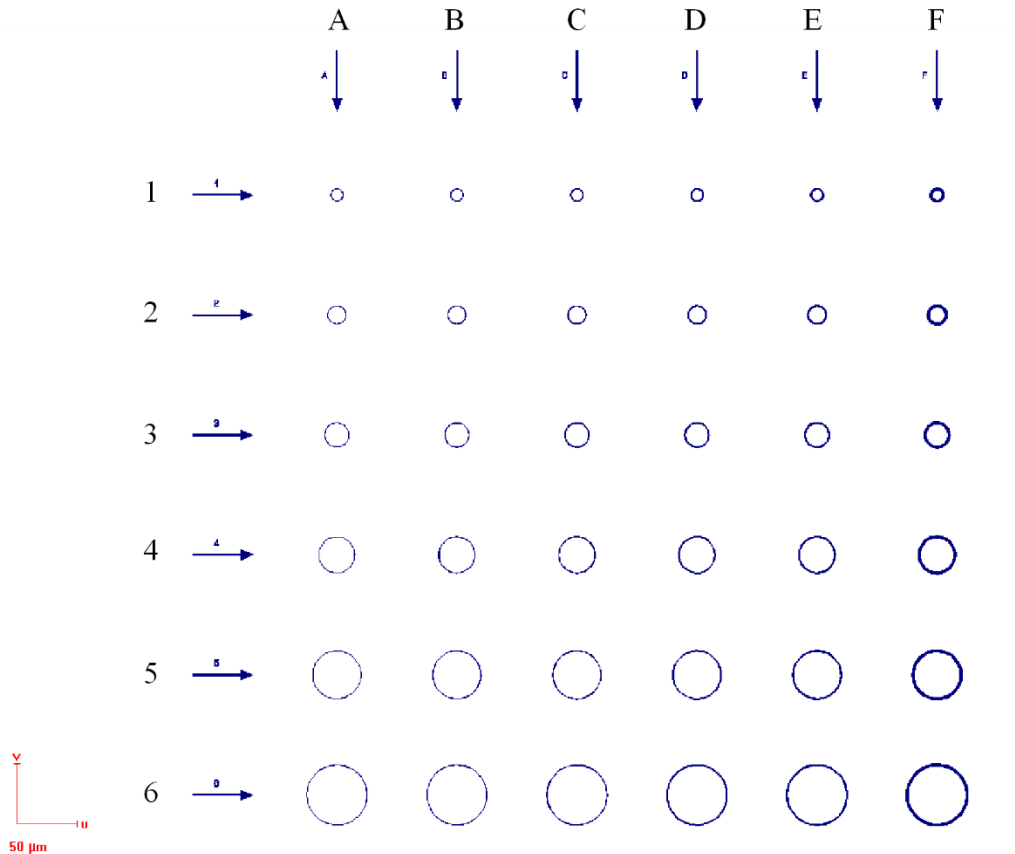


Figure 8.1 Diagram of the nanoring array created using electron beam lithography.

The wire width increases with 'letter' and the ring radius increases with 'number'.

8.3. Magnetic force microscopy of ring-shaped nanowires following saturation

In this study, the magnetic structure of nanorings created from reactively sputtered Fe_3O_4 thin films on Si and MgO substrates after an in-plane magnetic field is applied are investigated. The magnetic structure of the nanorings was imaged using magnetic force microscopy. Formation of DWs in the nanorings was expected to be driven by the shape anisotropy. Thus nanorings imaged in this chapter were primarily from row

“1” which had radii of 5 μm and varying wire width. This allowed the effects of the wire width, and thus strength of the shape anisotropy, had on domain wall formation to be probed. To attempt to form DWs in the rings the sample was placed in a 3.5 kOe magnetic field parallel to the sample surface and then relaxed to remanence. MFM imaging was then performed to probe the rings’ magnetisation configuration. Samples patterned from 50 nm thick films grown on both MgO and Si substrates at temperatures of 300 $^\circ\text{C}$ and 500 $^\circ\text{C}$ were studied.

For ease of notation the nanostructured samples will be referred to by their growth temperature and the substrate, e.g. those patterned from a film grown at 500 $^\circ\text{C}$ on a Si substrate will be referred to as “500 $^\circ\text{C}$ Si”.

Figure 8.2 & Figure 8.3 show MFM images of 500 $^\circ\text{C}$ Si (Figure 8.2) & 300 $^\circ\text{C}$ Si (Figure 8.3) nanorings with geometries A1-F1 after saturation and relaxation. The MFM lift height was 50 nm for both figures. Two prominent features can be seen in these images: a “speckling” of contrast across nanostructures surfaces, and lines of either light or dark contrast along surfaces approximately orthogonal to the initial saturating field.

The “speckling” can be seen most clearly in the rings with larger wire widths (Figure 8.2e & f). It is proposed that this was caused by the large surface roughness of the initial $\text{Fe}_3\text{O}_4/\text{Si}$ thin film. Figure 8.4 shows an illustration of how the surface roughness causes the MFM images to be speckled. The magnetisation is saturated in one direction, and the grains at the surface create north and south poles at the grain boundaries, which are illustrated as yellow and red lines in Figure 8.4a.

The lines of contrast at the rings edges can be seen in all of the rings, with exception that with the narrowest width (A1) in both Figure 8.2 and Figure 8.3 where no

discernible detail can be seen. It is proposed that this was due to the nanostructures retaining a high degree of saturation even after the applied field has been removed. This can be understood by considering the schematic diagram shown in Figure 8.5. North poles would form on the top edges of the nanowires resulting in dark contrast, while south poles would form on the bottom edges resulting in light contrast. The contrast would be expected to be strongest along horizontal edges, which would lie orthogonal to the magnetisation, and should fade towards the sides of the rings where the magnetisation would be parallel to the wires' edges. All of these features can be seen clearly in the MFM images. Further evidence towards this explanation can be seen in Figure 8.6 where MFM images were taken of C1 on 500 °C Si where the applied magnetic field direction was varied. It can be seen the edge contrast is controlled by the direction of the applied magnetic field, and therefore the direction of saturation in the nanostructures.

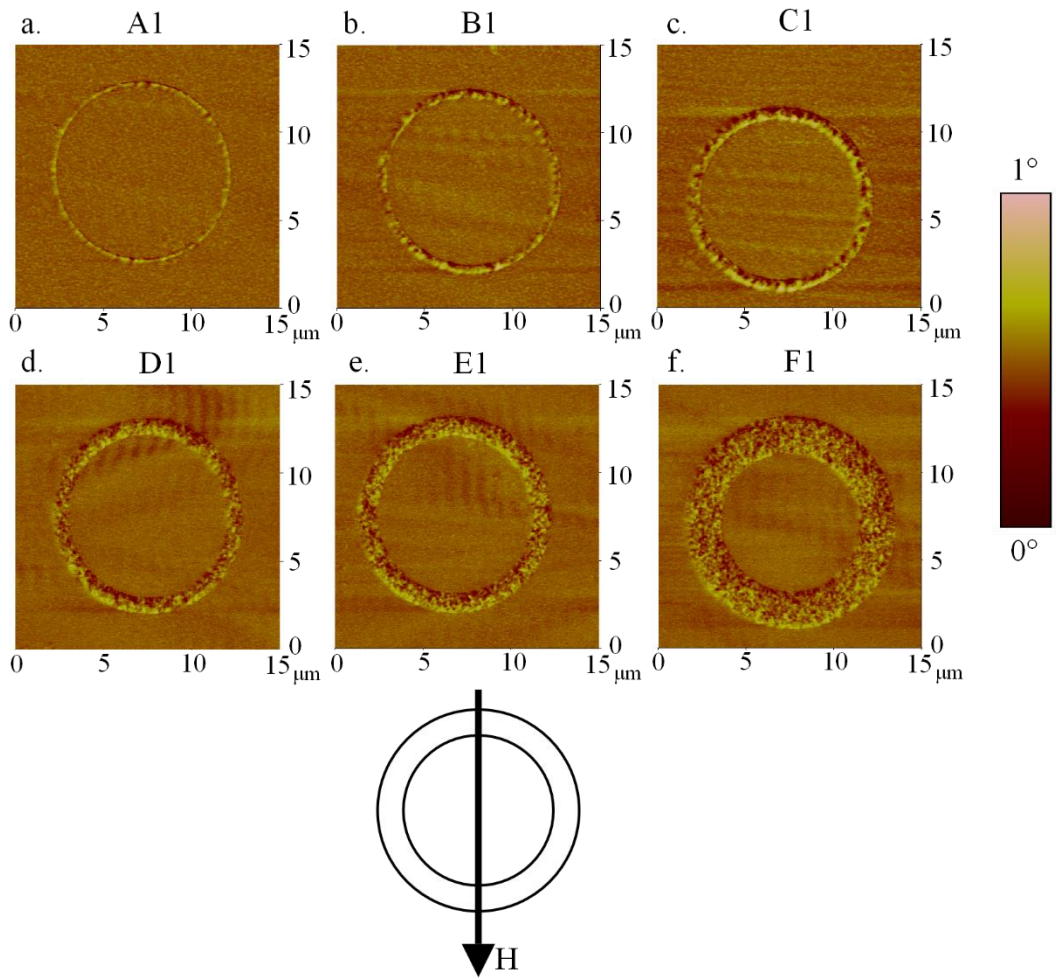


Figure 8.2. MFM images of nanorings from 500 °C Si taken at a lift height of 50 nm after a 3.5 kOe field is applied parallel to the sample surface. All nanorings have a radius of 5 μm and have a wire width of a) 100 nm (A1), b) 300 nm (B1), c) 500 nm (C1), d) 800 nm (D1), e) 1000 nm (E1) and f) 2000 nm (F1).

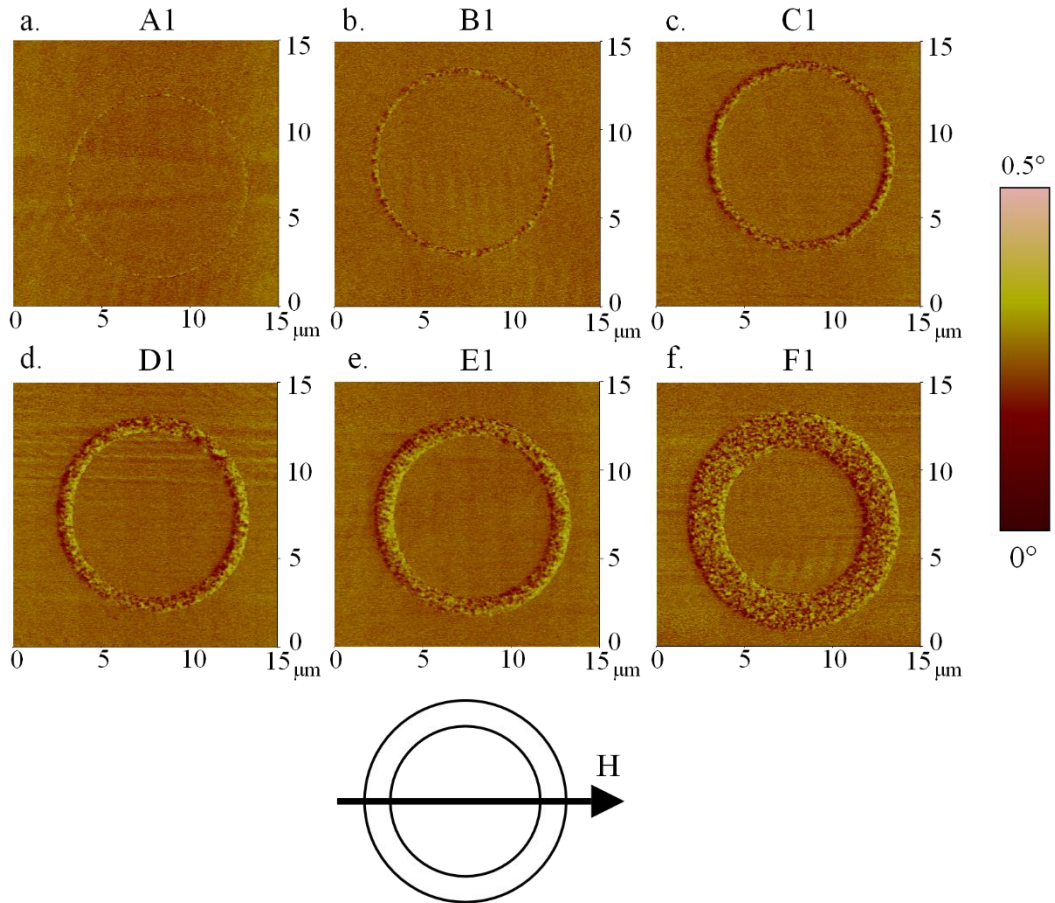


Figure 8.3. MFM images of nanorings from 300 °C Si taken at a lift height of 50 nm after a 3.5 kOe field is applied parallel to the sample surface. All nanorings have a radius of 5 μm and have a wire width of a) 100 nm (A1), b) 300 nm (B1), c) 500 nm (C1), d) 800 nm (D1), e) 1000 nm (E1) and f) 2000 nm (F1).

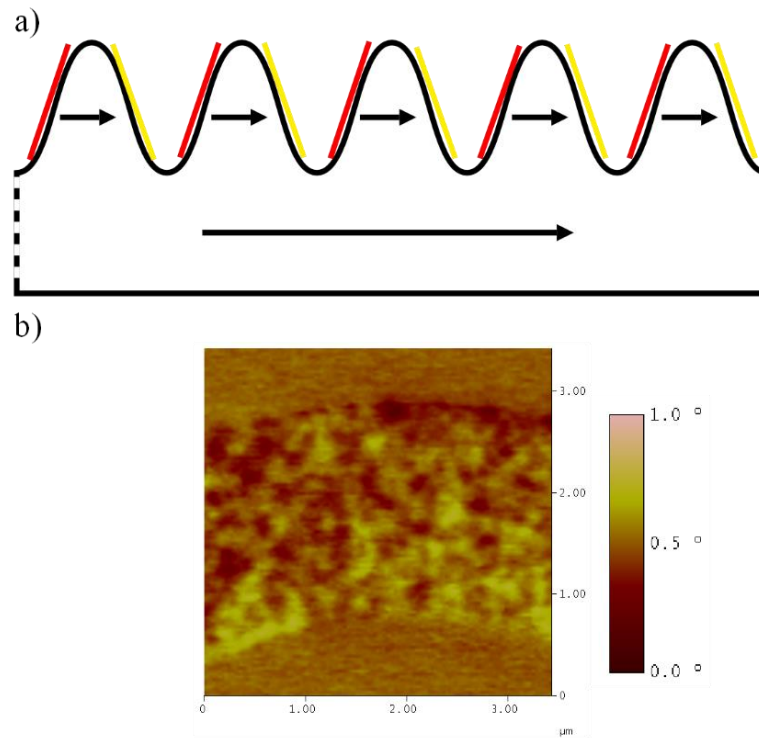


Figure 8.4. a) Schematic illustrating how the surface roughness of the thin film can produce the speckled effect when a film is saturated in-plane. b) MFM image of the speckled contrast of $\text{Fe}_3\text{O}_4/\text{Si}$ from F1 500 °C Si.

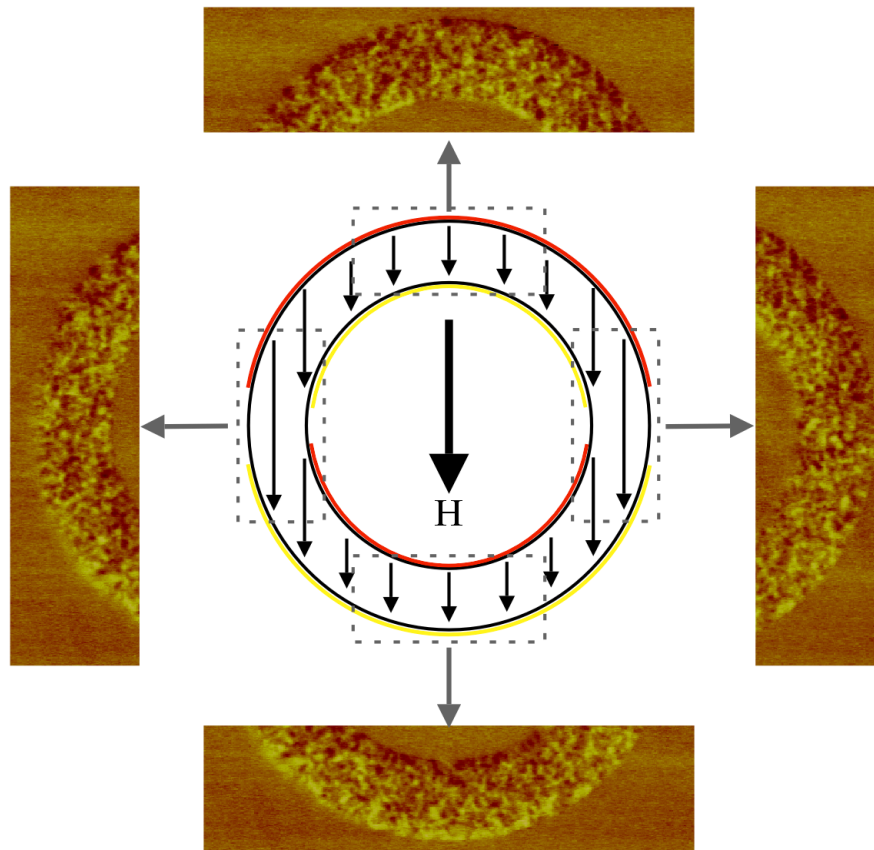


Figure 8.5. Schematic showing the MFM contrast of a saturated nanoring where the magnetisation is pointing to the bottom of the nanoring. Sections from the MFM image in Figure 8.2f used to illustrate the contrast.

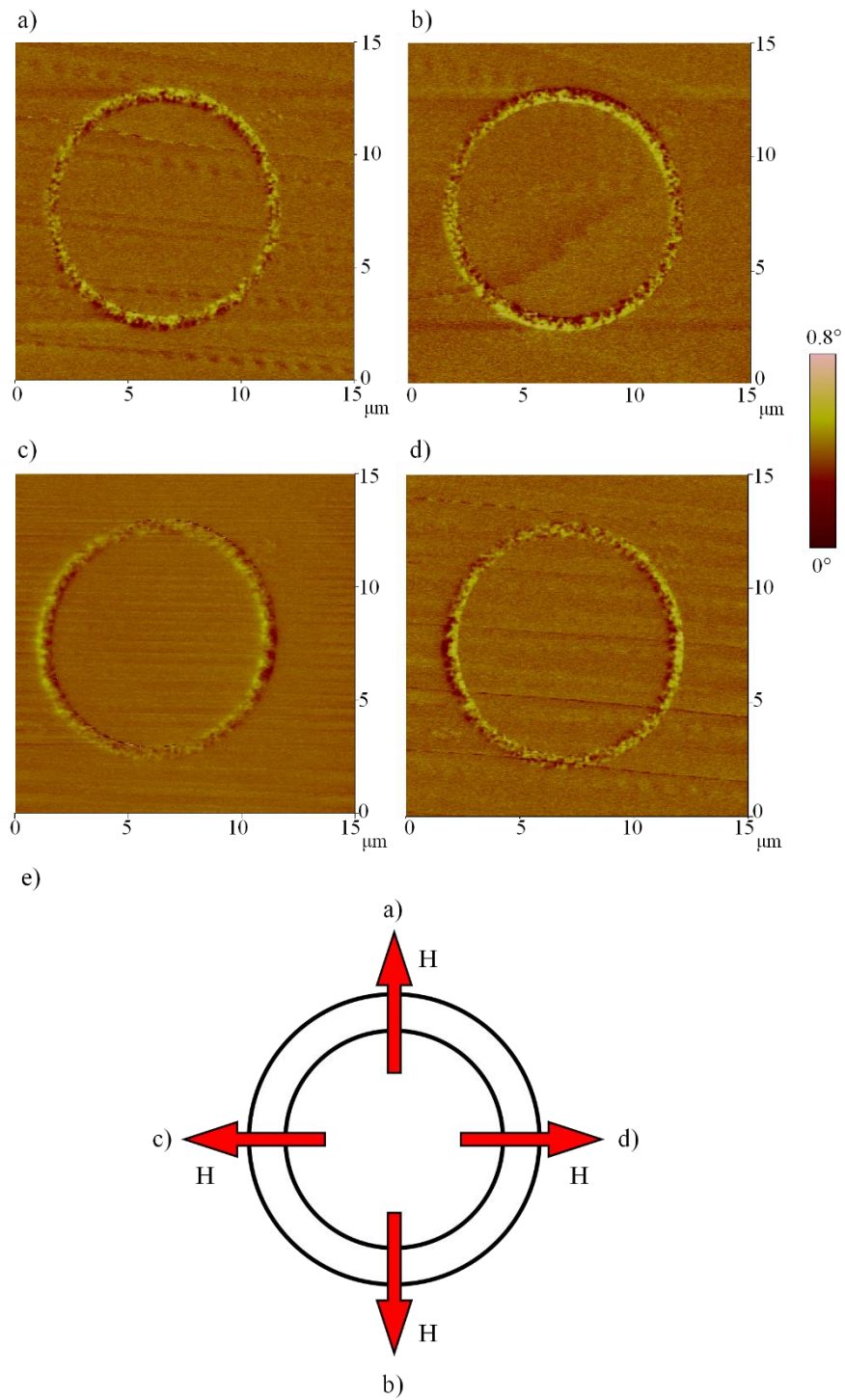


Figure 8.6. MFM images taken from C1 on 500°C Si with different applied magnetic field directions. The direction of the applied magnetic field is illustrated in the schematic.

Figure 8.7 & Figure 8.8 show MFM images of 300 °C MgO (Figure 8.7) & 500 °C MgO (Figure 8.8) nanorings with geometries A1-F1 after saturation and relaxation. The nanoring A1 on the 500 °C MgO sample did not form during the nanostructure process, and is therefore missing from Figure 8.8. The MFM lift height was 100 nm for both figures. All of the nanorings imaged show an edge contrast in the direction of applied magnetic field, which is caused by the nanorings remaining in a saturated state after the magnetic field is removed. This occurs for these nanostructures, and those on Si substrates, due to the large M_r/M_s and coercivity values observed in the $\text{Fe}_3\text{O}_4/\text{MgO}$ & $\text{Fe}_3\text{O}_4/\text{Si}$ thin films. Clearly, the rings' demagnetising field alone was not sufficient to force their magnetisation to relax along their circumferences.

Although the edge contrast is present for the nanorings on MgO as well as Si substrates, the MFM images of the nanorings on MgO do not have the same speckled effect as seen for the nanorings on Si. This can be explained by comparing the surface roughness and morphology of the pre-cursor films. It was shown in Chapter 6 that $\text{Fe}_3\text{O}_4/\text{Si}$ thin films had a granular structure and a large surface roughness, which is in contrast to the $\text{Fe}_3\text{O}_4/\text{MgO}$ thin films which had a nanocrystalline surface and a surface roughness < 1 nm. This smaller roughness greatly reduces the speckled effect in the MFM images of nanorings on MgO substrates, and in its place is a smooth surface.

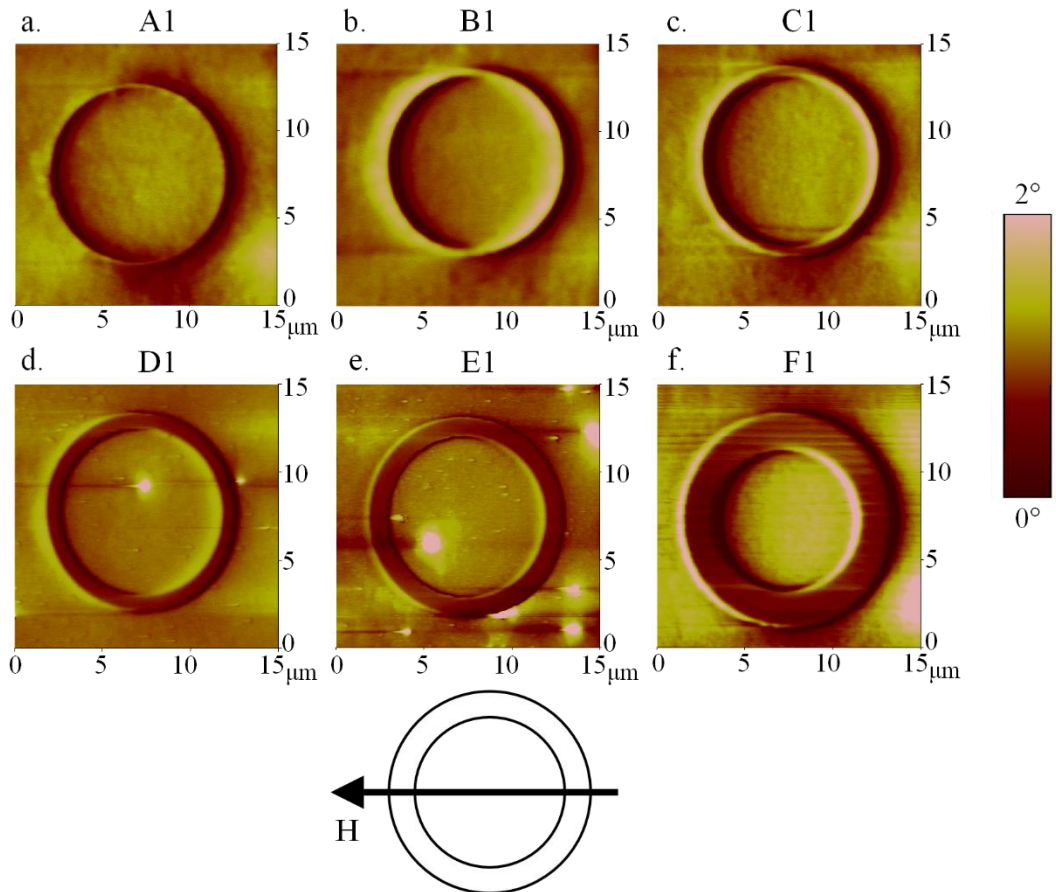


Figure 8.7. MFM images of nanorings from 300 °C MgO taken at a lift height of 100 nm after a 3.5 kOe field is applied parallel to the sample surface. All nanorings have a radius of 5 μm and have a wire width of a) 100 nm (A1), b) 300 nm (B1), c) 500 nm (C1), d) 800 nm (D1), e) 1000 nm (E1) and f) 2000 nm (F1).

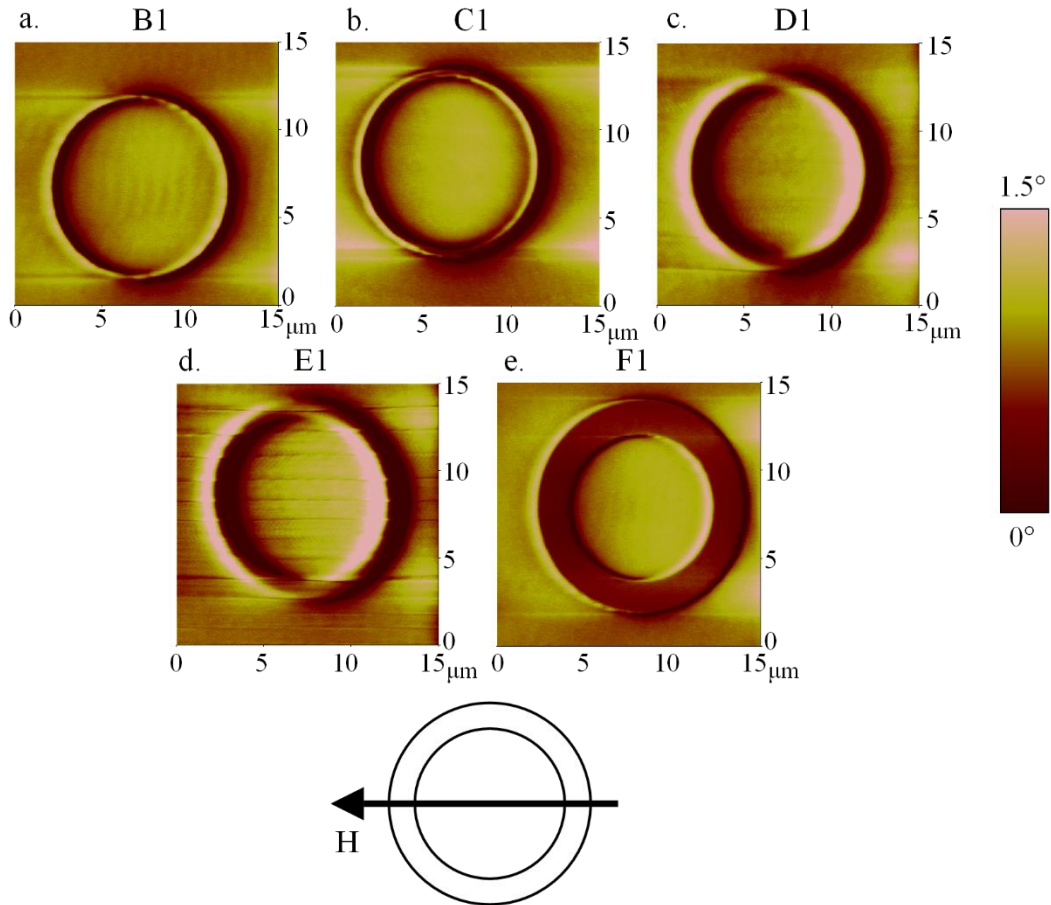


Figure 8.8. MFM images of nanorings from 500 °C MgO taken at a lift height of 100 nm after a 3.5 kOe field is applied parallel to the sample surface. All nanorings have a radius of 5 μm and have a wire width of a) 300 nm (B1), b) 500 nm (C1), c) 800 nm (D1), d) 1000 nm (E1) and e) 2000 nm (F1).

It has been shown using MFM images that nanorings created from reactively sputtered Fe_3O_4 thin films grown on Si & MgO substrates remain in a saturated state after an in-plane magnetic field is applied and removed. This saturated state produces contrast along the nanoring edges which has been shown to change direction depending on the applied field direction. The rings' demagnetising field alone was not sufficient to force the magnetisation to relax along their circumference. The large surface

roughness of the $\text{Fe}_3\text{O}_4/\text{Si}$ nanostructures produced a speckled effect on the nanostructure surface caused by the formation of north and south poles at the grain edges. This speckled effect is not seen for the nanostructures created on MgO substrates, as the surface roughness is < 1 nm. From this point onwards the Si nanorings were not imaged as the field gradients produced by the rough surface were very complex in the near field.

8.4. Magnetic force microscopy of ring-shaped nanowires following application of reverse magnetic fields

It was shown in Section 8.3 that the nanostructures created from $\text{Fe}_3\text{O}_4/\text{MgO}$ thin films remained in a saturated magnetic state after an in-plane magnetic field was applied and removed. The demagnetising field of the nanorings alone were not sufficient to force the magnetisation to follow the circumference. To reach a non-saturated state with the aim of creating a domain wall in the nanorings, a small negative field was applied to $\text{Fe}_3\text{O}_4/\text{MgO}$ nanorings after applying a 3.5 kOe magnetic field.

In this study, the 300 °C MgO nanorings from Section 8.3 were first saturated with a + 3.5 kOe in-plane magnetic field before a small negative field of -240 Oe was applied. The MFM images from these nanorings are presented in Figure 8.9. The nanorings are clearly no longer in a fully saturated state as the edge contrast is seen to alternate several times on the outer and inner circumference of the nanoring. Although the nanorings are no longer in the fully saturated state, domain walls have not been formed in these images.

The magnetic state seen in Figure 8.9 is similar to that produced by Fonin et al. [4] where nanorings were created from an epitaxial $\text{Fe}_3\text{O}_4/\text{MgO}$ (100) thin film with a 4-fold magnetocrystalline anisotropy. The MFM image taken after the nanorings were magnetised along their easy axis and its visual schematic of the magnetisation state are presented alongside Figure 8.9b as a comparison in Figure 8.10. It can be seen that the previous saturated state from Section 8.3 has started to collapse to follow the shape of the nanoring. This is in contrast to the MFM image in [4] where the magnetisation is forced by the magnetocrystalline anisotropy to follow the crystal axes.

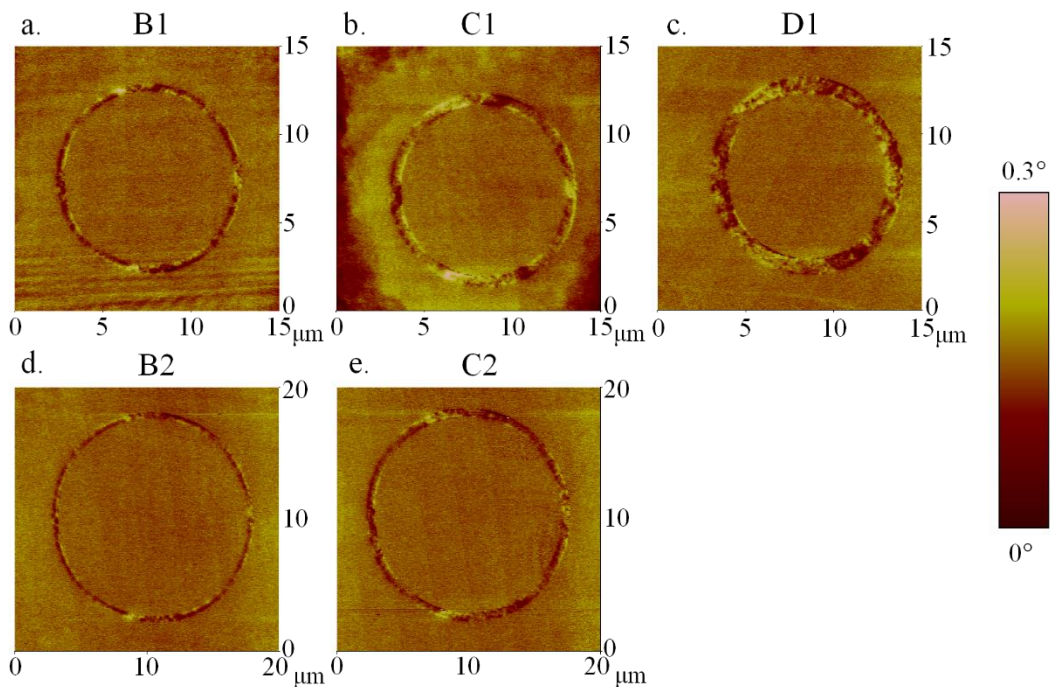


Figure 8.9. MFM images of nanorings from 300 °C MgO taken at a lift height of 50 nm after a negative field (- 240 Oe) was applied post saturation in a + 3.5 kOe field. The nanorings along the top row have a radius of 5 μm and the bottom row have a radius of 7.5 μm , with wire widths of a) 300 nm (B1), b) 500 nm (C1), c) 800 nm (D1), d) 300 nm (B2) and e) 500 nm (C2).

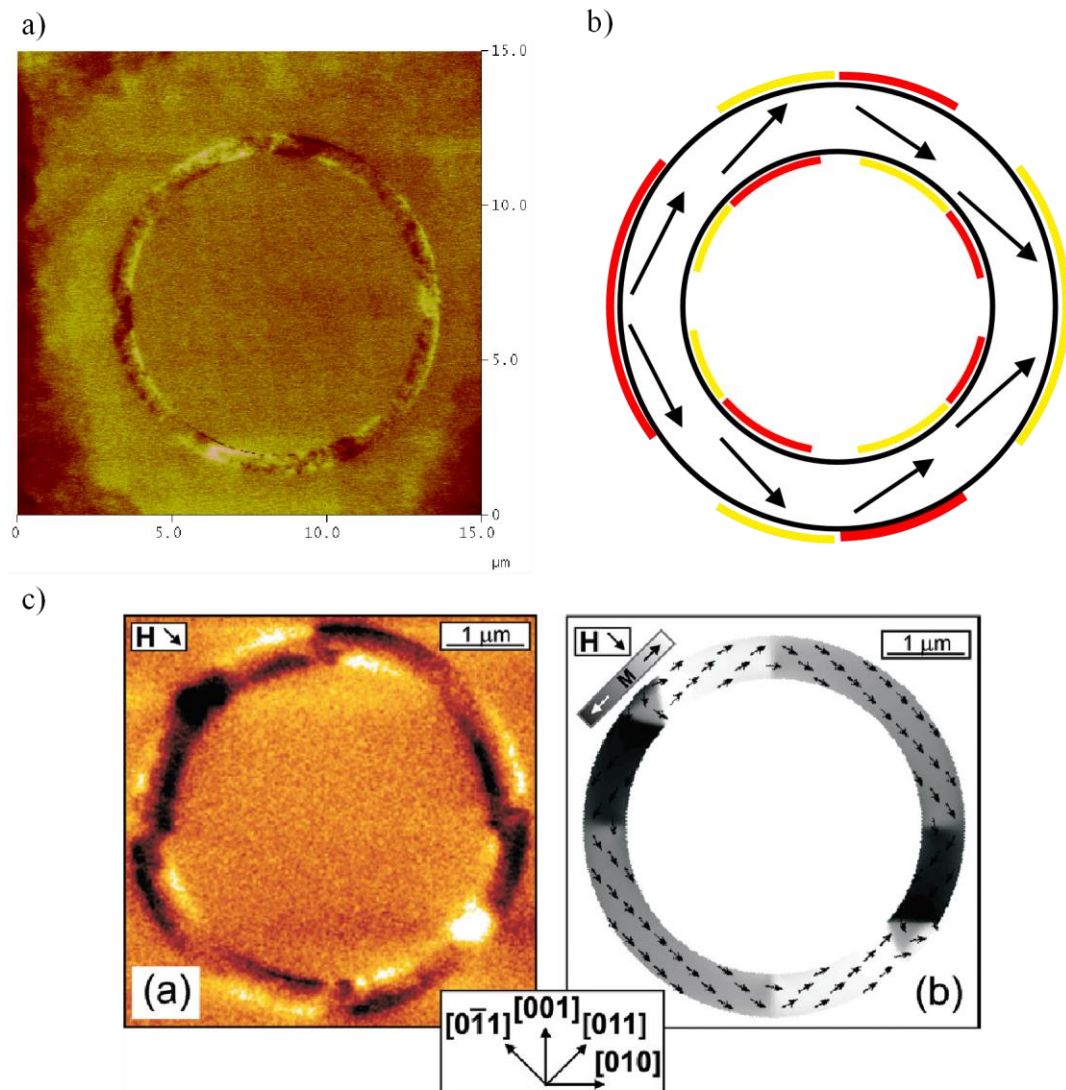


Figure 8.10. a) MFM image of C1 from 300 °C MgO after a -240 Oe magnetic field is applied following being saturated in a +3.5 kOe field. b) Schematic of the MFM image in a) illustrating how the magnetisation state creates the edge contrast. c) MFM image and corresponding OOMMF simulation from [4] where the $\text{Fe}_3\text{O}_4/\text{MgO}$ nanoring is magnetised along its easy axis.

To establish how the magnetic state in Figure 8.9 was formed, MFM images were taken of the nanorings at increasing negative magnetic fields after saturation. However, after trying to reach the saturated magnetic state seen in Figure 8.7 by applying a + 3.5 kOe field, only a magnetic state similar to that seen in Figure 8.9 is observed. The reason for this is unknown at time of writing.

Although the saturated state was not achieved, MFM images were taken at -50 Oe intervals to a final magnetic field of -450 Oe. The nanoring imaged in this negative magnetic field series was D1 from the 300 °C MgO nanoring array. These results are presented in Figure 8.11, with Figure 8.11a being measured after the + 3.5 kOe field was applied.

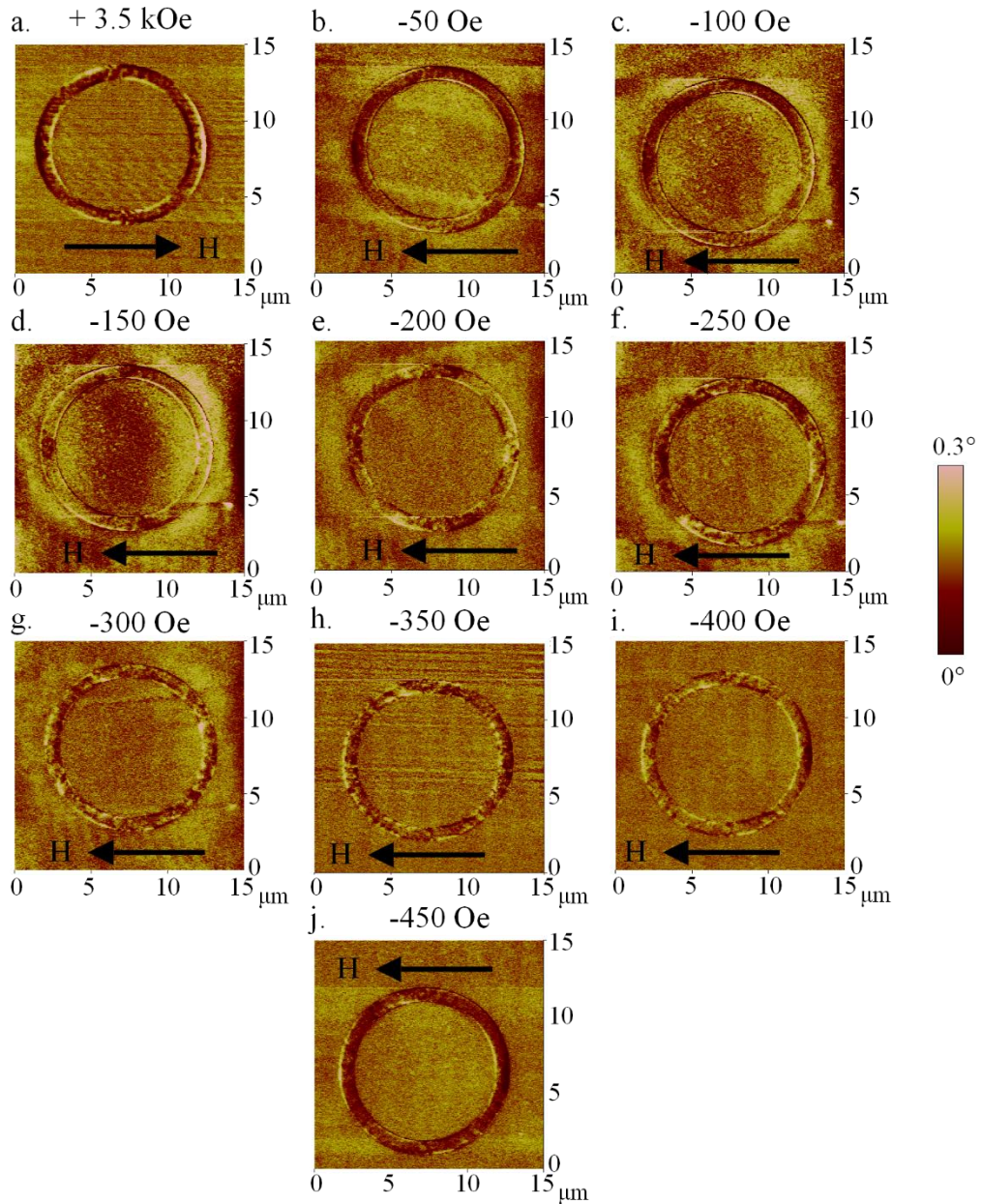


Figure 8.11. MFM images of “D1” from 300 °C MgO taken at increasing negative magnetic fields after an applied magnetic field of + 3.5 kOe, with an interval of - 50 Oe. (a) Post + 3.5 kOe magnetic field, (b-j) increasing negative magnetic field from - 50 Oe (b) to - 450 Oe (j). All images taken at a lift height of 50 nm.

An important feature about the MFM images in Figure 8.11 is the reverse in magnetic state between Figure 8.11a and Figure 8.11j. The magnetic state starts by pointing

predominately left to right, and finishes right to left with the change occurring around Figure 8.11d with a negative field of -150 Oe. It is in this image that we are closest to producing a domain wall in a nanoring.

It has been shown that domain wall formation in nanorings created from reactively sputtered $\text{Fe}_3\text{O}_4/\text{MgO}$ thin films is challenging. These nanorings remain in a saturated magnetic state after a $+3.5$ kOe in-plane magnetic field is applied. After applying a small negative field after saturation it has been shown that the magnetisation starts to collapse to follow the circumference of the nanoring. However, this does not form a domain wall in these nanorings. The saturated state of nanostructures could be utilised for the atom trapping application, where the stray field from the end of a nanowire that is magnetised along its length is used in place of a domain wall.

8.5. Using a magnetised Fe_3O_4 nanostructure as a nanoscale magnetic field source

As there has been no clear formation of a domain wall in the Fe_3O_4 nanorings on Si & MgO substrates, MFM images have been taken of an Fe_3O_4 nanowire that has been magnetised along its length with a 3.5 kOe magnetic field. The stray field from the end of the nanowire could be utilised for the atom trapping application in place of a domain wall.

The nanowire imaged here has a width of 300 nm and length of 50 μm , and is from the same substrate as the 300 $^\circ\text{C}$ MgO nanoring array measured above in Section 8.3.

These MFM images are presented along with the corresponding AFM images in Figure 8.12.

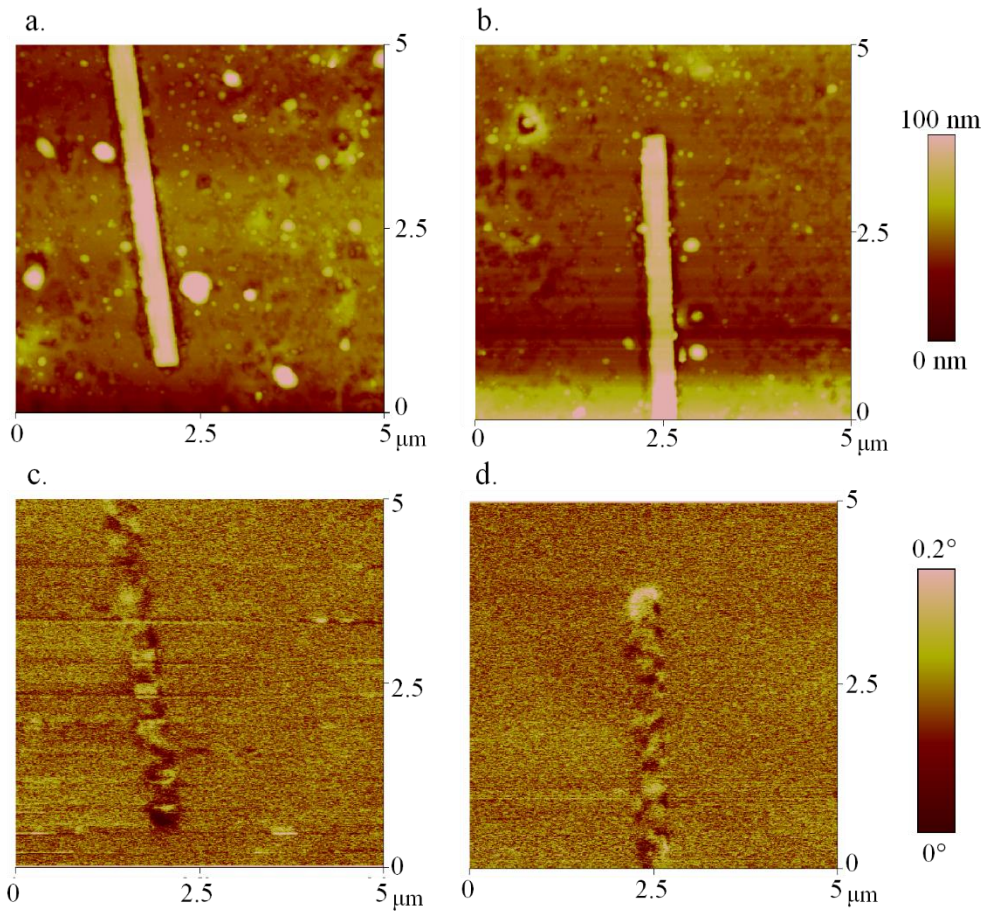


Figure 8.12. AFM (a & b) and MFM (c & d) images of a nanowire on 300 °C MgO after a 3.5 kOe magnetic field is applied along its length. The width of the nanowire is 300 nm and its length is 50 μm .

It can be seen in the MFM images (Figure 8.12c & d) that there is a bright and a dark spot at either end of the nanowire. The stray field emanating from the ends of the nanowire could be utilised as a stationary trap for ultra-cold atoms using the technique described in Section 3.2.4. The MFM images also show a stripy effect along the length

of the nanowire, which could be caused by edge roughness of the nanowire but also by APBs present in the wire causing oppositely magnetised domains.

As a comparison to the nanostructures fabricated and analysed in this chapter, an Fe_3O_4 thin film on an MgO (100) substrate which had a nano-tower surface morphology was analysed using MFM. The sample chosen for this investigation was a 35 nm $\text{Fe}_3\text{O}_4/\text{MgO}$ (100) thin film grown at 400 °C with a smooth background surface and range of different sized nano-towers. A 3.5 kOe in-plane magnetic field was applied to the sample prior to the imaging, with the MFM image taken using a lift height of 50 nm. Figure 8.13 shows the corresponding AFM and MFM images of this sample.

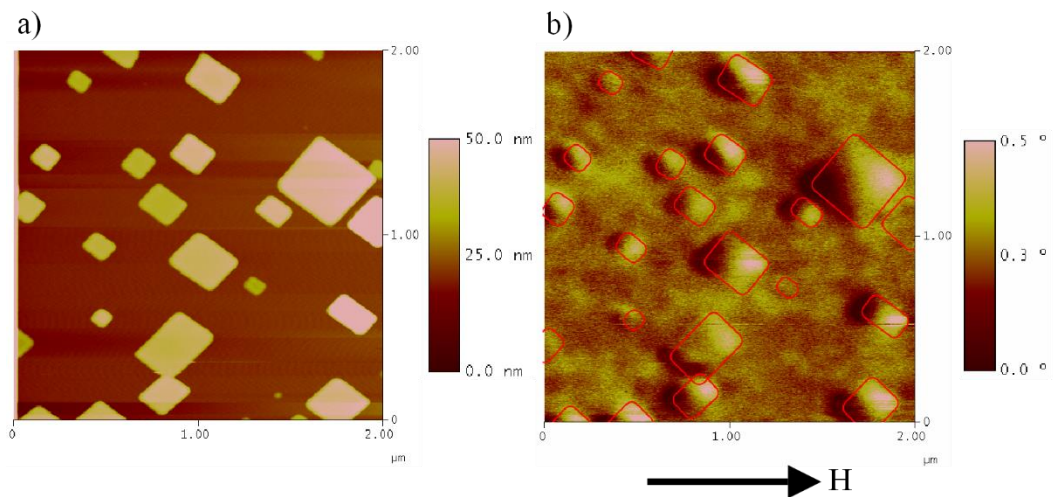


Figure 8.13. (a) AFM & (b) MFM images from a 35 nm $\text{Fe}_3\text{O}_4/\text{MgO}$ (100) using a lift height of 50 nm. The red outlines in the MFM image illustrate the outline of the nano-towers from the AFM image.

From Figure 8.13 it is clear to see that the nano-towers are magnetic from the large contrast across the towers which are outlined in red in the MFM image. It is also clear

that these structures are retaining their saturated state after the magnetic field is removed producing strong magnetic poles at the edges of the nano-towers. This is in stark contrast to the polycrystalline Fe_3O_4 patterned square dots on Si/SiO₂ created by Tsai et al [5], where the surface of the dots had a speckled pattern both in an applied field and in their remnant state. The remnant state of the nano-towers in Figure 8.13b is comparable to the fabricated $\text{Fe}_3\text{O}_4/\text{MgO}$ rings shown in Figure 8.7Figure 8.8, where magnetic poles are retained at the edge of the structures with a smooth surface for the rest of the structure.

The stray field from the remnant state nano-towers could also be used as a stationary nanoscale magnetic field source for trapping ultra-cold atoms. A similar thin film growth feature which was previously thought to be a hindrance has been shown to be useful was the random magnetisation inhomogeneities of a perpendicularly magnetised TbGdFeCo film. These inhomogeneities produced a corrugated potential which has been utilised to create a novel sensor for gravitational fields [6].

8.6. Conclusion

Nanostructures were created from reactively sputtered Fe_3O_4 thin films grown on Si and MgO substrates. These nanostructures were imaged using MFM after an in-plane magnetic field of 3.5 kOe was applied, and were shown to remain in a saturated state that was dependent on the direction of the applied field. The nanorings remained in a saturated state as the demagnetising field along for the nanorings was not sufficient to force the magnetisation to follow the circumference of the ring.

The nanorings on Si substrates produced a speckled effect on the surface of the nanorings, caused by the large surface roughness producing numerous north and south poles at the edges of grains. This speckled effect was missing from the nanorings on MgO substrates due to surface roughness being < 1 nm.

Attempts were made to form a domain wall in the nanorings on MgO substrates by applying a small negative magnetic field after saturation. Although this removed the saturated state of the nanorings, a domain wall was not produced. The magnetic state appeared to resemble a slightly collapsed saturated state, where the magnetisation deviates slightly from the saturated state to follow the shape of the nanoring.

By magnetising a $\text{Fe}_3\text{O}_4/\text{MgO}$ nanowire along its length, a possible nanoscale magnetic field source is created at the ends of the nanowire which could be used for a stationary atom trap. Another possible nanoscale magnetic field source was found after magnetising a $\text{Fe}_3\text{O}_4/\text{MgO}$ (100) thin film with a nano-tower surface morphology. The nano-towers remained saturated in a remnant state, which produced strong magnetic poles at the edges of the structures.

References

- [1] D. A. Allwood, T. Schrefl, G. Hrkac, I. G. Hughes, and C. S. Adams, "Mobile atom traps using magnetic nanowires," *Applied Physics Letters*, vol. 89, pp. 014102-014104, 2006.
- [2] M. Negoita, T. J. Hayward, and D. A. Allwood, "Controlling domain walls velocities in ferromagnetic ring-shaped nanowires," *Applied Physics Letters*, vol. 100, pp. 072405-072409, 2012.
- [3] M. Negoita, M. P. P. Hodges, M. T. Bryan, P. W. Fry, M.-Y. Im, P. Fischer, *et al.*, "Linear transport of domain walls confined to propagating 1-D potential wells," *Journal of Applied Physics*, vol. 114, pp. 163901-163906, 2013.
- [4] M. Fonin, C. Hartung, U. Rudiger, D. Backes, L. Heydeman, F. Nolting, *et al.*, "Formation of magnetic domains walls in epitaxial Fe₃O₄ (100) elements (invited)," *Journal of Applied Physics*, vol. 109, pp. 07D315-07D318, 2011.
- [5] J. L. Tsai, K. T. Huang, W. C. Cheng, M. D. Lee, T. S. Chin, S. U. Jen, *et al.*, "Magnetic properties of patterned Fe₃O₄ films," *Journal of Magnetism and Magnetic Materials*, vol. 272, pp. 1664-1665, 2004.
- [6] B. V. Hall, S. Whitlock, R. Anderson, P. Hannaford, and A. I. Sidorov, "Condensate splitting in an asymmetric double well for atom chip based sensors," *Physical Review Letters*, vol. 98, pp. 1-4, 2007.

9. Conclusion

Iron oxide thin films have been grown on Si substrates using reactive dc magnetron sputtering from Fe targets. The iron oxide phase has been shown to vary with the substrate growth temperature used, with Fe_3O_4 being grown at temperatures of 200 – 500 °C and a mixed iron oxide phase of Fe_3O_4 and $\alpha\text{-Fe}_2\text{O}_3$ being grown at RT & 100 °C. Glancing angle XRD and AFM measurements have been shown that the $\text{Fe}_3\text{O}_4/\text{Si}$ films are polycrystalline and granular.

It has been shown that when Fe_3O_4 thin films are grown on MgO (100) substrates they form a textured film with a smooth surface. This is likely to be due to the similar oxygen lattice structure between Fe_3O_4 & MgO. Multiple different surface morphologies have been imaged for Fe_3O_4 thin films grown on MgO substrates, which is possibly caused by variations in thermal contact between the substrate and substrate holder. The coercivity of the Fe_3O_4 films has a negative trend with the film thickness for both substrates, whereas the grain size ($\text{Fe}_3\text{O}_4/\text{Si}$) has a positive trend with both film thickness and growth temperature. The coercivity values of the Fe_3O_4 films grown on MgO substrates have been shown to be ~ 100 Oe smaller than those grown on Si substrates.

Following an annealing treatment of Fe_3O_4 thin films at 250 °C in air for just 4 minutes the composition of the film was altered to become a mixed iron oxide of Fe_3O_4 & $\gamma\text{-Fe}_2\text{O}_3$. Dramatic changes in coercivity have been observed, with a large increase seen for the films on Si and negligible change seen for the films on MgO. However, a significant decrease in coercivity has been seen for a smooth film on MgO and the

CONCLUSION

increase in coercivity on Si is dependent on the presence of Fe₃O₄ regions amongst the mixed iron oxide.

Nanostructures of Fe₃O₄ were created from thin films on Si & MgO, with the nanorings remaining in a saturated state after an in-plane magnetic field is removed. Applying a small negative field to the nanorings on MgO produces a magnetic structure similar to that seen in nanostructures with a 4-fold magnetocrystalline anisotropy. However, none of these magnetic states produce a domain wall in the nanoring. As an alternative to a domain wall, a nanowire magnetised along its length has been shown to produce a strong magnetic stray field from its ends. A similar strong magnetic stray field has been produced from the edges of nano-towers that featured on the surface of some Fe₃O₄/MgO thin films. These both could be used as a nanoscale source of magnetic field for a stationary atom trap.

The following future work has been proposed:

- A study where the Ar:O₂ ratio is varied for iron oxides grown at room temperature. In this thesis a single Ar:O₂ ratio was used (15:0.9 sccm) which produced a mixed iron oxide phase when grown at room temperature. Removing the elevated growth temperature for the Fe₃O₄ thin films will remove the need to use a hard mask and ion milling to create the nanostructures, and would also reduce the variation due to thermal contact with the sample holder during growth.
- Further work where the effect of surface morphology of Fe₃O₄/MgO thin films on the coercivity of annealed Fe₃O₄ thin films is studied. For this study, a series of Fe₃O₄/MgO thin films would be needed with a range of different

surface morphologies: smooth surface, nano-tower surface & flattered nano-tower surface. These films would be analysed using AFM, MFM, MOKE & Raman spectroscopy both prior and post annealing to establish what compositional, magnetic and surface morphology changes occur.

- An investigation into the nano-towers observed on several of the $\text{Fe}_3\text{O}_4/\text{MgO}$ (100) films using a focussed-MOKE to establish the switching behaviour of the individual nano-towers. It would also be interesting to compare the magnetic switching behaviour of these nano-towers compared to their size. This would provide useful information if the nano-towers on a $\text{Fe}_3\text{O}_4/\text{MgO}$ thin film were to be used as a nano-sized magnetic field source.
- A repeat of the annealing study where the treatment was performed in a variety of different atmospheres would be interesting to establish the greatest coercivity decrease whilst maintaining the same film composition. A variation changing the annealing atmosphere would be to vary the annealing time using the same procedure in Chapter 7 to establish whether the Fe_3O_4 thin films become fully converted to $\gamma\text{-Fe}_2\text{O}_3$.

CONCLUSION

List of Acronyms, Symbols and Constants

Materials:

Fe₃O₄: Magnetite

γ-Fe₂O₃: Maghemite

α-Fe₂O₃: Hematite

FeO: Wüstite

Acronyms:

AAO: Anodic aluminium oxide (template)

AFM: Atomic force microscope

APB: Anti-phase boundary

CEMS: Conversion electron Mössbauer spectroscopy

CVD: Chemical vapour deposition

DW: Domain wall

MBE: Molecular beam epitaxy

MFM: Magnetic force microscopy

LIST OF ACRONYMS, SYMBOLS AND CONSTANTS

MOKE: Magneto-optic Kerr effect

MOT: Magneto-optical trap

MR: Magneto-resistance

M-TXM: Magnetic transmission x-ray microscope

OOMMF: Object oriented micromagnetic framework

PEEM: Photoemission electron microscopy

PLD: Pulsed laser deposition

QIP: Quantum information processing

SEM: Scanning electron microscope

SQUID: Superconducting quantum interference device

TEM: Transmission electron microscope

TOP: Time-orbiting potential

XMCD: X-ray magnetic circular dichroism

XPS: X-ray photoelectron spectroscopy

XRD: X-ray diffraction

Symbols:

A: Material specific exchange stiffness constant

B: Magnetic induction (Magnetic flux density)

B_b: Bias magnetic field

B_{dw} : Domain wall stray field

$B_J(\alpha)$: Brillouin function

$D(E)$: Density of states

D : Domain size

E_d : Magneto-static energy

E_{ex} : Exchange energy

E_F : Fermi energy

E_K : Magneto-crystalline anisotropy energy

E_{me} : Magneto-elastic energy

E_{total} : Total energy of a magnetic system

E_Z : Zeeman energy

e_φ : Azimuthal unit vector in cylindrical coordinates

F : Force

\mathbf{F} : Total spin of the particle

g_F : Landé-factor of the hyperfine state

H : Magnetic field strength

\hbar : Reduced Planck constant

H_c : Coercivity

H_d : Demagnetising field

H_w : Molecular field

LIST OF ACRONYMS, SYMBOLS AND CONSTANTS

I_0 : Current in a wire

J : Total angular momentum quantum number

k : Photon wavenumber

K_0, K_{C1} & K_{C2} : Anisotropy constants of a material

$L(\alpha)$: Langevin function

l : Magnet length

m : Magnetic moment

M : Magnetisation

m_F : Magnetic quantum number

M_r : Remanence

M_s : Saturation magnetisation

M_{spont} : Spontaneous magnetisation

N : Number of atoms per unit volume

N_d : Demagnetising factor

p_i : Pole strength

r : Pole separation

t : Film thickness

T : Temperature

T_C : Curie temperature

T_M : Morin temperature

T_N : Néel temperature

T_V : Verwey temperature

U : Trap depth

V_{mag} : Potential energy

α_i : Directional cosine

γ : Molecular field constant

θ : Angle between x-ray and sample

μ : Magnetic permeability

ρ : Resistivity

σ : Angle between magnet and magnetic field

τ : Torque

χ : Susceptibility

ψ : Angle between magnetisation and hexagonal axis

ω_L : Larmor frequency

ω_{trap} : Trap frequency

Constant:

k_B : Boltzmann constant = 1.38×10^{-23} J/K

μ_0 : Permeability of free space = $4\pi \times 10^{-7}$ H/m

μ_B : Bohr magneton = 9.27×10^{-24} J/T